Welcome to Twin Particles: From Novel ZZ Estimate to Searches for Supersymmetric Sleptons and Higgsinos using the ATLAS Run-2 Data and at the High-Luminosity LHC

Jorge Andrés Sabater Iglesias

Fakultät für Mathematik und Physik
Albert-Ludwigs-Universität Freiburg

Welcome to Twin Particles: From Novel ZZ Estimate to Searches for Supersymmetric Sleptons and Higgsinos using the ATLAS Run-2 Data and at the High-Luminosity LHC

Dissertation
zur Erlangung des Doktorgrades der
Fakultät für Mathematik und Physik der
Albert-Ludwigs-Universität Freiburg

vorgelegt von

Jorge Andrés Sabater Iglesias

April 2021

Dekan

Prof. Dr. Michael Thoss

Betreuer der Arbeit

Prof. Dr. Beate Heinemann, Dr. Federico Meloni

Datum der mündlichen Prüfung: 05.07.2021

Prüfer

Prof. Dr. Gregor Herten

Prof. Dr. Beate Heinemann

Prof. Dr. Harald Ita

Acknowledgments

First and foremost, I would like to acknowledge my supervisor Prof. Dr. Beate Heinemann and ex-supervisor Dr. Pieter Everaerts, who first showed interest in me and made all this possible. Although the time was short with Pieter, I definitely enjoyed it. Thanks to Prof. Dr. Beate Heinemann for her wise mentoring, guidance and for always making sure that I was in a comfortable working environment, this certainly helped me during my PhD. Her experience and expertise have also led to a great improvement of the research quality of my work, as well as her great care in proofreading the thesis. Second, I would like to thank my supervisor Dr. Federico Meloni for his invaluable advice, inspirational guidance and his technical comments, all of which have contributed in my preparation as an independent researcher, and for which I will always be grateful. Also thanks to Dr. Sergio Cornell-Diez for guiding me through my first contact with a hardware project.
It has also been a huge privilege working in such a diverse and enjoyable environment such as the DESY ATLAS group, I think the atmosphere could not have been better. I owe special thanks to Marius and Daniel for guiding me through my first months in Hamburg and at DESY, my office mates: Emily, Fang-Ying and Hamish and also all my other friends at DESY: Vincent, Alessandro Guida, Surabhi, Alessia, Marco, Sonia, Alessandro Biondini, Eloisa .... Also to all the people in the ATLAS group at DESY that at some point I approached to ask some question. I also want to thanks Thomas Mclachlan, Kurt Brendlinger, Jan Küchler and Daniela Küchler for the useful comments on the thesis.
Special mention to Margherita Primavera, Sonia Carra, and the entire 2L0J analysis team, for continuously ensuring a good quality of the slepton analysis, and to Marco Rimoldi for his help in the technical aspects. Thanks also to the upgrade team: Claudia Merlassino, Simone Amoroso, Brian Petersen and John Anders.
I also want to thank the people who made me disconnect from work with whom I think I have built a life-long relationship: Pilar, Mari, Jan, Winston, Jose and Denis. My friends from Nikhef which made my stays at CERN really enjoyable: Alice, Anamika, Michiel and Mauricio. I would also like to thank my friends from college

who have always been there, and where everything started. Un saludo para toda la squadra: Diego, Pablo, Manolo, Dani, David, Drago, Alberto, Leire, Mica, Rafa y Martín. Gracias también a todo el 4bc por las eternas risas que me han brindado siempre, a Sara y a Rubén (y su tío) por sus visitas. No me puedo olvidar de Paula, la persona que me ha acompañado durante los últimos años y que siempre se ha preocupado por mí, gracias por todo. También a mi hermano Jose por las risas, por el apoyo, y por la pesca del lucio, tak tak tak. Por último quiero dedicar esta tesis a mi madre y a mi padre, que estoy seguro de que estarían muy orgullosos de mí, les quiero.

Abstract

After the Higgs boson discovery by the ATLAS and CMS collaborations at CERN, one of the main goals of the Large Hadron Collider programme is to find Beyond the Standard Model particles. This thesis focuses on the search for supersymmetric partners of the leptons (sleptons) and presents the prospects of a search for the supersymmetric partners of the electroweak gauge bosons and the Higgs boson (higgsinos). The detectable final state for both signatures consists of two electrons or muons with opposite electric charge. The search for the sleptons is performed using the full Run-2 data collected by the ATLAS detector, corresponding to an integrated luminosity of 139 fb^{-1} at $\sqrt{s} = 13$ TeV. In the regions sensitive to the slepton signal, the selected events are found to be consistent with the Standard Model predictions. The higgsino search is developed in the context of the next major upgrade of the LHC, the High-Luminosity LHC (HL-LHC). The thesis assesses the sensitivity reach on the search for higgsinos by the end of the HL-LHC era, by which the ATLAS detector is expected to have recorded an integrated luminosity of 3000 fb^{-1} at $\sqrt{s} = 14$ TeV. The results obtained show that using the full HL-LHC dataset, higgsinos with masses of about 200 GeV could be discovered, and masses up to 350 GeV could be excluded. The thesis also discusses the possibility of estimating the Standard Model ZZ process using $Z\gamma$ events from data in Beyond the Standard Model searches, showing that theoretical uncertainties of about 4% can be achieved. In addition to the LHC data analyses, the thesis reports on the design of a cooling setup with the aim of testing the silicon modules that will be placed in the upgraded ATLAS Inner Detector.

Zusammenfassung

Nach der Entdeckung des Higgs Bosons durch die ATLAS und CMS Kollaborationen am CERN ist eines der primären Ziele des Large Hadron Collider Programms Teilchen zu finden, die über das Standardmodell der Teilchenphysik hinausgehen. Fokus dieser Arbeit ist die Suche nach supersymmetrischen Partnern der Leptonen (Sleptonen), sowie die Perspektiven einer Suche nach supersymmetrischen Partern der elektroschwachen Eichbosonen und des Higgs Bosons (Higgsinos). Der detektierbare Endzustand beider Signaturen beinhaltet zwei Elektronen oder Muonen mit entgegengesetzter elektrischer Ladung. Die Suche nach Sleptonen basiert auf dem vollen Run-2 Datensatz aufgenommen vom ATLAS Detektor, entsprechend einer intergrierten Luminosität von 139 fb^{-1} bei $\sqrt{s} = 13$ TeV. In den Bereichen, die auf das Slepton Signal sensitiv sind, erweisen sich die selektierten Ereignisse als konsistent mit den Vorhersagen des Standardmodells. Die Suche nach Higgsinos wird im Kontext der nächsten großen Erweiterung des LHC entwickelt, dem High-Luminosity LHC (HL-LHC). Die Arbeit bestimmt die erwartete Sensitivität der Suche nach Higgsinos am Ende des HL-LHC Programms, mit einem erwarteten Datensatz des ATLAS Detektors von 3000 fb^{-1} bei $\sqrt{s} = 14$ TeV. Die erzielten Ergebnisse zeigen, dass Higgsinos mit Massen von etwa 200 GeV mit dem vollen HL-LHC Datensatz entdeckt werden könnten, und Massen bis 350 GeV ausgeschlossen werden könnten. In der Arbeit wird auch die Möglichkeit zur Abschätzung des Standardmodell ZZ Prozesses in Suchen nach Physik jenseits des Standardmodells besprochen, die auf der Selektion von $Z\gamma$ Ereignissen in Daten basiert und eine Theorieunsicherheit von 4% erreicht. Zusätzlich zur Analyse der LHC Daten wird in dieser Thesis über den Entwurf eines Kühlungsaufbaus berichtet, mit dem Ziel, die Silizium Module zu testen, die im aufgerüsteten inneren Detektor des ATLAS Experiments installiert werden sollen.

Contents

1 Introduction

During the last century, huge progress has been made in the understanding of elementary particles and their interactions. The strong, weak and electromagnetic interactions are described by the Standard Model (SM) of particle physics. Experiments have verified this theory up to very high energies (10^{12} eV) and down to attometer distances (10^{-18} m). Cosmology and astrophysical observations have also proven it to be a very successful theory. However, we know that the SM is not the ultimate theory: gravity is not incorporated, there is no explanation for the number of generations of quarks and leptons, and there are ~ 20 free parameters (masses, coupling constants and mixing angles) that have to be determined experimentally. Furthermore, the SM does not explain the matter-antimatter asymmetry that we observe. The astrophysical evidence of dark matter and dark energy also remains unexplained. All these arguments suggest (i) the existence of new particles, and (ii) that the SM is the low-energy limit of a more fundamental theory.

The last missing piece of the Standard Model, the Higgs boson, was discovered in 2012 by the ATLAS and CMS detectors at CERN, with a measured mass of about 125 GeV. This confirmed the electroweak symmetry breaking mechanism of the Standard Model, but also emphasized the *hierarchy problem*. The Higgs boson mass is affected in the Standard Model by radiative corrections. Since these higher-order (loop) corrections depend on the scale of new physics[1], the Higgs boson mass can, in principle, have values up to the Planck scale $\sim 10^{19}$ GeV. To obtain the measured mass value, the cancellation of all possible corrections contributing to the Higgs boson mass have to be fine-tuned to 1 part in 10^{15}. This would be an astonishing coincidence if it is not enforced by some symmetry.

The most popular symmetry that solves, or at least strongly mitigates, the hierarchy problem is Supersymmetry. In a supersymmetric theory, any fermionic state is accompanied by a bosonic one, and vice versa. This implies that for each Standard Model particle loop, there is always an accompanying loop of superpartners. The negative sign of fermionic loops and the supersymmetric relations between masses

[1] The new physics scale corresponds to the scale beyond which the low-energy theory (Standard Model) no longer applies.

and couplings, guarantee the cancellation of terms. If it is an exact symmetry, the supersymmetric particles have the same mass as the Standard Model particles. However, no "selectron" (the superpartner of the electron) has been observed with a mass of 0.511 MeV, for example. This requires Supersymmetry to be broken. The argument for the superpartners to have a mass around the TeV (10^{12} eV) scale is that the counter-term cancellation argument fails if the superpartners are too heavy. A natural question that the reader may ask is whether Supersymmetry can still be realised in Nature. The answer to this question is yes, however not every mass hierarchy of the superpartners is able to explain the shortcomings of the SM with the same ease. Therefore, in this dissertation I explore the range of masses where Supersymmetry is more likely to manifest itself, increasing in this way the probability of a potential discovery.

In order to search for the Supersymmetric particles in a collider, enough energy in the collision is needed to be able to produce them. At present, the highest-energy collider that has been built is the Large Hadron Collider (LHC). The LHC collides protons at a center-of-mass energy of 13 TeV. For this reason, it is the best-suited machine to look for supersymmetric particles, since it explores the desired energy range.

The LHC consists of a 27-km-long ring that accelerates protons and lead ions. The collisions take place at four interaction points. A detector is located at each interaction point: ATLAS, CMS, LHCb and ALICE.

ATLAS is a multipurpose detector designed to cover a large variety of physics aspects, from Standard Model measurements to Beyond the Standard Model physics (e.g. Supersymmetry searches). This thesis will present the search of the supersymmetric partners of the Standard Model leptons (sleptons) with the data recorded by the ATLAS detector. Sleptons are unstable and decay into a lepton and the lightest neutralino, resulting in a final state with two same-flavour opposite-sign leptons and missing transverse momentum coming from the undetected neutralinos. The flavour asymmetry of this final state (100% probability of same-flavour leptons) will be exploited in order to discriminate the Supersymmetry signal from known Standard Model processes.

In Beyond the Standard Model searches, it is often the case that the SM backgrounds are taken directly from Monte Carlo simulation, leading in some cases to large modelling uncertainties. In this thesis, I will also discuss a novel technique developed in order to estimate the ZZ Standard Model background in new physics searches by using a data driven approach. This can help in reducing the associated uncertainties and thus enhance the sensitivity of the searches. I will show that an uncertainty of

about 4% can be achieved by using a photon replacement technique that exploits the greater production cross section of the $Z\gamma$ Standard Model process.

During the writing of this thesis, the LHC is in the Long Shutdown 2 and has delivered 156 $fb^{-1}$of integrated luminosity during Run 2. Run 3, which begins in 2022, will deliver a total of 350 $fb^{-1}$of data over 3 years. The last major upgrade of the LHC will be the high-luminosity upgrade (HL-LHC), where the instantaneous luminosity will be a factor of five greater than the current nominal value and the center-of-mass energy will be increased to 14 TeV. By the end of this phase, the LHC is expected to deliver 3000 $fb^{-1}$of data. In order to cope with the challenging environment of the HL-LHC, major detector components of the ATLAS detector will be replaced in the Long Shutdown 3. The Inner Detector will be replaced by a new tracker (ITk) in this phase. The modules that will be installed in the ITk will operate at very low temperatures in the HL-LHC phase. Therefore, all modules will go through electrical tests to validate their performance. In order to test how the module responds after applying temperature changes, I designed a test setup to evaluate the performance of the module in response to thermal cycles. The results and potential improvements will also be discussed in this document.

Since no significant sign of Supersymmetry has been observed in any detector so far, it could be that the dataset collected by ATLAS is not large enough, or that the energy needed to produce the hypothetical particles has not been reached yet. These aspects will be decisive for the future of particles physics when considering the construction of new machines after the LHC era. To this end, I studied the expected sensitivity and discovery potential in the electroweak sector of Supersymmetry: chargino and neutralino production. The heavy neutralino will go through a decay chain resulting in two charged leptons, as well as an undetected (dark matter) particle whose presence can be inferred from the transverse momentum imbalance in the event. This channel is especially interesting since these type of scenarios probe the hierarchy problem and tackle the dark matter problem simultaneously.
The thesis is organised as follows: in Chapter 2, a theoretical introduction to the Standard Model and Supersymmetry is given, as well as a description on how proton-proton collisions are simulated. The Large Hadron Collider, the ATLAS detector, and the High Luminosity-LHC upgrade is presented in Chapter 3. The process of particle reconstruction and identification is presented in Chapter 4. Chapter 5 reports on the ZZ background estimation technique in new physics searches. Chapter 6 and Chapter 7 present the Run-2 slepton search and the HL-LHC higgsino prospects,

respectively. Final remarks and conclusions are given in Chapter 8.

2 The Standard Model and beyond

There are four fundamental forces in Nature that we know of: strong, electromagnetic, weak and gravitational. The first three of the listed forces are described by the Standard Model (SM) of particle physics. The gravitational force is not included, since it is too weak compared to the other interactions to play a significant role in particle physics. The elementary particles that constitute the SM are classified according to their spin and interaction. We can group them into matter particles (fermions) and interaction particles (bosons). The fermions can be further classified according to their interaction, we distinguish between quarks and leptons. Leptons are spin half particles that interact via the electromagnetic and weak force (they do not interact via the strong force). Three families (known as generations) of leptons are known. The first generation is composed of the electron e and its corresponding neutrino, the electron neutrino ν_e. The muon μ and the tau τ, together with their neutrinos ν_μ and ν_τ correspond to the second and third generation, respectively. Each generation of lepton pairs carries a quantum number (lepton number), which is conserved in the Standard Model.

The strongly interacting particles, called hadrons, are composed of quarks q, which again come in three generations. In the first generation, we have the up-quark u and down-quark d, these make up the proton and neutron. The strange-quark s and charm-quark c, correspond to the second generation, and the bottom-quark b and top-quark t correspond to the third generation. Free quarks have never been observed in Nature, this is a consequence of asymptotic freedom and is one of the most important features of the strong interactions. Each of the particles presented previously has a corresponding antiparticle. Systems of a quark and its antiquark $q\bar{q}$ are called mesons, and systems of three quarks qqq are called baryons. A summary of the elementary particles of the SM is depicted in Figure 1. Each baryon is assigned quantum number (baryon number) $B = 1$. In the Standard Model, baryon number is conserved, forbidding proton decay.

The SM particles interact through forces. Each of these forces has a spin one particle that mediates the interaction. The electromagnetic force is mediated by the photon

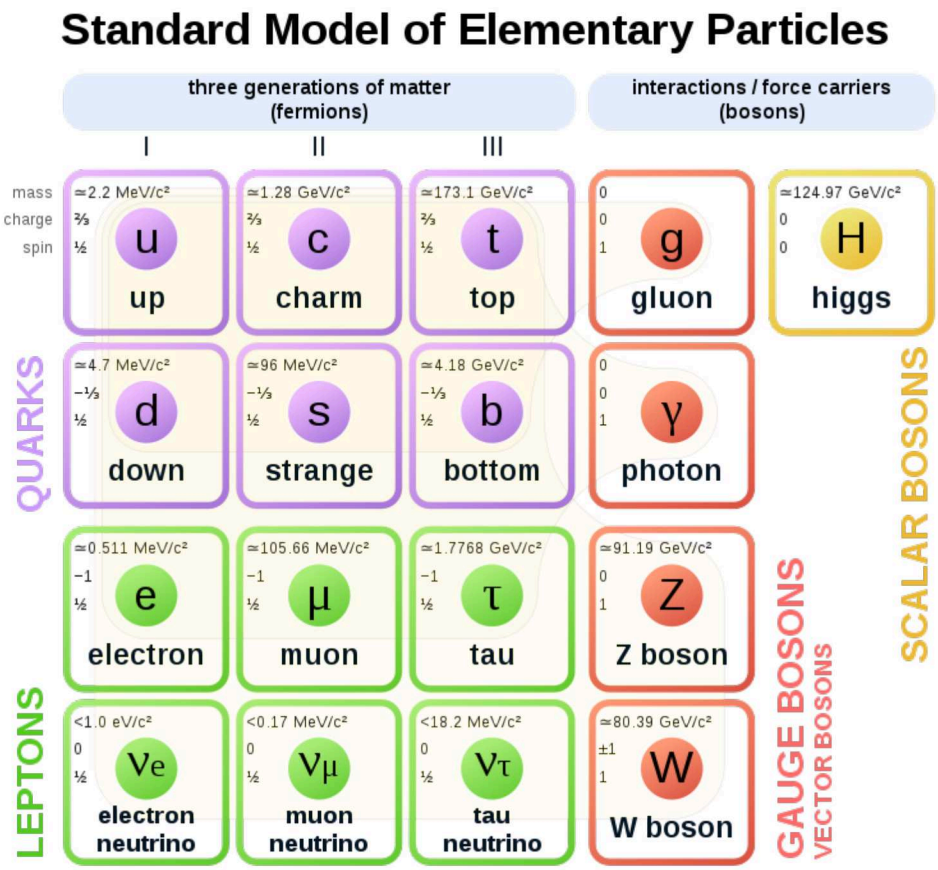

Figure 1: Elementary particles of the Standard Model: quarks (violet), leptons (green), spin-1 bosons (red) and the spin-0 Higgs boson (yellow). The mass, charge and spin is also shown for each particle. Figure taken from [1].

γ, the weak interaction by the vector bosons $W^{\pm}$ and Z^0 and the strong interaction by the gluon g. If gravity was included in the SM, the hypothetical graviton would mediate the gravitational force.

The Standard Model is based on the gauge group $G = SU(3) \times SU(2) \times U(1)$. The $SU(3)$ group is used to construct the theory of the strong interaction, Quantum Chromodynamics (QCD). The SU(3) factor has gauge coupling g_s and 8 gauge bosons, the gluons. The electroweak sector of the Standard Model is based on $SU(2)$ and $U(1)$ groups. The SU(2) group has gauge coupling g and gauge bosons $W^i, i = 1, 2, 3$. The U(1) factor has gauge coupling g' and gauge boson B. These symmetries are exact if all the particles are massless. The Higgs mechanism breaks the $SU(2) \times U(1)$

symmetry, providing mass to the particles (except for the massless photon and gluon). The particle corresponding to the Higgs field is the Higgs boson, which was discovered by the ATLAS and CMS experiments at CERN in 2012 [2, 3].

2.1 The Standard Model

Electroweak interactions

Quantum Electrodynamics (QED), is the quantum theory describing all the electromagnetic interactions involving electrically charged particles by means of photon exchange. For instance, QED describes the well known Compton scattering, where an incoming photon interacts (transferring its energy) with an electron, i.e. $\gamma e \to \gamma e$. The classical Lagrangian that describes a spin 1/2 charged fermion, represented by a field ψ, reads

$$\mathcal{L}_{em} = -\frac{1}{4}F^2 + \bar{\psi}(i\not{D} - m)\psi, \tag{1}$$

where D is the covariant derivative[1] $D_\mu\psi = (\partial_\mu + ieA_\mu)\psi$, m and e the mass and electric charge of ψ, A_μ the gauge field for the electromagnetic interaction and $F^{\mu\nu}$ the field strength[2]. This Lagrangian is invariant under local $U(1)$ transformations[3], and its associated equations of motion are the Dirac equation and the Maxwell equations. On the other hand, the weak interaction describes radiative decays, e.g. the known β^- decay, where a d quark inside the neutron emits a W^- boson becoming a u quark. The W boson then decays into an electron and an electron antineutrino, i.e., $n \to p + e^- + \bar{\nu}_e$. In 1968, Sheldon Glashow, Abdus Salam and Steven Weinberg [4, 5, 6] realised that the electromagnetic and the weak interaction can be described by only one interaction, termed the electroweak interaction (GSW theory). Its underlying symmetry group is $SU(2)_L \times U(1)_Y$, where $SU(2)_L$ represents the weak isospin and $U(1)_Y$ the hypercharge. The gauge vector fields for $U(1)$ and $SU(2)$ are $\mathbf{W}^i_\mu = (W^1_\mu, W^2_\mu, W^3_\mu)$ and B_μ, with gauge couplings g and g', respectively.
Left-handed fermions are doublets of $SU(2)_L$, whereas right-handed fermions are

[1] $\not{D} = \gamma^\mu D_\mu$
[2] $F^{\mu\nu} = \partial^\mu A^\nu - \partial^\nu A^\mu$, $F^2 = F^{\mu\nu}F_{\mu\nu}$.
[3] Local $U(1)$ transformations correspond to phase (α) rotations of the field, $\psi(x) \to e^{-i\alpha(x)}\psi(x)$

Particle	T	T_3	Q	Y
$\nu_{e,\mu,\tau}$	1/2	+1/2	0	−1
e_L, μ_L, τ_L	1/2	−1/2	−1	−1
u_L, c_L, t_L	1/2	+1/2	+2/3	+1/3
d_L, s_L, b_L	1/2	−1/2	−1/3	+1/3
e_R, μ_R, τ_R	0	0	−1	−2
u_R, c_R, t_R	0	0	+2/3	+4/3
d_R, s_R, b_R	0	0	−1/3	−2/3

Table 1: Weak isospin T, its third component T_3, electric charge Q and hypercharge Y for the Standard Model fermions.

singlets of $SU(2)_L$, for the first generation we have

$$\text{leptons}: \quad \ell_L = \begin{pmatrix} \nu_e \\ e^- \end{pmatrix}_L, \quad e_R, \tag{2}$$

$$\text{quarks}: \quad q_L = \begin{pmatrix} u \\ d \end{pmatrix}_L, \quad u_R, \quad d_R. \tag{3}$$

Note that there is no right-handed neutrino. The weak isospin T, its third component T_3 and the hypercharge Y for the SM fermions are listed in Table 1. The weak hypercharge is related to the electric charge through $Q = T_3 + \frac{1}{2}Y$.
The $SU(2) \times U(1)$ Lagrangian can be expressed as,

$$\mathcal{L}_{SM} = \mathcal{L}_{gauge} + \mathcal{L}_{fermion} + \mathcal{L}_{Yukawa} + \mathcal{L}_{Higgs}. \tag{4}$$

The first term $\mathcal{L}_{gauge}$ corresponds to the kinetic term which describes the gauge bosons and their interactions,

$$\mathcal{L}_{gauge} = -\frac{1}{4}F_i^{\mu\nu}F_{\mu\nu}^i - \frac{1}{4}B^{\mu\nu}B_{\mu\nu}. \tag{5}$$

The second term encodes how interaction particles (bosons) interact with matter particles (fermions),

$$\mathcal{L}_{fermion} = \sum_{\psi_L} \bar{\psi}_L i\not{D}\psi_L + \sum_{\psi_R} \bar{\psi}_R i\not{D}\psi_R. \tag{6}$$

Since the right-handed fermions have $T_3 = 0$, they do not couple to weak isospin, while the left-handed fermions do, therefore their covariant derivatives read

$$\begin{aligned} D_\mu \psi_L &= (\partial_\mu + igW_\mu + ig' Y_L B_\mu)\psi_L, \\ D_\mu \psi_R &= (\partial_\mu + ig' Y_R B_\mu)\psi_R, \end{aligned} \tag{7}$$

where g' and g are the $U(1)$ and $SU(2)$ couplings, respectively. In order to reproduce the electromagnetic interactions described by QED with the GSW theory, the unification condition

$$e = g \sin\theta_W = g' \cos\theta_W, \tag{8}$$

has to be set. Up to this point the theory is mathematically consistent. However, (i) the theory has to give physical predictions and (ii) the fermions and gauge bosons are massless and have to acquire mass. To solve (i) and be able to calculate observables, Richard Feynman invented a graphical formalism to visualize the perturbative expansion in the coupling constants in terms of diagrams (Feynman diagrams). The computation of each Feynman diagram is carried out using Feynman rules. Higher order terms in the perturbative series give rise to loops in the diagrams and the Feynman rules require integrating over the particle momentum in each loop. This usually results in divergences that one has to take care of. Fortunately, 't Hooft and Veltman showed that locally gauge-invariant theories can absorb these infinities [7], these theories are called renormalizable. For instance, since the photon is massless, QED is locally gauge-invariant, and therefore renormalizable. However, we have massive $W^\pm$ and Z bosons in Nature. In fact, a bosonic (fermionic) mass term of the form $m^2 A_\mu A^\mu$ ($m\bar{\psi}\psi$) which could be added to the Lagrangian, breaks gauge-invariance under local $SU(2)_L \times U(1)_Y$. This is where the Brout-Englert-Higgs mechanism (Higgs mechanism for short) [8, 9, 10] comes into play, providing masses to the particles, while preserving gauge invariance. The Higgs mechanism predicts a new boson (Higgs boson), where the mass is a free parameter that needs to be determined by experiment. The Higgs boson was observed by the ATLAS and CMS experiments in 2012, with a measured mass[4] of about 125 GeV [2, 3].
The argument starts with all particles being massless, and introducing a complex scalar doublet field ϕ with which all particles can interact, defined as

$$\phi = \begin{pmatrix} \phi^+ \\ \phi^0 \end{pmatrix}. \tag{9}$$

[4]Natural units are used throughout the thesis, $\hbar = c = 1$.

Renormalizability and $SU(2)_L \times U(1)_Y$ invariance, require that the potential energy associated with this field has to be

$$V(\phi) = -\mu^2 \phi^\dagger \phi + \lambda \left(\phi^\dagger \phi\right)^2, \tag{10}$$

where μ and λ are positive real constants. The vacuum state of the field (obtained by minimizing the potential) occurs for a non-zero value of ϕ. Therefore, the quanta of the field correspond to excitations with respect to the non-zero field values, and the vacuum acquires a non-zero vacuum expectation value[5] (vev),

$$\langle \phi^\dagger \phi \rangle_0 = \sqrt{\frac{\mu^2}{2\lambda}} \equiv \frac{v}{\sqrt{2}}, \tag{11}$$

where $v = |\mu|/\sqrt{\lambda} \approx 246$ GeV, which defines the electroweak scale. Electric charge conservation implies that only the neutral field from the doublet can acquire a vev and since $V(\phi)$ only depends on the combination of $\phi^\dagger \phi$, we choose

$$\langle \phi \rangle_0 = \frac{1}{\sqrt{2}} \begin{pmatrix} 0 \\ v \end{pmatrix}, \tag{12}$$

which spontaneously breaks the symmetry,

$$SU(2)_L \times U(1)_Y \to U(1)_{EM}. \tag{13}$$

Now we are able to write $\mathcal{L}_{Higgs}$, which describes how the electroweak gauge bosons couple to the Higgs field,

$$\mathcal{L}_{Higgs} = (D^\mu \phi)^\dagger (D_\mu \phi) - V(\phi), \tag{14}$$

where[6]

$$D_\mu \phi = \left(\partial_\mu + igT^i W_\mu^i + \frac{1}{2} g' B_\mu\right) \phi. \tag{15}$$

When a gauge invariant vector field is added and spontaneous symmetry breaking (SSB) occurs, the vector field interacts with the scalar field and acquires a mass due to the non-zero vev of the scalar field.
In the same way, the Yukawa term, $\mathcal{L}_{Yukawa}$, describes how fermions couple to the

[5] There is also the trivial solution $\langle \phi \rangle_0 = 0$.
[6] $T^i = \frac{\tau^i}{2}$, being τ^i the Pauli matrices.

Higgs field and thereby obtain mass, for the first generation we have

$$\mathcal{L}_{Yukawa} = -f_u \bar{q}_L \tilde{\phi} u_R - f_d \bar{q}_L \phi d_R - f_e \bar{\ell}_L \phi e_R + h.c., \tag{16}$$

where $f_{u,d,e}$ are the coupling constants, ℓ_L, q_L the quark and lepton doublets and $\tilde{\phi} = i\tau_2 \phi^*$. The mass contribution to the Lagrangian density is obtained by substituting the Higgs vev into the Lagrangian densities,

$$\begin{aligned} \mathcal{L}_{MASS} = &- \frac{v}{\sqrt{2}}(f_u \bar{u}u + f_d \bar{d}d + f_e \bar{e}e) + \left(\frac{vg'}{2}\right)^2 W^+_\mu W^\mu_- \\ &+ \frac{v^2}{8}\left(W^3_\mu B_\mu\right) \begin{pmatrix} g'^2 & -gg' \\ -gg' & g^2 \end{pmatrix} \begin{pmatrix} W^\mu_3 \\ B^\mu \end{pmatrix} \end{aligned} \tag{17}$$

We see that the SM does not predict the mass of the fermions, but it predicts that the Higgs boson coupling to matter fermions is proportional to the fermion mass,

$$m_\alpha = \frac{v}{\sqrt{2}} f_\alpha \quad (\alpha = u, d, e, ...). \tag{18}$$

Since the mass matrix for the neutral bosons is not diagonal (see Equation 17), after SSB the W_3 and B states mix forming the physical Z_μ and A_μ fields. The electromagnetic interaction A^μ is a linear combination of W^3_μ and B_μ, and their orthogonal combination produces the weak neutral current Z^0. The usual way to form this linear combination is by using a rotation angle θ_W (the weak mixing angle),

$$\begin{aligned} A_\mu &= +B_\mu \cos\theta_W + W^3_\mu \sin\theta_W, \\ Z_\mu &= -B_\mu \sin\theta_W + W^3_\mu \cos\theta_W. \end{aligned} \tag{19}$$

Before SSB all fields are massless, but after the symmetry is broken, we end up with 3 physical spin 1 massive bosons $W^\pm, Z^0$ and a massive scalar boson H (Higgs boson), whereas the photon γ remains massless,

$$\begin{aligned} m_W &= \frac{1}{2}vg, \qquad & W^\pm &= \frac{1}{\sqrt{2}}(W^1_\mu \mp iW^2_\mu), \\ m_Z &= \frac{1}{2}v\sqrt{g^2 + g'^2}, \qquad & Z_\mu &= \frac{1}{\sqrt{g^2 + g'^2}}(gW^3_\mu - g'B_\mu), \\ m_A &= 0, \qquad & A_\mu &= \frac{1}{\sqrt{g^2 + g'^2}}(g'W^3_\mu + gB_\mu). \end{aligned} \tag{20}$$

The W to Z mass ratio is fixed by

$$\frac{m_W}{m_Z} = \cos\theta_W. \tag{21}$$

Strong interactions

Approximately 50% of the momentum of a proton is carried by particles that do not interact electromagnetically or weakly. These particles are called gluons (g), have spin one, interact through the strong force and carry *color* charge (8 gluons in total). The theory of strong interactions is called Quantum Chromodynamics (QCD) [11, 12, 13] and is based on the symmetry group $SU(3)$.
In QCD, quarks and gluons interact with a strength proportional to the strong coupling constant α_s. However, α_s varies with the scale Q^2 of the process studied, this effect is usually referred to as *running of the coupling constant*. Already in QED, the value of the coupling constant $\alpha(Q^2)$ increases with energy[7], resulting in a 7% difference between $\alpha(Q = m_e)$ and $\alpha(Q = m_Z)$.
In the QCD case, the scale dependence can be written as

$$\alpha_s(Q^2) = \frac{12\pi}{(33 - 2n_f)\ln\left(Q^2/\Lambda^2_{QCD}\right)}, \tag{22}$$

where n_f is the number of active flavours, and Λ_{QCD} is the cutoff scale, which is an unknown parameter and has to be determined by the experiment. We see that for $n_f < 17$ the value of $\alpha_s(Q^2)$ decreases with increasing Q^2. This has strong implications:

- At large Q^2, α_s becomes small enough for perturbation theory to be valid[8]. This is called asymptotic freedom. In this regime quarks and gluons can be treated as free particles.

- When Q^2 becomes small (~ 1 GeV^2), α_s approaches unity and perturbation theory is no more valid. The consequence of this is that (at large distances) quarks and gluons are confined into hadrons, they do not appear as free particles in Nature. This is called color confinement.

[7] At low energies, $\alpha \sim 1/137$.
[8] At the Z boson mass scale, $\alpha_s(m_Z) \sim 0.12$.

2.2 Supersymmetry

Supersymmetry (SUSY) is a hypothetical symmetry that relates fermionic and bosonic degrees of freedom. As a consequence, new supersymmetric particles are predicted, which are (super)partners of all the known Standard Model particles, differing in spin by half a unit. The total number of bosonic and fermionic degrees of freedom must be equal. All the quantum numbers, except the spin, are identical to those of the Standard Model particles. In a supersymmetric theory, two Higgs doublets are introduced. If only a single Higgs doublet is included, anomalies arise and theory becomes inconsistent.

An important feature of supersymmetric theories is that the mass matrices for supersymmetric particles in general mix particles with the same quantum numbers. Therefore, one should distinguish between "interaction eigenstates" and "mass eigenstates". The correct mass eigenstates should be determined by the experiment or predicted by the theoretical model.

There are many reasons why Supersymmetry and the relation between fermions and bosons is interesting. Here, some will be listed and later explained in more detail throughout this section. First, it solves the so-called *hierarchy problem*. The mass of the Higgs boson receives radiative corrections due to fermion loops. All fermions contribute to these corrections, but the dominant one, due to its large mass, is the top quark. In the Standard Model, corrections to the Higgs boson mass are of the form

$$(\Delta m_H)^2 = -\frac{g_f^2}{8\pi^2}\Lambda^2, \tag{23}$$

where g_f is the coupling constant for the fermion-Higgs boson interaction and Λ is a cutoff which represents the new physics energy scale. In Supersymmetry, due to the additional contributions from the accompanying superpartners, an additional correction is introduced

$$(\Delta m_H)^2 = \frac{g_s}{16\pi^2}\Lambda^2, \tag{24}$$

where g_s is the coupling constant for the scalar interaction. If we now compare both equations, we see that a perfect cancellation is found if $g_s = g_f^2$ and we have two scalar superpartners for the Standard Model fermions (from left and right-handed particles). A second motivation for Supersymmetry is the unification of couplings. In the supersymmetric extension of the Standard Model, the coupling unification is more successful than in the SM. The extrapolation of $SU(3)$, $SU(2)$ and $U(1)$ gauge couplings results in a unification of the three into a single one at high energy scales

($M_{\mathrm{U}} \sim 10^{15}$ GeV). Furthermore, Supersymmetry could also connect particle physics with the large scale structure of the universe, since it yields a candidate for dark matter, providing a density matching with current astrophysical observations. The anomaly in the anomalous magnetic moment of the muon, which has been measured to be greater than the predicted value [14], can also be explained considering light supersymmetric partners [15, 16].
Although the SUSY phenomenology can be very complex, the emergence of some sparticles in the Minimal Supersymmetric extension of the Standard Model relevant for the supersymmetry searches considered in this thesis will be explained.

2.3 The Minimal Supersymmetric Standard Model

In order to construct the Minimal Supersymmetric version[9] of the Standard Model (MSSM), for each chiral fermion of the Standard model we introduce a chiral superfield, and for each gauge field we introduce a vector superfield. Starting with the fermion sector, for the first generation we have

$$\tilde{\ell}_L = \begin{pmatrix} \tilde{\nu} \\ \tilde{e}^- \end{pmatrix}_L, \quad \tilde{e}_R, \quad \tilde{q}_L = \begin{pmatrix} \tilde{u} \\ \tilde{d} \end{pmatrix}_L, \quad \tilde{u}_R, \quad \tilde{d}_R, \tag{25}$$

where $\tilde{\ell}_L$ are called left-handed sleptons[10], $\tilde{e}_R$ is the right-handed selectron and $\tilde{q}$ are the squarks. The generalisation for the three lepton generations can be done similarly.
In the gauge sector, a vector superfield corresponding to each gauge field is introduced. Thus, for the Standard Model $U(1),\ SU(2),\ SU(3)$ gauge fields $B_\mu, \mathbf{W}_\mu, g^a_\mu$ we have the spin half gaugino fields $\tilde{B}, \tilde{\mathbf{W}}_\mu, \tilde{g}^a$.
Finally, in the Higgs sector, at least two Higgs doublets chiral fields are needed. The two Higgs doublets[11] are denoted as H_u (up type) and H_d (down type).

$$H_u = \begin{pmatrix} H_u^+ \\ H_u^0 \end{pmatrix}; \quad H_d = \begin{pmatrix} H_d^0 \\ H_d^- \end{pmatrix}. \tag{26}$$

[9] The prefix minimal refers to the minimal set of supersymmetric particles and fields required to construct a supersymmetric Standard Model.
[10] here L (and R) does not stand for helicity of selectrons but to that of their partners, since selectrons are spin-0 particles
[11] If up-type and down-type fermions couple to different Higgs doublets (H_u, H_d), one ensures that flavour changing neutral currents are suppressed at tree-level [17, 18].

Now, after spontaneous symmetry breaking $SU(2)_L \times U(1)_Y \to U(1)_{EM}$, the Higgs vacuum expectation values are given by real, positive quantities v_u and v_d. These arise from the minimisation of the Higgs potential, and are expressed as

$$\langle H_u \rangle = \frac{1}{\sqrt{2}} \begin{pmatrix} 0 \\ v_u \end{pmatrix}; \quad \langle H_d \rangle = \frac{1}{\sqrt{2}} \begin{pmatrix} v_d \\ 0 \end{pmatrix}. \tag{27}$$

This means that the W and Z boson masses now read

$$\begin{aligned} m_W &= \frac{1}{2} g \sqrt{v_u^2 + v_d^2}, \\ m_Z &= \frac{1}{2} \sqrt{g'^2 + g^2} \sqrt{v_u^2 + v_d^2}, \\ v &= \sqrt{v_u^2 + v_d^2} \simeq 246 \text{ GeV}. \end{aligned} \tag{28}$$

Furthermore, a parameter β is defined,

$$\tan \beta = v_u / v_d, \tag{29}$$

and enters as a free parameter in the theory.
The fermionic partners of the Higgs bosons, the higgsinos, are given by

$$\tilde{H}_u = \begin{pmatrix} \tilde{H}_u^+ \\ \tilde{H}_u^0 \end{pmatrix}; \quad \tilde{H}_d = \begin{pmatrix} \tilde{H}_d^0 \\ \tilde{H}_d^- \end{pmatrix}. \tag{30}$$

All the states corresponding to the component fields of the superfields described until now are just interaction eigenstates. In the following sections we will go through the mass eigenstates of the supersymmetric particles of interest for this thesis.

In general, the MSSM contains interaction vertices that violate the baryon number B and lepton number L. If both are violated, proton decays of the type $p \to \pi^0 + e^+$ can occur. Since there has been no experimental evidence for any of both violations, the simplest approach to overcome this is to postulate an additional symmetry. A simple solution is to impose a discrete symmetry known as R-parity. It usually expressed as $R_p = (-1)^{3(B-L)+2S}$, where S, B and L are the spin, baryon number and lepton number of the particle. In this way, all the Standard Model particles and the Higgs bosons have even parity ($R_p = +1$), whereas squarks, sleptons, gauginos and higgsinos have odd R-parity ($R_p = -1$). This new symmetry not only avoids the proton decay, it also has a striking consequence: the lightest supersymmetric

particle (LSP) is stable. Thus, supersymmetry produces a dark matter candidate. Throughout this thesis a conserved R-parity will be assumed.

As of this writing, no supersymmetric particles have been observed in any experiment, thus supersymmetry has to be broken. With an unbroken supersymmetry we would have discovered selectrons ($\tilde{e}_L$, $\tilde{e}_R$) with a mass corresponding to the ordinary electron, $m_e = 0.511$ MeV, long ago. Therefore, if supersymmetry is a symmetry of Nature, it must be a broken symmetry. We saw in Section 2.2 that a perfect cancellation of quadratic divergences can be obtained with a relation between the couplings (e.g. $g_s = g_f^2$). If we want to keep this nice feature of supersymmetry, the cancellation must occur even with non-degenerate mass spectrum. To avoid the reappearance of the hierarchy problem, the breaking should be *soft*. The MSSM lagrangian can then be written as

$$\mathcal{L}_{MSSM} = \mathcal{L}_{SUSY} + \mathcal{L}_{SOFT} \tag{31}$$

where $\mathcal{L}_{SUSY}$ preserves supersymmetry invariance and contains all the gauge and Yukawa interactions, and $\mathcal{L}_{SOFT}$ violates supersymmetry. There are three types of soft breaking terms: soft scalar masses, gaugino masses and trilinear scalar couplings. The inclusion of soft supersymmetry breaking terms introduces numerous free parameters in the theory since the exact SUSY breaking mechanism is not known.

2.3.1 Gauginos, higgsinos and sleptons

Chargino mass matrix

As described in the SM introduction, the electroweak gauge symmetry $SU(2) \times U(1)_Y$ is associated in the SM with the spin one gauge bosons $W^{\pm}, W^3$ and B^0. The spin half superpartners are $\tilde{W^{\pm}}, \tilde{W^3}$ (winos), and $\tilde{B^0}$ (binos). After electroweak symmetry breaking $SU(2)_L \times U(1)_Y \to U(1)_{EM}$, the W^3 and B states mix and form the Z and γ bosons. The corresponding mixtures of W^3 and B in Supersymmetry are the $\tilde{Z}$ (zino) and $\tilde{\gamma}$ (photino). To see how the mass eigenstates emerge after electroweak symmetry breaking, it is convenient to define the wino fields as

$$\tilde{W}^{\pm} = \frac{1}{\sqrt{2}}(\tilde{W}^1 \mp i\tilde{W}^2). \tag{32}$$

Once the fields (Equation 26) acquire vevs (after electroweak symmetry breaking), the mass terms of the non-matter charged fermions (gauginos and higgsinos) can be

written as

$$\mathcal{L}^c_{MASS} = -\frac{g}{\sqrt{2}}(v_d\tilde{W}^+\tilde{H}^+_d + v_u\tilde{W}^-\tilde{H}^+_u + h.c.) - (M_2\tilde{W}^+\tilde{W}^- + \mu\tilde{H}^-_d\tilde{H}^+_u + h.c.), \quad (33)$$

where M_2 is the wino mass parameter (corresponding to the $SU(2)_L$ gaugino field) and μ the supersymmetric Higgs mass parameter. This mass term can be more compactly written in terms of a 2×2 matrix $\mathbf{X}$,

$$\mathcal{L}^c_{MASS} = -(\psi^-)^T\mathbf{X}\psi^+ + h.c., \quad (34)$$

where we have defined

$$\psi^+ = \begin{pmatrix} \tilde{W}^+ \\ \tilde{H}^+_u \end{pmatrix}; \quad \psi^- = \begin{pmatrix} \tilde{W}^- \\ \tilde{H}^-_d \end{pmatrix}; \quad (35)$$

and the matrix $\mathbf{X}$ is given by

$$\mathbf{X} = \begin{pmatrix} M_2 & \sqrt{2}m_W \sin\beta \\ \sqrt{2}m_W \cos\beta & \mu \end{pmatrix}. \quad (36)$$

One can now find two unitary 2×2 matrices U and V such that

$$U^*\mathbf{X}V^{-1} = \mathbf{M}_C = \begin{pmatrix} m_{\tilde{\chi}^\pm_1} & 0 \\ 0 & m_{\tilde{\chi}^\pm_2} \end{pmatrix}, \quad (37)$$

here, $\mathbf{M}_C$ is a 2×2 diagonal matrix and has real positive entries $m^\pm_{\tilde{\chi}_1}$ and $m^\pm_{\tilde{\chi}_2}$. The two mass eigenstates are related to the gaugino fields, and we can write Equation 34 as

$$\mathcal{L}^c_{MASS} = \chi^-(\mathbf{M}_c)\chi^+ + h.c. \quad (38)$$

being $\chi^+_k = V\psi^+$ and $\chi^-_k = U\psi^-$ $(k = 1, 2)$. Defining now the chargino fields as

$$\tilde{\chi}^+_1 = \begin{pmatrix} \tilde{\chi}^+_1 \\ \overline{\chi^-_1}^T \end{pmatrix}, \tilde{\chi}^+_2 = \begin{pmatrix} \tilde{\chi}^+_2 \\ \overline{\chi^-_2}^T \end{pmatrix}, \quad (39)$$

Equation 38 can be written as

$$\mathcal{L}^c_{MASS} = m_{\tilde{\chi}^\pm_1}\overline{\tilde{\chi}^+_1}\tilde{\chi}^+_1 + m_{\tilde{\chi}^\pm_2}\overline{\tilde{\chi}^+_2}\tilde{\chi}^+_2, \quad (40)$$

and a clear Dirac mass term can be read. Usually $m_{\tilde{\chi}_1}$ is taken to be lighter than $m_{\tilde{\chi}_2}$, i.e., $m_{\tilde{\chi}_1} < m_{\tilde{\chi}_2}$. Now, since

$$M_c^2 = V\mathbf{X}^\dagger\mathbf{X}V^{-1} = U^*\mathbf{X}\mathbf{X}(U^*)^{-1}, \tag{41}$$

$m_{\tilde{\chi}_1}$ and $m_{\tilde{\chi}_2}$ can be seen as the positive square roots of the eigenvalues of the $\mathbf{X}^\dagger\mathbf{X}$. Since they are 2×2 matrices, analytical expressions for the eigenvalues can be derived. The chargino square masses are given by

$$m^2_{\tilde{\chi}_{1,2}} = \frac{1}{2}\left[|M_2|^2 + |\mu|^2 + 2m_W^2 \mp \sqrt{(|M_2|^2 + |\mu|^2 + 2m_W^2)^2 - 4|\mu M_2 - m_W^2 \sin 2\beta|^2)}\right] \tag{42}$$

Neutralino mass matrix

Following the same philosophy as for the charginos, one can calculate now the mass eigenstates of neutral non-matter fermions. Taking now the terms from the Lagrangian relevant to the neutral sector,

$$\begin{aligned}\mathcal{L}^n_{MASS} = &-\frac{g}{2}\tilde{W}_3(v_d\tilde{H}_d^0 - v_u\tilde{H}_u^0) + \frac{g'}{2}\tilde{B}(v_d\tilde{H}_d^0 - v_u\tilde{H}_u^0) \\ &+ \mu\tilde{H}_d^0\tilde{H}_u^0 - \frac{1}{2}M_2\tilde{W}_3\tilde{W}_3 - \frac{1}{2}M_1\tilde{B}\tilde{B} + h.c.,\end{aligned} \tag{43}$$

where M_1 is the bino mass parameter (corresponding to the $U(1)_Y$ gaugino field). This expression is similar to the chargino Equation 33 but this time with the neutral components. In a similar procedure than with the charginos, defining the row vector

$$(\psi^0)^T \equiv \left(\tilde{B}\ \tilde{W}_3\ \tilde{H}_d^0\ \tilde{H}_u^0\right) \tag{44}$$

we can rewrite Equation 43 as

$$\mathcal{L}^n_{MASS} = -\frac{1}{2}(\psi^0)^T\mathcal{M}\psi^0 + h.c. \tag{45}$$

being the mass matrix $\mathcal{M}$ the 4×4 matrix

$$\mathcal{M} = \begin{pmatrix} M_1 & 0 & -m_Z\cos\beta\sin\theta_W & m_Z\sin\beta\sin\theta_W \\ 0 & M_2 & m_Z\cos\beta\cos\theta_W & -m_Z\sin\beta\cos\theta_W \\ -m_Z\cos\beta\sin\theta_W & m_Z\cos\beta\cos\theta_W & 0 & -\mu \\ m_Z\sin\beta\sin\theta_W & -m_Z\sin\beta\cos\theta_W & \mu & 0 \end{pmatrix}. \tag{46}$$

We can now diagonalize the matrix $\mathcal{M}$ with a unitary matrix N in order to obtain the mass eingenstates, i.e.

$$\tilde{\chi}_i = N_{ij}\psi_j^0, \qquad i,j = 1,2,3,4. \tag{47}$$

satistfying

$$N^*\mathcal{M}N^{-1} = \begin{pmatrix} m_{\tilde{\chi}_1} & 0 & 0 & 0 \\ 0 & m_{\tilde{\chi}_2} & 0 & 0 \\ 0 & 0 & m_{\tilde{\chi}_3} & 0 \\ 0 & 0 & 0 & m_{\tilde{\chi}_4} \end{pmatrix}, \tag{48}$$

where the indices i, j in N_{ij} are mass and gauge eigenstate labels. The mass eigenvalues can be expressed in terms of M_1, M_2, μ and $\tan\beta$, however these are more tedious to solve since it is a 4×4 matrix, and does not give too much physical insight. The $\tilde{\chi}_i^0$ are linear combinations of the neutral gaugino and higgsino states which are determined by the matrix elements of N. The neutralinos are ordered, as for the charginos, depending on their mass. The $\tilde{\chi}_1^0$ being the lightest from them all and the $\tilde{\chi}_4^0$ the heaviest, i.e., $m_{\tilde{\chi}_1^0} < m_{\tilde{\chi}_2^0} < m_{\tilde{\chi}_3^0} < m_{\tilde{\chi}_4^0}$. The neutralinos are of special interest since, if R-parity is conserved, the $\tilde{\chi}_1^0$ is stable and if it is the lightest supersymmetric particle (LSP), then it becomes a good candidate for the constituent of dark matter.

Sleptons

There are two scalar leptons, denoted by $\tilde{\ell}_L$ and $\tilde{\ell}_R$ for each generation of leptons ℓ. One of them is associated with the left-handed lepton ℓ_L and the other one with the right-handed lepton ℓ_R (weak SU(2) singlet). As for the gauginos case, the two sleptons $\tilde{\ell}_{L,R}$ are expected to mix, and the mass eigenstates will be linear combinations of these states. The sfermion mass terms can be collected under

$$\mathcal{L}_{MASS}^{\tilde{f}} = \sum_{\tilde{f}} \tilde{f}^\dagger \mathcal{M}_{\tilde{f}}^2 \tilde{f}, \tag{49}$$

where $\tilde{f} = \begin{pmatrix} \tilde{f}_L \\ \tilde{f}_R \end{pmatrix}$. For the scalar sleptons ($\tilde{\ell} = \tilde{e},\ \tilde{\mu},\ \tilde{\tau}$), the 2×2 mass matrix is

$$\mathcal{M}_{\tilde{\ell}}^2 = \begin{pmatrix} M_{\tilde{\ell}_L}^2 + M_Z^2(T_{3L}^{\tilde{\ell}} - Q_\ell \sin^2\theta_W)\cos 2\beta + m_\ell^2 & X_\ell m_\ell \\ X_\ell^* m_\ell & M_{\tilde{\ell}_R}^2 + Q_\ell M_Z^2 \cos 2\beta \sin^2\theta_W + m_\ell^2 \end{pmatrix}, \tag{50}$$

where $T_{3L}^{\tilde{\ell}}$ is the third component of the weak isospin, Q_ℓ the electromagnetic charge of the lepton and[12] $X_\ell = A_\ell - \mu^* \tan\beta$. Note that the off-diagonal LR mixing terms $X \cdot m_\ell$ of the matrix is proportional to the lepton mass, therefore the mixing is largest for the third generation. Similar expressions hold for $\tilde{u}, \tilde{d}, \tilde{c}, \tilde{s}, \tilde{t}, \tilde{b}, \tilde{\nu}$ but the appropriate values of T_{3L} and Q must be inserted; for the up-type squarks $(\tilde{u}, \tilde{c}, \tilde{t})$ and sneutrinos $\tilde{\nu}$, $\tan\beta$ should also be replaced by $\cot\beta$.

2.4 Solving the SM problems

Dark matter in the MSSM

In the early Universe, shortly after the Big Bang, the SM particles were in thermal equilibrium with the dark matter. As the Universe expanded, the temperature dropped until the gas of Dark Matter (DM) reached such a low density that the DM particles annihilation processes ceased. The dark matter then "freezes out" and the number approaches a constant: the thermal relic density. This relic abundance has been measured by WMAP and Planck, being $\Omega h^2 = 0.1188 \pm 0.0010$ [19, 20]. In order to obtain this thermal abundance, the DM annihilation cross section (into SM particles) has to be[13] $\langle \sigma v \rangle \approx 3 \times 10^{-26} \mathrm{cm}^3/\mathrm{s} \approx 1\mathrm{pb}$.

To see how compatible this is with the MSSM, we have to recall that, after electroweak symmetry breaking (EWSB), four neutralino mass eigenstates are obtained by means of mass matrix diagonalization. The matrix in Equation 46 contains the soft SUSY breaking mass gaugino mass parameters M_1, M_2 and the SUSY preserving higgsino mass parameter μ. The hierarchy of μ, M_1, M_2 determines the nature of the neutralino: bino, higgsino or wino.

Bino case (SU(2) singlet): $|M_1| \ll \mu, M_2$. The correct dark matter relic density is obtained (at leading order) by pair annihilation of bino-like neutralinos through slepton exchange, as illustrated in Figure 2.

The thermal cross section for bino-like neutralino is [21]

$$\langle \sigma v \rangle_{\tilde{B}} = \sum_{\tilde{f}} \frac{g'^4 Y_{\tilde{f}}^4}{40\pi} \frac{m_{\tilde{\chi}^0}^2 \left(m_{\tilde{f}}^4 + m_{\tilde{\chi}^0}^4 \right)}{\left(m_{\tilde{f}}^2 + m_{\tilde{\chi}^0}^2 \right)^4}, \tag{51}$$

[12] A_ℓ correspond to the matrices of the trilinear scalar couplings.

[13] The annihilation cross section is inversely proportional to the relic density, i.e., $\Omega_{DM} \propto \frac{1}{\sigma v}$

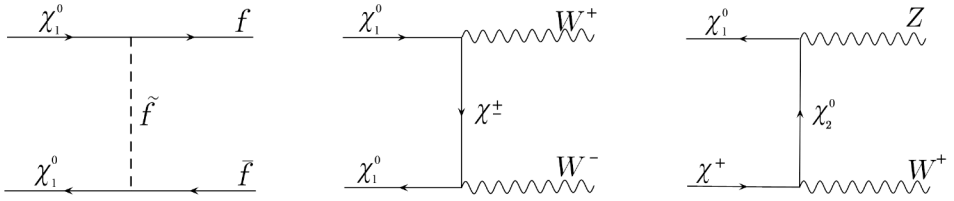

Figure 2: Dark matter annihilation at tree-level for a pure bino neutralino (left) and a pure higgsino neutralino (middle). Example of a coannihilation channel for a pure higgsino neutralino (right). Figure taken from [22].

where $m_{\tilde{f}}$ is the mass of the sfermion and $Y_{\tilde{f}}$ the hypercharge. If one assumes that only selectrons and smuons contribute in the light SUSY spectrum, and that the left and right states have the same mass, substituting $Y_{\tilde{f}_L} = -1/2, Y_{\tilde{f}_R} = -1$, cross sections of about 1 pb are obtained in the $m_{\tilde{\chi}^0} < m_{\tilde{f}} \lesssim 100$ GeV range, which is a region already excluded by the experiments [23]. One way to evade this collider limits is by a mechanism called *coannihilation*. If the bino and the sfermions are nearly degenerate in mass, the neutralinos can coannihilate with the sfermions into SM particles, e.g., $\tilde{\chi}^0\tilde{\ell} \to \ell\gamma$, as shown in Figure 3, in this way the observed DM relic density constraint can be satisfied.

Higgsino case (SU(2) doublet). The higgsino case is realised when $|\mu| \ll M_1, M_2$. After EWSB, the four higgsinos states give rise to two neutralinos $\tilde{\chi}_1^0, \tilde{\chi}_2^0$ and a chargino $\tilde{\chi}_1^\pm$. The tree level mass splitting between the two higgsino states is [24]

$$\Delta m(\tilde{\chi}_2^0, \tilde{\chi}_1^0) = m(\tilde{\chi}_2^0) - m(\tilde{\chi}_1^0) \simeq m_Z^2 \left(\frac{\sin^2\theta_W}{M_1} + \frac{\cos^2\theta_W}{M_2} \right), \tag{52}$$

which is of the order of tens of GeV for $\mu \ll M_1, M_2$. In order to compute the thermal cross section for the higgsinos, all the possible annihiliations ($\tilde{\chi}^0\tilde{\chi}^0 \to$ SMSM) and coannihilations ($\tilde{\chi}^0\tilde{\chi}^\pm \to$ SMSM) have to be taken into account. Therefore, a thermal-averaged cross section is calculated, where all the higgsino-like neutralinos and charginos are mass degenerate [21]

$$\langle\sigma v\rangle_{\tilde{H}}^{\text{eff}} \approx \frac{g^4}{512\pi\mu^2}(21 + 3\tan\theta_W^2 + 11\tan\theta_W^4), \qquad \Omega_{\tilde{H}}h^2 = 0.10\left(\frac{\mu}{1\text{ TeV}}\right)^2. \tag{53}$$

Substituting $\tan\theta_W \sim 0.54$ and using the relation in Equation 8, one finds that overall the cross section is > 1 pb, except for $\mu \gtrsim 1$ TeV. Therefore, a 1 TeV higgsino-like neutralino is a good candidate for the constituent of dark matter. For masses below ~ 1 TeV, the higgsinos would have to coexist with other dark matter candidates in

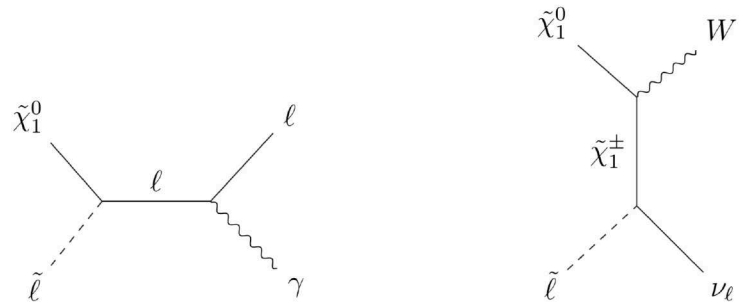

Figure 3: Example of coannihilation diagrams between $\tilde{\chi}_1^0$ and $\tilde{\ell}$ for s-channel (left) and t-channel (right).

order to explain the observations.

Wino case (SU(2) triplet). EWSB causes the neutralino to be dominated by the superpartner of the W_3 in the $|M_2| \ll \mu, M_1$ limit. In this case one finds a (nearly) mass degenerate neutralino $\tilde{\chi}^0$ and chargino $\tilde{\chi}^\pm$. The mass splitting between the $\tilde{\chi}_1^0$ and the $\tilde{\chi}^\pm$ is $\Delta M_{\tilde{W}} = (\frac{g^2}{4\pi}) m_W \sin^2(\theta_W/2) \approx 166$ MeV [25]. As for higgsinos, the thermal annihilation cross section is dominated by the coannihilation of the three wino states [21],

$$\langle \sigma v \rangle_{\tilde{W}}^{\text{eff}} = \frac{3g^4}{16\pi M_2^2}, \qquad \Omega_{\tilde{W}} h^2 = 0.13 \left(\frac{M_2}{2.5 \text{ TeV}} \right)^2, \tag{54}$$

obtaining a good dark matter candidate for neutralino masses of $m_{\tilde{\chi}_1^0} \sim 2.2$ TeV. In this case of large DM masses and very low mass splittings, the Sommerfeld enhancement[14] cannot be neglected [26], yielding a good DM candidate for $m_{\tilde{\chi}_1^0} \sim$ 2.8 TeV. For lighter winos the DM relic density is not satisfied.

Moreover, mixed states can also be realised. Even though these cases are very interesting since they can circumvent experimental constraints, here they will not be discussed in detail. The thermal annihilation cross section will depend on the relative contribution of each of the states. Depending on the value of μ, M_1 and M_2, we find the following cases

- $|M_1| \sim |\mu| \ll |M_2| \rightarrow$ Bino-Higgsino case.
- $|M_1| \lesssim |M_2| \ll |\mu| \rightarrow$ Bino-Wino case.

[14] For slowly moving heavy DM particles (above the TeV), the weak interaction can play the role of long range force since the W, Z bosons are much lighter. Attractive forces become then strong between DM particles, enhancing their annihilation cross section.

- $|M_2| \sim |\mu| \ll |M_1| \rightarrow$ Wino-Higgsino case.

It should be stressed that since SUSY is not the only SM extension that provides a dark matter candidate, it could be that dark matter consists of more than one type of particle. One of the most popular dark matter candidates (excluding the neutralino), is the axion, due to its capability of solving the strong CP problem [27, 28]. In this way, neutralinos and axions could coexist in Nature, satisfying the dark matter relic density constraint [29].

Muon magnetic moment

In classic electrodynamics, the magnetic moment of a particle arises from the spinning of a charge distribution. In the SM the elementary particles are understood as point-like particles, but nevertheless they still carry a magnetic moment $\boldsymbol{\mu}$. The magnetic moment can be expressed as $\boldsymbol{\mu} = g(q/2m)\boldsymbol{s}$, where q and m are the charge and mass of the particle, $\boldsymbol{s}$ its spin, and g the g-factor. The g-factor for elementary spin 1/2 particles was first predicted by Dirac to be exactly 2 [30, 31]. This however, was the leading order prediction, and when radiative corrections are included, this factor differs from 2. In fact, the first higher-order correction was calculated by Schwinger, which lead to the so-called anomalous magnetic moment [32]

$$a \equiv \frac{g-2}{2} = \frac{\alpha}{2\pi}. \tag{55}$$

However, this calculation only includes the one loop QED correction. The most precise theoretical prediction of the anomalous magnetic moment of the muon, including QED, electroweak and hadronic contributions, is [14]

$$a_\mu^{SM} = 116\ 591\ 810(43) \times 10^{-11}. \tag{56}$$

The experimental measurement of a_μ is also performed with extraordinary precision. The most precise measured value is the result of the E821 experiment at Brookhaven [33]

$$a_\mu^{BNL} = 116\ 592\ 089(63) \times 10^{-11}, \tag{57}$$

which results in a 3.7σ discrepancy between theory and experiment, $\Delta a_\mu = a_\mu^{BNL} - a_\mu^{SM} = 279(76) \times 10^{-11}$. During the writing of this thesis, the Fermilab Muon $g-2$ collaboration has released a new measurement of the muon $g-2$ [34] which is consistent with the previous BNL result. When both experimental values are combined,

the difference with respect to the SM prediction becomes $\Delta a_\mu = a_\mu^{Exp} - a_\mu^{SM} = (251 \pm 59) \times 10^{-11}$, corresponding to a significance of 4.2σ. The discrepancy is comparable to the SM electroweak contribution to the anomalous magnetic moment, $a_\mu^{EWK} = 153.6(1.0) \times 10^{-11}$. This means that if this discrepancy arises from Beyond Standard Model (BSM) contributions, the scale of new physics may be around $100 - 1000$ GeV, which is exactly the scale that the LHC is currently probing. Among several BSM physics proposals, low-energy Supersymmetry could be the answer. In the MSSM, two types of one-loop corrections contribute to the muon $g-2$: the contribution from a chargino-sneutrino loop $a_\ell^{\tilde{\chi}^\pm}$ and the one coming from a neutralino-slepton loop $a_\ell^{\tilde{\chi}^0}$. The contributions are classified into four types[15] and approximated as (see e.g. [35, 36, 37, 38])

$$a_\mu(\tilde{W}, \tilde{H}, \tilde{\nu}_\mu, \tilde{\mu}_L) = \frac{g^2 m_\mu^2}{16\pi^2 M_2 \mu} \tan\beta \cdot f_C\left(\frac{M_2^2}{m_{\tilde{\nu}_\mu}^2}, \frac{\mu^2}{m_{\tilde{\nu}_\mu}^2}\right) - \frac{g^2 m_\mu^2}{32\pi^2 M_2 \mu} \tan\beta \cdot f_N\left(\frac{M_2^2}{m_{\tilde{\mu}_L}^2}, \frac{\mu^2}{m_{\tilde{\mu}_L}^2}\right), \tag{58}$$

$$a_\mu(\tilde{B}, \tilde{H}, \tilde{\mu}_L) = \frac{g'^2 m_\mu^2}{32\pi^2 M_1 \mu} \tan\beta \cdot f_N\left(\frac{M_2^1}{m_{\tilde{\mu}_L}^2}, \frac{\mu^2}{m_{\tilde{\mu}_L}^2}\right), \tag{59}$$

$$a_\mu(\tilde{B}, \tilde{H}, \tilde{\mu}_R) = -\frac{g'^2 m_\mu^2}{16\pi^2 M_1 \mu} \tan\beta \cdot f_N\left(\frac{M_1^2}{m_{\tilde{\mu}_R}^2}, \frac{\mu^2}{m_{\tilde{\mu}_R}^2}\right), \tag{60}$$

$$a_\mu(\tilde{B}, \tilde{\mu}_L, \tilde{\mu}_R) = \frac{g'^2 m_\mu^2 M_1 \mu}{16\pi^2 m_{\tilde{\mu}_L}^2 m_{\tilde{\mu}_R}^2} \tan\beta \cdot f_N\left(\frac{m_{\tilde{\mu}_L}^2}{M_1^2}, \frac{m_{\tilde{\mu}_R}^2}{M_1^2}\right), \tag{61}$$

where the loop functions f_N and f_C are defined as

$$\begin{aligned} f_C(x,y) &= xy\left[\frac{5-3(x+y)+xy}{(x-1)^2(y-1)^2} - \frac{2\ln x}{(x-y)(x-1)^3} + \frac{2\ln y}{(x-y)(y-1)^2}\right], \\ f_N(x,y) &= xy\left[\frac{-3+x+y+xy}{(x-1)^2(y-1)^2} + \frac{2x\ln x}{(x-y)(x-1)^3} - \frac{2y\ln y}{(x-y)(y-1)^2}\right], \end{aligned} \tag{62}$$

with $f_C(1,1) = 1/2$ and $f_N(1,1) = 1/6$. Therefore, we can match the experimentally measured values by tuning the individual parameters in Equations 58 – 61. By observing the above formulae, the first three terms, corresponding to Equations 58 – 60, are enhanced by increasing $\tan\beta$ and by reducing μ, whereas Equation 61 is enhanced by increasing $\mu\tan\beta$. For illustration purporses, the SUSY contributions to a_μ according to the approximated formulae[16] in Equa-

[15] Scalar trilinear terms are neglected for simplicity.

[16] For more detailed studies using the exact formulae the reader is referred to e.g. [39].

tions 58 − 61 are shown in Figure 4. Here, two benchmark scenarios are considered: the bino case, where $M_1 = 200$ GeV, $\mu = 2M_1$, $\tan\beta = 10$, $m_{\tilde{\mu}_R} = m_{\tilde{\mu}_L}$, whereas M_2 and $m_{\tilde{\nu}_\mu}$ are decoupled from the spectrum, and the wino case, where $M_1 = 100$ GeV, $M_2 = \mu = 400$ GeV, $\tan\beta = 40$, $m_{\tilde{\mu}_R} = m_{\tilde{\mu}_L}$ and $m_{\tilde{\nu}_\mu} = 600$ GeV. It is observed that in all the cases considered, the experimentally measured a_μ can be recovered by adding the SUSY contributions discussed above. As a general rule, to generate sizable contributions to the muon $g-2$ while satisfying the observed dark matter relic abundance, sleptons and electroweakinos (charginos and neutralinos) should have masses of $\mathcal{O}(100$ GeV) [15, 16, 40].

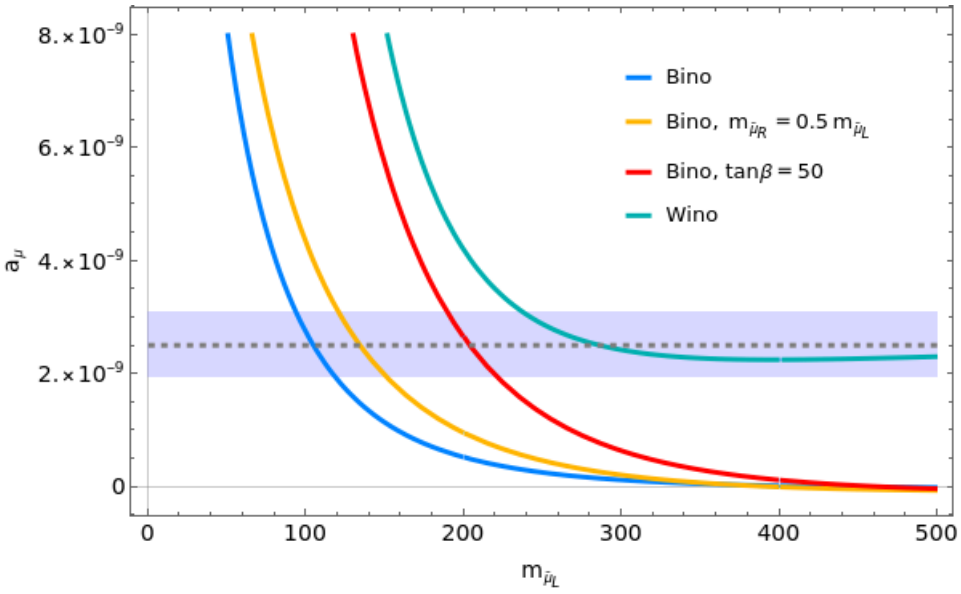

Figure 4: MSSM contributions to the anomalous magnetic moment of the muon as function of the mass of the left-handed smuon $m_{\tilde{\mu}_L}$. The gray dashed line corresponds to the difference between the experimental value and the SM prediction $\Delta a_\mu = 251 \times 10^{-11}$, with its uncertainty (blue band). The different colors represent different choices of the SUSY parameters M_1, M_2, μ, $\tan\beta, m_{\tilde{\mu}_R}$ and $m_{\tilde{\nu}_\mu}$. Left-handed and right-handed smuons are considered mass degenerate except where explicitly stated. The blue curve corresponds to the bino benchmark scenario, where $M_1 = 200$ GeV, $\mu = 2M_1$, $\tan\beta = 10$, $m_{\tilde{\mu}_R} = m_{\tilde{\mu}_L}$, whereas M_2 and sneutrinos are decoupled. Variations of the bino benchmark scenario are realised by changing $m_{\tilde{\mu}_R} = 0.5 m_{\tilde{\mu}_L}$ (yellow curve) and $\tan\beta = 50$ (red curve). The wino benchmark (green curve), inspired by [39], corresponds to the choice $M_1 = 100$ GeV, $M_2 = \mu = 400$ GeV, $\tan\beta = 40$ and $m_{\tilde{\nu}_\mu} = 600$ GeV.

Fine-tuning

In the MSSM, the mass of the Z boson can be related to SUSY parameters through

$$\frac{m_Z}{2} = \frac{m_{H_d}^2 - m_{H_u}^2 \tan^2\beta}{\tan^2\beta - 1} - \mu^2 \simeq -m_{H_u}^2 - \mu^2. \tag{63}$$

This means that m_{H_u} and μ have to be adjusted in such a way to reproduce the measured Z boson mass. The tuning is considered *natural* if the cancellation is not very sensitive to small variations of the parameters. This occurs for values of $\mu \lesssim 300$ GeV, implying the existence of light higgsinos $\tilde{\chi}_1^0, \tilde{\chi}_2^0$ and $\tilde{\chi}_1^\pm$ with masses of about $100 - 300$ GeV [29].

2.5 Simulation of proton-proton collisions

In order to simulate a proton-proton collision, we have to remember that protons are composite particles, thus, multiple quarks and (or) gluons (partons) collisions occur in the same pp collision. Therefore we normally identify the *hard process* with large momentum transfer that we are interested in, accompanied by an *underlying event*. The underlying event is just a consequence of the interaction of the partons that did not participate in the hard process. The underlying event is usually modelled using phenomenological models that describe the scattering process at small angles. A general sketch of a usual proton-proton collision is depicted in Figure 5.

The probability of finding a parton with momentum fraction x inside a proton is given by the Parton Distribution Functions (PDFs), shown in Figure 6. At the LHC, most of the collisions that take place involve gluons due to the high gluon densities inside the proton. In hard collisions, the cross section of a given process $pp \to cd$ can be calculated through

$$\sigma_{pp\to cd} = \sum_{a,b} \int_0^1 \int_0^1 dx_a dx_b f_a(x_a, \mu_F^2) f_b(x_b, \mu_F^2) \hat{\sigma}_{ab\to cd}(\mu_F^2, \mu_R^2), \tag{64}$$

where the sum runs over all the partons (quarks and gluons), $f(x, Q^2)$ are the PDFs and $\hat{\sigma}$ is the parton-parton cross section. The momenta of the partons are given by $p_{a,b} = x_{a,b}\sqrt{s}/2$. We have introduced two scales μ_F and μ_R, called factorization and renormalization scales, respectively. The factorization scale separates long and

short distance physics and arises from the infrared (collinear) divergences[17]. The renormalization scale has its origin in the ultraviolet divergences[18]and the need to renormalize the theory. Both scales are usually set to a characteristic scale that describes the hard process.

Since the hard process has large momentum transfer, the partons involved will be accelerated, radiating gluons, which can then split into quark-antiquark pairs ($g \to q\bar{q}$), and these quarks could further radiate more gluons, creating a *parton shower*. We distinguish between intial state showers (initial state radiation) and final state showers (final state radiation). The final state radiation occurs when an outgoing parton creates the shower. The initial state radiation develops when an incoming parton from the hard process radiates partons. The showering of the (initial state) partons stops when the hard collision occurs. As a result of this radiation, the parton also acquires transverse momenta (which was zero before the radiation), and is then transferred to the hard process.

The parton shower will evolve until the scale drops to $Q^2 \sim 1$ GeV^2, entering the non-pertubative regime of α_s. At this point, quarks and gluons are confined into colour neutral hadrons. This process is called *hadronization*. In order to describe this non-perturbative effects in generators, dedicated phenomenological models are used.

[17]Infrared divergences occur when the momentum of a massless particle approaches zero.
[18]These arise from divergent loop momentum integrations in Feynman diagrams.

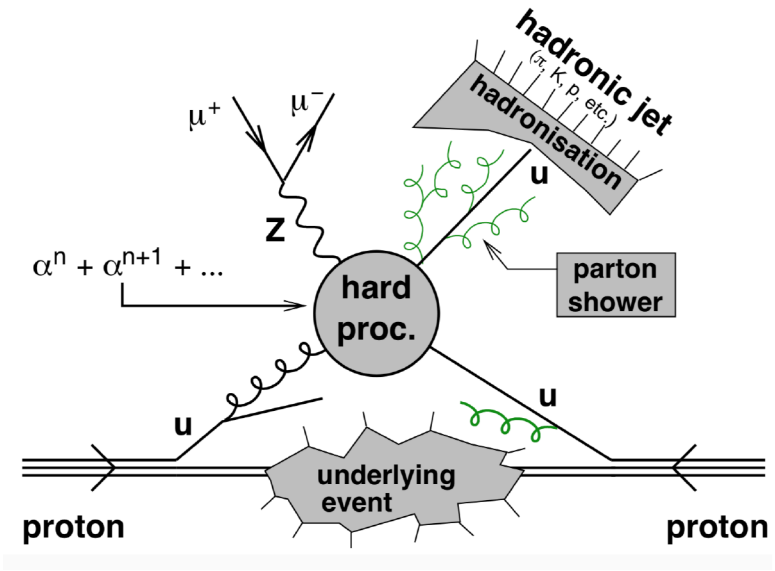

Figure 5: Sketch of a proton-proton collision. Figure taken from [41].

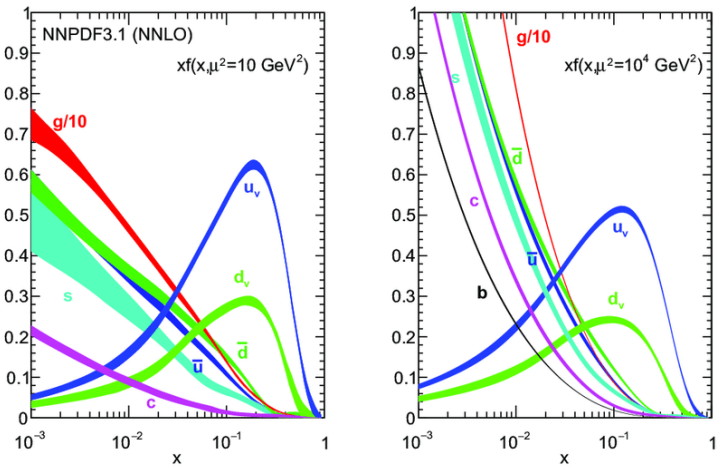

Figure 6: Parton distribution functions obtained in NNLO NNPDF3.0 global analysis [42] at scales $\mu^2 = 10$ GeV^2 (left) and $\mu^2 = 10^4$ GeV^2 (right) using $\alpha_s(M_z^2) = 0.118$.

A popular and intuitive model is the Lund String model [43], which is the approach taken by the Pythia event generator [44]. Other event generators like Sherpa use a cluster model for hadronization [45].
Finally, the produced hadrons (mostly pions, kaons and nucleons) are in general unstable and will eventually decay.
General-purpose event generators in proton-proton collisions use different models and approaches, the most commonly used ones in ATLAS are: Sherpa [46], Herwig++ [47] and Pythia [48].

After the physics simulation, in order to compare with real data obtained from the ATLAS detector, the simulated events have to go through the detector simulation. In this step, it is crucial to understand the detector and its subcomponents precisely. The ATLAS detector simulation relies on Geant 4 toolkit [49]. The ATLAS detector geometry is built into Geant 4 and the program provides physics models (physics interactions) for particles travelling through the detector parts. The energy deposits produced by the generated particles are recorded as *hits*. Then, the digitalization software converts the hits into detector responses. The result of the simulation is then processed, triggered and reconstructed using the same algorithms as if it was normal data [50].

2.6 Electroweak production of sparticles

If R-parity is conserved, the Supersymmetric partners of the Standard Model particles are produced in pairs. Electroweakinos (charginos and neutralinos) and sleptons are produced as in Figure 7. In the s-channel, the production of the electroweakinos and slepton pairs is mediated by a Z, W or γ boson. In the t-channel, the production proceeds through squark mediation, but, as we will discuss, in the models considered throughout this thesis the squarks are very heavy and therefore this production mechanism is highly suppressed. The production rate of sparticles depend on the couplings and the masses of the produced particles. In Figure 8 the production cross section of sleptons and electroweakinos as a function of their mass at proton-proton collisions for a center of mass energy of $\sqrt{s} = 13$ TeV is shown. First, we see that the $\chi\chi$ production cross section is about two orders of magnitude greater than for sleptons. We also observe that the $\tilde{\chi}_1^{\pm}\tilde{\chi}_1^{\pm}$ cross section is the lowest of all $\chi\chi$, and $\tilde{\chi}_1^0\tilde{\chi}_2^0$ the highest. Secondly, for sleptons, the left-handed slepton cross section is about three times higher than that for right-handed sleptons one due to interferences between Z and γ s-channel diagrams.

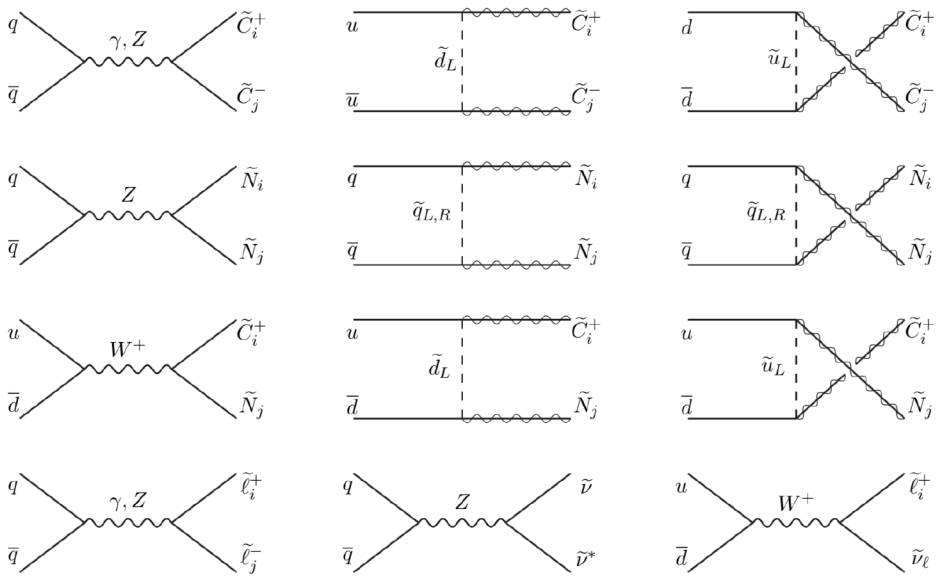

Figure 7: Sample of chargino, neutralino and slepton production diagrams at a hadron collider from quark-antiquark annihilation. Charginos are represented with $C_{i,j}^{\pm}$ and neutralinos with $N_{i,j}$. Diagrams taken from [51].

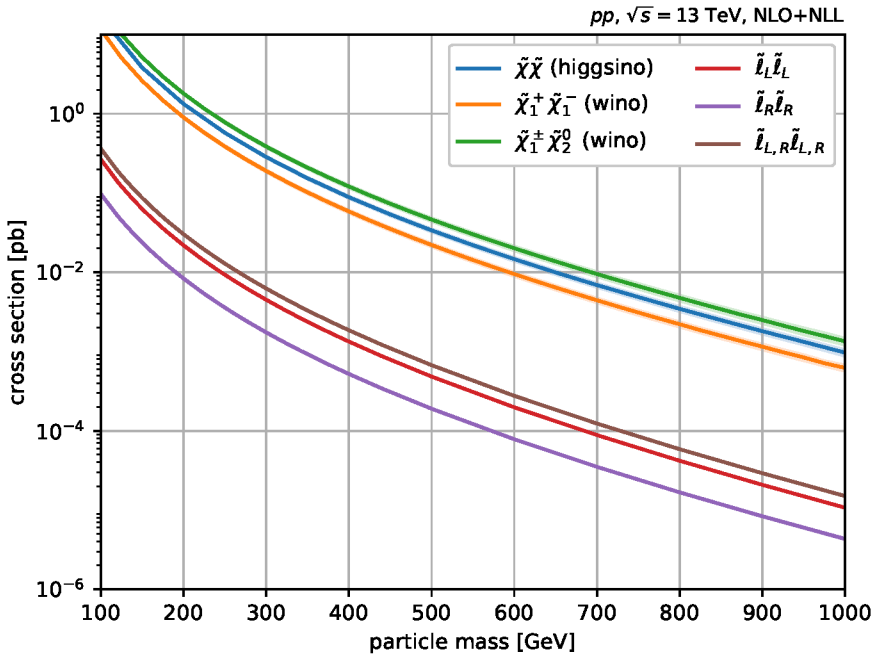

Figure 8: Production cross sections for electroweakinos and sleptons as a function of their mass, for pp collisions at $\sqrt{s} = 13$ TeV. The cross sections are calculated at next-to-leading order. Figure taken from [52].

Simplified models

Supersymmetric models usually predict a number of experimental observables as a function of theoretical parameters. In some cases the number of theoretical parameters is too large and a more model independent search is desired. To this end, simplified models [53] were proposed. They are effective models that are built with the minimal particle content required to produce the required SUSY final state. In this way, the dimensionality of the theoretical parameter space is reduced, simplifying the problem down to the sparticle masses and decay branching ratios. This allows for the interpretation of the results in terms of the cross sections times branching fractions as a function of the sparticle masses. As a consequence, the results interpreted in terms of simplified models can be used to test a wide variety of BSM models that predict a similar phenomenology.

The usual way of decoupling the other sparticles, is by setting their masses to values above the TeV scale. Example are squarks, which in this case are too heavy to contribute to the $t-$channel production mechanisms presented in Figure 7. Two sets

of simplified models are considered in this thesis: direct production of sleptons pairs and direct production of higgsino states. For the first scenario, left and right-handed sleptons are assumed to be degenerate in mass $m_{\tilde{\ell}_L} = m_{\tilde{\ell}_R}$. Furthermore, sleptons decay with a 100% branching ratio into their corresponding lepton and a (pure bino) LSP, $\tilde{\ell}_{\mathrm{L}}, \tilde{\ell}_{\mathrm{R}} \to \ell\tilde{\chi}_1^0$.
The higgsino model includes the production of $\tilde{\chi}_2^0\tilde{\chi}_1^{\pm}, \tilde{\chi}_2^0\tilde{\chi}_1^0$ and $\tilde{\chi}_1^{\pm}\tilde{\chi}_1^{\pm}$. The $\tilde{\chi}_1^{\pm}$ and the $\tilde{\chi}_2^0$ also decay with a 100% branching fraction into W and Z bosons, respectively, accompanied by the LSP, $\tilde{\chi}_1^{\pm} \to W^{\pm} + \tilde{\chi}_1^0$, $\tilde{\chi}_2^0 \to Z + \tilde{\chi}_1^0$. While the masses of the $\tilde{\chi}_1^0, \tilde{\chi}_2^0$ are varied, the $\tilde{\chi}_1^{\pm}$ masses are set to $m(\tilde{\chi}_1^{\pm}) = \frac{1}{2}\left[m(\tilde{\chi}_1^0) + m(\tilde{\chi}_2^0)\right]$.
Finally, the lifetimes of sleptons and charginos depend on the mass splittings with respect to the $\tilde{\chi}_1^0$. These particles only acquire a significant lifetime to be detected directly in the detector for mass splittings below few hundreds of MeV. Since the mass splittings considered in this thesis are above this threshold, the sparticles will decay promptly, and only the decay products will reach the detector.

3 The LHC and the ATLAS detector

3.1 Particle colliders: the Large Hadron Collider

Particle colliders are used to accelerate particles to certain energy and then collide them. They can be used to study the small scale structure of the universe, since smaller distances are reached as the energy of the collision increases ($\lambda \propto 1/E$). It is well known that a symmetric collider with beam energy E is more efficient in reaching higher energies than a fixed target experiment, since the center of mass energy at a collider is given by

$$\sqrt{s} = 2E, \tag{65}$$

opposed to a fixed target (with mass m) experiment, where $\sqrt{s} = \sqrt{2mE}$ $(E \gg m)$. However, in colliders it is much more challenging to achieve high luminosities. Furthermore, when charged particles are accelerated in a circular machine, they emit synchrotron radiation and thus lose part of their energy. For an ultra-relativistic particle with mass m the power emitted is

$$P = \frac{2}{3}\frac{r_c m \gamma^4}{\rho^2}, \tag{66}$$

where γ is the Lorentz factor $\gamma = (1 - \frac{v^2}{c^2})^{-1/2} = E/mc^2$, ρ the radius of curvature and $r_c = e^2/4\pi\epsilon_0 mc^2$. Therefore, for protons, the energy loss due to synchrotron radiation is negligible (but not for electrons).
The beams also have to be guided and focused through the beam pipe. The bending of the charged particle trajectory is done with dipole magnets, which provide a vertical magnetic field. The radius of the trajectory for a particle with momentum p, mass m and charge q is given by

$$r = \frac{p}{qB}, \tag{67}$$

where B is the magnetic field. To avoid protons escaping from the accelerator, the particle bunches have to be squeezed and focused, which is achieved by using quadrupole magnets.

The acceleration of the charged particles is done with metallic chambers containing electromagnetic fields called Radiofrequency (RF) cavities. Since the nature of the electromagnetic field inside the cavity is oscillating (switches direction with time), the beams need to enter the accelerating cavity at the right time, leading to a bunched structure of the beam.

The Large Hadron Collider (LHC) is a 27 km long circular particle collider situated beneath the France and Switzerland border, near Geneva. It accelerates beams of protons[1] up to an energy of 6.5 TeV and collides them with a center of mass energy of $\sqrt{s} = 13$ TeV. The LHC is embedded in an accelerator complex at CERN, which consists in a succession of different machines which increasingly accelerate the protons, until they are injected in the LHC. All the different components of the accelerator complex are included in Figure 9. The protons path start at a Hydrogen bottle that contains Hydrogen atoms. The electrons from the Hydrogen atoms are stripped from the atoms by applying electric fields. The proton beam is then accelerated through the following steps:

1. The beam is injected into the PS booster at an energy of 50 MeV from LINAC 2, where it is accelerated to an energy of 1.4 GeV.

2. The beam enters the Proton Synchrotron (PS) and is accelerated to 25 GeV.

3. The protons are then sent to the Super Proton Synchrotron (SPS), where they are accelerated to an energy of 450 GeV.

4. Finally they enter the LHC, where they are accelerated to an energy of 6.5 TeV in about 20 minutes. In normal operation mode the protons circulate for some hours along the beam pipe.

Once the protons reach the desired energy, they collide at four points where the two rings of the machine intersect. Surrounding each of these four points there is a detector: ATLAS, CMS, LHCb and ALICE. ATLAS and CMS are multipurpose detectors that study a wide variety of physics. LHCb is dedicated to the study of the bottom-quark physics and ALICE is specialized in analysing lead-ion collisions to better understand the quark-gluon plasma.

[1] It also accelerates heavy ions, but this will not be discussed in this thesis

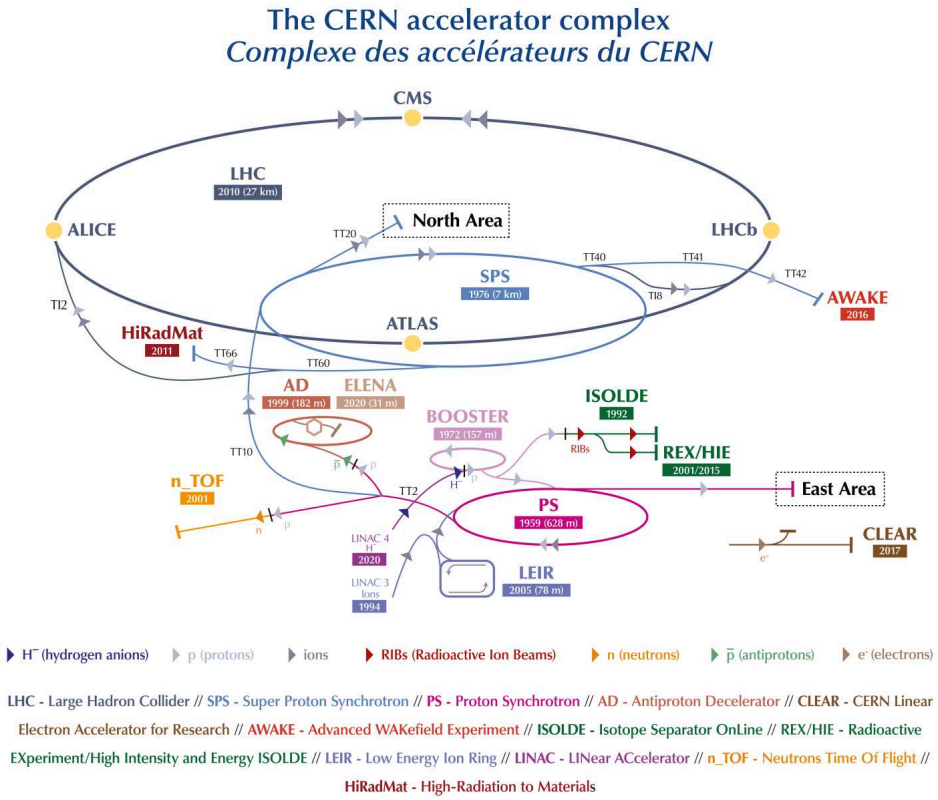

Figure 9: CERN accelerator complex. Figure taken from [54].

Luminosity

One of the most important quantities in a particle collider, together with the center of mass energy, is the luminosity. The number of produced events is given by the integral of the instantaneous luminosity $\mathcal{L}$ over time, multiplied with the cross section σ of the process of interest,

$$N = \sigma \times \int \mathcal{L}(t)dt. \tag{68}$$

If we consider two proton bunches colliding head-on with a revolution frequency f_r ($\sim$ 10 kHz at the LHC), the luminosity can be expressed as

$$\mathcal{L} = \frac{N_b^2 n_b f_r}{4\pi\beta^*\epsilon} F, \tag{69}$$

where

- N_b is the number of protons per bunch[2], about 10^{11} at the LHC
- $n_b \sim 2500$ the number of colliding bunches
- β^* the focusing function (at the interaction point) is a measure of the width of the beam.
- the emittance ϵ is the area in the (x, p_x) plane occupied by the beam particles[3].
- F is the geometrical factor that takes into account geometric effects as crossing angle and finite bunch length, its value is of order one.

By optimizing each one of the above parameters the luminosity can be increased. First, it is clear that, increasing the number of protons per bunch and the bunches per beam will increase the luminosity. On the other hand, lowering emittances and the focusing can also result in an increase of the luminosity. Low emittances are achieved by having the beam particles confined together to small distances, while having similar momentum. The decrease of β^* is achieved by having strong focusing quadrupole magnets, reducing the transverse beam size. At the LHC, the collisions take place every 25 ns, and about 34 collisions per bunch crossing occur (see Figure 11). The design instantaneous luminosity at the LHC corresponds to $\mathcal{L} = 2 \times 10^{34}$ cm^{-2}s^{-1}. If we integrate over time, we get the total (integrated) luminosity. The delivered luminosity at the ATLAS detector for various years of LHC operation is shown in Figure 10. The luminosity used for physics analyses at $\sqrt{s} = 13$ TeV in ATLAS adds up to about 139 fb^{-1}.

The luminosity is measured by counting the number of interactions each time the beams cross. In ATLAS, the LUCID detector is used [56], situated at either sides of the interaction point. The calibration of the detector is done using van der Meer (vdM) scans using special low luminosity LHC fills. During these special runs, the beams are separated, vertically and horizontally, varying the overlap between the beams. The mean number of interactions per bunch crossing is then measured as a function of the separation to determine the beam width in x and y. Then, the total number of protons in each colliding bunch from the measurement of the beam currents is determined. Combining all these ingredients, the luminosity for each colliding bunch pair can be computed.

[2]Equation 68 assumes that the two bunches have the same number of protons, $N_{b_1} = N_{b_2}$.
[3]At constant energies (x, p_x) can be replaced by $(x, x' = dx/dz)$. Where z is the longitudinal component and x one of the transverse components.

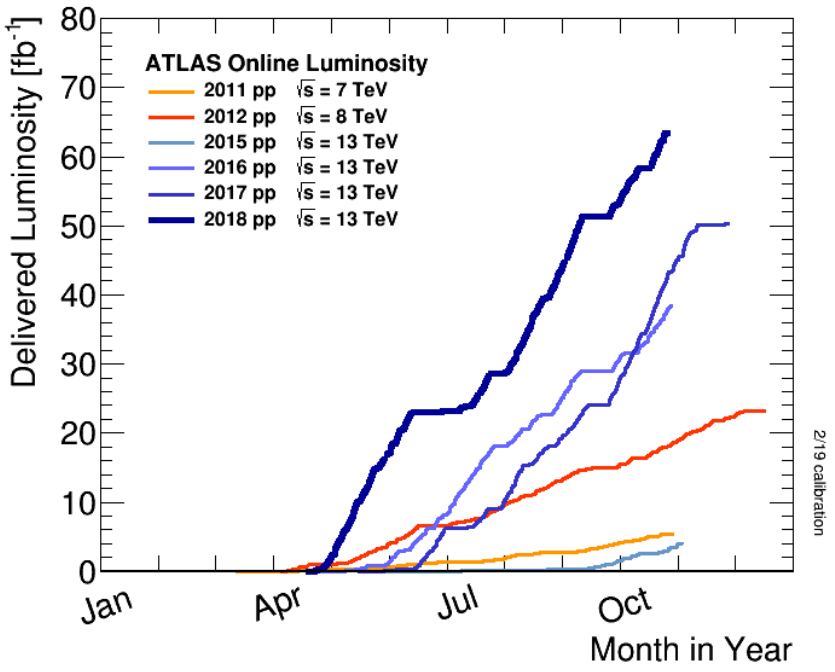

Figure 10: Cumulative luminosity as a function of the day it was delivered to the ATLAS detector for pp collisions. Figure taken from [55].

The averaged number of interactions per bunch crossing $\langle\mu\rangle$ can be calculated from

$$\langle\mu\rangle = \frac{\mathcal{L}\sigma_{\text{inel}}}{N_{\text{bunch}} f_r}, \tag{70}$$

where σ_{inel} is the pp inelastic cross section (80mb, see e.g. [57]). The integrated luminosity as a function of the mean number of interactions per bunch crossing is shown in Figure 11.

Pile-up

Out of all the collisions that occur in each bunch crossing, usually only one is energetic enough to be of interest. The rest of collisions happening during the same crossing are called pile-up interactions, and they represent a challenge in physics analyses. There are several sources of pile-up:

- In-time pile-up: collisions occurring during the same bunch crossing as the collision of interest.

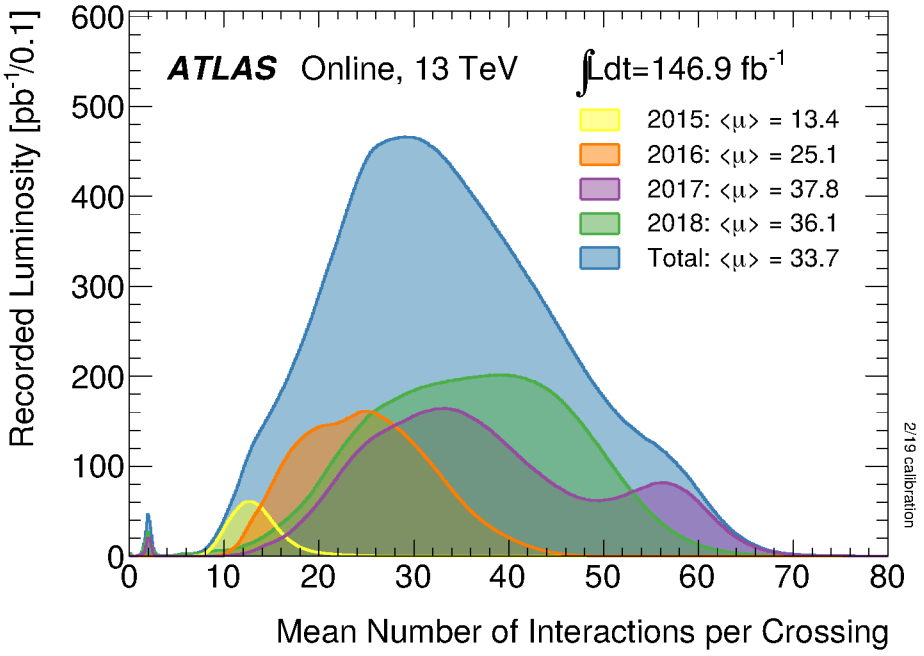

Figure 11: Integrated luminosity as a function of the mean number of interactions per bunch crossing at 13 TeV. Figure taken from [55].

- Out-of-time pile-up: collisions happening right before or right after the collision of interest. When a subdetector electronics integration time is greater than 25 ns, the out-of-time pile-up can lead to changes in the signal.
- Cavern background: neutrons and photons present in the LHC cavern, which leave random hits in the different subdetectors.
- Beam-halo events: off-orbit protons interact with the beam-pipe, creating hadronic showers parallel to the beam-pipe.
- Beam gas events: collisions of protons and residual gas present in the beam pipe.

3.2 The ATLAS detector

The ATLAS detector [58], situated in one of the four interaction points at the LHC, is a multipurpose detector that studies a wide variety of physics processes. The general structure of the detector is depicted in Figure 12. The coordinate system adopted by

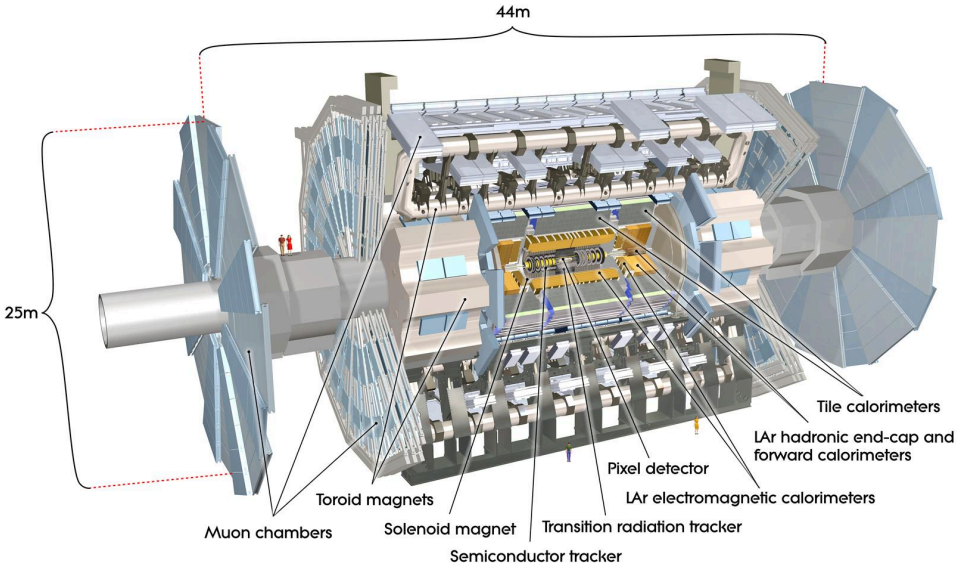

Figure 12: View of the ATLAS detector and subdetectors. Figure taken from [58].

ATLAS has the origin centered at the nominal collision point inside the experiment, the y-axis pointing vertically upward, and the x-axis pointing radially inward toward the center of the LHC. Thus, the z-axis points along the counterclockwise-beam direction. The azimuthal angle ϕ is measured from the x-axis in the $x-y$ plane, around the beam axis. The polar angle θ is measured from the z-axis. In hadron colliders, a more convenient variable is used instead of the polar angle, the rapidity, defined as

$$y = \frac{1}{2} \ln \left[(E + p_Z)/(E - p_Z) \right], \tag{71}$$

where E and p_z are the energy and z component of the momentum along the beam direction, respectively. Differences in rapidity are invariant under Lorentz transformations along the beam direction. At high energies ($E \gg m$) the rapidity can be approximated by the pseudorapidity,

$$\eta = -\ln \tan (\theta/2). \tag{72}$$

In this way, $\eta = 0$ $(\theta = \pi/2)$ is perpendicular to the beam line and $\eta = \infty$ $(\theta = 0)$ is parallel to the beam line. To measure the angular separation between two points, the combined angle $\Delta R = \sqrt{\Delta\eta^2 + \Delta\phi^2}$ is used, where $\Delta\eta = \eta_2 - \eta_1$ and $\Delta\phi = \phi_2 - \phi_1$. The momentum transverse to the beam direction (transverse momentum) p_{T} is thus

computed from the x and y components[4], $p_T = \sqrt{p_x^2 + p_y^2}$. The vector sum of all transverse momenta before and after the collision is zero, and any imbalance of the momentum in the transverse plane is accounted in the missing transverse momentum, denoted by E_T^{miss}.

The ATLAS detector follows the usual structure of a high energy physics detector, from the innermost to outermost layers we have:

- Inner tracker: high precision silicon and transition radiation detectors which are immersed in a magnetic field. The magnetic field bends the trajectory of charged particles and thus the particle momentum can be computed. It is also used for vertex reconstruction, e.g., secondary vertices created by long-lived hadrons originating from b and c quark hadronization. Surrounding the ATLAS tracker, a solenoid that provides a magnetic field of 2 T is placed.

- Calorimeters: the electromagnetic (EM) calorimeter provides precision measurements of electrons and photons. The hadronic calorimeter (HCAL) is used to calculate the energy of hadrons. Except for muons and neutrinos (and/or neutralinos), all the SM particles will deposit their energy in the calorimeters. Thickness and good $|\eta|$ coverage is crucial for a good E_T^{miss} measurement.

- Muon spectrometer: the only remaining Standard Model particles at this stage will be muons (and neutrinos). Immersed in a magnetic field created by toroid magnets, muons trajectories are bent and measured in the muon chambers.

3.2.1 Magnet system

The ATLAS magnet system is composed of a thin superconducting solenoid surrounding the Inner Detector cavity and three large toroids (a barrel toroid and two end-cap toroids), as shown in Figure 13. The solenoid is aligned with the beam axis and provides a 2 T magnetic field to the inner detector. The barrel and end-cap toroids provide a magnetic field of 0.5 T and 1 T to the muon detectors in the barrel and end-cap regions, respectively. The advantage of this field configuration is that it allows two independent measures of the muon momentum.

[4]Cartesian coordinates are obtained from the p_{T}, $p_x = p_{\text{T}} \cos\phi, p_y = p_{\text{T}} \sin\phi, p_z = p_{\text{T}} \sinh\eta$.

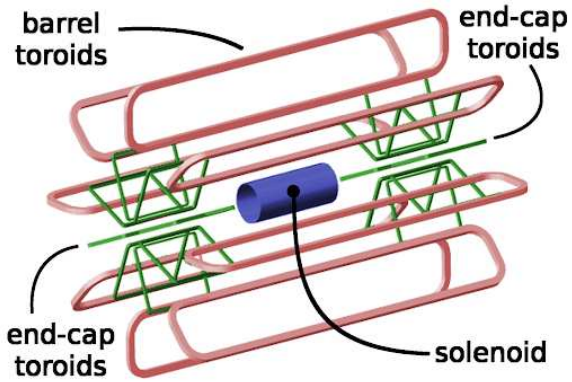

Figure 13: Schematic view of the ATLAS magnet system. Figure taken from [59].

Energy and momentum resolution

The resolution of a charged particle track can be approximated as[5]

$$\frac{\sigma(p_{\mathrm{T}})}{p_{\mathrm{T}}} \approx \frac{8 p_{\mathrm{T}} \delta s}{0.3 B l^2}, \tag{73}$$

where δs is the uncertainty on the position of the track in the midpoint. It is seen that, for a track measured over a length l and with constant magnetic field B, the resolution degrades as the p_{T} is increased (straighter tracks). In a real detector, however, the resolution also has to take into account multiple scattering effects. Since the scattering angle goes as $\theta \propto 1/p$, the contribution will cause a constant uncertainty on $\sigma(p_{\mathrm{T}})/p_{\mathrm{T}}$, parametrized as

$$\frac{\sigma(p_{\mathrm{T}})}{p_{\mathrm{T}}} = C \oplus D p_{\mathrm{T}}, \tag{74}$$

where C is the contribution from the multiple scattering, and D from the spatial precision. Thus, the precision is limited by multiple scattering at low p_{T}, and by spatial resolution at high p_{T}. Typical values for the ATLAS detector can be consulted in Table 2.
The resolution of a calorimeter can be parameterized as

$$\frac{\sigma(E)}{E} = \frac{a}{\sqrt{E}} \oplus \frac{b}{E} \oplus c, \tag{75}$$

[5]The approximation assumes that the track is measured with high precision at the beginning and end of the trajectory.

Detector	Resolution	$\lvert\eta\rvert$ coverage
Tracking	$\sigma_{p_{\mathrm{T}}}/p_{\mathrm{T}} = 0.05\%\ p_{\mathrm{T}} \oplus 1\%$	< 2.5
EM calorimeter	$\sigma_E/E = 10\%\ \sqrt{E} \oplus\ 0.7\%$	< 3.2
HCAL		
Barrel and end-cap	$\sigma_E/E = 50\%\ \sqrt{E}\ \oplus 3\%$	< 3.2
Forward	$\sigma_E/E = 100\%\ \sqrt{E}\ \oplus 10\%$	$< 3.1\ \lvert\eta\rvert < 4.9$
Muon Spectrometer	$\sigma_{p_{\mathrm{T}}}/p_{\mathrm{T}} = 10\%\ p_{\mathrm{T}}$ at $p_{\mathrm{T}} = 1$ TeV	< 2.5

Table 2: Resolution for the different detector components in ATLAS [58].

being a, b and c constants (see Table 2 for typical ATLAS values). The constant a is called the stochastic term, b corresponds to the electronic noise and c is a constant term. The stochastic term can be interpreted as a statistical term $a/\sqrt{E} \sim 1/\sqrt{N}$, where N is the number of photons detected. The noise term b is usually negligible at high energies and can be reduced with good calibration. The constant term c includes effects from detector instabilities and miscalibration. When the detector is in operation, effects like pile-up and radiation damage can also degrade the resolution of the calorimeters.

3.2.2 Inner detector

The ATLAS Inner Detector (ID) is the innermost subdetector. It is composed of two silicon detectors, the Silicon Detector and the Semi-conductor Tracker (SCT), and the Transition Radiation Tracker (TRT), as depicted in Figure 14. The Inner Detector angular coverage is $|\eta| < 2.5$. All these parts are immersed in a 2 T magnetic field produced by the solenoid magnet surrounding the Inner Detector. During the LHC shutdown period in $2013 - 2014$ the inner detector was upgraded with the installation of a new pixel detector layer, together with a new beam pipe, referred as insertable B-layer (IBL). The new beam pipe is made of beryllium[6] with 23.5 mm of inner radius and ranging from 24.3 mm ($|z| < 30$ mm) to 28.2 mm ($|z| > 311$ mm). The pixel detector (with IBL) covers the radial region (measured from the interaction point) of 33 to 150 mm. The SCT and TRT span the radial regions from $299 - 560$ mm and $563 - 1066$ mm, respectively.

As charged particles travel through the detector, they leave hits allowing to reconstruct the particle trajectory. Since silicon is a semiconducting material (with a band-gap of 1.1 eV), when a charged particle passes through, it interacts with the silicon creating

[6] Beryllium is ideal for beampipes since it minimizes multiple scattering

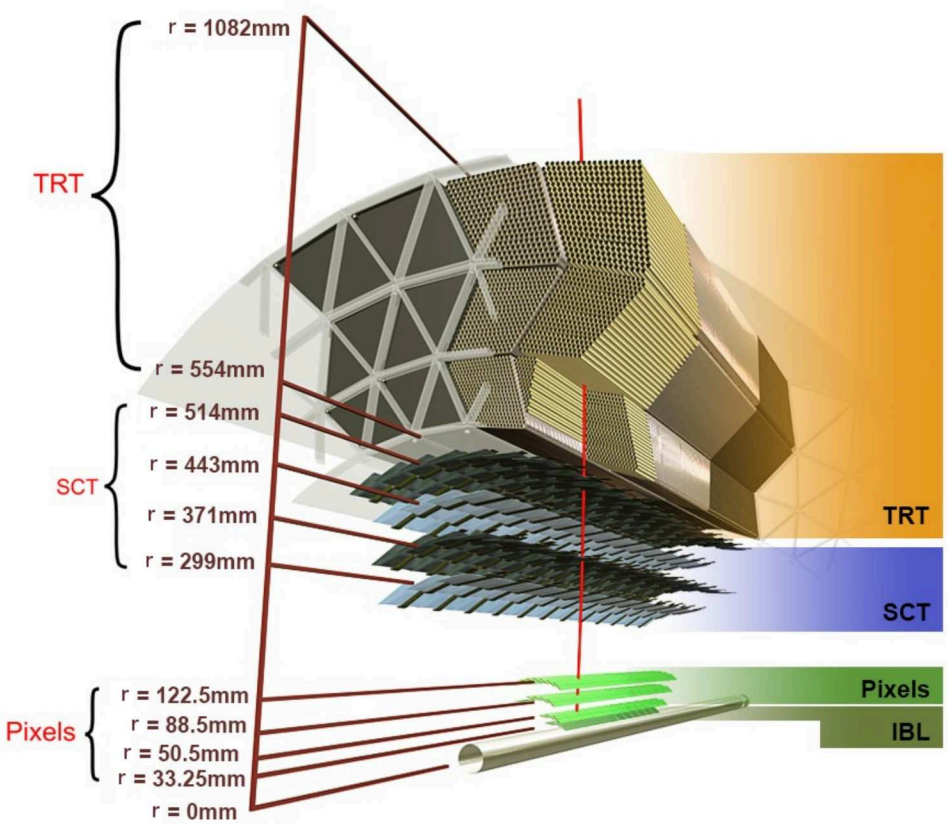

Figure 14: ATLAS Inner Detector. Figure taken from [60].

charge carriers (electron-hole pairs). Most of the energy goes into phonons, so the energy loss per electron-hole pair is larger, about 3.6 eV. For a minimum ionizing particle, this corresponds to 80 electron-hole pairs per micrometer. The electron-hole pairs are then separated applying an electric field, sweeping the charges carriers to electrodes. The motion of the electrons and holes induces a current into the external circuit, which can be measured. The current is then amplified and digitised by the readout electronics. The number of electron-hole pairs is proportional to the absorbed energy, thus integrating the signal current, the signal charge is obtained. The spatial resolution of the silicon detectors depend on the segmentation of the silicon into individual detector channels. If a particle causes a hit and all the charge is collected in a single strip, the spatial resolution in this direction is $x/\sqrt{12}$. The spatial resolution can be further improved by using signal information from neighbour channels, giving extra information on the location of the hit. One of the main advantages of pixel over strip detectors is their low capacitance (from their smaller size), resulting in low

noise.

Pixel detector

The pixel detector consists of four barrel layers and two end-caps with three disks each. The innermost pixel layer, the IBL, situated at 3.3 cm from the beam axis, has 14 staves that cover the region $|\eta| < 3.3$ with more than 12 million silicon pixels with a size of $50\,\mu m \times 250\,\mu m$ each.
The remaining layers are composed of 1744 pixel sensor modules, with each module containing 46080 pixels with a size of $50\,\mu m \times 400\,\mu m$ each. The smaller dimension is placed in the bending plane of the magnetic field in order to maximize the momentum resolution. The radii of the three barrel layers are 50.5 mm, 88.5 mm and 122.5 mm. Overall, the detector has over 80 million pixels (80 million channels) distributed in $2m^2$ of sensor area.

Semi-conductor Tracker

The SCT has 4088 two-sided silicon micro-strip modules (providing 2-dimensional position measurements), arranged in four barrel layers and two end-caps with nine wheels each. It has about $60m^2$ of silicon strips with 6×10^6 strip detector channels.

Transition radiation tracker

Beyond 56 cm of radius, we find the TRT (barrel and end-cap), which consists of more than 350×10^3 gas filled straw tubes (350×10^3 channels). The TRT barrel consists of 73−layer straw tubes filled with gas providing at least 40 hits per track. The TRT end-caps consists of two sets of identical wheels. The first set has 12288 radial straws and the second set 6144. The tubes are filled with a mixture composed primarily of Argon (for good X-ray absorption).
The TRT uses transition radiation[7]. When a high energetic particle crosses the boundary between two media with different dieletric constant, transition-radiation photons are emitted[8]. This is accomplished by filling the spaces between the straws with polymer fibres (barrel) and foils (end-cap). The transition radiation increases with the Lorentz factor γ, and therefore the TRT is useful to distinguish between high energy electrons and charged hadrons (pions).

[7] Particles traversing the TRT also ionize the gas inside the straws, the resulting electrons drift towards the wire creating a measurable current.
[8] These photons are in the X-ray regime. Typical TR photon energies for electrons and pions are $8 - 10$ keV and 2 keV, respectively.

3.2.3 Calorimetry system

When a particle interacts with the calorimeter, it deposits its energy creating a cascade of secondary particles[9]. All the particles except muons and neutrinos usually deposit all their energy in the calorimetry system. There are electromagnetic calorimeters and hadronic calorimeters to measure electromagnetic and hadronic showers, respectively. The electromagnetic showers tend to be more compact in volume than the hadronic ones, thus requiring a greater segmentation in the EM calorimeter. The components of the ATLAS calorimetry system are the Liquid Argon (LAr) Calorimeter and the Tile Hadronic Calorimeter (TileCal). The LAr technology is also used in the detection of hadronic activity in the Hadronic End-Cap Calorimeter and in the Forward Calorimeter (FCal), providing a coverage up to $|\eta| < 4.9$. All these components are shown in Figure15.

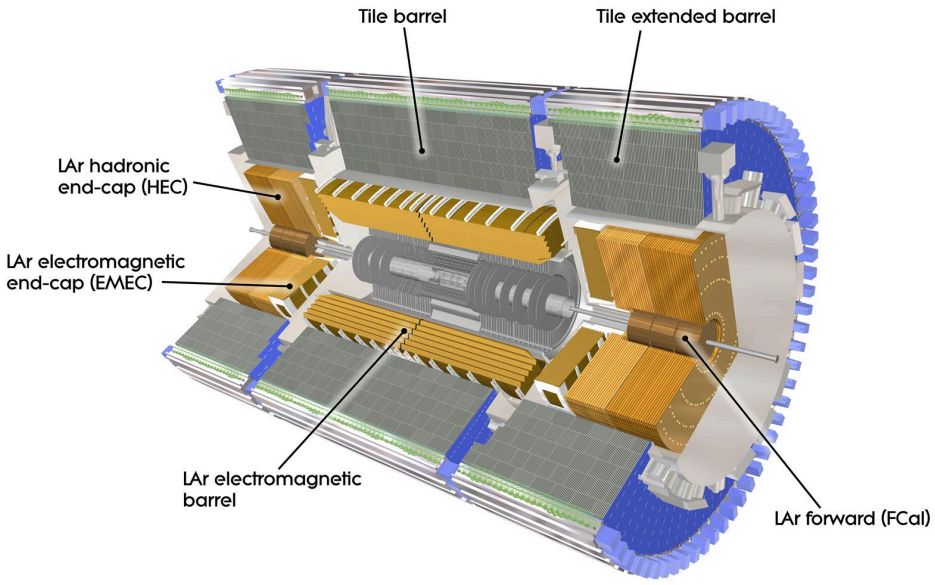

Figure 15: ATLAS calorimetry system. Figure taken from [58].

The electromagnetic calorimeter

The EM calorimeter absorbs the energy coming from electrons and photons. The emerging shower depth is determined by the ability of the calorimeter to stop these particles. There are "sampling" and "homogeneus" calorimeters. Since ATLAS only

[9]Showers of particles originating from the fragmentation and hadronization of quarks are called jets

uses sampling calorimeters, only the former is discussed. The sampling calorimeters contain successive layers of an active material and passive (absorbing) material. Most of the energy of the particles is deposited in the passive layers. The passive material is usually a material with high atomic number Z. The energy deposited in the active layer is only a small fraction of the total energy deposited.
The EM calorimeter consists of a barrel part ($|\eta| < 1.475$) and two end-caps ($1.375 < |\eta| < 3.2$). The barrel consists of two identical half-barrels separated by a gap of 4 mm at $z = 0$. It is 6.4 m long, has 53 cm of thickness and contains 110 000 channels. The end-cap calorimeter is divided into two wheels, one covering the region $1.375 < |\eta| < 2.5$ and the other one covering $2.5 < |\eta| < 3.2$. The passive material is lead (Pb) and the active material liquid Argon, which operates at -183°C. It has accordion-shaped kapton electrodes and lead absorber plates. In the region $|\eta| < 1.8$, a presampler detector is placed in order to correct for the energy losses of electrons and photons upstream in the calorimeter.

The Hadronic Calorimeter

Placed outside the EM calorimeter we find the hadronic calorimeter as depicted in Figure 15. The barrel of the hadronic calorimeter covers the region $|\eta| < 1.0$, is made of 64 wedges, each 5.6 m long and weighs 20 000 kg. The two extended barrels cover the region $0.8 < |\eta| < 1.7$, each has 64 wedges, each 2.6 m long and weighing 9 600 kg.
It is, as for the EM case, a sample calorimeter using steel as absorber and scintillating tiles (about 500 000) as active material.

3.2.4 The Muon Spectrometer

Surrounding the calorimetry system we find the Muon Spectrometer, shown in Figure 16. The ATLAS Muon Spectrometer (MS) has a cylindrical structure of 22 m in diameter and 45 m in length. Its angular coverage is $|\eta| < 2.7$. In the MS, the muons are identified, triggered and their charge sign and momenta are measured. For triggering, Resistive Plate Chambers (RPC's) and Thin Gap Chambers (TGC's) are used in the barrel and end-cap regions, respectively. They also measure the coordinates of the muon in the non-bending plane. Over most of the η range, the tracking is performed by Monitored Drift Tubes (MDT's). The MDT's provide precision particle tracking in the $r - z$ plane, defined by the beam axis (z) and the radial distance to the beam (r). In the more forward region, $2 < |\eta| < 2.7$, Cathode

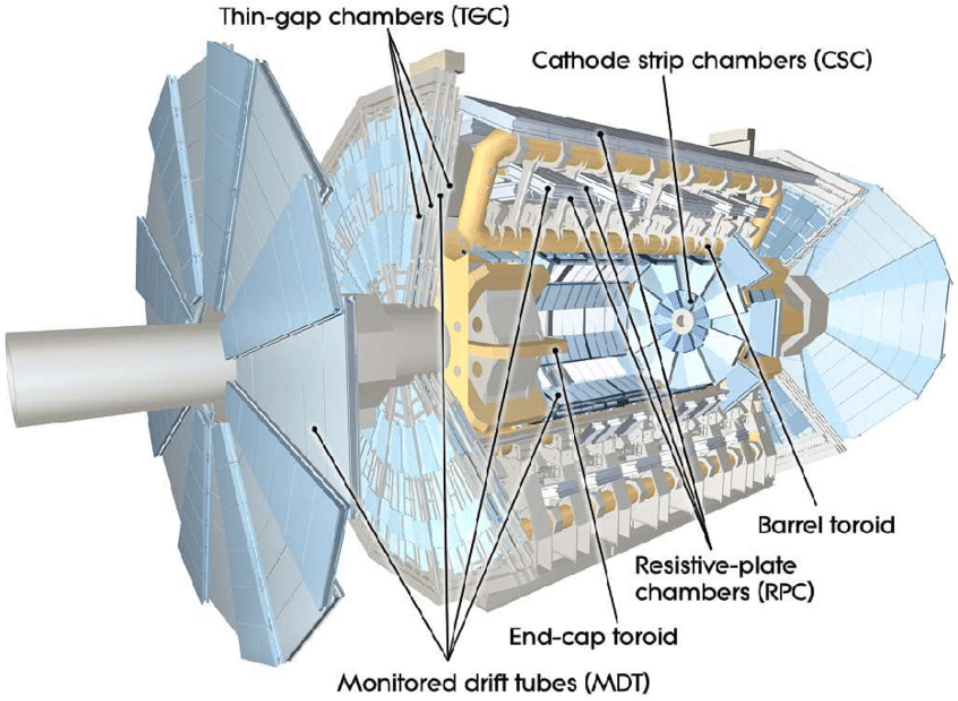

Figure 16: Muon spectrometer in ATLAS. Figure taken from [58].

Strip Chambers (CSC's) with higher granularity are used. The MDT's are made of cylindrical aluminium drift tubes, and filled with 93% Argon and 7% CO_2. When a muon traverses a drift tube, it causes ionization of the gas, creating electron-ion pairs along its trajectory. Electrons drift towards the anode wire and the (slower) ions drift towards the cathode. The number of electron-ion pairs is increased due to high energy electrons being able to ionize the gas further[10]. When the electrons reach the anode, they create a measurable current, which is proportional to the original number of ions created. Since the electrons drift with uniform velocity towards the anode, this can be translated into a measurement of the distance of the muon to the anode, providing an accurate measurement of the position of the muon.

3.2.5 Trigger system and data acquisition

The triggering and data acquisition is an essential component at the LHC: triggering interesting event candidates while maintaining high readout rate. This, however, is usually very challenging due to the high levels of hadronic activity and high collision

[10] When the electrons are close to the wire, the electric field is very high and the electrons acquire energies to further ionize the gas, creating an avalanche process.

rate.
The ATLAS trigger system is composed of a first-level hardware based trigger (L1) and a software based high-level trigger (HLT). The L1 trigger reduces the event rate from 40 MHz to 100 kHz. It uses custom electronics to determine Regions-of-Interest (ROIs) around the trigger signal in the detector. It takes as input calorimetry and muon detector information. The data is stored in a pipelined system in order to cope with the 25 ns between bunch crossings. The decision is taken in about 2.5 ms after the collision, and the event is then retrieved from the pipelined storage buffers. The L1 trigger uses distinctive signatures to make the trigger decision: high missing transverse momentum, high p_{T} muons, electrons, or jets. It contains configurable algorithms to trigger electrons, photons, hadronically decaying tau leptons, muons, jets and E_T^{miss}. The candidate events are then fed into the HLT.
In the HLT, the events are reconstructed in large CPU farms with algorithms, forming a decision in about 300 ms. Here, the ROIs formed by the L1 are sent to the HLT. The HLT then runs dedicated algorithms on the whole event. In this step the rate is reduced from 100 kHz to about 1 kHz. These events are then sent to the CERN storage, and prepared for the offline analysis.

3.3 The High-Luminosity LHC

The LHC will receive a major upgrade between 2025 and 2027, referred to as High-Luminosity LHC (HL-LHC) upgrade. The integrated luminosity delivered at the end of its lifetime is expected to be 3000 fb^{-1}. In this regime, the average proton-proton inelastic collisions per bunch crossing will reach $\langle\mu\rangle = 200$. This will of course represent a challenging environment for the ATLAS experiment. In order to cope with the radiation while maintaining high tracking performance, the ATLAS collaboration decided to replace the Inner Detector with a new all-silicon tracker Inner Tracker (ITk).

3.3.1 Motivation for detector upgrade

The current ATLAS Inner Detector was designed for 10 years of operation with a center of mass energy of 14 TeV, 25 ns spacing between bunch crossings and 23 pile-up interactions per bunch crossing. Despite that some of these numbers have been surpassed, the ATLAS Inner Detector has shown good performance so far. Although it has been well suited until now, there are few limitations for the future:

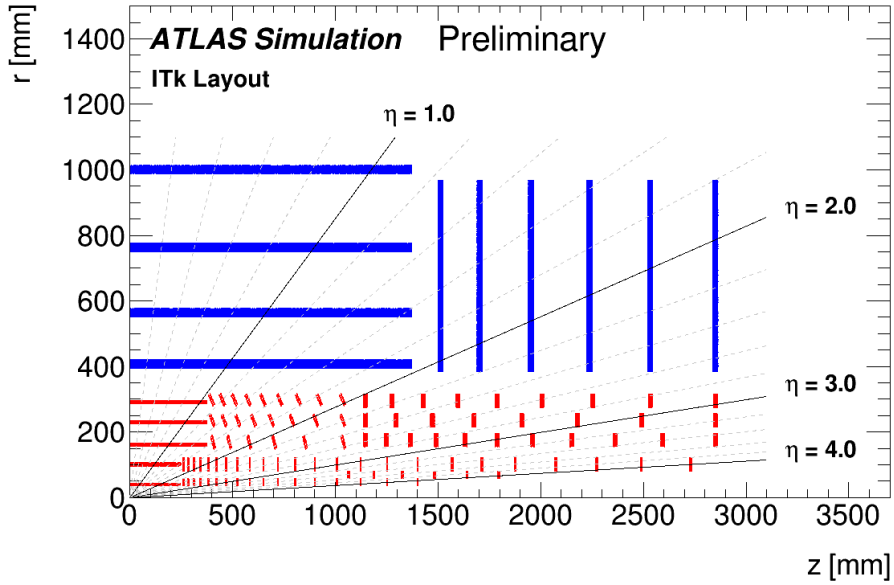

Figure 17: ATLAS ITk layout from [61].

- Radiation damage. The Pixel detector and the Semi-Conductor Tracker were designed to tolerate the radiation damage equivalent to roughly 400 fb^{-1} and 700 fb^{-1} of integrated luminosity, respectively. Therefore, the detector as it is right now is not ready to survive the HL-LHC phase.

- Bandwidth saturation. The Inner Detector electronics will saturate due to the high collision rate, leading to inefficiencies and to loss of data.

- Detector occupancy. If the number of tracks rises due to the higher pile-up but the granularity is not increased, this will also lead to inefficiencies in pattern recognition and track finding.

- Trigger. The L1 trigger does not receive any tracking information from the Inner Detector in its current state. By providing tracking information to the L1 trigger, the trigger thresholds could be lowered, benefiting physics analyses.

The ITk consists of a pixel subsystem with coverage up to $|\eta| < 4$ and a strip subsystem covering $|\eta| < 2.7$. The pixel system consists in five barrel layers and five layers of inclined rings. The strips detector has four strip module layers in the barrel and six disks in the end-cap. A schematic view of the ITk layout is shown in Figure 17.

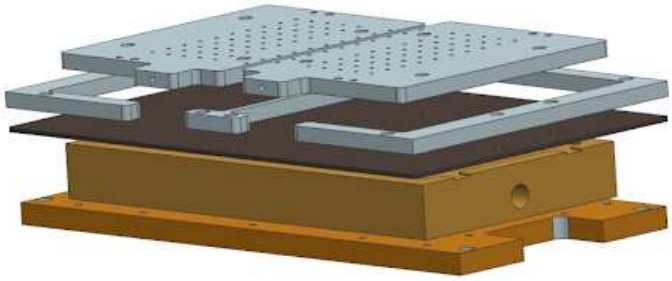

Figure 18: Exploded view of the cooling setup. From top to bottom: Vaccum chucks (gray), noise sheet (black), cooling jig (copper) and brass plate (orange).

3.3.2 Thermal cycling and experimental setup

The end-cap structure of the ITk consists of six disks on which petals are mounted. Each petal has nine modules of different types per side. These modules will be operated at very low temperatures in the HL-LHC environment. In order to test their performance at these low temperatures, cooling tests emulating the HL-LHC environment are needed. The modules have to be able to perform the temperature cycle -35°C $\rightarrow$ 40°C $\rightarrow$ -35°C. To this end, I designed a cooling setup where the modules are placed and thermally cycled. An exploded view of the setup design is shown in Figure18. The cooling cycle starts by injecting cold water from a chiller to the cooling jig made out of copper for good thermal conductivity. The water (or the liquid mixture) flows inside the cooling block and is emitted to the other side, where it is then fed back again to the chiller. Sitting on top of the copper block we have four Peltier elements[11], which are electrical components used for cooling. The heat emitted by the Peltier is absorbed by the cooling jig. The more heat we are able to remove, the lower the temperature will be on the other side (the cold side) of the Peltier. The next layer of the setup consists of an aluminium sheet to avoid electronic noise coming from the Peltier. On the top, we have the vacuum chucks that hold the module in place, restricting any movement during testing. Finally, the module, held by a test-frame, is placed on the top most part.
I was involved in the first preliminary tests checking the performance of the setup. Since no well-insulated box was designed by the time of the tests, a non-optimal box used for the test-beam was selected. The cooling setup inside the box is depicted in

[11]The Peltier element is based on the Peltier effect: when an electric current passes through the junction of two conductors a heat exchange occurs.

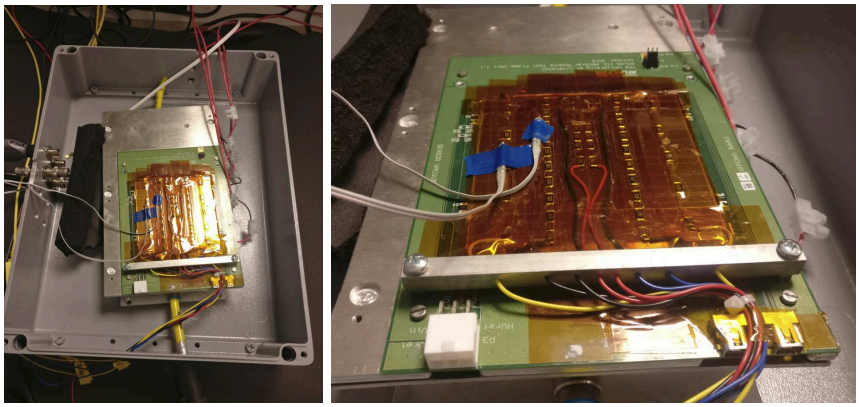

Figure 19: Laboratory setup with the cooling jig and the box used for tests.

Figure 19. Since no real modules were available at the time of the testing, a "heat load" was placed to emulate the heat emitted by a powered sensor. Two temperature lines were constantly taking the temperature at two different points of the heat load, one where the real silicon sensor would sit (outermost), and one where the hybrid would sit (innermost). To avoid condensation, there was a constant flow of dry air entering the box at room temperature.
At $t = 0$ s the chiller and the heat load were turned on. Here, the two temperature lines began recording the temperature T. The graph in Figure 20 shows the temperature as a function of time. We can see that the temperature drops in the first 10 minutes and then begins to level off to a constant value around -20°C. Finally, at $t = 40$ min the heat load was turned off while keeping the Peltier elements on and the temperature drops again due to this fact. As observed, the desired temperature of -35°C was not reached due to several limitations:

- The box used was old and had bad insulation, leading to leakages of the dry air and a reduction in temperature.
- The dry air was at room temperature when it came inside the box. Cold Nitrogen will replace the dry air in future versions of the setup.
- The cold jig, where the water flows through, was preliminary and made out of aluminium instead of copper, reducing the thermal conductivity.

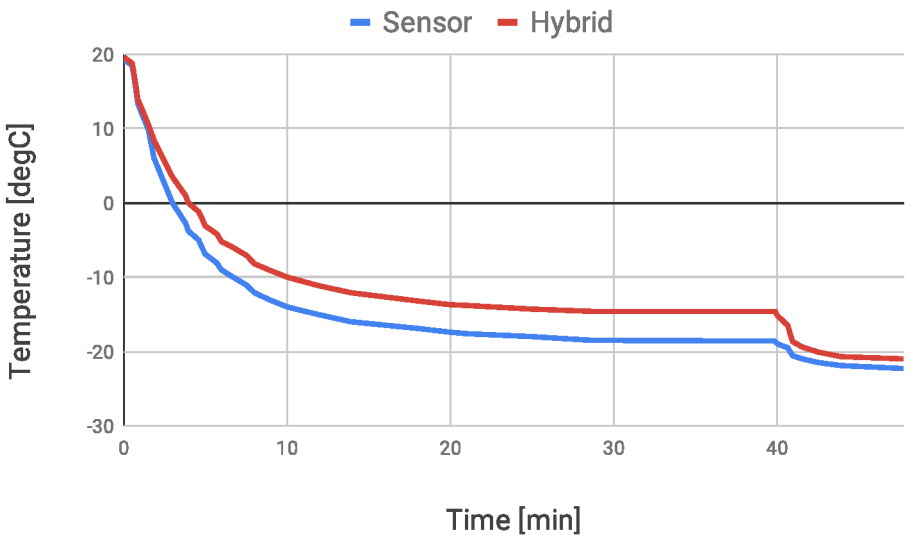

Figure 20: Temperature (°C) vs time (min) measured in the heat load at the sensor position (blue) and at the hybrid position (red). The drop at $t = 40$ min is due the turn off of the heat load.

4 ATLAS reconstruction and identification

Each subcomponent of the ATLAS detector is designed to identify and reconstruct specific types of particles. A general overview of the particles interactions through the ATLAS detector is shown in Figure 21. Charged particles travel through a trajectory bent by the magnetic field and leave hits in the Inner Detector. All particles follow their path to the calorimeters, where they deposit their energy. Muons are the exception as they leave almost no energy in the calorimetry system and travel to the Muon Spectrometer, where their track is reconstructed. Photons travel through the Inner Detector without leaving hits and are absorbed by the EM calorimeter. Photons can also interact with a charged nucleus from the detector and convert into an electron-positron pair (photon conversion), which also leave hits in the Inner Detector. *Invisible* particles, like neutrinos, travel through the whole detector without leaving any signature. Their presence can only be inferred from momentum conservation, as they can leave a momentum imbalance in the event. A more detailed explanation of the reconstruction and identification of the particles is discussed in this chapter.

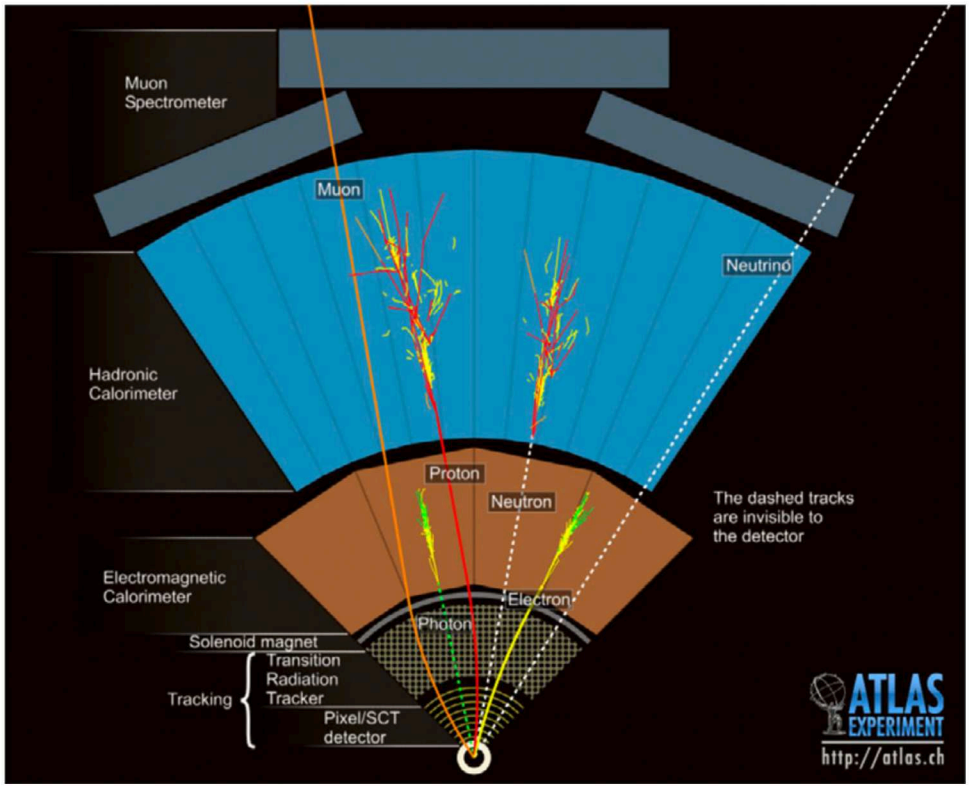

Figure 21: Different particle interactions within the ATLAS detector

4.1 Tracks, vertices and clusters

To identify and reconstruct objects, it is useful to clarify the concepts of hit, track and cluster.

- Hit and cluster. When charged particles pass through the silicon detectors (pixel or strip), they leave charge deposits (hits). The charge is usually collected in multiple pixels. A connected component analysis (CCA) [62] groups connected pixels and strips in a given sensor, where the energy deposited yields a charge above threshold, into clusters.

- Tracks are then formed by fitting clusters in different layers of the silicon detectors. The process starts by building three-dimensional measurements from the clusters (space-points). These space-points correspond to the point where the particle traversed the active material of the Inner Detector. Track seeds are then defined from sets of three space-points. Tracks are then built from the track seeds by using the Kalman filter [63]. This algorithm creates track

candidates by adding space-points to the preliminary trajectory. The track candidates are then processed through a ambiguity solver in order to remove tracks that have shared clusters. Track candidates are rejected by the ambiguity solver if they fail some of the following requirements:

  - $p_{\mathrm{T}} > 500$ MeV,
  - $|\eta| < 2.5$,
  - Minimum of 7 pixel and SCT clusters
  - Maximum of one shared pixel cluster or two shared SCT clusters on the same layer
  - Not more than two holes in the pixel and SCT detectors,
  - Not more than one hole in the pixel detector,
  - $|d_0| < 2.0$ mm,
  - $|z_0 \sin\theta| < 3.0$ mm,

  where d_0 is the transverse impact parameter, defined as the shortest distance in the transverse plane between a track and the beam line. The longitudinal impact parameter, z_0, is defined as the distance (in the z direction) between the primary vertex and the point on the track used to measure d_0. The polar angle of the track is denoted with θ.

- Vertex seed positions are determined by the beam spot position and tracking information. The tracks and the seed are then used to find the optimal vertex positions with a fit. Tracks that are incompatible with a given vertex, are removed from that vertex and are used to reconstruct the other vertices. The hard scattered primary vertex is defined as the vertex with the greatest sum of the squared transverse momenta of the associated tracks $\sum p_T^2$.

- Calorimeter energy clusters are formed around seed cells with an energy $|E_{\mathrm{cell}}|$ of more than 4σ above the noise[1]. These clusters then grow by iteratively adding neighboring cells that have $|E_{\mathrm{cell}}|$ with at least 2σ above the noise, across all electromagnetic and hadronic calorimeter layers. The procedure stops when $|E_{\mathrm{cell}}|$ is below the 2σ threshold, and a final boundary shell is added to the cluster. The set of all the gathered cells is called a *topocluster*. A sketch of this procedure is shown in Figure 22.

[1] Electronic noise and effects of pile-up

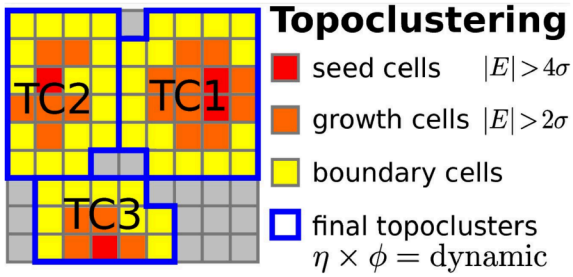

Figure 22: Topocluster construction procedure in ATLAS. Figure taken from [64].

4.2 Electrons and photons

When an electron or a photon reaches the EM calorimeter, it interacts with the lead absorber and creates an EM shower. The particles in the EM showers ionize the LAr, the ionized electrons drift due to the applied electric field and induced currents are created in the electrodes. The total energy detected in the active layers (LAr) is only a fraction of the total deposited by the electrons and photons.
An electron is defined from a cluster built from energy deposits in the calorimeter and a matched track. Electrons (and positrons) are reconstructed by fitting a track using the information from the ID and matching it to a cluster built from energy deposits in the EM calorimeter.
A converted photon consists in a cluster matched to a conversion vertex. An unconverted photon (prompt photon) corresponds to a cluster that is not matched to an electron track nor a conversion vertex. At low values of pseudorapidity, about 20% of the photons convert in the ID, whereas at $|\eta| \approx 2.3$, the fraction goes up to 65%.
To improve the quality of selected electrons, further identification criteria are required. To do so, several variables are constructed in order to discriminate between prompt isolated electrons from (i) energy deposits from hadronic jets, (ii) from converted photons and (iii) from electrons coming from heavy-flavour hadron decays. These quantities are then used to construct a likelihood (LH) discriminant. Information from the number of hits in the tracker (Pixel, SCT, TRT), as well as shower shapes are used to build the variables. Depending on the likelihood discriminant values, four working points are defined in order to satisfy specific background rejection requirements from the different ATLAS analyses. The working points (WP) defined are: `VeryLoose`, `Loose`, `Medium`, and `Tight` [65]. A variation of the `Loose` WP (`LooseAndBLayer`) is defined using the same discriminant threshold but also requires a hit in the innermost pixel layer. In Figure 23 the identification efficiencies as a function of the electron

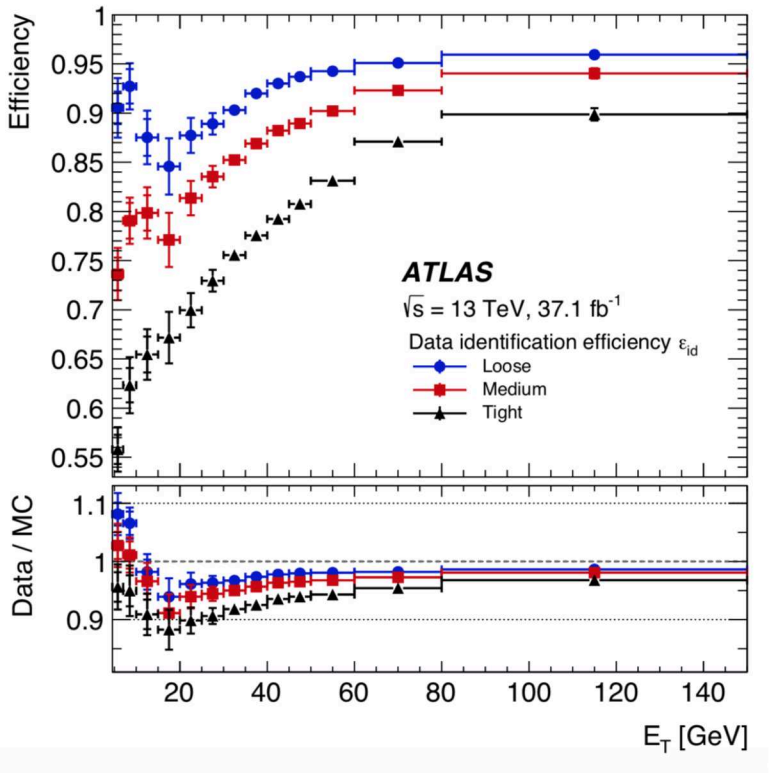

Figure 23: Electron identification efficiencies in $Z \to ee$ events as a function of the electrons transverse energy E_T for three operation points: Loose (blue), Medium (red) and Tight (black). The bottom frame shows the data to simulation efficiency ratio. Figure taken from [65].

E_T for different identification WPs are shown. The identification efficiencies of an electron with a transverse energy of 40 GeV are 93%, 88%, and 80% for the `Loose`, `Medium`, and `Tight` WPs, respectively. In the analysis described in Chapter 6 the `Tight` WP is used for electrons.

In the same way, in order to efficiently select prompt, isolated photons while maintaining high hadronic jets rejection, the selected photons use primarily information from the first layer of the EM calorimeter. This can be used to distinguish a prompt photon from photons coming from a $\pi^0 \to \gamma\gamma$ decay, since the latter results in two collimated showers in the EM calorimeter.

Furthermore, isolation criteria have also to be fulfilled. A cone is built around the electron track (or cluster) or the photon cluster direction. The energy contained in the cone is required to have less than a certain fraction of the energy of the electron or photon. For the electron, track-based isolation is defined by sum-

ming the transverse momentum of the particles around the cone. The cone size[2] is $\Delta R^{\text{var}} = \min(10\ \text{GeV}/p_{\text{T}}, \Delta R_{\text{max}})$, where ΔR_{max} is typically 0.2. For the calorimeter isolation, the energies of the topological clusters that have their barycenter within the cone radius are summed. Specific analyses use different isolation requirements, to this end isolation working points are defined, some commonly used WPs are listed in Table 3.

Particle	WP	Calorimeter isolation	Track isolation
Electron	`FCLoose`	$\boldsymbol{E_T^{\text{iso}}(\Delta R < 0.2)/E_T < 0.2}$	$\boldsymbol{p_T^{\text{iso}}(\Delta R^{\text{var}} < 0.2)/E_T < 0.15}$
	`FCTight`	$E_T^{\text{iso}}(\Delta R < 0.2)/E_T < 0.06$	$p_T^{\text{iso}}(\Delta R^{\text{var}} < 0.2)/E_T < 0.06$
Muon	`FCLoose`	$\boldsymbol{E_T^{\text{iso}}(\Delta R < 0.2)/E_T < 0.3}$	$\boldsymbol{p_T^{\text{iso}}(\Delta R^{\text{var}} < 0.3)/E_T < 0.15}$
	`FCTight`	$E_T^{\text{iso}}(\Delta R < 0.2)/E_T < 0.15$	$p_T^{\text{iso}}(\Delta R^{\text{var}} < 0.3)/E_T < 0.04$

Table 3: Definition of the electron, muon and photon isolation working points. The WPs in bold correspond to the ones used in the analysis in Chapter 6. The prefix FC is used when the requirement on calorimeter and track isolation variables is fixed.

4.3 Muons

Muon reconstruction is first performed independently in the ID and MS. Then, the combination ID-MS is performed using algorithms that use information coming from the ID, MS and calorimeters. Depending on the subdetectors used for the reconstruction, four muon types are defined:

- Combined muon: the track is first reconstructed separately in the ID and in the MS. Then, a global fit uses information from both subdetectors to form a combined track.
- Segment-tagged muons: if a track is reconstructed in the ID, and it is associated with at least one local track segment in the MDT or CSC, it is a segmented-tagged muon.
- Calorimeter-tagged muons: if a track in the ID can be matched to an energy deposit in the calorimeter from a minimum ionizing particle, then the particle is a calorimeter tagged muon.

[2]In boosted topologies, other particles can be very close to the signal electron direction, therefore the cone shrinks as the p_{T} increases.

- Extrapolated muons: if the muon trajectory is reconstructed from a track in the MS and a loose requirement on the compatibility of the particle coming from the IP is fulfilled, the particle is tagged as a extrapolated muon.

Muons also have to pass quality requirements in order to be identified. These are built to suppress backgrounds from pion and kaon decays[3]. Specific hits in the ID and MS as well as track quality are required. Depending on the background rejection rate and muon reconstruction efficiency, four identification working points are defined for physics analyses [66]: `Loose`, `Medium` (used in Chapter 6), `Tight` and High-p_{T}. High muon purity is achieved with the `Tight` and High-p_{T} WPs, whereas the `Loose` WP maximises the muon reconstruction efficiency. The muon reconstruction efficiency for the `Medium` and `Loose` WPs as a function of the pseudorapidity are depicted in Figure 24.
Muons coming from resonances like W, Z and the Higgs are normally isolated from other particles, in contrast to semileptonic decays from heavy-flavour hadrons, which are usually contained inside jets. To define the detector activity in the surroundings of the muon, two types of cones are defined. For the track-based isolation cone, a p_{T}-dependent cone around the muon is defined $\Delta R^{\mathrm{var}} = \min(10\ \mathrm{GeV}/p_{\mathrm{T}}, 0.3)$. The calorimeter-based isolation is defined as the sum of the transverse energy of topological clusters within a $\Delta R = 0.2$ cone around the muon, after subtracting the energy deposits from the muon itself, and correcting for pile-up effects. Depending on the isolation requirement, WPs are defined in order to satisfy physics analysis needs [66]. Commonly used muon WPs are listed in Table 3.

[3] $\pi \to \mu\nu_{\mu}, K \to \mu\nu_{\mu}$

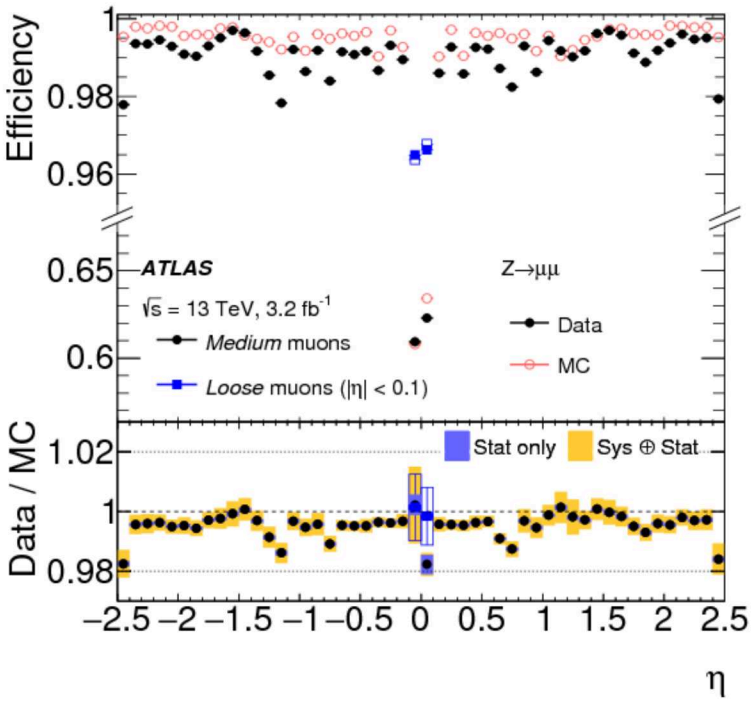

Figure 24: Muon reconstruction efficiency measured in $Z \to \mu\mu$ events for data and simulation as a function of the pseudorapidity for the Medium operating point. For $|\eta| < 0.1$ the Loose working point is also shown (blue). The bottom frame shows the data to simulation efficiency ratio. Figure taken from [66].

4.4 Jets

High-energy quarks and gluons are not directly observed in the detector due to the confinement nature of QCD. Instead, they radiate quarks and gluons at small angles. These hadronize and result in color neutral final states (hadrons). Therefore, in the detector a bunch of collimated hadrons, referred to as jets[4], are observed. In order to try and infer all the particles emerging from a single quark or gluon that produced the jet, recombination algorithms are used. In the LHC, the anti-k_t algorithm [67] is the commonly used. To see how it works, we first define two quantities for each pair

[4]About 65% of energy in a jet is carried by charged particles, 25% by photons (from π^0 decays) and 10% from neutral hadrons (neutrons and K_L).

of clusters i and j, the interparticle distance $d_{i,j}$ and beam distance d_{iB} as

$$\begin{aligned} d_{i,j} &= \min(p_{T,i}^{-2}, p_{T,j}^{-2}) \frac{\Delta R_{ij}^2}{R^2}, \\ d_{iB} &= p_{T,i}^{-2}, \end{aligned} \tag{76}$$

where R is a free parameter called jet radius. The typical value used in ATLAS is $R = 0.4$. The algorithm proceeds as follows:

1. Take all particles as a list of objects
2. Find the smallest distance among all the $d_{i,j}$ and d_{iB}
   - If $d_{i,j}$ is the smallest, then the corresponding pair of objects i and j are combined into a single entity, and it is then added to the list again
   - If d_{iB} is the smallest, the object i is tagged as a jet and removed from the list.
3. The distances are recalculated and step 2 is repeated until there are no more objects in the list.

With the definition in Equation 76, the meaning of R becomes intuitive: when $\Delta R_{ij} > R$, the beam distance is smaller than the interparticle distance ($d_{iB} < d_{i,j}$) and objects are not recombined, therefore R is a measure of the size of the jet.
The anti-k_t algorithm is built in such a way that it favours hard particles. The hard jet will grow by adding soft particles surrounding it until it reaches a distance R. The anti-k_t algorithm was selected because the resulting jets have a circular shape, and (the shape) is not influenced by soft radiation and pile-up, facilitating the calibration.
A Particle Flow (PFlow) algorithm [68] was used to reconstruct jets in this work. This approach combines tracker and calorimeter information to form the signals, which ideally represent individual particles. The energy deposited in the calorimeter by the charged particles is removed (since a track exists). The remaining calorimeter energy (mainly neutral particles) and well measured tracks matched to the hard interaction are then used in the reconstruction of the PFlow jets. A more detailed sketch of how the algorithm proceeds is shown in Figure 25.
Jets measured in the ATLAS detector have to be calibrated in order to recover the true energy of a jet. To achieve this, Monte Carlo simulations are used, and the process is described in the diagram in Figure 26. In the last step (in situ calibration), the jet response difference between Monte Carlo simulations and data are computed. To this end, the p_{T} of the jets are balanced with other well-measured objects, e.g.

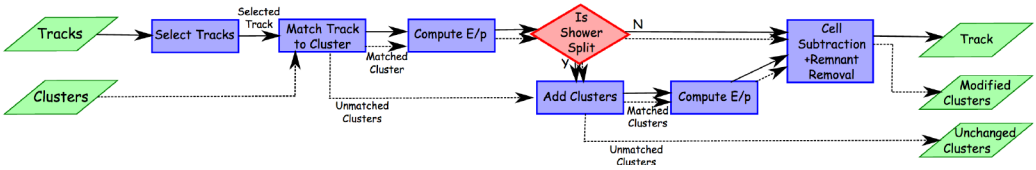

Figure 25: PFlow algorithm steps. The algorithm starts with track-cluster matching and finishes with the removal of the energy associated with the selected tracks. At the end of the procedure what remains are: tracks from charged particles, clusters which had part of their energy removed and clusters that were not modified [68].

photons or Z bosons. The well-measured p_{T} of the photon can be used to calibrate the jet energy scale (JES) by looking at $p_T^{\mathrm{jet}}/p_T^{\gamma}$ for data and Monte Carlo.

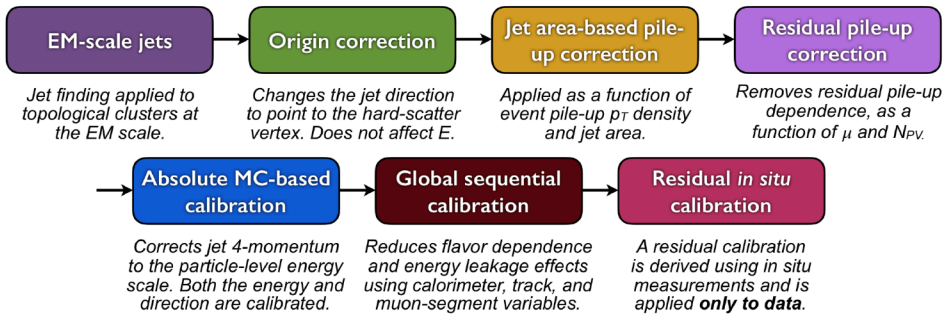

Figure 26: Jet energy calibration procedure [69]. The procedure starts by correctly pointing the jet direction to the hard-scatter vertex. Then pile-up energy excesses are removed. MC simulations are then used to correct the 4-momentum of the jet. The reconstructed energy is further improved using calorimeter, MS, and track-based variables. A final calibration is performed using well-measured objects.

Flavour tagging

Jets are labeled depending on the quark (or gluon) originating the shower. We distinguish three types: jets arising from bottom-quarks (b-jets) from charm-quarks (c-jets) and from up, down, strange-quarks or gluons (light-jets). The identification of b and c-jets is called heavy-flavour tagging. Heavy flavour tagging algorithms exploit the hard fragmentation, long lifetimes and large masses of b and c hadrons in order to identify heavy flavour jets. For instance, B mesons (containing a b-quark) have a relatively long lifetime ($\tau \sim 1.6$ ps) and will travel hundreds of micrometers

($c\tau \sim 500\,\mu\text{m}$) inside the ATLAS tracker before the decay. Therefore, it will create a secondary vertex at the point of the decay, which can be reconstructed, and the products will leave displaced tracks in the detector. All the kinematic properties from the secondary vertices, displaced tracks, and soft leptons (from leptonic decays from mesons) are processed using multivariate analysis (MVA) techniques. The MVA techniques map all these kinematic properties into a single discriminator value. In ATLAS, two main algorithms are used: MV2 [70] and DL1 [70]. The output discriminant of the DL1 b-tagging algorithm is shown in Figure 27. We can see that, very high b-jet purity can be achieved at high discriminant values.

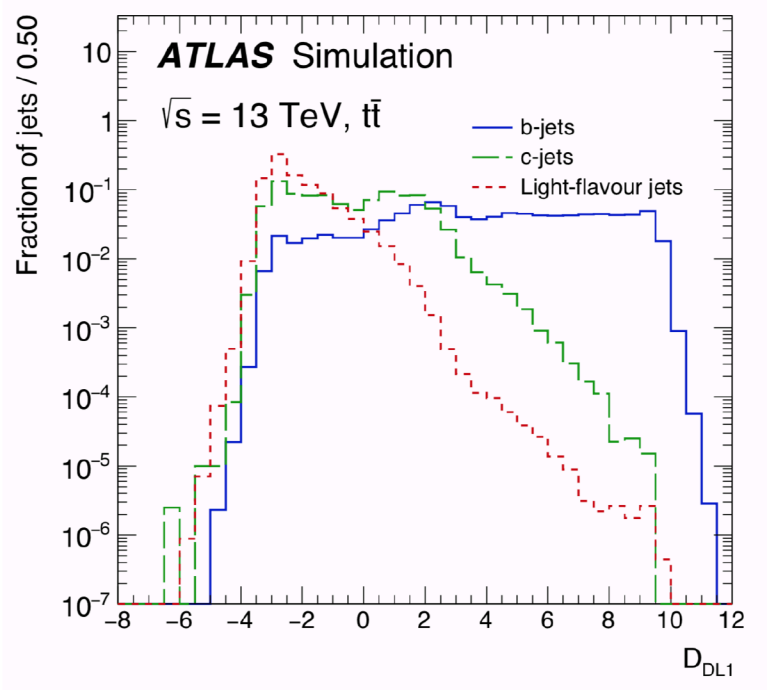

Figure 27: Output discriminant of the DL1 b-tagging algorithm [71].

Jet vertex tagging

Jet calibration and reconstruction is sensitive to the effect of jets coming from pile-up interactions. It is then desired to discriminate pile-up jets from hard-scattered jets. To do so, two new variables are introduced: JVF and $R_{p_{\text{T}}}$. The JVF is defined as the scalar sum of all the tracks associated with the primary vertex, over the scalar

sum of all associated tracks

$$\mathrm{JVF} = \frac{\sum_j p_T^{\mathrm{trk}_k}(PV_0)}{\sum_l p_T^{\mathrm{trk}_l}(PV_0) + \sum_{n\geq 1}\sum_l p_T^{\mathrm{trk}_l}(PV_n)}, \tag{77}$$

where PV_0 is the hard-scatter vertex, and $PV_j (j \geq 1)$ corresponds to pile-up interactions in the same bunch crossing. JVF values are usually greater for hard-scattered jets than for pile-up jets. A second variable $R_{p_{\mathrm{T}}}$, is defined as the scalar sum of the hard-scattered vertex tracks associated with the jet, over the jet transverse momentum,

$$R_{p_{\mathrm{T}}} = \frac{\sum_k p_T^{\mathrm{trk}(PV_0)}}{p_T^{jet}}. \tag{78}$$

Since pile-up jets will not contain tracks originating from the hard scattered vertex, $R_{p_{\mathrm{T}}}$ peaks at low values for pile-up jets. The multivariate combination of these two variables is used to reject pile-up jets and is called jet-vertex-tagger (JVT) [72, 73].

4.5 Missing transverse momentum

In the ATLAS detector, conservation of momentum in the transverse plane (xy) implies that the vector sum of all the particles produced in the collision has to be zero. The momentum imbalance in the transverse plane is called missing transverse momentum $\mathbf{E}_T^{\mathrm{miss}}$. It can be produced by weakly interacting particles escaping detection, like neutrinos, from particles lost down the beam pipe (e.g. at high $|\eta|$), or by mismeasured objects. Two terms are defined in ATLAS to measure the E_T^{miss}. The first one comprises fully reconstructed and calibrated objects: electrons, muons, photons, τ leptons and jets (hard objects). The second term, *soft term*, comes from reconstructed signals that are not associated with any of the hard objects. The x, y components of the missing transverse momentum are expressed as

$$E_{x(y)}^{\mathrm{miss}} = -\sum_{i\in\text{hard objects}} p_{x(y),i} - \sum_{j\in\text{soft signals}} p_{x(y),j}. \tag{79}$$

The variables that are constructed from the $\mathbf{E}_T^{\mathrm{miss}}$ are,

$$\begin{aligned} \mathbf{E}_T^{\mathrm{miss}} &= (E_x^{\mathrm{miss}}, E_y^{\mathrm{miss}}), \\ E_T^{\mathrm{miss}} &= |\mathbf{E}_T^{\mathrm{miss}}| = \sqrt{(E_x^{\mathrm{miss}})^2 + (E_y^{\mathrm{miss}})^2}, \\ \phi^{\mathrm{miss}} &= \tan^{-1}(E_y^{\mathrm{miss}}/E_x^{\mathrm{miss}}), \end{aligned} \tag{80}$$

where E_T^{miss} is the magnitude of the vector $\mathbf{E}_T^{\text{miss}}$.

Object based E_T^{miss} significance

The object based E_T^{miss} significance is computed in exactly the same way as the E_T^{miss}, but in this case the transverse momentum resolution of the objects are also considered in the calculation. The E_T^{miss}significance is determined from the log-likelihood ratio that the reconstructed $\mathbf{E}_T^{\text{miss}}$ is consistent with the null hypothesis of having zero real $\mathbf{E}_T^{\text{miss}}$. Therefore, large values E_T^{miss} significance indicate that the $\mathbf{E}_T^{\text{miss}}$ cannot be explained by momentum resolution effects, and is likely to come from *invisible* particles. The mathematical definition is [74]

$$E_T^{\text{miss}}\text{significance} = \frac{|\mathbf{E}_T^{\text{miss}}|^2}{\sigma_L^2(1-\rho_{LT}^2)}, \tag{81}$$

where σ_L^2 is the total variance in the longitudinal direction of $\mathbf{E}_T^{\text{miss}}$ and ρ_{LT} is the correlation factor of the longitudinal and transverse measurements.

5 Standard Model ZZ background estimation using $Z\gamma$ events

In every search for new physics or Standard Model measurement, it is crucial to distinguish between the new process we want to detect (*signal*), and the Standard Model processes which yield the same detector signature (*backgrounds*). Any measurement or search relies on how well this background is known. In addition, as the LHC luminosity increases, the statistical uncertainties decrease, and as a consequence, the precision to which the background can be estimated is becoming increasingly more important. Typically, there are two approaches used to estimate the background processes: using Monte Carlo simulations or using data driven estimates. Although calculations up to N^{3}LO in QCD exist for some processes [75], MC simulations can, in some cases, be subject to large uncertainties. In an attempt to reduce the associated uncertainty, data-driven background estimates have become more popular.

In this chapter it is explored whether the $Z\gamma$ process can be used to obtain a precise estimate of the ZZ process by using the γ as a proxy for the Z boson. A similar strategy has been successfully used for many Supersymmetry searches to estimate the background of Z+jets events using γ+jets events [76, 77]. The $ZZ \to \ell^+\ell^-\nu\bar{\nu}$ background populates searches where two leptons are reconstructed with significant E_T^{miss} in the event. Examples are resonances decaying to two Z bosons $X \to ZZ$ [78, 79], $Z + E_T^{\text{miss}}$ searches such as $ZH \to Z +$ invisible [80, 81] or searches for Supersymmetry in final states $Z + E_T^{\text{miss}}$+jets [77, 82].

The strategy begins by identifying a process that is similar to the background process to be studied and that occurs at a sufficiently high rate. One could think of $ZZ \to \ell\ell\ell\ell$ ($\ell = e, \mu$), however, the branching ratio of the Z boson decaying leptonically is very low[1], leading to low event rates. In fact, accounting for the branching ratio difference and the finite identification efficiencies of charged leptons, typically there are about 10 times less identified $ZZ \to \ell^+\ell^-\ell^+\ell^-$ events than $ZZ \to \ell^+\ell^-\nu\bar{\nu}$ events in a given kinematic region. Therefore, events where a Z boson is produced in association with a

[1] BR($Z \to \ell\ell$) = 3.4 % per lepton flavour.

photon are used, the former decaying into two leptons, $Z\gamma \to \ell^+\ell^-\gamma$. The advantage of the $Z\gamma$ process is that the statistical precision is high since there is no branching ratio to consider for the photon.
The idea is to extract a pure $Z\gamma$ sample from the data collected by the experiment and predict the ZZ contribution in a given region of the phase space as

$$N_{ZZ\to\ell^+\ell^-\nu\bar{\nu}} = N^{\text{reco}}_{Z\gamma\to\ell^+\ell^-\gamma} \times \frac{1}{\epsilon_\gamma^{\text{gen}\to\text{reco}}} \times \frac{\sigma_{ZZ}}{\sigma_{Z\gamma}}, \tag{82}$$

where $N^{\text{reco}}_{Z\gamma\to\ell^+\ell^-\gamma}$ are the number of $Z\gamma \to \ell^+\ell^-\gamma$ reconstructed events, $\epsilon_\gamma^{\text{gen}\to\text{reco}}$ the reconstruction efficiency of the photon and σ_{ZZ} and $\sigma_{Z\gamma}$ the ZZ and $Z\gamma$ production cross sections, respectively. Throughout this chapter, a special focus on the determination of the ratio of cross sections and its associated uncertainties will be given.
Leading order (LO) and next-to leading order (NLO) theoretical predictions have been available for some time for the ZZ [83, 84] and $Z\gamma$ [85, 86] processes. Recent theoretical developments [87, 88] have provided next-to-next-to leading order (NNLO) calculations for both processes, which are used in this chapter to derive the results. The LO Feynman diagrams for the ZZ and $Z\gamma$ processes are depicted in Figure 28. The production at LO proceeds via quark-antiquark ($q\bar{q}$) annihilation. At NLO, qg and $\bar{q}g$ interactions give rise to jets in the final state. At NNLO ($\mathcal{O}(\alpha_s^2)$), both diboson processes receive an extra contribution via loop-induced gluon fusion (gg) interactions as shown in Figure 29. This production mechanism is of special importance in hadron colliders due to the high gluon densities. Recently, a new loop-induced gg NLO calculation, corresponding to $\mathcal{O}(\alpha_s^3)$ has become available for ZZ production [89] and is used in this analysis. Higher order EW corrections have been calculated for diboson processes by various groups [90, 91, 92, 93, 94, 95, 96, 97], and will also be discussed throughout this chapter. The numbers in this chapter were provided by the authors of Ref. [93] based on the OpenLoops generator [98].

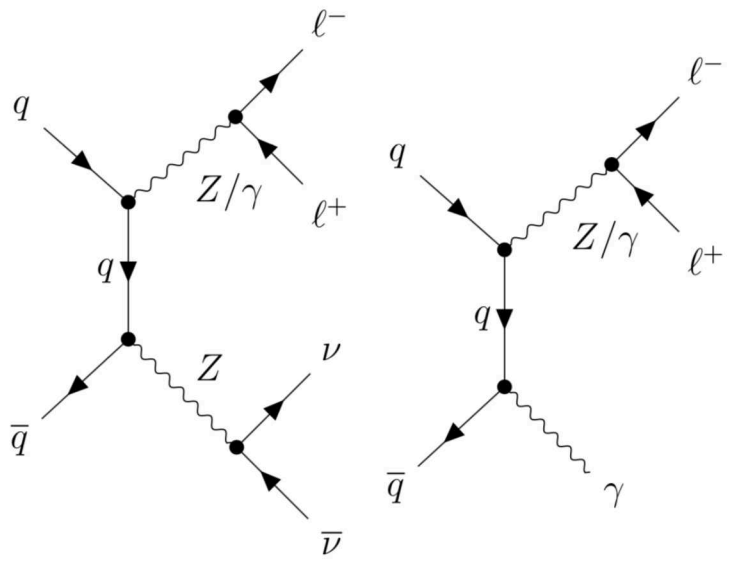

Figure 28: Example of leading order Feynman diagram for ZZ (left) and $Z\gamma$ (right) production processes.

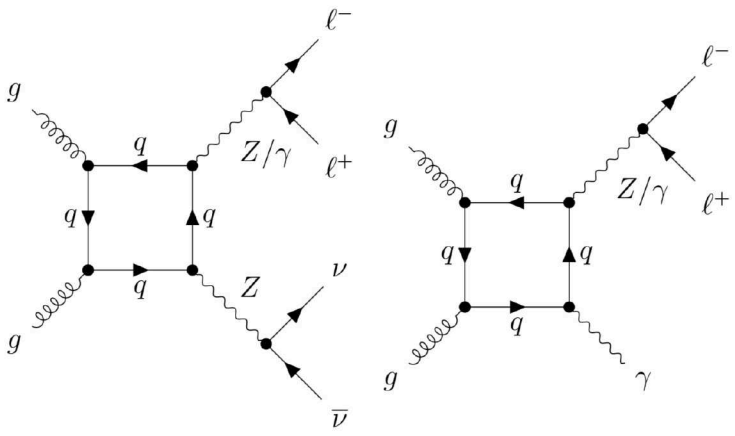

Figure 29: Loop-induced gluon fusion contribution at LO, corresponding to the NNLO QCD correction for ZZ (left) and $Z\gamma$ (right) production processes.

5.1 Cross Section Calculation

The calculation is performed using the computational framework MATRIX [99]. Proton-proton collisions are simulated at $\sqrt{s} = 13$ TeV, using NNLO CT14 [100] Parton Distribution Function (PDF) set. The renormalisation and factorisation scales chosen are $\mu_{R,F} = \sqrt{m_Z^2 + p_T^{V^2}}$, where p_T^V ($V = \gamma, Z(\to \nu\bar{\nu})$) is the transverse momentum

of the boson.
In the theoretical calculation, collinear divergences arise when the QCD radiation is emitted in the direction of the photon, therefore a *smooth cone* isolation prescription proposed by Frixione [101] is often applied. The photon has to satisfy

$$\sum_{i=\text{partons/hadrons}} p_T^i(r) \leq \varepsilon_\gamma p_T^\gamma \left(\frac{1-\cos r}{1-\cos R_0}\right)^n \qquad r \leq R_0, \tag{83}$$

with ε_γ, R_0 and n being free parameters. The smooth cone limits the hadronic activity in the vicinity of the photon, being gradually more restrictive as one gets closer to the photon. Here, by default these parameters are set to

$$\varepsilon_\gamma = 0.075, \qquad R_0 = 0.2, \qquad n = 1.$$

It was already noted in [102] that requiring an isolation on the photon can alter the higher order corrections for $Z\gamma$. Since the ZZ does not require isolation, at high p_T^V both processes can receive significantly different QCD corrections. In order to mitigate this difference, a dynamic cone isolation was proposed [102] and is discussed in Appendix A. An alternative theoretical prescription is that of using photon fragmentation functions, as will be discussed in Section 5.4.1. However, the smooth cone is adopted as the nominal isolation prescription since it is similar to what is done in the experiments.

5.2 Event Selection

The event selection for the $ZZ \to \ell^+\ell^-\nu\bar{\nu}$ process follows closely the one adopted in the ATLAS analyses [78, 80]. The presence of exactly two electrons or muons in the event is required in the detector angular coverage $|\eta_\ell| < 2.5$, with the leading (subleading) lepton $p_{\mathrm{T}}^\ell > 30$ GeV (20 GeV). The dilepton system invariant mass has to be in the resonant mass window of the Z boson $76 < m_{\ell\ell} < 106$ GeV.

For the $ZZ \to \ell^+\ell^-\nu\bar{\nu}$ process, $E_T^{\mathrm{miss}} > 60$ GeV is required, and for $Z\gamma \to \ell^+\ell^-\gamma$ events $p_T^\gamma > 60$ GeV is required. In addition, for the $Z\gamma$ process it is necessary to require $|\eta_\gamma| < 2.5$ to ensure a high experimental selection efficiency, and the angular separation between the two leptons and the photon must fulfill $\Delta R(\ell, \gamma) > 0.4$. This latter cut is primarily applied to suppress photons coming from lepton radiation.
The photon has to be isolated from hadronic activity for both theoretical and experimental reasons. On the experimental side, it rejects reducible backgrounds

coming from hadron decays ($\pi^0 \to \gamma\gamma$) produced in fragmentation processes of quarks and gluons. The experimental isolation cut typically requires the energy within a (η, ϕ) cone of 0.2 around the photon direction to be less than 5-10% of the photon energy. A summary of the event selection is given in Table 4.

Variable	ZZ	$Z\gamma$
N_{lepton}	2	
$p_T^{\ell_1}$	> 30 GeV	
$p_T^{\ell_2}$	> 20 GeV	
$\lvert\eta^\ell\rvert$	< 2.5 GeV	
$m_{\ell\ell}$	76 GeV $< m_{\ell\ell} <$ 106 GeV	
E_T^{miss}	> 60 GeV	–
p_T^γ	–	> 60 GeV
$\lvert\eta^\gamma\rvert$	–	< 2.5
$\Delta R(\ell, \gamma)$	–	> 0.4
γ isol.	–	applied

Table 4: Event selection for $ZZ \to \ell^+\ell^-\nu\bar{\nu}$ (left column) and $Z\gamma \to \ell^+\ell^-\gamma$ (right column) events.

5.3 ZZ and $Z\gamma$ cross sections and their ratio

The cross sections as a function of the boson transverse momentum p_T^V ($V = \gamma, Z(\to \nu\bar{\nu})$) at LO, NLO and NNLO with the selections discussed in Section 5.2 are depicted in Figure 30. The correction from LO to NLO is larger for the $Z\gamma$ process than the ZZ process at low p_T^V, but at high p_T^V both become similar. The correction from NLO to NNLO is smaller and again similar for both processes above $p_T^V \sim 200$ GeV. Part of the difference between NNLO and NLO can be attributed to the loop-induced gluon-gluon processes which only enter at NNLO as they are of $\mathcal{O}(\alpha_s^2)$. The relative contribution of the gg process differs significantly between the two processes as seen in Figure 30 (right): at low p_T^V this contribution is about 6% for ZZ and 2% for $Z\gamma$ production. For $p_T^V \gtrsim 600$ GeV the contribution decreases to 2% and below 0.5% for the ZZ and $Z\gamma$ processes, respectively.
Since both processes behave similarly at high p_T^V, we proceed to study the ratio

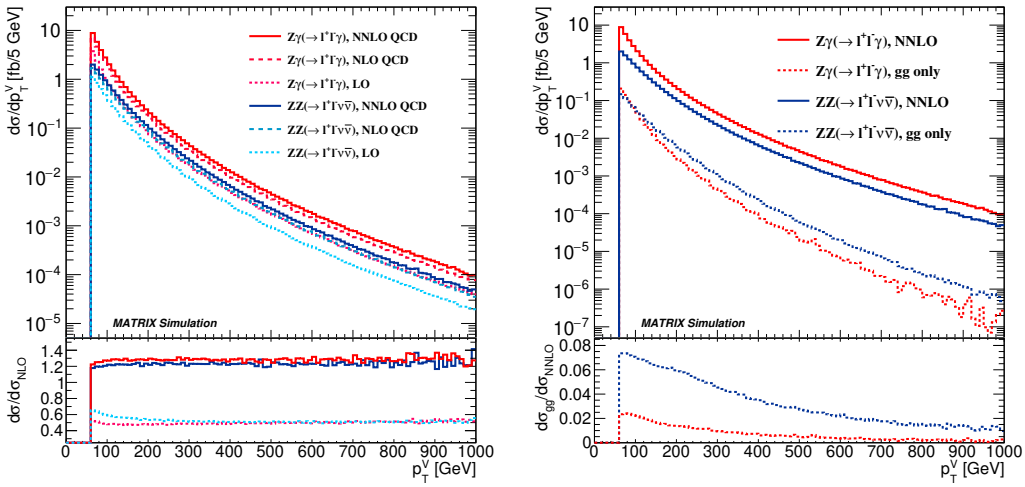

Figure 30: Left: p_T^V distributions for ZZ (blue) and Zγ (red) at LO (dotted), NLO (dashed) and NNLO (solid) at $\sqrt{s} = 13$ TeV. The bottom frame shows the ratio of LO and NNLO calculations to the NLO prediction. Right: p_T^V distribution for the inclusive cross section (solid) and for the gg contribution separately (dotted). The bottom frame shows the fractional contribution of the gg process.

between their differential cross sections, defined as

$$R^{N^kLO}(p_T^V) = \frac{d\sigma^{N^kLO}_{ZZ\to\ell^+\ell^-\nu\bar{\nu}}/dp_T^V}{d\sigma^{N^kLO}_{Z\gamma\to\ell^+\ell^-\gamma}/dp_T^V}. \tag{84}$$

Figure 31 shows the ratio versus p_T^V at LO, NLO and NNLO. At all three orders the ratio increases rapidly up to $p_T^V \approx 200$ GeV, since the ZZ cross section is suppressed due to the large Z boson mass. At LO the ratio then decreases while at NLO and NNLO it remains constant at a value of $R \approx 0.5$. The reason the ratio is not unity is due to the difference in branching fractions and different SM couplings of the Z and γ bosons to quarks. For $p_T^V \gtrsim 500$ GeV all three ratios seem to converge. In order to benefit from the plateau behaviour and gain greater statistics, in the rest of the studies the following binning in p_T^V will be used, $p_T^V = [60, 70, 80, 90, 100, 125, 150, 200, 250, 300, 400, 500, 1000]$ GeV.

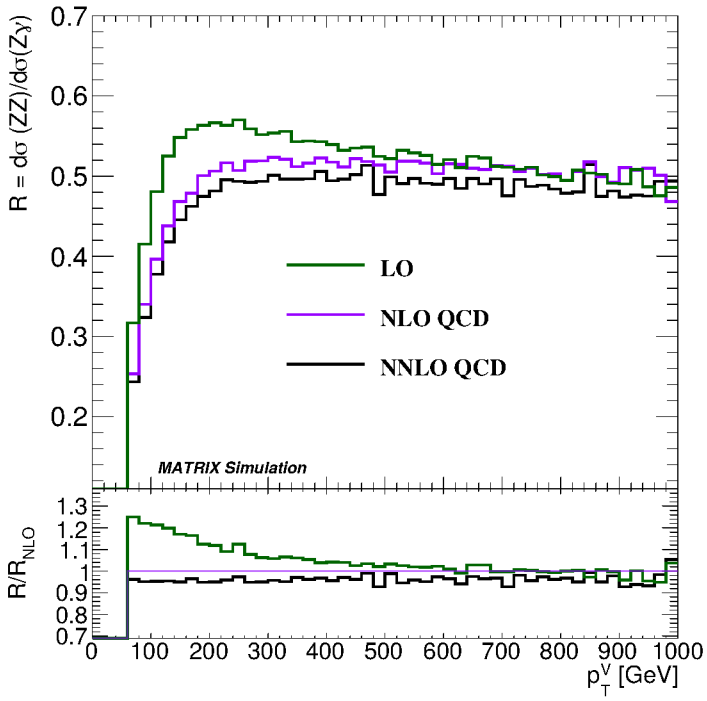

Figure 31: Ratio R between the $ZZ \to \ell\ell\nu\nu$ and $Z\gamma \to \ell\ell\gamma$ differential cross sections at $\sqrt{s} = 13$ TeV as a function of p_T^V in bins of 20 GeV at LO (green), NLO (violet) NNLO (black). The bottom frame shows the ratios normalised to the NLO calculation.

5.4 Uncertainty estimate

In this section the theoretical uncertainty on the ratio $R(p_T^V)$ is estimated. The following uncertainties are considered: QCD (δ^{QCD}), isolation (δ^{iso}), PDF (δ^{PDF}) and electroweak (δ^{EW}).

QCD Uncertainties

For the QCD uncertainties the discussion in Ref. [102] is closely followed. The QCD uncertainties are divided in three terms: $\delta^{scale}, \delta^{shape}$ and δ^{HO}. The term δ^{scale} is estimated by varying the factorisation and renormalisation scales. Both scales are varied up and down by a factor of two but the variations where they differ by a factor of four are discarded (7-point variation). When estimating the uncertainty on R the scales are varied coherently for the two processes. The scale uncertainty on the cross

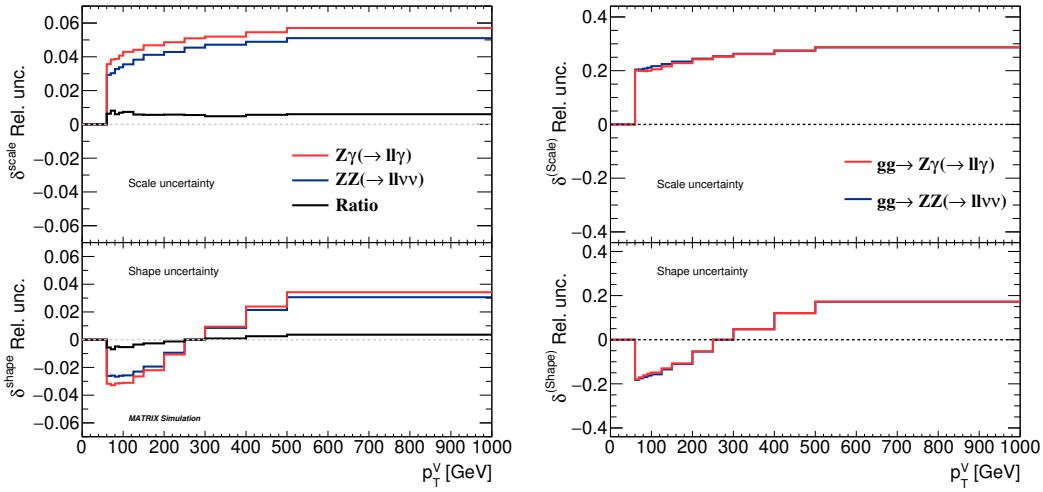

Figure 32: Relative scale δ^{scale} (top) and shape δ^{shape} (bottom) uncertainties for ZZ (blue) and $Z\gamma$ (red). Left: uncertainty on the full cross section and on the ratio R (black). Right: uncertainty calculated taking only the loop-induced gg contribution into account.

sections and on the ratio are then symmetrized,

$$\delta^{scale}\sigma(p_T^V) = \frac{1}{2}\left(|\sigma^{(V,max)}(p_T^V) - \sigma^{(V,min)}(p_T^V)|\right), \tag{85}$$

where $\sigma^{(V,max)}(p_T^V)$, $\sigma^{(V,min)}(p_T^V)$ are the maximum and minimum values of the cross section obtained after the 7-point scale variations, respectively. The scale uncertainties δ^{scale} are shown in Figure 32 (top frame) for the differential cross sections and for the cross section ratio $R(p_T^V)$. The uncertainty taking only the gg process is also shown in Figure 32 (right). The cross section uncertainties for ZZ and $Z\gamma$ range between 3% and 6%. For the ratio, due to the partial cancellation of uncertainties, the uncertainty ranges between 0.5% and 0.8%. This arises from the fact that the uncertainty among processes were varied coherently, thus, assuming to be correlated. The scale uncertainties for the gg process are about 20% to 30%. This, however, has little impact on the full cross section uncertainty due its low relative contribution.

Since the above $\mu_{R,F}$ are varied by constant factors $(\frac{1}{2}, 2)$, the variations affect mostly the overall normalisation of p_T^V, and it can lead to an underestimation of the shape uncertainties. Therefore, a supportive shape uncertainty is applied in order to account for a possible p_T^V dependence of the uncertainty. To estimate the shape

uncertainty, the scale uncertainty is multiplied by a function that is p_T^V dependent,

$$\delta^{shape}\sigma(p_T^V) = \omega_{shape}(p_T^V)\delta^{scale}\sigma(p_T^V), \tag{86}$$

being $\omega_{shape}(p_T^V)$ a function defined as in [102]

$$\omega_{shape}(p_T^V) = \frac{p_{\mathrm{T}}^2 - p_{T,0}^2}{p_{\mathrm{T}}^2 + p_{T,0}^2}, \tag{87}$$

where $p_{T,0}$ is a free parameter, chosen to be $p_{T,0} = 250$ GeV. The shape uncertainty is shown in Figure 32 (bottom frame). The uncertainty δ^{shape} on the cross section raises up to 3% while on the ratio it stays below 1% at all p_T^V values. Again, for the loop-induced gluon part, these are significantly larger. They are, however, part of the total uncertainties discussed above.
For both the shape and scale uncertainties, it was assumed that the renormalisation and factorisation scales of the $Z\gamma$ and ZZ processes were fully correlated. However, it is not clear if this is a valid assumption. Therefore, an additional higher order correction uncertainty is estimated, δ^{HO}. This uncertainty is estimated by directly comparing the K-factors, defined as

$$k_{N^KLO}(p_T^V) = \frac{d\sigma^{N^KLO}/dp_T^V}{d\sigma^{N^{K_{N-1}}LO}/dp_T^V}. \tag{88}$$

The idea behind this is that, assuming the correction of order $(N+1)$ is smaller than that of order N, the missing higher order corrections can be constrained. In this way, by comparing the ZZ and $Z\gamma$ K-factors, one has access to potential higher order correction differences among processes. Therefore, δ^{HO} is defined as the difference between K-factors,

$$\delta^{HO} = k_{NNLO}^{Z\gamma}(p_{\mathrm{T}}^{\gamma}) - k_{NNLO}^{ZZ}(p_T^V). \tag{89}$$

The NLO and NNLO (without the gg contribution, termed qqNNLO) K-factors are shown in Figure 33. Comparing the K-factors, especially at low p_T^V, the agreement between the ZZ and $Z\gamma$ (smooth) K-factors is $\sim 20-25\%$. However, in the NLO case, they tend to get closer at high p_T^V, whereas at qqNNLO, it stays above 5% even at high p_T^V.

As stated before, the NNLO (order α_s^2) corrections includes LO loop-induced gluon-gluon processes (gg_{LO}). Moreover, full gg_{NLO}(order α_s^3) corrections (termed nNNLO) have been calculated [103] for ZZ but not for $Z\gamma$. Figure 34 (left) shows the ZZ

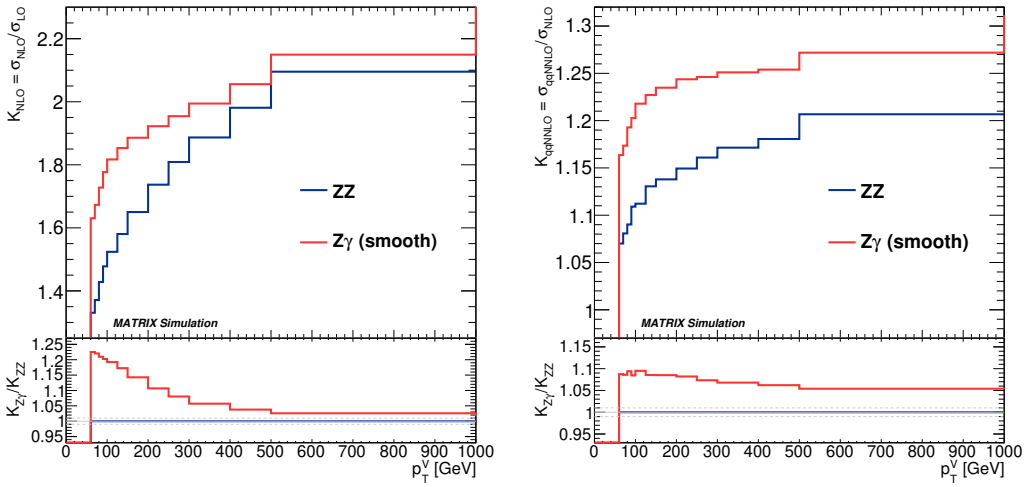

Figure 33: K-factor calculated at NLO (left) and at qqNNLO (right) for ZZ (blue) and $Z\gamma$ with smooth cone isolation (red). The bottom panels show the ratio between $Z\gamma$ and ZZ K-factors.

and $Z\gamma$ K-factor at NLO for the loop-induced gg contribution together with its scale uncertainty. For ZZ, the $\mathrm{gg}_{NLO}/\mathrm{gg}_{LO}$ ratio stays around 1.5 and looks stable in the whole p_T^V range. In the $Z\gamma$ case, since this contribution has not been calculated yet, in what follows it will be assumed that it receives the same correction as for ZZ.
For the purpose of seeing how δ^{HO} changes with the extra contribution of gg_{NLO}, Figure 34 (right) shows how k_{NNLO} evolves. As a reference, the K-factors with gg_{LO}(NNLO) is also shown. First, it is observed that including the gg_{NLO} contribution affects more the ZZ than the $Z\gamma$ due to the relative contributions to each process. Secondly, due to the inclusion of the loop-induced gluon fusion processes, the K-factor difference is much lower over the whole p_T^V range. If only the K-factors using gg_{LO} are compared (see Figure 34 (right)), a δ^{HO} uncertainty of 5% (4%) at low (high) p_T^V for the smooth cone would be obtained. But if now the gg_{NLO} contribution is included, the picture changes, being δ^{HO} in the order of 1% at low p_T^V and $2-3\%$ at high p_T^V. This reduction of δ^{HO} suggests that the K-factors for both processes tend to converge as more higher order terms are included in the calculation.
All the individual contributions together with the uncertainties added in quadrature are displayed in Figure 35. At low p_T^V we see that the three uncertainties have similar values, of about 1%. Both the scale uncertainties and shape uncertainties tend to decrease as p_T^V increases, underestimating higher perturbative corrections and motivating the inclusion of δ^{HO}. In this high p_T^V regime is where δ^{HO} complements

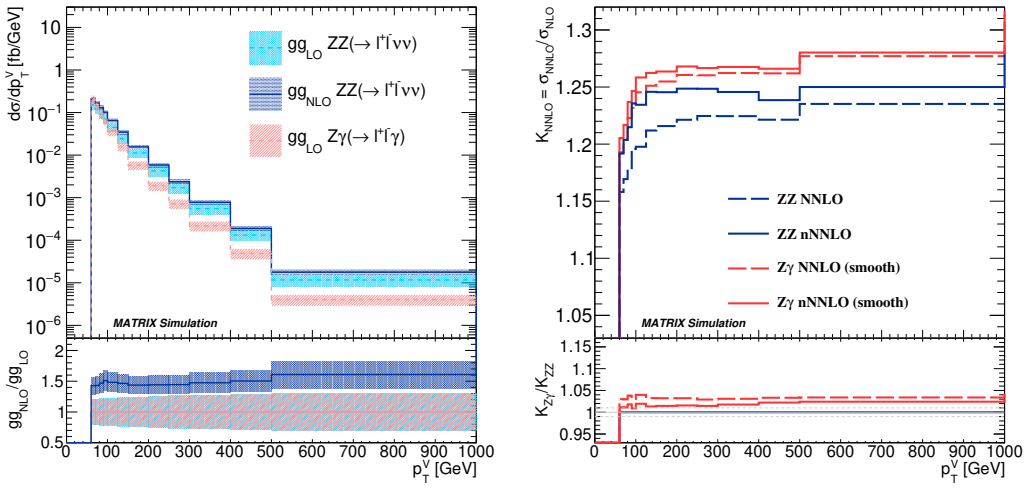

Figure 34: Top left: gluon-gluon induced process K-factor for ZZ (blue) and $Z\gamma$ (red) at LO and NLO together with their scale uncertainty (coloured bands). Bottom left: cross sections normalised to the gg_{LO} prediction. Top right: K-factor at nNNLO (solid) and NNLO (dashed) for ZZ (blue) and $Z\gamma$ (red). Bottom right: ratio between $Z\gamma$ and ZZ K-factors at the same perturbative orders.

the scale and shape uncertainties, rising up to 2%.

Finally, Figure 36 shows the ratio R at the three different perturbative orders, together with their uncertainties[2]. The R-values are very similar at NLO and nNNLO, and the uncertainty is substantially reduced at nNNLO compared to NLO. We also see that due to the inclusion of δ^{HO}, the nNNLO uncertainty band covers the NLO central prediction.

[2]The NLO uncertainties were calculated in the same way as the NNLO uncertainties described in the text.

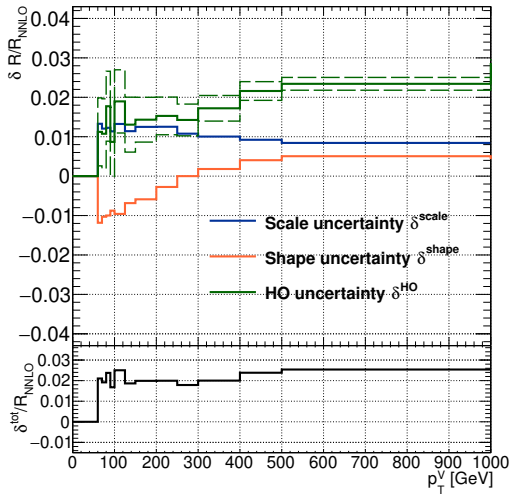

Figure 35: Breakdown of the different uncertainties described in the text: scale (blue), shape (orange) at NNLO and higher order (green) at nNNLO. The dashed green represents the same as the solid green but where the $Z\gamma$ ggNLO component has been varied by 25%. The uncertainties shown are the relative uncertainties on the ratio R. In the bottom frame the uncertainties are added in quadrature.

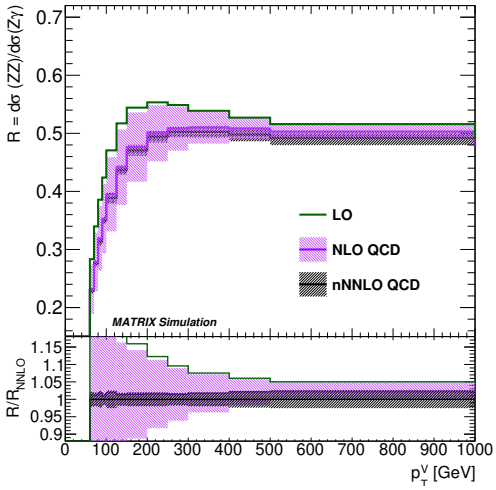

Figure 36: Ratio at the three different orders LO (green), NLO (purple), nNNLO (gray). The bands shown correspond to the QCD uncertainties ($\delta^{scale}, \delta^{shape}, \delta^{HO}$) added in quadrature. For the LO case only $\delta^{scale}, \delta^{shape}$ are considered. The bottom frame shows the ratios normalised to the nNNLO prediction.

5.4.1 Isolation uncertainty

In theory and experiment different photon isolation prescriptions are applied. Experimentally, hadronic energy has to be allowed inside the photon isolation for a variety of reasons (e.g. to cope with pile-up interactions). Furthermore, detector resolution effects have an impact in the measurement of the hadronic activity around the photon, therefore an exact smooth cone as defined in Equation 83 cannot be applied in the experiment. Typically, the ATLAS and CMS collaborations use an isolation cone with a cone size that varies from $R_0 = 0.2$ to $R_0 = 0.4$ depending on the analysis, which limits the allowed energy fraction in a cone around the photon. Since the required energy fraction requirement can vary between experiments and parts of the detector, the smooth cone parameters that approximate the experimental isolation are not straightforward to choose. Previous studies have shown that, for a tight enough isolation, the differences between theoretical and experimental isolation tend to become small [104, 105]. Following the recommendations from [104], we conclude that the cone parameters adopted along this thesis are tight and safe enough to proceed.

In order to see how the cross section varies when adopting different smooth cone isolation parameters, Figure 37 (left) shows the NNLO MATRIX calculation for different ε_γ and n, taking $R_0 = 0.2$. They agree within 0.5% except for the extreme choice of $\varepsilon_\gamma = 0.5$ which differs by 3%, however the value $\varepsilon_\gamma = 0.5$ is very loose and far from the experimental isolation used in ATLAS and CMS. If these parameters are further loosened (decreasing R_0, n or increasing ε_γ), the collinear region is encountered giving rise to divergences in the calculation.

In former data driven methods [106, 107], the uncertainty associated with the transition from theoretical to experimental isolation was taken from varying the smooth cone parameters. Here, a more conservative approach is adopted and different quark-to-photon fragmentation function sets using NLO predictions from the MCFM [108, 109] event generator are compared. Collinear singularities arising when a final state quarks radiates a highly energetic photon can be factorized and absorbed into photon fragmentation functions. However, these fragmentation functions are taken from fits to experimental data and are only implemented at LO in the MCFM program[3]. Two types of fragmentation functions are considered, which are obtained fitting the data collected by the LEP experiments: BFG [112], GdRG [113, 114].

The comparison between both fragmentation functions is shown in Figure 37 (right).

[3] Previous studies on the diphoton cross section have shown unphysical results when matching LO fragmentation functions to NLO cross section calculations [104, 110, 111].

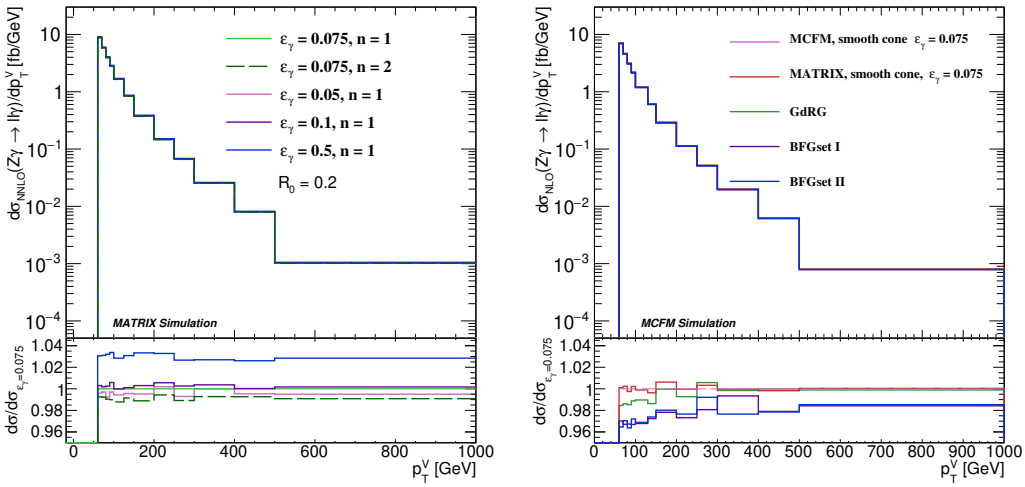

Figure 37: $Z\gamma$ cross section at $\sqrt{s} = 13$ TeV for different smooth cone isolation parameters (left) and for different fragmentation sets (right). The bottom frames show the cross section normalised to the nominal smooth cone parameters: $\varepsilon_\gamma = 0.075, n = 1, R_0 = 0.2$.

First we note that both generators MATRIX and MCFM agree in their NLO predictions when employing the smooth cone. Now, if we compare the different fragmentation functions, we see a discrepancy of at most 2% between the GdRG set and both BFG sets. This arises from the fact that the BFG and GdRG are calculated using different phase space of LEP data: BFG corresponds to a more inclusive data, whereas GdRG is estimated for lower values of the ϵ_γ parameter. Comparing fragmentation functions and smooth cone isolation, we see that the difference is always lower for the GdRG set, being 2% at low p_T^V and negligible at high p_T^V. As discussed in [104], a calculation using smooth cone isolation is much more reliable than using fragmentation functions at a lower order as done here. Therefore, a 1% uncertainty of is applied in the whole p_T^V range.

5.4.2 Uncertainty due to the parton distribution functions

The uncertainty on R due to the limited knowledge on the Parton Distribution Functions (PDFs) is estimated using the 30 eigenvectors provided by PDF4LHC15_30 set. This uncertainty is evaluated using NLO predictions with NNLO PDFs using

MCFM in the following way [115]

$$\delta^{PDF}\sigma = \sqrt{\sum_{k=1}^{N}(\sigma^{(k)} - \sigma^{(0)})^2},$$
$$\delta^{PDF}R = \sqrt{\sum_{k=1}^{N}(R^{(k)} - R^{(0)})^2}, \tag{90}$$

where N corresponds to the number of PDF sets, in our case $N = 30$. $\sigma^{(k)}, R^{(k)}$ and $\sigma^{(0)}, R^{(0)}$ are the cross sections and ratios evaluated for each set and for the nominal PDF set respectively. In Figure 38 the PDF uncertainty for both the cross sections and the ratio is shown, being around 2% and 1% in the whole p_T^V range respectively.

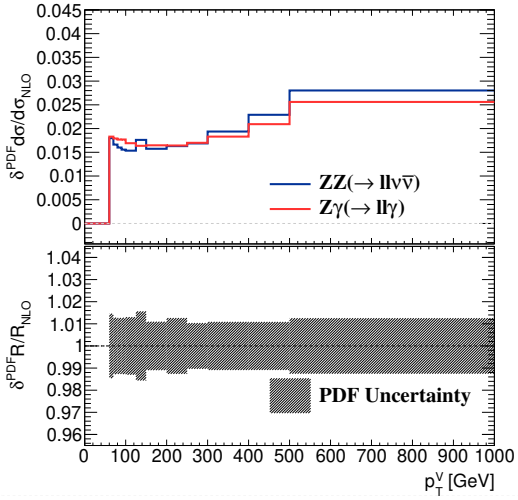

Figure 38: Top frame: relative PDF uncertainty on the ZZ (blue line) and $Z\gamma$ (orange line) cross sections. Bottom frame: PDF uncertainty normalised to R_{NLO} (black band).

5.5 Electroweak corrections

The impact of electroweak corrections in the method has also been studied and is described in this section. The electroweak corrections in this thesis were provided by the authors of [93] based on the OpenLoops generator [98]. NLO EW corrections are defined as

$$d\sigma_{\text{NLO EW}} = d\sigma_{\text{LO}}(1 + \Delta_{\text{EW}}). \tag{91}$$

Since no simultaneous calculation of QCD and EW corrections exists, they are combined by assuming they are independent of each other. Two prescriptions are defined,

$$\begin{aligned} \text{Additive:} \quad & d\sigma_{\text{NNLO QCD+ EW}} = d\sigma_{\text{LO}}(1 + \Delta_{\text{QCD}} + \Delta_{\text{EW}}) + d\sigma^{gg}, \\ \text{Multiplicative:} \quad & d\sigma_{\text{NNLO QCDx EW}} = d\sigma_{\text{LO}}\,(1 + \Delta_{\text{EW}})(1 + \Delta_{\text{QCD}}) + d\sigma^{gg}, \end{aligned} \tag{92}$$

where Δ_{QCD} and Δ_{QCD} correspond to the relative QCD and electroweak corrections respectively. Here the average between both is taken as the nominal. Therefore, there is an intrinsic uncertainty related to this choice, and the difference between the average and either of both prescriptions is taken as an uncertainty, i.e.

$$\delta^{(1)}_{\text{EW}} d\sigma_{\text{QCD}\times\text{EW}} = \frac{1}{2}|d\sigma_{\text{QCDxNLO EW}} - d\sigma_{\text{QCD+NLO EW}}|. \tag{93}$$

In order to see the impact of the EW corrections on the individual processes, in Figure 39 the cross sections at LO and NLO EW are shown. A correction of around $-10\%(-10\%)$ is observed at low p_T^V, being at most $-40\%(-30)\%$ at high p_T^V for $ZZ(Z\gamma)$. It is also seen that the EW corrections have similar shapes for ZZ and $Z\gamma$, but the ZZ ones are always greater. When combining QCD and EW calculations, (negative) corrections of 40% are obtained at $p_T^V = 500-1000$ GeV for ZZ. Differences of about 5% are observed when comparing additive and multiplicative prescriptions. To show how this affects the ratio $R(p_T^V)$, in Figure 40 the behaviour of the ratio after applying EW corrections is depicted. We see that, after taking the ratio between cross sections, the NLO EW correction becomes $\sim 5\%$ at low values of the bosons p_T, reaching 10% at high p_T^V. Similar numbers are obtained when combining QCD and EW calculations. We note that the plateau at high p_T^V, observed when applying only QCD corrections, is lost when including EW corrections, and the ratio tends to be lower, especially for the multiplicative prescription. This comes from the fact that the ZZ EW corrections are greater (with negative sign) than the $Z\gamma$ ones, resulting in a shift towards lower R values. From Figure 40 differences between additive and multiplicative prescriptions of about $1\%(6\%)$ are observed at low (high) p_T^V.
Finally, in Figure 41 all the different sources of uncertainties are displayed. One can observe that, at low p_T^V, the QCD uncertainties dominate, but they are comparable with the other sources. However, for $p_T^V \gtrsim 300$ GeV the electroweak uncertainties become dominant, increasing with p_T^V. The uncertainties are then combined in quadrature, resulting in a total uncertainty below 3% for $p_{\text{T}} < 300$ GeV and up to 4.5% at highest p_{T}. If no electroweak uncertainties are considered, the total

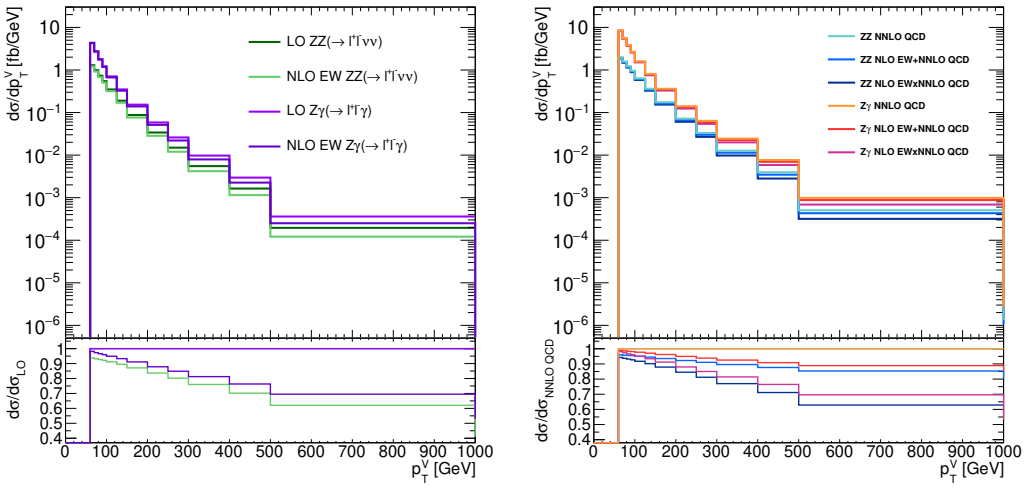

Figure 39: Left: Born and NLO EW cross sections at $\sqrt{s} = 13$ TeV for ZZ (green) and $Z\gamma$ (violet) production. The bottom frame shows the cross section normalised to the LO prediction. Right: NNLO QCD prediction (black) and combination of NNLO QCD and NLO EW using the multiplicative (blue), additive (orange) prescriptions and their average (violet). The bottom panel shows the cross sections normalised to the NNLO QCD calculation.

uncertainty stays stable across the whole p_T^V range, being about 3%.

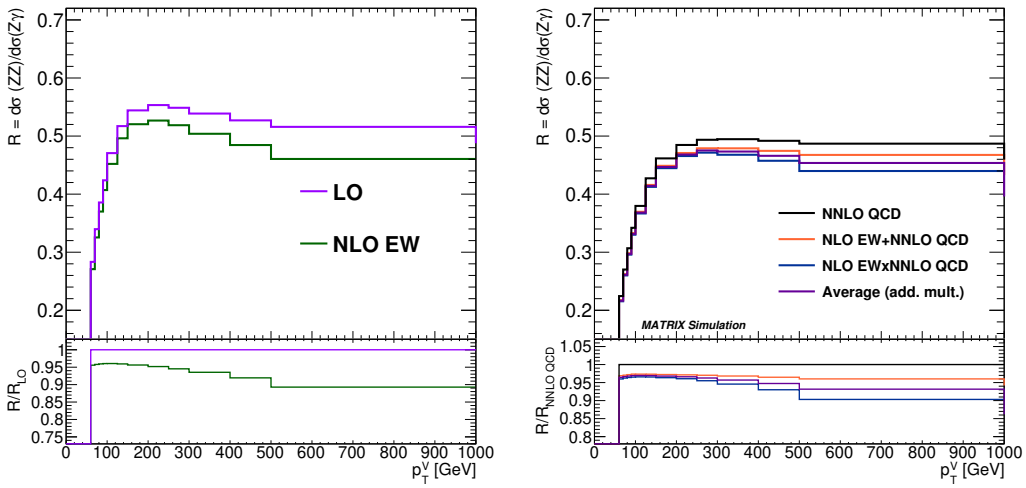

Figure 40: Left: Born (violet) and NLO EW (green) cross section ratio versus p_T^V at $\sqrt{s} = 13$ TeV. The bottom frame shows the cross section normalised to the LO prediction. Right: NNLO QCD cross section ratio (green) and the combination of NNLO QCD and NLO EW using the multiplicative (blue) and additive prescriptions (orange). The bottom panel shows the cross sections normalised NNLO QCD calculation.

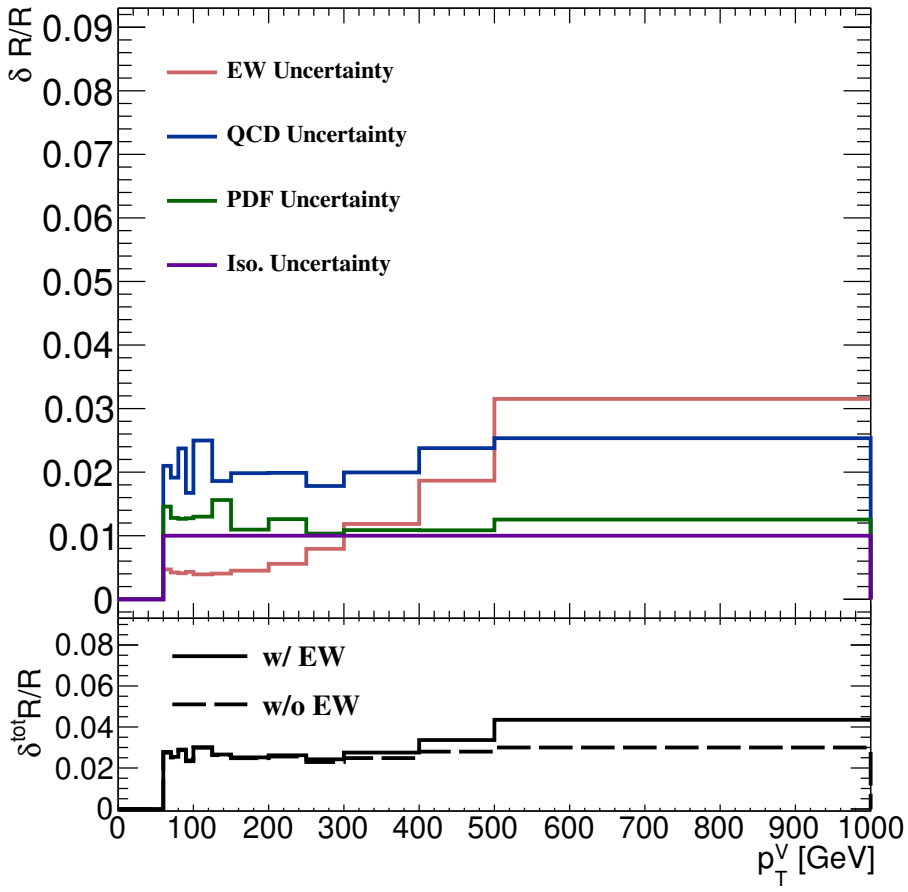

Figure 41: Top frame: electroweak δ^{EW} (red), QCD δ^{QCD} (blue), PDF δ^{PDF} (green) and isolation δ^{iso} (violet) relative uncertainties on the ratio R. In the bottom frame the uncertainties are added in quadrature. The combined uncertainty is shown including (solid) and without including (dashed) electroweak corrections.

6 Search for direct production of sleptons decaying into final states with two leptons and missing transverse momentum

For each generation of Standard Model leptons, the Minimal Supersymmetric Standard Model predicts two scalar superpartners, the left-handed slepton ℓ_L (partner of the $SU(2)$ doublet), and the right-handed slepton ℓ_R (partner of the $SU(2)$ singlet). In principle, the left and right-handed states can mix, but since the slepton off-diagonal terms in the mass matrix are proportional to the lepton mass, mixings are usually only considered for the third generation. In the search presented in this chapter only superpartners of electrons (selectrons) and muons (smuons) are studied, being e_L, e_R, μ_L and μ_R the physical eigenstates.

The analysis is designed and interpreted in terms of Simplified Models [53]. Therefore, the slepton pair production cross section depends only on the mass of the sleptons. The main production mechanism is via Drell-Yan, $q\bar{q} \to \tilde{\ell}^+_{L,R}\tilde{\ell}^-_{L,R}$, since the squarks masses are set above the TeV scale and t-channel production mechanisms with exchange of squarks are suppressed. Right and left-handed sleptons are also assumed to be mass degenerate, i.e. $m_{\tilde{\ell}_L} = m_{\tilde{\ell}_R}$. The sleptons are unstable and are assumed to decay with a 100% branching ratio into a SM lepton and a pure bino neutralino[1], $\tilde{\ell}\tilde{\ell} \to 2\tilde{\chi}^0_1 2\ell$, depicted in Figure 42. The detectable signature consists in two opposite sign (OS) same flavour (SF) leptons (electrons or muons) and E_T^{miss} originating from the neutralinos escaping detection.

This signature has already been explored by the ATLAS [117, 118] and CMS [119] collaborations. The ATLAS result [117] was only sensitive in the high mass splitting region[2] $\Delta m(\tilde{\ell}, \tilde{\chi}^0_1) = m_{\tilde{\ell}} - m_{\tilde{\chi}^0_1} \gtrsim m_W$, leaving an unexplored gap for mass splittings

[1] The kinematics of the process are independent from the nature of the neutralino [116].

[2] The reason for which [117] was not sensitive for mass splittings above the W boson mass is discussed in Appendix B.

below the W boson mass. The present analysis targets, instead, the direct production of charged slepton pairs with $\Delta m(\ell, \tilde{\chi}_1^0) = m(\tilde{\ell}) - m(\tilde{\chi}_1^0) \lesssim m_W$. This search uses a dedicated data driven technique to estimate the dominant SM background. In fact, while the slepton signal produces events with two same flavour (SF) opposite sign (OS) leptons in the final state, background processes like WW, $t\bar{t}$, Wt and $Z(\rightarrow \tau\tau)$ backgrounds (flavour symmetric backgrounds) have a 50% probability of producing SF lepton pairs and a 50% probability of producing different flavour (DF) lepton pairs. This can be exploited by using the DF channel in order to predict the backgrounds in the SF channel.

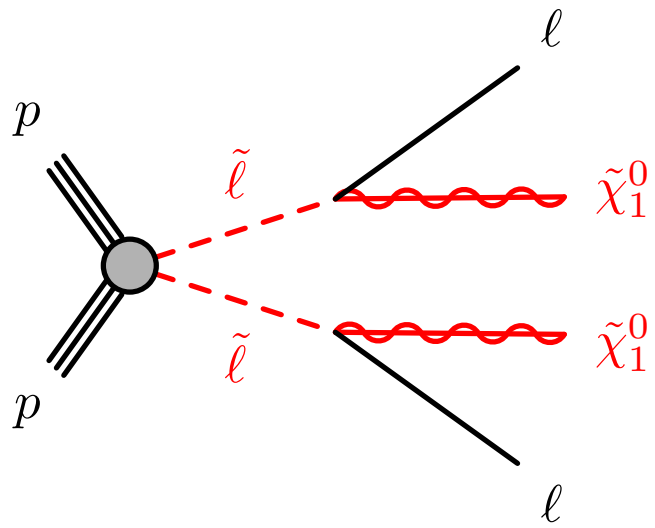

Figure 42: Diagram showing a proton-proton collision producing a slepton pair decaying into two leptons and two neutralinos.

6.1 Event reconstruction

In this analysis the full data collected during Run2 by the ATLAS detector is used, corresponding to 3.2 fb^{-1} of data collected in 2015, 33.0 fb^{-1} of data collected in 2016, 44.3 fb^{-1} of data collected in 2017 and 58.45 fb^{-1} of data collected in 2018, adding up to a total integrated luminosity of 138.95 fb^{-1}.

6.1.1 Trigger

Events are selected using single lepton triggers, which employ different lepton p_{T} thresholds depending on the data-taking period. The different triggers are summarised

in Table 5.
The performance of these triggers can be found in [120, 121] for electrons and muons, respectively. Trigger efficiencies of about 95% and 85% (in the endcap region) are obtained for electrons and muons with $p_{\mathrm{T}} \sim 60$ GeV, respectively.

	Single electron	Single muon
2015	HLT_e24_lhmedium HLT_e60_lhmedium HLT_e120_lhloose	HLT_mu20_iloose HLT_mu50
2016	HLT_e24_lhtight_nod0_ivarloose HLT_e26_lhtight_nod0_ivarloose HLT_e60_lhmedium_nod0 HLT_e140_lhloose_nod0	HLT_mu26_ivarmedium HLT_mu50
2017-2018	HLT_e26_lhtight_nod0_ivarloose HLT_e60_lhmedium_nod0 HLT_e140_lhloose_nod0	HLT_mu26_ivarmedium HLT_mu50

Table 5: Summary of the single lepton triggers used in the analysis, for electrons (left column) and muons (right column). The numbers shown in the name string correspond to the p_{T} thresholds. Some triggers also include quality requirements on the leptons. 'lh' corresponds to the likelihood discriminant described in Chapter 4, followed by its requirement. Triggers with the suffix 'nod0' do not include requirements on the transverse impact parameter relative to the beam-line, d_0, and its significance $|d_0/\sigma(d_0)|$. 'ivarloose','iloose' and 'ivarmedium' stand for an additional requirement on the isolation. More details can be found in [121, 120].

6.1.2 Object definition

This section is dedicated to define the objects used for the analysis: electrons, muons, jets and E_T^{miss}. We distinguish between *baseline* leptons/jets (looser requirements) and signal leptons/jets (tighter requirements and used in the final result). The object definition criteria for electrons, muons and jets can be found in Tables 6, 7 and 8, respectively.

Electrons

Electrons are required to reside within $|\eta| < 2.47$. At baseline level, electrons must have $p_{\mathrm{T}} > 9$ GeV, satisfy the `LooseAndBLayerLLH` Particle Identification (PID) quality criteria [65] and also satisfy the Interaction Point (IP) condition $|z_0 \sin\theta| < 0.5$ mm. Signal electrons must have $p_{\mathrm{T}} > 9$ GeV and have to satisfy the `FCLoose` isolation criteria [65] in order to be isolated from other high-p_{T} charged particles. Signal electrons must pass `TightLLH` quality criteria [65] and also satisfy the impact parameter (IP) condition $|d_0/\sigma(d_0)| < 5$, where $\sigma(d_0)$ denotes the uncertainty on the IP. The electron selection is summarised in Table 6.

Baseline electron	
Acceptance	$p_{\mathrm{T}} > 9$ GeV, $\lvert\eta^{\mathrm{clust}}\rvert < 2.47$
PID Quality	`LooseAndBLayerLLH`
Impact parameter	$\lvert z_0 \sin\theta\rvert < 0.5$ mm

Signal electron	
Acceptance	$p_{\mathrm{T}} > 9$ GeV, $\lvert\eta^{\mathrm{clust}}\rvert < 2.47$
PID Quality	`TightLLH`
Isolation	`FCLoose`
Impact parameter	$\lvert d_0/\sigma(d_0)\rvert < 5$

Table 6: Summary of the electron selection criteria for baseline (top table) and signal (bottom table) selection requirements. The signal selection requirements are applied on top of the baseline selection and after overlap removal has been performed (see Section 6.1.3).

Muons

Muons used in this analysis must have $p_{\mathrm{T}} > 9$ GeV and reside within $|\eta| < 2.6$. Baseline muons must pass the `Medium` quality requirement [66] and also satisfy the IP condition $|z_0 \sin\theta| < 0.5$ mm. Signal muons must have $p_{\mathrm{T}} > 9$ GeV, pass the `Medium` quality criteria [66], be isolated with respect to other high-p_{T} charged particles, satisfying the `FCLoose` isolation criteria [66] and additionally having $|d_0/\sigma(d_0)| < 3$ constraint on the IP. The muon selection criteria are summarised in Table 7.

Baseline muon	
Acceptance	$p_{\mathrm{T}} > 9$ GeV, $\lvert\eta\rvert < 2.6$
PID Quality	`Medium`
Impact parameter	$\lvert z_0 \sin\theta\rvert < 0.5$ mm

Signal muon	
Acceptance	$p_{\mathrm{T}} > 9$,GeV, $\lvert\eta\rvert < 2.6$
PID Quality	`Medium`
Isolation	`FCLoose`
Impact parameter	$\lvert d_0/\sigma(d_0)\rvert < 3$

Table 7: Summary of the muon selection criteria for baseline (top table) and signal (bottom table) selection requirements. The signal selection requirements are applied on top of the baseline selection after overlap removal has been performed (see Section 6.1.3).

Jets

This analysis uses `PFlow` jets reconstructed using the anti-k_t algorithm [67] with distance parameter $R = 0.4$. At baseline level these jets are required to have $p_{\mathrm{T}} > 20$ GeV and fulfill the pseudorapidity requirement of $|\eta| < 2.8$. To reduce the effects of pile-up, signal jets are further required to pass a cut on the Jet Vertex Tagger (JVT) [72, 73], JVT$>$ 0.5 (`Tight` WP), if their p_{T} is in the 20-60 GeV range and they reside within $|\eta| < 2.4$. Only jet candidates with $p_{\mathrm{T}} > 20\,\mathrm{GeV}$ and $|\eta| < 2.4$ are finally considered[3], although jets with $|\eta| < 4.9$ are included in the missing transverse momentum calculation and are considered when applying the procedure to remove reconstruction ambiguities, which is described later in this section.
For b-jet identification, the DL1r [70] algorithm is used. A selection that provides 85% efficiency for tagging b-jets in simulated $t\bar{t}$ events is employed. The choice of 85% b-tagging working point ensures a strong $t\bar{t}$ and single top (Wt) rejection, without a significant loss of signal events. The jet selection criteria are summarised in Table 8.

Baseline jet	
Acceptance	$p_{\mathrm{T}} > 20$ GeV, $\lvert\eta\rvert <2.8$
Signal jet	
JVT	`Tight`
Acceptance	$p_{\mathrm{T}} > 20\,\mathrm{GeV}$, $\lvert\eta\rvert < 2.4$
Signal b-jet	
b-tagger Algorithm	DL1r
Efficiency	`FixedCutBEff_85`
Acceptance	$p_{\mathrm{T}} > 20$ GeV, $\lvert\eta\rvert < 2.4$

Table 8: Summary of the jet and b-jet selection criteria. The signal selection requirements are applied on top of the baseline requirements after overlap removal has been performed (see Section 6.1.3).

Missing transverse momentum

The missing transverse energy is built from the transverse momenta of all physics objects considered in the analysis (jets, muons and electrons), as well as photons and

[3]Hadronic τ-lepton decay products are treated as jets.

all tracks matched to the primary vertex not associated with these objects. Objects entering the MET are required to satisfy the baseline selection criteria defined above. Jets are required to be tagged as originating from the hard scatter, using the Jet Vertex Tagger.

6.1.3 Overlap Removal

To solve ambiguities in the object reconstruction, an overlap removal (OR) is applied. The following steps are applied:

- jet candidates within $\Delta R = \sqrt{\Delta y^2 + \Delta\phi^2} = 0.2$ of an electron candidate, or jets with fewer than three tracks that lie within $\Delta R = 0.4$ of a muon candidate are removed, as they mostly originate from calorimeter energy deposits from electron shower or muon bremsstrahlung;
- electrons and muons within $\Delta R' = \min(0.4, 0.04 + 10/p_T)$ of the remaining jets are discarded, to reject leptons from the decay of b- or c-hadrons;
- calorimeter-tagged muon candidates sharing an ID track with an electron are removed. Electrons sharing an ID track with remaining muons are removed.

6.2 Monte Carlo simulations

Standard Model processes that share the same final state as the sleptons signal constitute a background in the search. The processes considered throughout this chapter are: top ($t\bar{t}, Wt, tZ, t\bar{t}+X$), diboson (VV), triboson (VVV), $Z/\gamma^* \to \mu\mu$+jets, $Z/\gamma^* \to ee$+jets, $Z/\gamma^* \to \tau\tau$+jets, $W \to \mu\nu$+jets, $W \to e\nu$+jets, $W \to \tau\nu$+jets.
The production of $t\bar{t}$ and $t\bar{t}$ H events is modelled using the POWHEG -Box v2 [122, 123, 124] generator at NLO with the NNPDF3.0NLO [42] parton set of distribution functions (PDF) and the hdamp parameter[4] set to 1.5 m_{t} [125]. The events are interfaced to PYTHIA8 [126] to model the parton shower, hadronisation, and underlying event, with parameters set according to the A14 tune [127] and using the NNPDF2.3LO [128] set of PDFs. The decays of bottom and charm hadrons are performed by EvtGen v1.6.0 [129]. The associated production of top-quarks with W bosons (Wt) is modelled using the POWHEG -Box v2 generator at NLO in QCD using the five-flavour scheme and the NNPDF3.0NLO set of PDFs. The diagram

[4]The hdamp parameter is a resummation damping factor and one of the parameters that controls the matching of Powheg matrix elements to the parton shower and thus effectively regulates the high-p_{T} radiation against which the $t\bar{t}$ system recoils.

removal scheme [130] is used to remove interference and overlap with $t\bar{t}$ production. The events are interfaced to PYTHIA8 using the A14 tune and the NNPDF2.3LO set of PDFs. The production of $t\bar{t}+V$, tWZ and tZq events is modelled using the MADGRAPH5_aMC@NLO v2.3.3 [131] generator at NLO with the NNPDF3.0NLO parton distribution function (PDF). The events are interfaced to PYTHIA 8.2 [126] using the A14 tune and the NNPDF2.3LO PDF set. The production of $t\bar{t}\,\gamma$ events is modelled using the MADGRAPH5_aMC@NLO v2.3.3 generator at LO with the NNPDF2.3LO parton distribution function. The events are interfaced with PYTHIA 8.2 using the A14 tune and the NNPDF2.3LO PDF set. Samples of diboson final states (VV) are simulated with the SHERPA v2.2.1 or v2.2.2 [132] generator depending on the process, including off-shell effects and Higgs-boson contributions, where appropriate.

6.3 Analysis optimisation and signal region definition

The analysis optimisation was performed using the benchmark signal point $m\left(\tilde{\ell}, \tilde{\chi}_1^0\right) = (100, 70)$ GeV, since this is a signal point close to the boundary of the observed exclusion limit obtained by the Run2 ATLAS soft-lepton analysis [133]. For the optimisation procedure, it is useful to define an estimator of the goodness of the chosen cut on a given variable, i.e. to adopt a significance definition. The significance definition used in this analysis is[5] [134]

$$Z_N = \sqrt{2\Big[n\log\left(\frac{n(b+\sigma^2)}{b^2+n\sigma^2}\right) - \frac{b^2}{\sigma^2}\log\left(1+\frac{\sigma^2(n-b)}{b(b+\sigma^2)}\right)\Big]}, \tag{94}$$

where n is the number of observed signal (S) and background (B) events ($n = S + B$) given a background prediction of $B \pm \sigma$ events. In order to exclude a model at 95% confidence level, a significance of $Z_N = 1.64$ is needed.

The optimisation is performed iterating over the following steps:

1. A preliminary event selection is applied, requiring two opposite-sign same-flavour leptons.

2. Sensitive variables are chosen by investigating the signal and background processes;

[5] Historically, the signal (S) over background (B) S/B or $S/\sqrt{B}$ was used in searches that were systematics or statistics dominated, respectively. However, it has been shown that when the event count is very low, both indicators tend to give a bad estimate of the significance.

3. An iterative cut-and-count procedure is performed in order to find the most favorable cut on a certain variable. The nested loop considers all the sensitive variables discussed below. At the end of this step a candidate signal region (SR) is defined;

4. Plots of the meaningful variables are produced after applying the optimal cuts obtained in the previous step, and checked to see if there is room for a further optimisation;

5. If no further optimisation is possible, the candidate SR is kept.

This procedure is repeated for other signal benchmark points $m\left(\tilde{\ell}, \tilde{\chi}_1^0\right) = (100, 50)$, $(150, 100)$, $(150, 120)$ GeV to ensure that the selection is not biased towards a single signal model or possible statistical fluctuations of that simulation. Little difference in the cuts has been observed in all the optimal selections.
Candidate events are firstly triggered by single-lepton triggers and selected by applying a basic preselection, described in Table 9. Exactly two OS leptons (electrons or muons) are required. The leading and sub-leading lepton transverse momenta are required to be > 27 GeV and > 9 GeV, respectively. An invariant mass of the dilepton system ($m_{\ell\ell} > 11$ GeV) cut is applied in order to remove low mass resonances ($J/\Psi, \Psi', \Upsilon, ...$). A veto on jets (both central non-b-tagged and b-tagged jets) with $p_{\mathrm{T}} > 20$ GeV and $|\eta| < 2.4$ removes the bulk of the $Z+$jets and top backgrounds. Jets in the forward region are not used at any point in the analysis, since they can suffer from pile-up dependence. The cut on E_T^{miss}significance > 3 and $|m_{\ell\ell} - m_Z| > 15$ GeV reduces further $Z+$jets event contamination. The variables which have been found sensitive

Variable	Cut
$N_{\text{OS leptons}}$	$= 2$
$p_T^{\ell_1}$	> 27 GeV
$p_T^{\ell_2}$	> 9 GeV
$m_{\ell\ell}$	> 11 GeV
n_{jet-20}	$= 0$
$n_{bjet-20}$	$= 0$
E_T^{miss}significance	> 3
$\lvert m_{\ell\ell} - m_Z \rvert$	> 15 GeV(for SF only)

Table 9: Preselection cuts on SF and DF events.

for this analysis are described in the following:

- The transverse momentum of the leading lepton $p_T^{\ell_1}$;
- The transverse momentum of the sub-leading lepton $p_T^{\ell_2}$;
- The number of jets with a p_{T} above 20 GeV, n_{jet-20}.
- The number of b-tagged jets with a p_{T} above 20 GeV, $n_{bjet-20}$.
- The invariant mass of the two leptons $m_{\ell\ell}$. In particular, a $m_{\ell\ell}$ veto close to the Z mass window helps to reject $Z+$jets events;
- The azimuthal angular separation between the two leptons $\Delta\phi_{\ell,\ell}$. Since in absence of jets sleptons are produced back to back, the leptons coming from their decay are expected to be well separated in the azimuthal plane. This is not the case for backgrounds like $t\bar{t}$ or ZZ;
- The azimuthal angular separation between E_T^{miss} and the sub-leading lepton $\Delta\phi_{E_T^{\mathrm{miss}},\ell_1}$. Momentum conservation implies that (in the absence of jets) the hardest $\tilde{\chi}_1^0$ and the sub-leading lepton come from the decay of the same slepton, therefore the E_T^{miss} vector (pointing towards the hardest of $\tilde{\chi}_1^0$) is expected to be well separated from the $p_T^{\ell_1}$ direction;
- The magnitude of the vector sum of the two leptons and the E_T^{miss}: $p_{\mathrm{T,boost}}^{\ell\ell}$. Since the final state consists of two leptons and two neutralinos, the vectorial sum of the system is expected (in the absence of jets) to have low values due to the p_{T} balance of the system;
- The angular variable $\cos\theta_{\ell\ell}^*$, defined as $\cos\theta_{\ell\ell}^* = \cos\left(2\tan^{-1}e^{\Delta\eta_{\ell\ell}/2}\right) = \tanh(\Delta\eta_{\ell\ell}/2)$, is sensitive to the spin of the produced particles [135]. Being sleptons scalar particles, their cross section is proportional to $\sin^2\theta^*$, where θ^* is the polar angle between the incoming quark in one of the protons and the produced slepton. For spin one particles or spin half particles, this dependence differs. Since θ^* is not directly accesible at the LHC, $\cos\theta_{\ell\ell}^*$ is built in such a way to capture the rapidity from the lepton parents.
- The stransverse mass m_{T2} [136, 137], which is a kinematic variable used to bound the masses of a pair of particles that are assumed to have each decayed into one visible and one invisible particle. It is defined as

$$m_{\mathrm{T2}}^{m_\chi}(\mathbf{p}_{\mathrm{T},1},\mathbf{p}_{\mathrm{T},2},\mathbf{p}_{\mathrm{T}}^{\mathrm{miss}}) = \min_{\mathbf{q}_{\mathrm{T},1}+\mathbf{q}_{\mathrm{T},2}=\mathbf{p}_{\mathrm{T}}^{\mathrm{miss}}}\{\max[\, m_{\mathrm{T}}(\mathbf{p}_{\mathrm{T},1},\mathbf{q}_{\mathrm{T},1};m_\chi), m_{\mathrm{T}}(\mathbf{p}_{\mathrm{T},2},\mathbf{q}_{\mathrm{T},2};m_\chi)\,]\}\,,$$

where m_{T} indicates the transverse mass, defined as[6]

$$m_T = (p_{\mathrm{T}}, q_T, m_\chi)\sqrt{m_\ell^2 + m_\chi^2 + 2\left(E_T^\ell E_T^q - \mathbf{p}_T \cdot \mathbf{q}_T\right)}. \tag{95}$$

$\mathbf{p}_{\mathrm{T},1}$ and $\mathbf{p}_{\mathrm{T},2}$ are the transverse-momentum vectors of the two leptons, and $\mathbf{q}_{\mathrm{T},1}$, $\mathbf{q}_{\mathrm{T},2}$ are trial vectors, satisfying $\mathbf{p}_{\mathrm{T}}^{\mathrm{miss}} = \mathbf{q}_{\mathrm{T},1} + \mathbf{q}_{\mathrm{T},2}$, m_χ is the mass of the invisible particle and $E_T^\ell = \sqrt{p_T^2 + m_\ell^2}$, $E_T^q = \sqrt{q_T^2 + m_\chi^2}$. The minimisation is performed over all the possible decompositions of $\mathbf{p}_{\mathrm{T}}^{\mathrm{miss}}$. Since the mass of the invisible particle is, a priori, unknown, it enters as a free parameter in the equation. The interesting property of m_{T2} is that, for $m_\chi = m_{\mathrm{inv}}$, the value of m_{T2} has a kinematic endpoint at the mass M of the mother particle. This is demonstrated in Figure 43, where the m_{T2}^{100} distribution is shown fixing the $m_{\tilde{\chi}_1^0}$ at 100 GeV (left) and fixing $m_{\tilde{\ell}}$ (right). It is observed that when the mass hypothesis is chosen, the distributions have an endpoint at $m_{\tilde{\ell}}$. However, for the wrong mass assumption, the endpoint is located at $\sim m_{\mathrm{inv}} + \Delta m$. Thus, by dividing the SR in bins of m_{T2}, sensitivity to a variety of slepton masses and mass splittings can be achieved. In this analysis we have found that the choices $m_{\mathrm{inv}} = 0$ GeV and $m_{\mathrm{inv}} = 100$ GeV give very similar sensitivity. Related studies can be found in Appendix C. The final choice is $m_{\mathrm{inv}} = 100$ GeV. In order to exploit the m_{T2}^{100} shape, a multi-bin fit as a function of m_{T2}^{100} is performed to obtain final result. The details of the fit is described in Section 6.7. Some of the statements claimed above about the kinematics of the process and some further

[6] When $m_\chi = 0$ is assumed, the transverse mass takes the known form $m_{\mathrm{T}} = \sqrt{2 \times |\mathbf{p}_{\mathrm{T},1}| \times |\mathbf{p}_{\mathrm{T},2}| \times (1 - \cos(\Delta\phi))}$, where $\Delta\phi$ is the difference in azimuthal angle between the particles with transverse momenta $\mathbf{p}_{\mathrm{T},1}$ and $\mathbf{p}_{\mathrm{T},2}$.

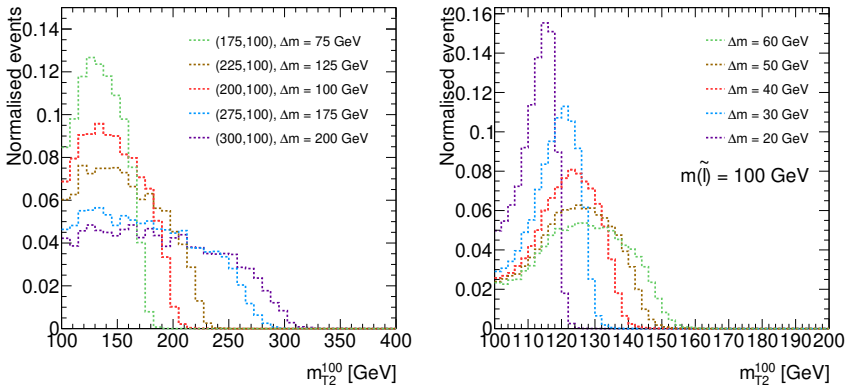

Figure 43: Normalised m_{T2}^{100} distributions ($m_{\mathrm{inv}} = 100$ GeV) for a fixed $m_{\tilde{\chi}_1^0} = 100$ GeV mass (left) and for a fixed $m_{\tilde{\ell}} = 100$ GeV mass (right).

checks related to the optimisation are discussed in Appendix D.
Since events where no jets are present have different kinematics than events with presence of jets, two SRs are defined: SR-0jet and SR-1jet.

6.3.1 SR-0jet

The full list of signal region (SR) cuts for SR-0jet in this analysis is detailed in Table 10. Only SF leptons are considered. The set of cuts used to define the signal region are visualized in the kinematic distributions in Figures 44 and 45, where the SR selection is applied except for the variable shown itself. The plot also includes the main SM backgrounds, and three signal benchmark points: $m\left(\tilde{\ell}, \tilde{\chi}_1^0\right) = (100, 70), (150, 110), (150, 90)$ GeV. Some interesting features can be observed. Although these models, with compressed mass splittings, tend to have soft leptons in the final state, due to the E_T^{miss}significance cut used to reduce the $Z+$jets, $p_T^{\ell_1}$ increases accordingly, while the $p_T^{\ell_2}$ is not affected as much (see Figure 74). It can also be observed that the $\Delta\phi_{\ell,\ell}$ and $\Delta\phi_{E_T^{\text{miss}},\ell_1}$ are already sculpted towards high values, due to the other selections applied.
The significance values Z_N obtained with this SR definition using all the signal samples (across the $m_{\tilde{\ell}}$ - $m_{\tilde{\chi}_1^0}$ plane), assuming a 20% systematic uncertainty on the background, are shown in Figure 46 (left). The expected background yields in the SR are reported in Table 11, where the category "others" comprises all the minor backgrounds (Higgs processes, $t\bar{t}$ +X, multitop, tWZ)
Since the diboson category encloses WW, WZ, ZZ processes, there could be contamination of three lepton final states where one of the leptons is lost in the detector. This contamination has been found to be negligible in the SR, contributing to 2% of the total diboson background[7].

[7]Four lepton final states, where two leptons are lost, contribute to 0.3% of the total diboson.

Variable	Cut
n_{jet-20}	$= 0$
$n_{bjet-20}$	$= 0$
$N_{\text{OS SF leptons}}$	$= 2$
$p_T^{\ell_1}$	> 140 GeV
$p_T^{\ell_2}$	> 20 GeV
E_T^{miss}significance	> 7
$m_{\ell\ell}$	> 11 GeV
$\lvert m_{\ell\ell} - m_Z \rvert$	> 15 GeV
$p_{\text{T,boost}}^{\ell\ell}$	< 5 GeV
$\lvert \cos\theta^*_{\ell\ell} \rvert$	< 0.2
$\Delta\phi_{\ell,\ell}$	> 2.2
$\Delta\phi_{E_T^{\text{miss}},\ell_1}$	> 2.2

Table 10: The full set of cuts defining the SR-0jet.

Background	Events
$t\bar{t}$	5.3 ± 0.5
Wt	4.7 ± 0.8
$Z/\gamma^* + jets$	1.2 ± 1.1
Diboson	39.1 ± 2.1
Others	0.1 ± 0.1
Total	50.5 ± 2.6

Table 11: Top: Expected background yields in SR-0jet. Uncertainties are statistical only.

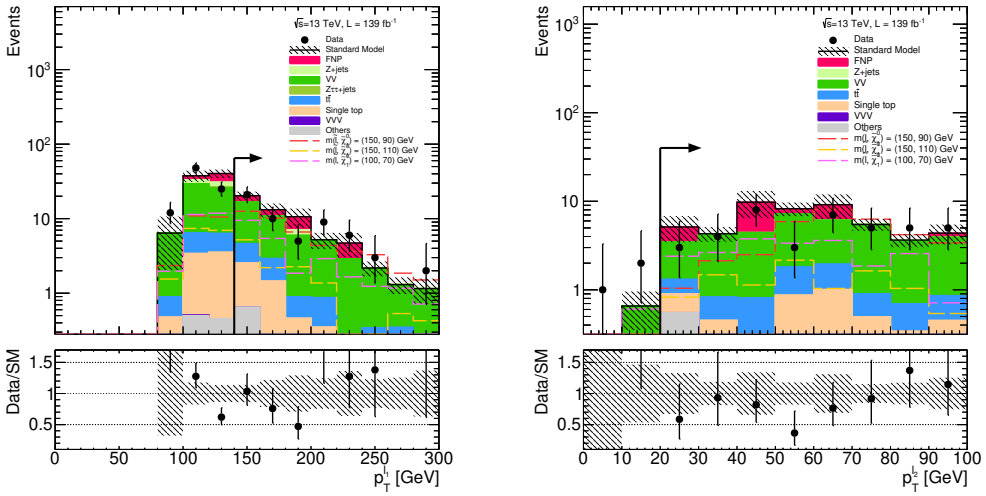

(a) $p_T^{\ell_1}$ **(b)** $p_T^{\ell_2}$

(c) E_T^{miss}significance **(d)** m_{T2}^{100}

Figure 44: Plots of the most sensitive variables used in the analysis, the main background and for three benchmark signal points ($m\left(\tilde{\ell}, \tilde{\chi}_1^0\right) = (100, 70), (150, 110), (150, 90)$ GeV), after all the cuts described in Table 10 (SR 0-jet), except the cut on the variable shown in the plot. The uncertainties shown are statistical only. In the bottom frame of each plot the data to MC ratio is shown.

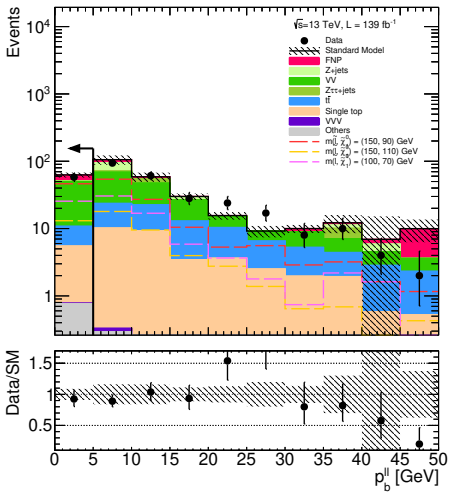

(a) $p^{\ell\ell}_{\mathrm{T,boost}}$

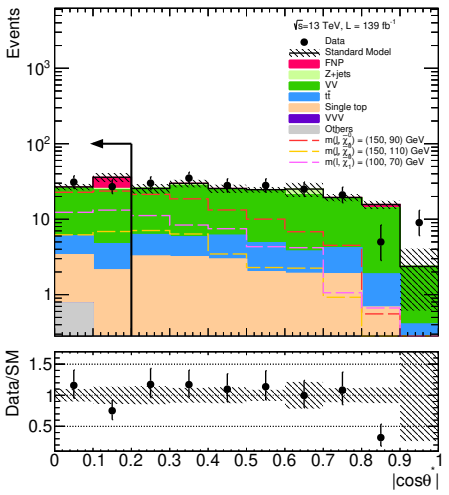

(b) $|\cos\theta^*_{\ell\ell}|$

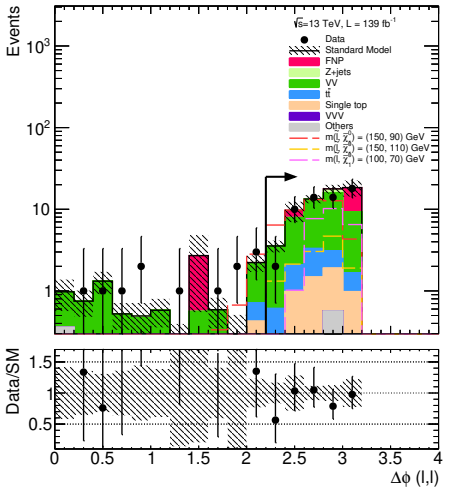

(c) $\Delta\phi_{\ell,\ell}$

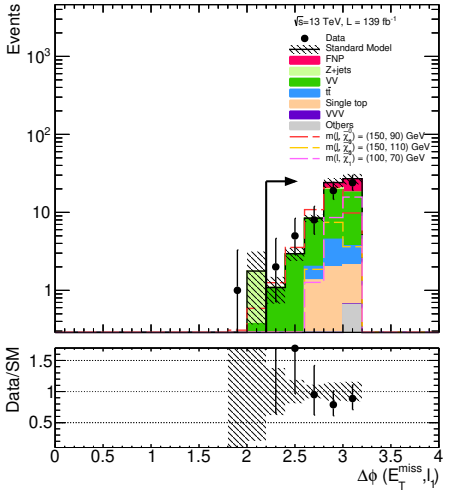

(d) $\Delta\phi_{E_T^{\mathrm{miss}},\ell_1}$

Figure 45: Plots of the most sensitive variables used in the analysis, the main background and for three benchmark signal points $\left(m\left(\tilde{\ell},\tilde{\chi}_1^0\right) = (100,70),(150,110),(150,90)\ \mathrm{GeV}\right)$, after all the cuts described in Table 10 (SR 0-jet), except the cut on the variable shown in the plot. The uncertainties shown are statistical only. In the bottom frame of each plot the data to MC ratio is shown.

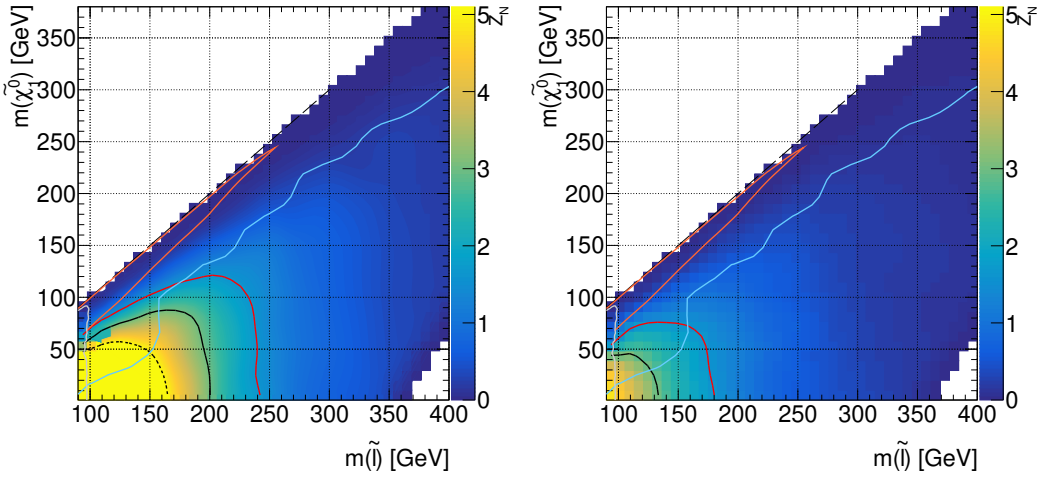

Figure 46: Significance values Z_N in the 0-jet SR (left) and 1-jet SR (right) in the $m_{\tilde{\ell}}$ - $m_{\tilde{\chi}_1^0}$ plane assuming a 20% systematic uncertainty on the background. The red, black and black dashed curves correspond to $2\sigma, 3\sigma$ and 5σ contours, respectively. The orange and blue curves correspond to the observed limits of previous ATLAS analyses [117, 133], the grey curve corresponds to the slepton limits from LEP [138].

6.3.2 SR-1jet

In a similar fashion to that of the 0-jet case, we perform an optimisation for events with exactly one (non b-tagged) jet. The cuts that define the SR-1jet are shown in Table 12. SR-1jet plots are depicted in Figures 47 and 48, where again all the SR-1jet cuts are applied except for variable shown itself. The main difference with respect to the 0-jet SR is that, since in the presence of jets the E_T^{miss} and the leptons p_{T} do not have to be balanced anymore, it is found that $p_{\text{T,boost}}^{\ell\ell}$ and $\Delta\phi_{E_T^{\text{miss}},\ell_1}$ are no longer useful. The background yields can be checked in Table 13. The dominant backgrounds, as for the 0-jet case, correspond to flavour symmetric backgrounds ($t\bar{t}$, Wt, WW and Z($\tau\tau$)+jets).

Variable	Cut
n_{jet-20}	$= 1$
$n_{bjet-20}$	$= 0$
$N_{\text{OS SF leptons}}$	$= 2$
$p_T^{\ell_1}$	> 100 GeV
$p_T^{\ell_2}$	> 50 GeV
E_T^{miss}significance	> 7
$m_{\ell\ell}$	> 60 GeV
$\lvert m_{\ell\ell} - m_Z \rvert$	> 15 GeV
$\lvert \cos\theta^*_{\ell\ell} \rvert$	< 0.1
$\Delta\phi_{\ell,\ell}$	> 2.8

Table 12: The full set of cuts defining the SR-1jet.

Background	Events
$t\bar{t}$	28.5 ± 1.0
Wt	11.9 ± 1.3
Z(ee,$\mu\mu$)+jets	5.6 ± 4.4
Z($\tau\tau$)+jets	< 1.0
Diboson	29.3 ± 2.0
Triboson	0.0 ± 0.0
others	0.2 ± 0.4
Total	75.5 ± 5.2

Table 13: Expected background yields in SR-1jet.

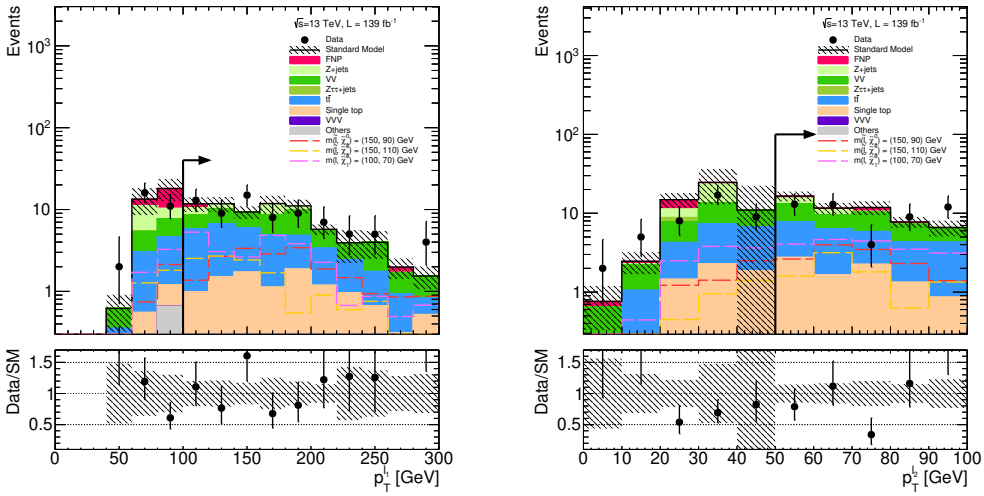

(a) $p_T^{\ell_1}$

(b) $p_T^{\ell_2}$

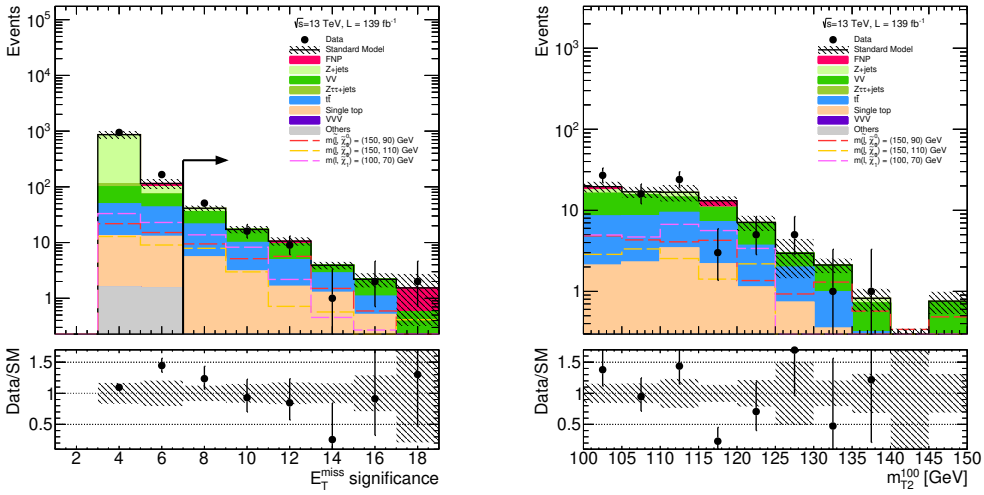

(c) E_T^{miss}significance

(d) m_{T2}^{100}

Figure 47: Plots of the most sensitive variables used in the analysis for the main background and for three benchmark signal points ($m\left(\tilde{\ell}, \tilde{\chi}_1^0\right) = (100, 70), (150, 110), (150, 90)$ GeV), after all the cuts described in Table 12 (SR 1-jet), except the cut on the variable shown in the plot. The uncertainties shown are statistical only. In the bottom frame of each plot the data to MC ratio is shown.

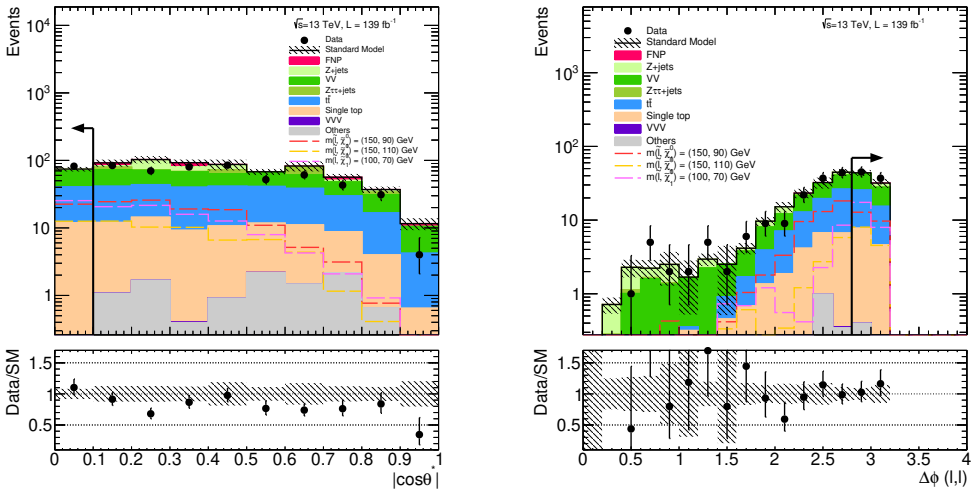

(a) $|\cos\theta^*_{\ell\ell}|$ **(b)** $\Delta\phi_{\ell,\ell}$

Figure 48: Plots of the most sensitive variables used in the analysis for, the main background and for three benchmark signal points $(m\left(\tilde{\ell},\tilde{\chi}_1^0\right) = (100,70)\,,(150,110)\,,(150,90)$ GeV), after all the cuts described in Table 12 (SR 1-jet), except the cut on the variable shown in the plot. The uncertainties shown are statistical only. In the bottom frame of each plot the data to MC ratio is shown.

6.4 Fake and non prompt leptons

Aside from the irreducible backgrounds that share exactly the same final state as the slepton signal, there is another type of background, the *reducible background*, that arises from detector mismeasurements[8], producing a *fake* signal. Leptons arising from W, Z, H and prompt tau decays (or from SUSY particle decays), referred to as prompt or real leptons, are distinguished from the fake (non-prompt) leptons. Non-prompt leptons arise from semileptonic decays of b and c-hadrons, meson decays (e.g. $K \to \mu\nu$), and from photon conversions. Fake leptons arise from misidentified light-flavour (u, d, s, g) jets. Fake and non-prompt (FNP) leptons are in general not well isolated and rejected by the lepton identification/isolation criteria and requirements on the impact parameter. The remaining contamination of reducible backgrounds is commonly estimated using the matrix method described in [139].
Two type of leptons are defined: (i) leptons as defined in the final analysis (tight) (ii) leptons that defined by relaxing or removing some of the tight or signal definitions (loose). The definitions of loose and tight leptons are exactly the ones used for baseline and signal lepton definition in Tables 6 and 7 for electrons and muons, respectively. From these definitions, we further denote as:

- T the leptons passing the tight identification criteria.
- L the leptons that pass the loose criteria (inclusive loose).
- l the leptons passing the loose but not passing the tight identification criteria (exclusive loose).

Events containing two inclusive loose leptons are classified into four different categories: $N_{TT}, N_{Tl}, N_{lT}, N_{ll}$, where the first subscript denotes the lepton with highest p_{T} of the two. Two probabilities are now defined: the real efficiency (r) and the fake rate (f). The real efficiency is defined as the probability that a real lepton passing the loose selection also passes the tight criteria. In the same way, the fake rate is defined as the probability that an FNP lepton that passes the loose criteria also passes the tight. For different flavour events, four probabilities are needed in total ($r_{1,2}, f_{1,2}$), since electrons and muons have in general different fake rates and real efficiencies. With all these quantities, the estimated number of events with two real leptons (N_L^{RR}), one real and one fake (N_{LL}^{FR} and N_{LL}^{RF}) and two fakes (N_{LL}^{FF}) can be estimated by

[8]The reducible background could be completely suppressed with a perfect detector

inverting the following matrix

$$\begin{bmatrix} N_{TT} \\ N_{Tl} \\ N_{lT} \\ N_{ll} \end{bmatrix} = \begin{bmatrix} r_1 r_2 & r_1 f_2 & f_1 r_2 & f_1 f_2 \\ r_1(1-r_2) & r_1(1-f_2) & f_1(1-r_2) & f_1(1-f_2) \\ (1-r_1)r_2 & (1-r_1)f_2 & (1-f_1)r_2 & (1-f_1)f_2 \\ (1-r_1)(1-r_2) & (1-r_1)(1-f_2) & (1-f_1)(1-r_2) & (1-f_1)(1-f_2) \end{bmatrix} \begin{bmatrix} N_{LL}^{RR} \\ N_{LL}^{RF} \\ N_{LL}^{FR} \\ N_{LL}^{FF} \end{bmatrix}, \tag{96}$$

obtaining

$$N_{LL}^{RR} = (1-f_1)(1-f_2)N_{TT} - [f_2(1-f_1)]\,N_{Tl} - [f_1(1-f_2)]\,N_{lT} + f_1 f_2 N_{ll}, \tag{97}$$

$$N_{LL}^{RF} = -(1-f_1)(1-r_2)N_{TT} + [r_2(1-f_1)]\,N_{Tl} + [f_1(1-r_2)]\,N_{lT} + f_1 r_2 N_{ll}, \tag{98}$$

$$N_{LL}^{RF} = -(1-f_2)(1-r_1)N_{TT} + [f_2(1-r_1)]\,N_{Tl} + [r_1(1-f_2)]\,N_{lT} + f_2 r_1 N_{ll}, \tag{99}$$

$$N_{LL}^{FF} = (1-r_1)(1-r_2)N_{TT} - [r_2(1-r_1)]\,N_{Tl} - [r_1(1-r_2)]\,N_{lT} + r_1 r_2 N_{ll}, \tag{100}$$

which correspond to the expected number of events with two, one and zero prompt real leptons in a sample of two inclusive loose leptons. Since the present slepton search targets final states with two tight leptons, Equation 97 - 100 have to be multiplied by the appropriate probabilities in order to obtain events with two tight leptons. This gives

$$N_{TT}^{RR} = r_1 r_2 N_{LL}^{RR}, \tag{101}$$

$$N_{TT}^{RF} = r_1 f_2 N_{LL}^{RF}, \tag{102}$$

$$N_{TT}^{FR} = f_1 r_2 N_{LL}^{FR}, \tag{103}$$

$$N_{TT}^{FF} = f_1 f_2 N_{LL}^{FF}. \tag{104}$$

The real efficiencies r and fake rates f are calculated in control regions enriched in either real or FNP leptons from data and MC, respectively. These regions are defined with exactly two inclusive loose leptons. To compute the r and f, the hardest lepton is tagged while the sub-leading lepton is used as a probe and checked whether it is tight or not. This process is then repeated but tagging the sub-leading and using the leading lepton as the probe, checking if it is tight.
Since the FNP leptons originate from different sources, the final fake rates used in

Variable	CR^{REAL}	$CR^{\text{FAKE}}_{\text{HF}}$		$CR^{\text{FAKE}}_{\text{CO}}$	$CR^{\text{FAKE}}_{\text{LF}}$
Data/MC	MC	Data			MC
p_T^{leptons} [GeV]	27, 9				
num. of leptons	2	2		3	2
type	$\boldsymbol{e^{\pm}e^{\mp}}$ or $\boldsymbol{\mu^{\pm}\mu^{\mp}}$	$\mu\boldsymbol{e}$	$\boldsymbol{\mu\mu}$	$\mu^{+}\mu^{-}\boldsymbol{e^{\pm}}$	$\boldsymbol{e^{\pm}e^{\pm}}$
invariant mass [GeV]	-	-	$\lvert m_{ll} - m_Z\rvert > 10$	$\lvert m_{\mu\mu e} - m_Z\rvert < 10$	-
E_T^{miss} [GeV]	> 80	< 50		< 50	< 40
$m_{\text{T}}(\text{tag}, E_T^{\text{miss}})$ [GeV]	-	< 50		-	-
num. of bjets	-	1		0	-
ΔR(lep,b-jet)	passOR	tag: < 0.3		passOR	passOR
ΔR(lep,jet)	passOR	probe: > 0.4		passOR	passOR

Table 14: The cuts used to define the control regions for extracting the real efficiencies and fake rates used as input to the Matrix Method. The leptons in bold indicate the one used as probe to calculate the real efficiency/fake rate. If both leptons are bold both are used as probes. HF stands for heavy-flavour, CO for photon conversion and LF for light-flavour. PassOR corresponds to leptons passing the overlap removal.

the Matrix Method are a linear combination of the different sources, given by

$$f_{total}(p_{\text{T}}) = \sum_i f_i(p_{\text{T}}) w_i(p_{\text{T}}), \tag{105}$$

where i runs over the different FNP sources and f_i is the corresponding fake rate for that source. The regions defined to extract the fake rates for each source are defined in Table 14. The weight, w_i, reflects the relative amount of each FNP lepton source, extracted from a signal-like region. The real efficiencies are calculated using MC in the same signal-like control regions.

The single lepton triggers used in the analysis include requirements on the identification quality (loose, medium or tight) and/or isolation of the lepton. When the trigger requirements are harder or similar to the loose lepton definition discussed above, it can lead to a bias in the fake rates and real efficiencies for the leptons being matched[9] to any of these triggers. If a lepton is matched to a trigger including both identification and isolation requirements it will have a lower fake rate and higher real efficiency than a lepton which is not matched to a trigger. In order to avoid this, the triggers are grouped depending on the quality requirement in Table 15. The unbiased fake rates and real efficiencies used in the analysis are shown in Figures 49 and 50.

[9]It is called trigger matched lepton when the lepton that triggered the event is the one used to calculate the efficiency.

iso (↓), ID (→)	lhtight	lhmedium	lhloose	no
medium	-	-	-	mu26_ivarmedium
i(var)loose	e24_lhtight_nod0 _ivarloose, e26_lhtight_nod0 _ivarloose	-	-	mu20_iloose
no	-	e60_lhmedium_nod0 e24_lhmedium	e120_lhloose, e140_lhloose_nod0	mu50

Table 15: The grouping of the triggers with respect to their requirement on isolation and ID. The triggers are grouped into four different categories as illustrated by the different colors.

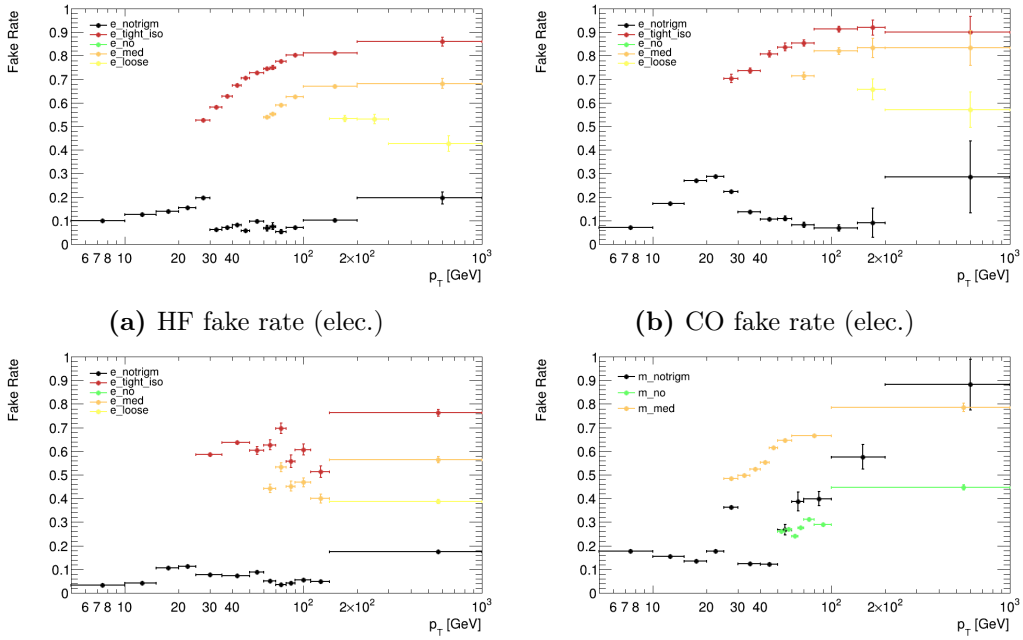

(a) HF fake rate (elec.)

(b) CO fake rate (elec.)

(c) LF fake rate (elec.)

(d) HF fake rate (muons)

Figure 49: The fake rates used in the FNP estimates corresponding to the data collected in 2017. Heavy-flavour (a), conversion (b) and light-flavour (c) fake rates for electrons are shown, respectively. The HF fake rate for muons is shown in (d). Only the heavy-flavour component is considered for muons since it is the dominant one. The different marker colors correspond to different trigger groups as defined in Table 15.

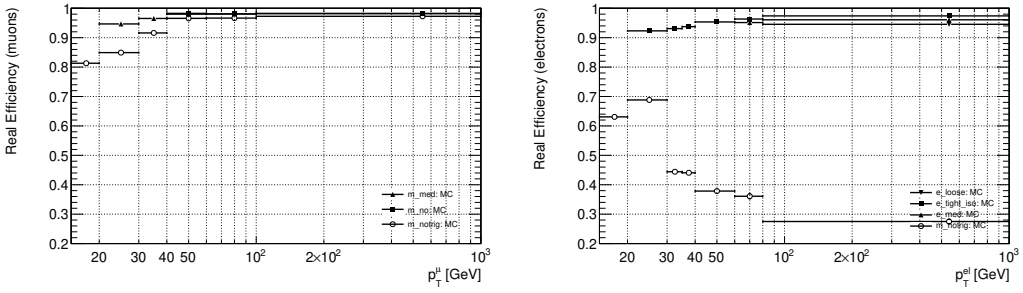

(a) Electrons **(b)** Muons

Figure 50: The real efficiencies used in the FNP estimates corresponding to the data collected in 2017. The different markers correspond to different trigger groups as defined in Table 15.

6.4.1 Validation of the FNP lepton estimate

In order to validate the fake leptons estimate, we consider the already defined SRs but requiring same-sign leptons, enriching significantly the FNP lepton contribution. However, a total of only 3 and 5 data events are found in the 0-jet and 1-jet same-sign SRs, respectively, which complicates the interpretation of the modelling. Therefore, a looser selection is considered, where the cuts on E_T^{miss}significance, $p_{\text{T,boost}}^{\ell\ell}$ and $\cos\theta_{\ell\ell}^{*}$ were relaxed, obtaining the SRlooseSS-0j and SRlooseSS-1j regions defined in Table 16. The m_{T2}^{100} variable with the binning used in the analysis is depicted in Figure 51 for SRlooseSS-0j and SRlooseSS-1j. Overall, we observe good modelling of the FNP leptons, except for the 4th and 7th m_{T2}^{100} bins in the SRlooseSS-1j, where an overestimation and underestimation of the fake leptons is seen. Since both deviations are not statistically significant ($< 2\sigma$ when considering all uncertainties), the method is considered validated.

Variable	SRlooseSS-0j	SRSS-0j	SRlooseSS-1j	SRSS-1j
E_T^{miss}significance	> 5	> 7	> 5	> 7
$p_{\text{T,boost}}^{\ell\ell}$	< 30 GeV	< 5 GeV	–	–
$\lvert\cos\theta_{\ell\ell}^{*}\rvert$	< 0.4	< 0.2	< 0.4	< 0.2

Table 16: Definition of the regions used in this section to validate the FNP estimate. In the loose region definition, only the cuts that are different from the usual sleptons SR are shown. The cuts for the usual SRs are shown for comparison.

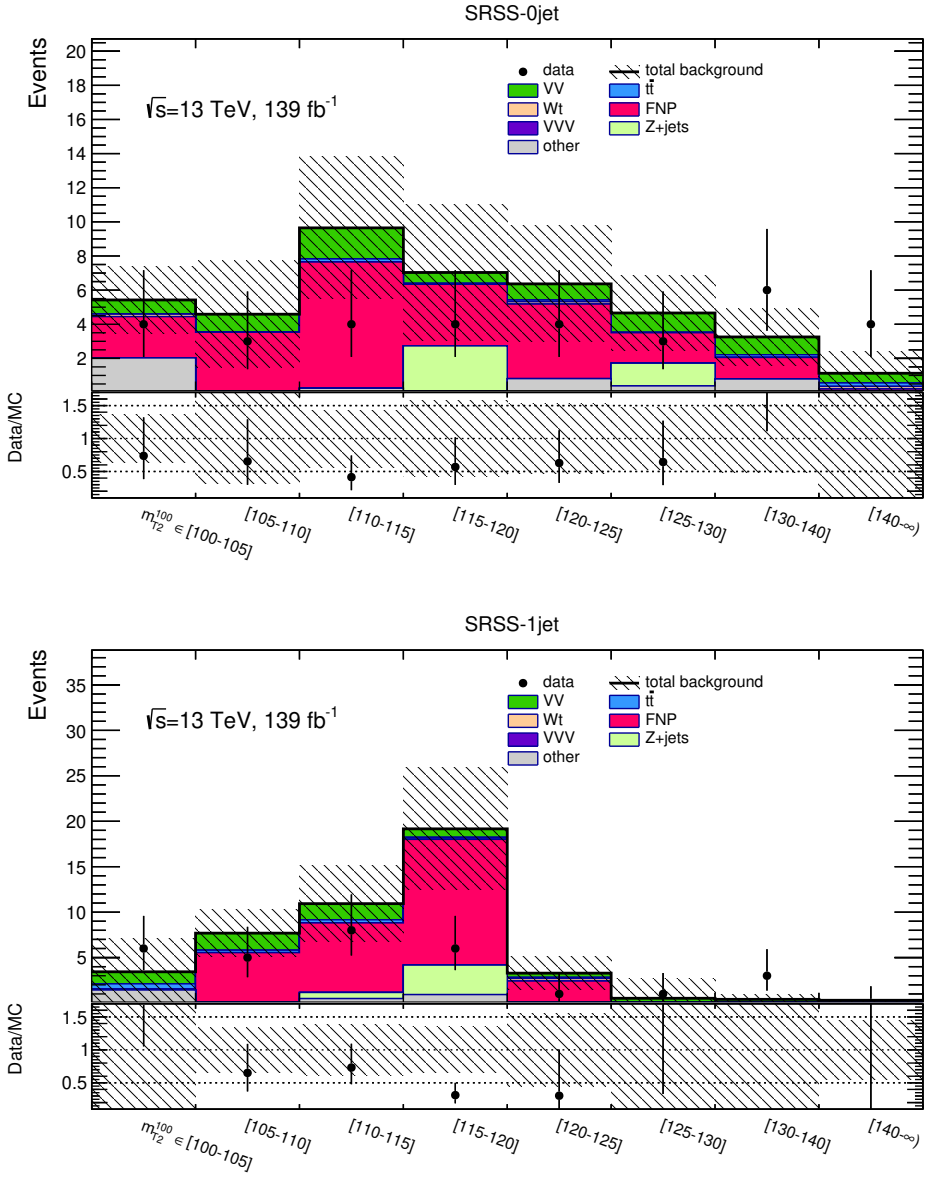

Figure 51: Data and MC comparison in the SRlooseSS-0j (top) and SRlooseSS-1j (bottom) region, as defined in Table 16. Statistical and systematic uncertainties are considered for the FNP estimate (red), whereas only statistical uncertainties are included for the other backgrounds.

6.5 Flavour symmetric background estimation

Flavour symmetric backgrounds (i.e. $WW, t\bar{t}, Wt$ and $Z(\rightarrow \tau\tau)$) produce SF and DF leptons in the final state with equal probabilities. The slepton signal, however, only generates SF leptons in the final state. We can therefore use the DF events from data after requiring the SR cuts in order to predict the flavour symmetric (FS) backgrounds in the SF channel.
In principle, one could simply count the number of DF events in the SR to obtain the flavour symmetric background events in the SF channel. This, however, is only true at generator level. The particles are identified by a detector, and since electrons and muons have different identification, isolation, reconstruction and trigger efficiencies, these differences have to be accounted for. Therefore, in order to extrapolate the count of DF events to the SF channel, efficiency corrections have to be applied.
Corrections are calculated using event-by-event weights (Section 6.5) and cross checked with an alternative method using transfer factors (Appendix E). This is done to avoid any bias of the regions used to obtain the corrections discussed below, and also serves as a good check in the SRs. The nominal method is described in Section 6.5. Less relevant backgrounds, which include: VVV, ZZ, WZ, Z, are estimated directly from MC predictions in the SRs.
The diboson process requires special attention here: since in the MC samples the diboson processes are all mixed (WW, WZ, ZZ), and not all of them are flavour symmetric, the sample requires special treatment. In fact, only the WW and the WZ (3-lepton event where one lepton from the Z decay is lost) are background symmetric. We have then the following cases

- $VV(\text{SF}) = WW + ZZ + WZ(\text{lepton from Z lost}) + WZ(\text{lepton from W lost})$,
- $VV(\text{DF}) = WW + WZ(\text{lepton from Z lost})$,

thus, in order to disentangle the ZZ and WZ, in what follows, we calculate

$$VV(\text{SF}) - VV(\text{DF}) = ZZ + WZ(\text{lepton from W lost}). \tag{106}$$

Efficiency correction method

This technique consists in reweighting, on an event-by-event basis, for the reconstruction, isolation, identification and trigger efficiencies. The number of expected events

$N_{SF}^{expected}$ using the DF events N_{DF} is given by[10]

$$\begin{aligned} N_{ee}^{expected} &= 0.5 \times \frac{1}{\kappa} \times \alpha \times N_{DF}, \\ N_{\mu\mu}^{expected} &= 0.5 \times \kappa \times \alpha \times N_{DF}, \\ N_{SF}^{expected} &= 0.5 \times \left(\kappa + \frac{1}{\kappa}\right) \times \alpha \times N_{DF}, \end{aligned} \tag{107}$$

where the factor 0.5 assumes that production rate of the DF events is twice the one for dimuon and dielectron. The κ and α factors take into account reconstruction and trigger efficiencies, respectively. These factors can be written as

$$\begin{aligned} \kappa &= \sqrt{\frac{N_{\mu^+\mu^-}}{N_{e^+e^-}}} \\ \alpha &= \frac{\sqrt{\epsilon_{\mu\mu}^{trig}\epsilon_{ee}^{trig}}}{\epsilon_{e\mu}^{trig}} \end{aligned} \tag{108}$$

where $N_{\mu^+\mu^-}$ and $N_{e^+e^-}$ are the number of dielectron and dimuon events, respectively, while $\epsilon_{\mu\mu}^{trig}, \epsilon_{ee}^{trig}$ and $\epsilon_{e\mu}^{trig}$ are the efficiencies of triggering dimuon, dielectron and muon-electron events with the trigger selection described in Section 6.1.1.
Since the lepton reconstruction and trigger efficiencies in general depend on the η of the lepton, κ and α factors have been calculated both inclusively and in different η regions of the detector. Furthermore, a dependency of κ was observed on the variables used in the analysis, while no dependency on these variables was observed for α. Finally, κ was parameterized as a function of $p_T^{\ell_1}$. [11]

The correction factor κ is computed in a control region ($\mathrm{CR}^{\mathrm{eff}}$). It is defined in the following way:

- E_T^{miss}significance cut relaxed to E_T^{miss}significance > 6;
- $p_T^{\ell_1}$ cut is also relaxed to 30 GeV in order to capture some possible shape dependency of the κ and α factors;
- $\cos\theta_{\ell\ell}^*$ cut is inverted, this enriches the control sample in diboson events, i.e. $|\cos\theta_{\ell\ell}^*| > 0.2$ and makes $\mathrm{CR}^{\mathrm{eff}}$ orthogonal to the SR.

The selection criteria are listed in Table 17.
The reason for which we computed the correction factors in a tighter region than the

[10] The derivation of the formula is detailed in Appendix F.
[11] A check was done to see the impact when using the sub-leading lepton p_T, observing differences $<$ 1% in the estimate of the flavour symmetric background in the SR.

preselection, with background purities similar to that in the SR, is because different reconstruction efficiencies were observed for different backgrounds. This is shown in Figure 52, where we see that for the $t\bar{t}$ and diboson processes similar $N_{\mu\mu}/N_{ee}$ ratios are observed, but for $Z+$jets the muon reconstruction efficiency is larger. This can be due to leptons with different p_{T}'s falling in different pseudorapidity regions for different MC samples, or just MC mismodelling in one of the channels (dieletron or dimuon). The Standard Model background modelling in the Control Region

Variable	Cut
n_{jet-20}	< 2
$N_{\text{OS leptons}}$	$= 2$
$p_T^{\ell_1}$	> 30 GeV
$p_T^{\ell_2}$	> 9 GeV
E_T^{miss}significance	> 6
$\lvert\cos\theta^*_{\ell\ell}\rvert$	> 0.2

Table 17: Selection criteria in $\mathrm{CR}^{\mathrm{eff}}$ used to estimate κ.

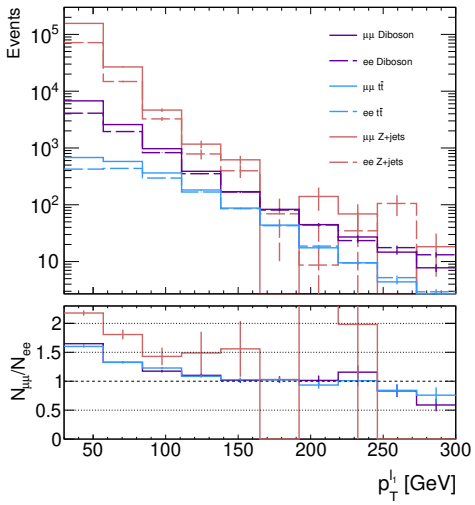

Figure 52: Number of dimuon (solid) and dielectron (dashed) events at preselection level for different backgrounds as a function of $p_T^{\ell_1}$. The bottom frame shows the ratio between the dimuon and dielectron events.

defined to estimate κ and α is investigated looking at the distributions of the relevant variables of the analysis after the selection criteria in Table 17. These distributions are shown in Appendix G, Figures 78, 79 and 80 for the ee, $\mu\mu$ and DF channels,

respectively.

The inclusive κ factor values for MC and data are reported in Table 18. Since the reconstruction efficiencies can depend on the pseudorapidity region where the leptons reach the detector, we also compute κ in different η regions: both leptons in the barrel $|\eta| < 1.05$ (bar-bar), both in the endcap regions $|\eta| > 1.05$ (end-end), one of the leptons in the barrel and the other in the endcap (bar-end) and when at least one of the leptons falls in $|\eta| < 0.1$ (central). As expected, we observe that in the barrel regions ($|\eta| < 1.05$) the κ factor tends to be lower due to the lack of muon coverage in this region. On the other hand, due to higher muon reconstruction efficiency in the end-end region, κ increases. In Figure 53 the κ efficiency correction factors as function of $p_T^{\ell_1}$ are shown. As κ can be process dependent, since the topology of the backgrounds is different, this could lead to different reconstruction efficiencies. For this reason, κ is shown for all the background symmetric[12] ($VV + t\bar{t} + Wt$) processes separately and summed together. A clear dependency on the $p_T^{\ell_1}$ is observed for both data and MC[13]. To account for this dependency, data values are fitted to the function:

$$\kappa(p_T^{\ell_1}) = b + \frac{a}{p_T^{\ell_1}}. \tag{109}$$

The parameter b determines the asymptotic behaviour of the function at large $p_T^{\ell_1}$, where we see that the distribution starts to flatten out. Actually, this parameter is the one we are interested in since our SRs require $p_T^{\ell_1} > 140$ GeV and $p_T^{\ell_1} > 100$ GeV, for SR-0jet and SR-1jet, respectively. Differences in data and MC w.r.t the fitted function are taken as input to the final uncertainty on the method.

	MC (FS)	Data
κ	1.1576 ± 0.0014	1.1942 ± 0.0043
$\kappa^{central}$	0.8509 ± 0.0042	0.852 ± 0.013
$\kappa^{bar-bar}$	1.0352 ± 0.0029	1.0655 ± 0.0089
$\kappa^{end-end}$	1.38526 ± 0.0042	1.440 ± 0.010
$\kappa^{bar-end}$	1.1947 ± 0.0020	1.2198 ± 0.0061

Table 18: Global reconstruction efficiencies κ calculated inclusively and in different η regions of the detector for MC (FS) and data. The uncertainties correspond to the statistical component only.

[12] We omit $Z(\rightarrow \tau\tau) +$ jets in the calculation due to the low contribution of this background

[13] Some dependency is also observed as a function of $p_T^{\ell_2}$, but we have checked the impact of reweighting with $p_T^{\ell_1}$ and $p_T^{\ell_2}$ and the difference in the SR is below 1%

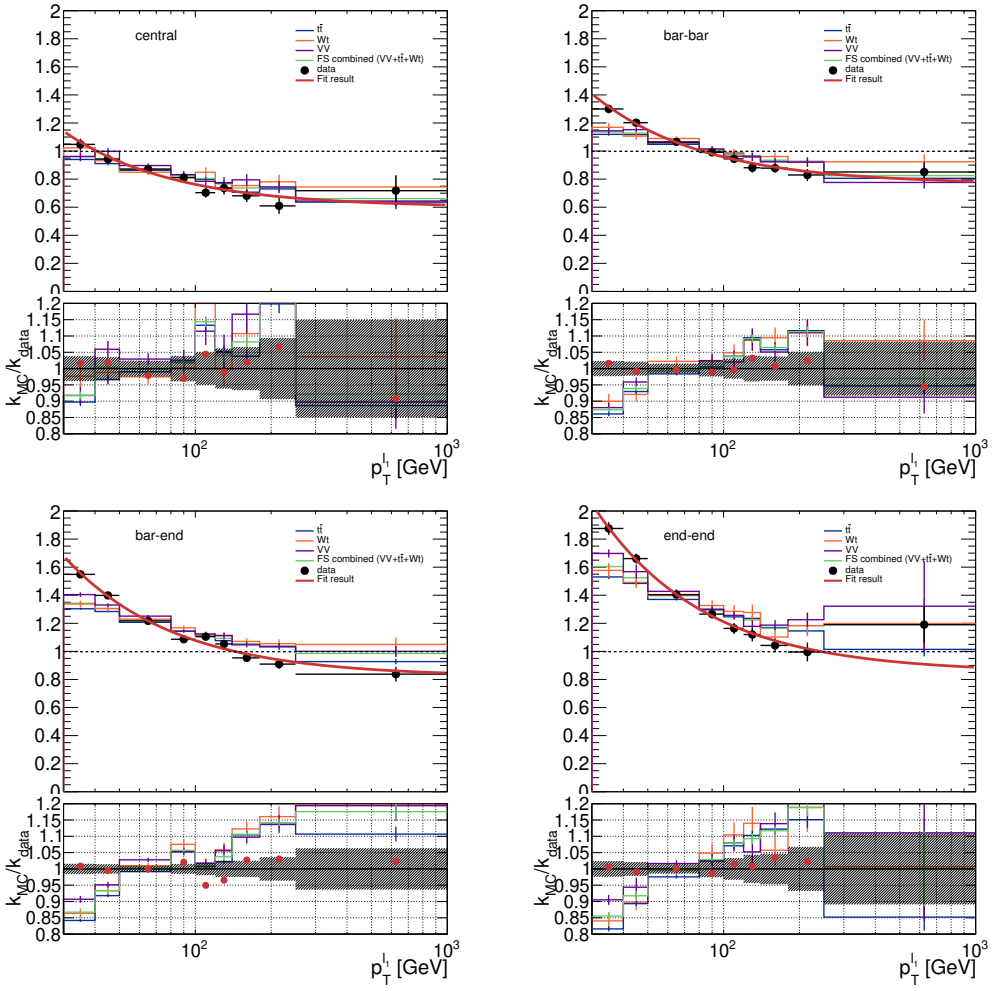

Figure 53: κ efficiency correction factors as a function of the leading lepton transverse momentum, $p_T^{\ell_1}$ for data (points) and MC (coloured lines) in the different $|\eta|$ regions: central (top left), bar-bar (top right), bar-end (bottom left) and end-end (bottom right). The MC correction factors are also shown for the different flavour symmetric backgrounds: $t\bar{t}$ (blue), single top (orange), diboson (purple). The fit on $\kappa(p_T^{\ell_1})$ is performed using all the data points. The bottom frames show the MC to data ratio. The values of the fitted function in the center of the bins are also shown (red points) for κ. The uncertainties are statistical only.

Before calculating α, first we have to compute the trigger efficiencies for the three channels: $ee, \mu\mu, e\mu$. Since both data and MC samples used in the analysis have already satisfied some trigger requirement (they have passed a lepton trigger) we also compute the trigger efficiencies using a different data sample skimmed using a logical

OR between MET and lepton triggers (lepORmet) to check any kind of bias. To this end, we compute the lepton trigger efficiencies defining first a set of events that pass the MET trigger to obtain unbiased trigger efficiencies. The lepton trigger efficiency is then

$$\varepsilon^{trig} = \frac{N^{\text{METtrig and singlepTrig}}}{N^{\text{METtrig}}}, \tag{110}$$

where the denominator corresponds to the number of events passing the MET trigger and the numerator passing both the MET and single lepton triggers. The region to calculate the trigger efficiencies asks for the same selection as at preselection level in Table 9, but removing the jet requirement, allowing at least 1 jet to enter the event (the b-jet veto is also removed). We also ask for $E_T^{\text{miss}} > 230$ GeV and $p_T^{\ell_1} > 30$ GeV to ensure that we are in the efficiency plateau of the E_T^{miss} and lepton triggers, respectively. A summary of the selection used to calculate $\varepsilon_{ee}^{trig}, \varepsilon_{\mu\mu}^{trig}, \varepsilon_{e\mu}^{trig}$ can be found in Table 19. The global trigger efficiencies obtained can be found in Table 20 for data and MC[14]. The global trigger efficiencies between data and MC agree in the different lepton channels. In Figure 54, the trigger efficiencies for data and MC for the different channels are shown. Once again similar behaviour is observed for both. No turn on curve is observed since the lepton cut at 30 GeV ensures that we are in the efficiency plateau region. The MC/data ratio is also reported in Figure 55, where a good agreement within statistical uncertainties is observed in the whole $p_T^{\ell_1}$ range. Finally, in Figure 56 the α values are shown for both data and MC. It is seen that the differences between data and MC stay around 1%, in agreement again within statistical uncertainties.

Now, in Figure 57 the trigger efficiency and α factors obtained with the, a priori, biased data sample and the unbiased one (lepORmet) are compared. We observe the expectation: the biased sample trigger efficiencies are about 1% to 6% greater than for the unbiased one. This, as explained before, comes from the fact that the nominal samples are already passing some lepton trigger requirement during the skimming. The effect on α is lower, being about 1 to 2% across $p_T^{\ell_1}$ range. The nominal α value chosen for the analysis is the one obtained with the unbiased samples.

[14]The uncertainties for MC were calculated using the normal approximation propagation (68% confidence level). The uncertainties for data were calculated using Clopper-Pearson interval (68% confidence level), where efficiencies are treated as binomial distributions. This choice comes from the fact that MC events are weighted (and therefore does not follow a binomial distribution) whereas data events are not.

Variable	Cut
n_{jet-20}	< 2
$N_{\text{OS SF leptons}}$	$= 2$
$p_T^{\ell_1}$	> 30 GeV
$p_T^{\ell_2}$	> 20 GeV
E_T^{miss}	> 230
$m_{\ell\ell}$	> 11 GeV
$\lvert m_{\ell\ell} - m_Z \rvert$	> 15 GeV

Table 19: Selections used to calculate the trigger efficiencies $\varepsilon_{ee}^{trig}, \varepsilon_{\mu\mu}^{trig}, \varepsilon_{e\mu}^{trig}$.

	MC	Data	Unbiased data
ε_{ee}^{trig}	0.9915 ± 0.0019	0.9945 ± 0.0039	0.9797 ± 0.0041
$\varepsilon_{\mu\mu}^{trig}$	0.9791 ± 0.0027	0.9803 ± 0.0080	0.9119 ± 0.0086
$\varepsilon_{e\mu}^{trig}$	0.9879 ± 0.0012	0.9865 ± 0.0045	0.9571 ± 0.0041
α	0.9973 ± 0.0021	$1.0008^{+0.0062}_{-0.0093}$	$0.9876^{+0.0066}_{-0.0074}$
$\alpha^{bar-bar}$	0.9968 ± 0.0035	$1.006^{+0.007}_{-0.016}$	$0.962^{+0.012}_{-0.013}$
$\alpha^{end-end}$	0.9902 ± 0.0048	$1.010^{+0.018}_{-0.037}$	$1.01088^{+0.015}_{-0.020}$
$\alpha^{bar-end}$	0.9996 ± 0.0031	$0.992^{+0.010}_{-0.018}$	$1.001^{+0.0096}_{-0.011}$

Table 20: Global trigger efficiencies calculated in data and in MC. The corresponding α values are also shown. α is also reported as found for different η regions. The uncertainties are statistical only. The nominal value corresponds to the one obtained with the unbiased data.

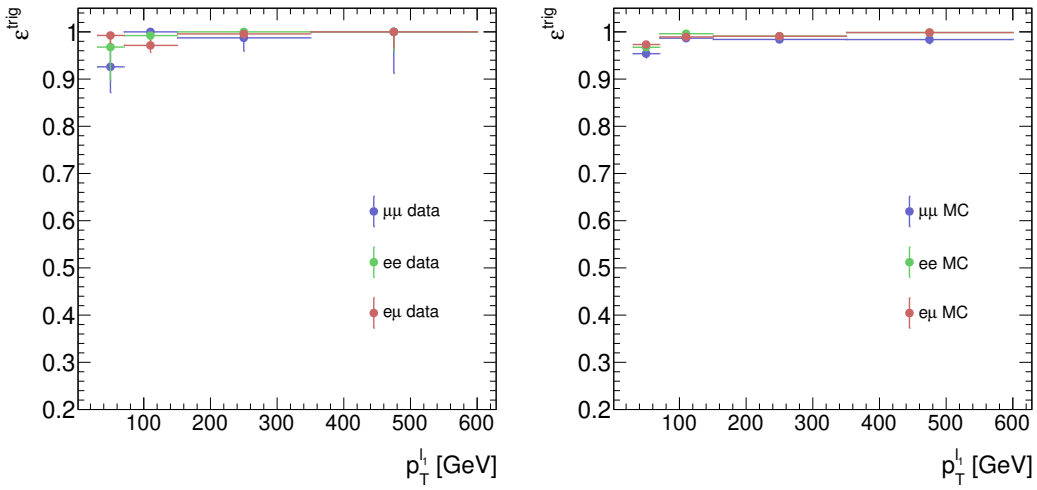

Figure 54: Trigger efficiencies for data (left) and MC (right) as a function of $p_T^{\ell_1}$ in the three different channels: $\mu\mu$ (blue), ee (green), $e\mu$ (red). MC includes: $t\bar{t}, Wt, Z(\to \tau\tau) + \text{jets}, VV, VVV$.

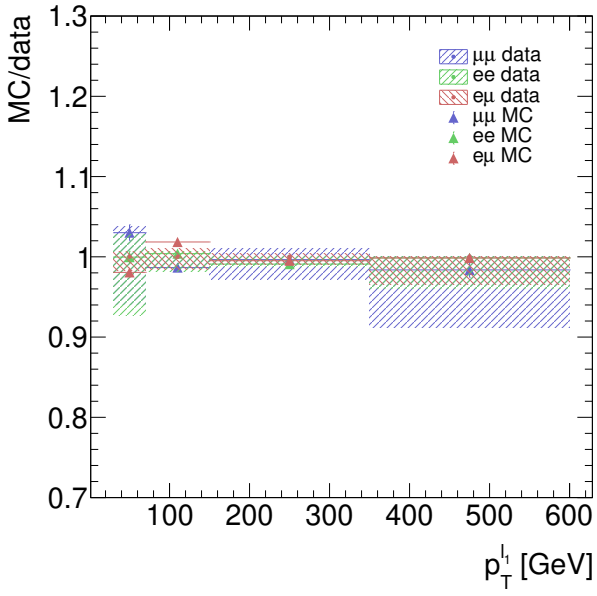

Figure 55: MC trigger efficiencies normalised to the data trigger efficiencies for $\mu\mu$ (blue), ee (green), $e\mu$ (red). MC includes: $t\bar{t}, Wt, Z(\to \tau\tau) + \text{jets}, VV, VVV$. The uncertainties are statistical only.

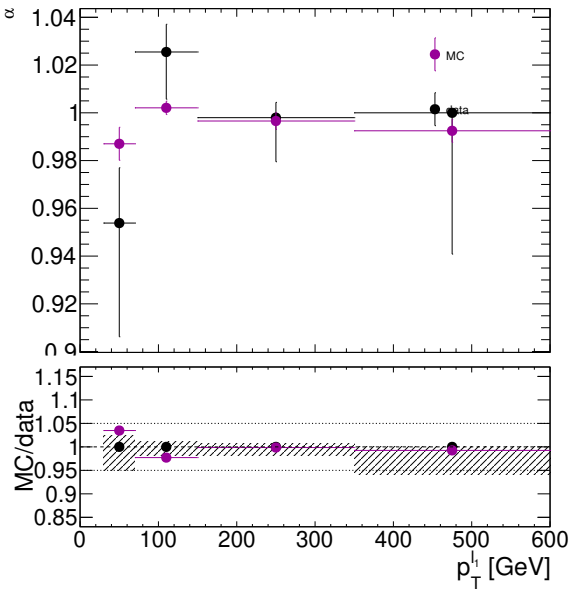

Figure 56: Trigger efficiency correction α calculated for data (black) and MC (purple). MC includes: $t\bar{t}, Wt, Z(\rightarrow \tau\tau) + \text{jets}, VV, VVV$. The bottom frame shows the α values normalised to data. The uncertainties are statistical only.

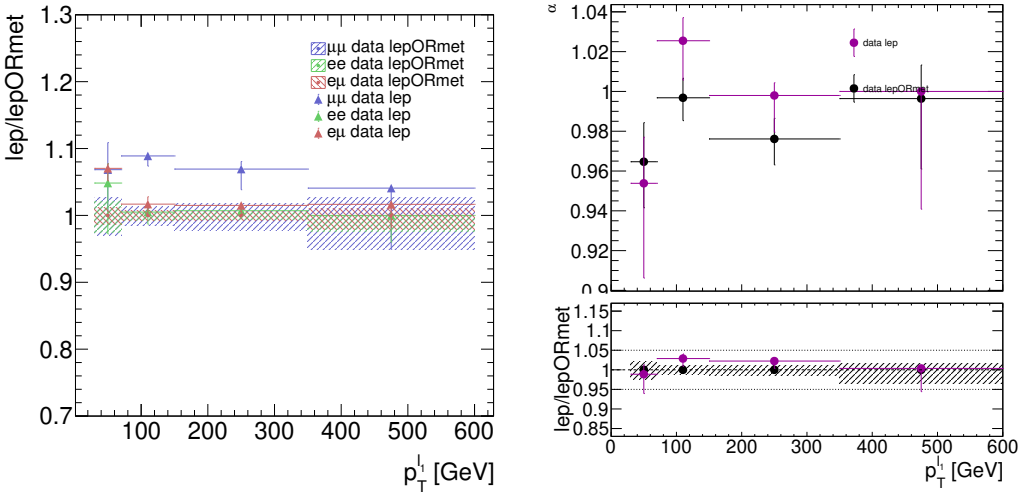

Figure 57: Left: biased data trigger efficiencies normalised to the unbiased data trigger efficiencies for $\mu\mu$ (blue), ee (green), $e\mu$ (red). Right: α factor calculated with biased (purple) and unbiased (black) data. The bottom panel shows the α values normalised to unbiased data. The uncertainties are statistical only.

6.5.1 Validation of flavour symmetric background estimation

In order to validate the technique described above, in the following we apply the κ and α efficiency correction factors as in Equation 107. First, it was checked that the shape of the relevant kinematic distributions for the dielectron and dimuon channels in $\mathrm{CR}^{\mathrm{eff}}$ was well modelled. Some of the distributions are shown in Appendix H. To validate the method, a validation region (VR) is used. The VRs are defined in the same way as the SRs but inverting the the $\cos\theta^*_{\ell\ell}$ cut. A summary of the VR/SR selections are shown in Tables 21 and 22. Since the final fit is performed in the m_{T2}^{100} variable, this variable requires special emphasis. Electron and muon channels are combined and the m_{T2}^{100} distributions is shown in Figure 58, where overall a good data/MC agreement is observed in all m_{T2}^{100} bins[15]. Additional tables with the yields in the VRs in each bin can be checked in Appendix I.

Variable	VR	SR
n_{jet-20}	$= 0$	$= 0$
$n_{bjet-20}$	$= 0$	$= 0$
$N_{\text{OS SF leptons}}$	$= 2$	$= 2$
$p_T^{\ell_1}$	> 140 GeV	> 140 GeV
$p_T^{\ell_2}$	> 20 GeV	> 20 GeV
E_T^{miss}significance	> 7	> 7
$m_{\ell\ell}$	> 11 GeV	> 11 GeV
$\lvert m_{\ell\ell} - m_Z\rvert$	> 15 GeV	> 15 GeV
$p^{\ell\ell}_{\text{T,boost}}$	< 5 GeV	< 5 GeV
$\lvert\cos\theta^*_{\ell\ell}\rvert$	> 0.2	< 0.2
$\Delta\phi_{\ell,\ell}$	> 2.2	> 2.2
$\Delta\phi_{E_T^{\text{miss}},\ell_1}$	> 2.2	> 2.2

Table 21: VR/SR definitions in the 0-jet region.

For completeness, the data DF events that are used for the final FS estimate in the SRs are shown in Figure 59. The distributions in the DF channel for the rest of the variables used in the analysis can be checked in Appendix G.2.

[15] Exception is the first m_{T2}^{100} bin in the VR-0jet, where the significance of the data to MC difference is about 1.4σ.

Variable	Cut	
n_{jet-20}	$= 1$	$= 1$
$n_{bjet-20}$	$= 0$	$= 0$
$N_{\text{OS SF leptons}}$	$= 2$	$= 2$
$p_T^{\ell_1}$	> 100 GeV	> 100 GeV
$p_T^{\ell_2}$	> 50 GeV	> 50 GeV
E_T^{miss}significance	> 7	> 7
$m_{\ell\ell}$	> 60 GeV	> 60 GeV
$\lvert m_{\ell\ell} - m_Z \rvert$	> 15 GeV	> 15 GeV
$\lvert \cos\theta^*_{\ell\ell} \rvert$	> 0.1	< 0.1
$\Delta\phi_{\ell,\ell}$	> 2.8	> 2.8

Table 22: VR/SR definitions in the 1-jet region.

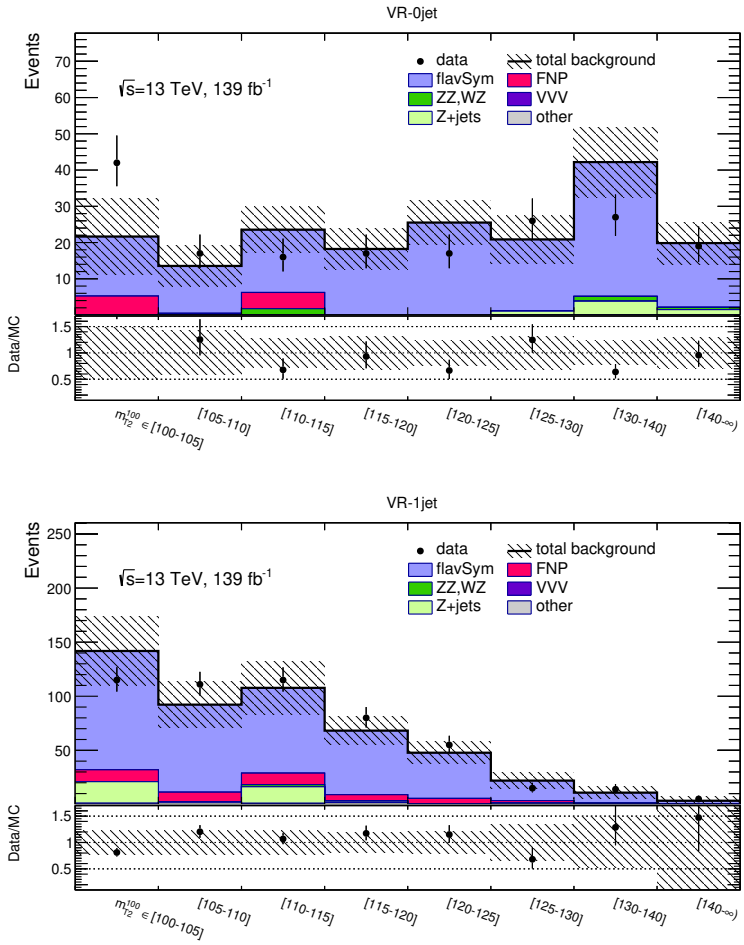

Figure 58: m_{T2}^{100} data and MC comparison in the VR-0jet (top) and VR-1jet (bottom) as defined in Tables 21 and 22. Uncertainties in the background combine statistical and systematic uncertainties are considered.

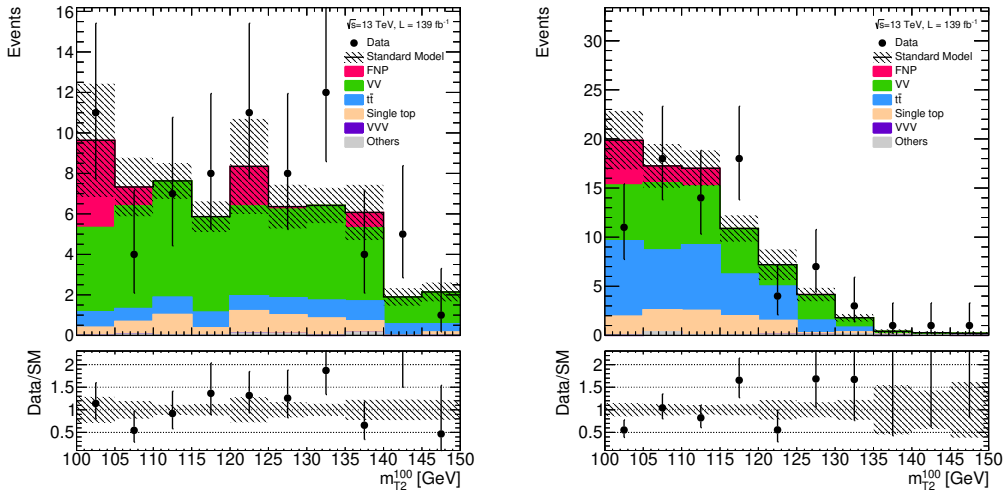

(a) m_{T2}^{100} **(b)** m_{T2}^{100}

Figure 59: m_{T2}^{100} data and MC distributions for the DF channel in SR-0jet (left) and SR-1jet (right). This data is used in the final estimate of the flavour symmetric background. Only statistical uncertainties are shown.

6.6 Systematic uncertainties

Several systematic uncertainties are considered for the SM background predictions. Since the SM backgrounds are estimated with different techniques, they are subject to different uncertainties. In this section all the systematic uncertainties considered are summarised.

Data-driven flavour symmetric. Different sources of systematic uncertainties arising from the reweighting method are considered:

- Uncertainty on α. Difference between the data and MC global trigger efficiencies as a systematic uncertainty. This is then combined with their statistical uncertainty and propagated to α, assuming they are uncorrelated among flavour channels.

- Uncertainty on κ. Difference between the global κ factors calculated in the different $|\eta|$ regions to cover small data-MC deviations.

- Choice of the reweighting variable. The backgrounds yields have been computed using $p_T^{\ell_2}$ as the reweighing variable and found differences below 1%.

- Uncertainty on the fit function $\kappa(p_T^{\ell_1})$. The fit parameters (a, b) are varied by their uncertainty keeping the other parameter fixed. After the variations, the background yield changes by Δ_1, Δ_2. The variance is then given by

$$\sigma = \mathbf{\Delta}^T C \mathbf{\Delta} = \begin{pmatrix} \Delta_1 \Delta_2 \end{pmatrix} \begin{pmatrix} 1 & C_{12} \\ C_{12} & 1 \end{pmatrix} \begin{pmatrix} \Delta_1 \\ \Delta_2 \end{pmatrix}, \tag{111}$$

Where C is the covariance matrix given by the fit, and C_{12} are the off-diagonal values of C. The uncertainty on the predicted yields is then the square root of the variance. All the systematic uncertainties listed above range from 1% to 2% in the final yield estimate. In order to also cover data-MC mismodeling in the validation regions used to validate the flavour symmetric estimate (shown in Section 6.5.1), the total systematic uncertainty applied to the final estimate is 10%. This 10% uncertainty applied corresponds to the leading systematic uncertainty of the analysis.
An additional uncertainty is considered from the subtraction of non-flavour symmetric backgrounds from the DF sample used to estimate the FS background. The dominant subtracted background corresponds to the FNP background.

FNP systematic uncertainties. FNP leptons are subject to the following uncertainties:

- MC scale factors. The light-flavour fake rate for electrons and the real efficiencies are calculated from MC. Trigger, identification and reconstruction scale factors[16] are used to quantify this uncertainty.

- Subtraction of real leptons. For the heavy-flavored fake rate, real leptons, taken from MC, are used to subtract the real lepton contamination in the control regions. An uncertainty is added to the subtraction procedure by scaling the MC up and down with 10%.

- Uncertainties on the weights. As explained in Section 6.4, the weights are obtained in signal-like regions. Two types of uncertainties are considered

  1. a 1σ variation on the relative fraction of each fake component: heavy-flavour, light-flavour and photon conversion.

  2. if a given event passes more than one signal-region like control region used to extract the weights, the maximum and minimum weights for each fake component is included in the uncertainty.

- Statistical Uncertainties. The 1σ statistical uncertainty on the fake rates and real efficiencies are also considered for the final FNP estimate uncertainty.

Experimental systematic uncertainties. For the background estimated directly from MC, the following systematic uncertainties are considered:

- Uncertainty on the jet energy scale and resolution. Jet uncertainties are derived as a function of the p_{T} and η of the jet, as well as pile-up conditions and the jet flavour composition of the selected sample [140].

- Uncertainty on the lepton energy scale, energy resolution, isolation and identification efficiency [66, 141].

- Uncertainty to cover differences in the modelling of trigger efficiencies between data and simulation.

- Uncertainty on the E_T^{miss} from energy deposits not associated with reconstructed objects (resolution of the E_T^{miss} soft term) [142].

[16] Scale factors correspond to the efficiency ratio calculated in data and MC.

- Uncertainty due to the b-tagging efficiency and mistag probability.
- Uncertainty on the integrated luminosity (1.7%).
- Uncertainty on the modelling of the pile-up. The MC events are weighted to match the pile-up distribution observed in the data.
- Uncertainty to account for the residual contamination from pile-up jets after pile-up suppression (JVT uncertainty).

Theory systematic uncertainties. Systematic uncertainties due to limitations in theoretical models are estimated by applying to the renormalization, factorization scales factor two rescalings around their nominal value. Uncertainties on the choice of PDF set are also considered. Uncertainties due to the resummation scale and matching scale between the matrix elements and parton showers are estimated applying factor two rescalings to the corresponding parameters in SHERPA . These theory uncertainties are only applied to the diboson (ZZ, WZ) and Z+jets samples, but are minor and not the limiting factor in the analysis.
The main systematic uncertainties, per m_{T2}^{100} bin, are shown in Tables 23 and 24 for SR-0jet and SR-1jet, respectively.

$m_{\mathrm{T2}}^{100} \in$	$[100-105]$	$[105-110]$	$[110-115]$	$[115-120]$	$[120-125]$	$[125-130]$	$[130-140]$	$[140-\infty)$
FS syst.	4%	10%	8%	8%	10%	10%	9%	7%
FNP syst.	16%	$< 1\%$	7%	4%	$< 1\%$	$< 1\%$	6%	$< 1\%$
Subtraction syst.	6%	5%	$< 1\%$	$< 1\%$	11%	$< 1\%$	$< 1\%$	$< 1\%$
E_T^{miss} soft-term	$< 1\%$	$< 1\%$	12%	2%	$< 1\%$	$< 1\%$	$< 1\%$	4%
ZZ parton match.	$< 1\%$	$< 1\%$	$< 1\%$	3%	$< 1\%$	$< 1\%$	$< 1\%$	7%
ZZ resummation	$< 1\%$	$< 1\%$	$< 1\%$	1%	$< 1\%$	$< 1\%$	$< 1\%$	3%
ZZ PDF	$< 1\%$	$< 1\%$	$< 1\%$	1%	$< 1\%$	$< 1\%$	$< 1\%$	2%

Table 23: Dominant systematic uncertainties contributing to each m_{T2}^{100} bin in SR-0jet. Systematic uncertainties not shown are negligible and have no impact in the analysis. Note that the individual uncertainties can be correlated, and do not necessarily add up quadratically to the total background uncertainty. The percentages show the size of the uncertainty relative to the total expected background.

$m_{\mathrm{T2}}^{100} \in$	$[100-105]$	$[105-110]$	$[110-115]$	$[115-120]$	$[120-125]$	$[125-130]$	$[130-140]$	$[140-\infty)$
FS syst.	5%	10%	9%	8%	8%	10%	9%	9%
FNP syst.	4%	$< 1\%$	$< 1\%$	3%	$< 1\%$	$< 1\%$	$< 1\%$	$< 1\%$
Subtraction syst.	13%	8%	8%	$< 1\%$	$< 1\%$	$< 1\%$	$< 1\%$	$< 1\%$
E_T^{miss} soft-term	2%	$< 1\%$	6%	$< 1\%$	3%	$< 1\%$	$< 1\%$	1%

Table 24: Dominant systematic uncertainties contributing to each m_{T2}^{100} bin in SR-1jet. Systematic uncertainties not shown are negligible and have no impact in the analysis. Note that the individual uncertainties can be correlated, and do not necessarily add up quadratically to the total background uncertainty. The percentages show the size of the uncertainty relative to the total expected background.

6.7 Results and interpretation

The statistical interpretation of the final results is performed using the HistFitter framework [143], which uses a profile-likelihood-ratio statistical test [144] with the CL_s prescription [145]. A description of the statistical techniques are discussed in Appendix J.

A multi-bin fit as a function of m_{T2}^{100} is performed. The choice of the variable is motivated by the fact that different slepton signals have different endpoints in this variable. The binning chosen is $m_{T2}^{100} = [100, 105, 110, 115, 120, 125, 130, 140, \infty)$ GeV. The plots in Figure 60 show the graphical representation of the yields together with the significance of the difference between SM expectation and the observed data. Starting with the SR-0jet, the expected background overestimates the observed data in two m_{T2}^{100} bins, with a significance of about -2σ. These bins, however, are likely to be statistical fluctuations by looking at the Figures in Appendix G.3 (see Figure 83(e)), where the same distribution is shown but in this case the FS background prediction is taken directly from MC simulations. As the same behaviour is observed when using the data-driven and the MC predictions, it is concluded that the observed disagreement is most likely arising from statistical fluctuations of the data.

For the SR-1jet, two bins with excesses of about 1.5σ and one bin with an overestimation of the background (-3.5σ) are observed. In this case, to understand the behaviour, it is useful to look at the m_{T2}^{100} distribution in SRDF-1jet in Figure 59 (right), which is the DF data used to estimate the flavour symmetric background. It is observed that the discrepancies are strongly correlated with what looks like statistical fluctuations in the data DF channel. For completeness, the same cross-check as in the 0-jet case is performed using pure MC instead of the data-driven estimate for the flavour symmetric background (Figure 84(e)), where a similar behaviour with respect to the data-driven estimate is observed.

Therefore, for the largest fluctuation (-3.5σ), we have concluded that it is a combined result of an upward fluctuation in the DF background estimate and a downward fluctuation in the SF data. In Figure 59 (right) it is seen that there is an upward fluctuation of the DF data compared to the simulation by a factor of about 1.7 ± 0.4. However, even if the true FS background was lower by that factor, the background estimate in that bin would still be about 10, compared to a SF data count of 3. The discrepancy in this case would be reduced from -3.5σ to $\sim -1.5\sigma$. Additional tables with the yields per bin can be consulted in Appendix I.

Since no clear sign of new physics is observed, it is now useful to see if any slepton

Simplified Model can be excluded. Models with CL_s values lower than 0.05 are excluded at 95% confidence level. The exclusion limits, assuming mass-degenerate selectrons and smuons are shown in Figure 61 in the $\Delta m(\tilde{\ell}, \tilde{\chi}_1^0) - m_{\tilde{\ell}}$ plane, together with existing exclusion limits from other ATLAS analyses and from LEP experiments. It is observed that the present analysis is able to exclude mass splittings ranging from 30 GeV to about 60 GeV for $\tilde{\chi}_1^0$ masses ranging from 100 GeV to 200 GeV, where the limits coming from LEP experiments were still the world-leading constraints. This analysis has therefore been able to cover part of the existing gap between previous ATLAS slepton searches [117], [133]. With the increased amount of data that the ATLAS detector will record during the following years, together with the employment of more advanced optimisation techniques (e.g. multivariate analysis), larger slepton masses and broader mass splitting ranges will be probed. In fact, SUSY particle spectra compatible with the measured muon $g - 2$ has already been proven to be discoverable using deep neural networks in the HL-LHC and HE-LHC upgrades [146].

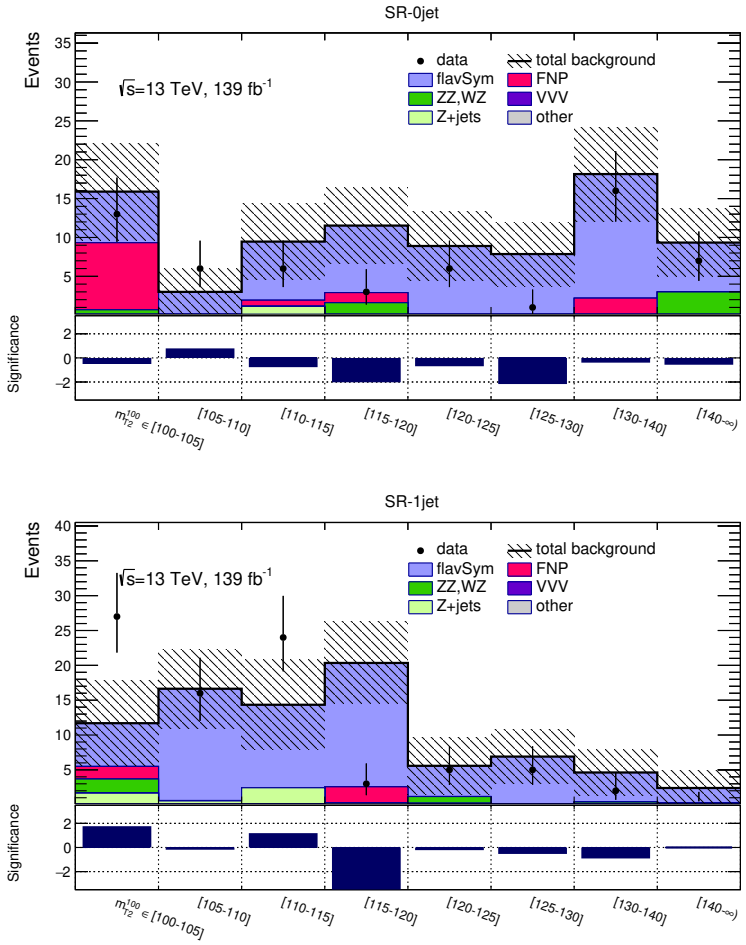

Figure 60: Observed data and expected background yields with systematic and statistical uncertainties included in the different m_{T2}^{100} bins. Top: SR-0jet. Bottom: SR-1jet. The dominant background (light blue) is obtained by extracting the data from the DF channel shown in Appendix G.2 and applying the efficiency corrections. The bottom frame shows the significance of the difference between the expected SM background and the observed data.

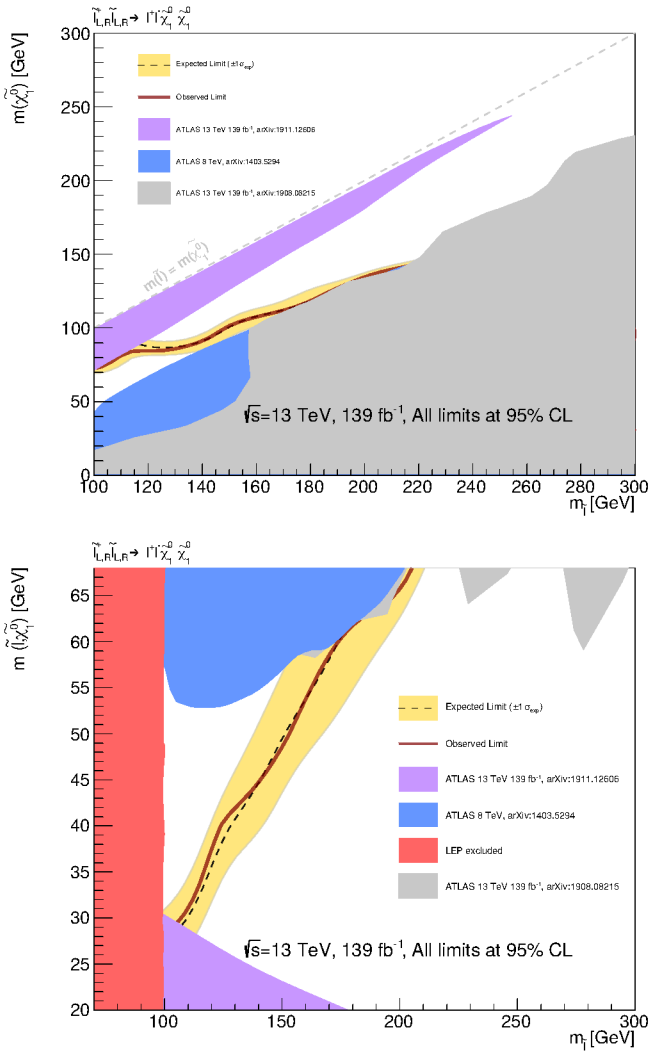

Figure 61: Expected 95% CL exclusion limit (black dashed line) with $\pm 1\sigma_{exp}$ (yellow band) from systematic and statistical uncertainties, and observed limits (red solid line). A multi-bin fit in m_{T2}^{100} including SR-0jet and SR-1jet is performed to obtain the presented limits. The limits are shown in the $m_{\tilde{\ell}}$-$m_{\tilde{\chi}_1^0}$ (top) and $\Delta m(\tilde{\ell}, \tilde{\chi}_1^0) - m_{\tilde{\ell}}$ (bottom) planes. The coloured regions represent observed limits from other analysis and/or experiments: [117] (gray), [133] (purple), [118] (blue), [138] (red).

Inclusive signal regions and model independent fit

In this section one-bin inclusive signal regions are considered. The fit performs a model independent hypothesis test, which includes a signal to be constrained by the observed data, to estimate potential contributions of Beyond the Standard Model phenomena. In order to quantify the compatibility of how the observed data is with the background-only hypothesis, the discovery p-values are calculated for each inclusive region. The signal regions are defined using the same list of cuts as of SR-0jet and SR-1jet, but now performing an inclusive selection using the m_{T2}^{100} variable,

- $m_{\mathrm{T2}}^{100} > 100,\ m_{\mathrm{T2}}^{100} > 110,\ m_{\mathrm{T2}}^{100} > 120,\ m_{\mathrm{T2}}^{100} > 130,\ m_{\mathrm{T2}}^{100} > 140.$

This gives ten inclusive regions in total. The CL_s prescription is used to set 95% CL limits on observed (S_{obs}^{95}) and expected (S_{exp}^{95}) number of signal events. Dividing S_{obs}^{95} over the integrated luminosity gives the limits on the visible cross section $\langle\epsilon\sigma\rangle_{\mathrm{obs}}^{95}$. The results for each inclusive SR is shown in Table 25.

Signal region	$\langle\epsilon\sigma\rangle^{95}_{\text{obs}}$[fb]	S^{95}_{obs}	S^{95}_{exp}	$p(s=0)$
$\text{SR}^{\text{0-jet}}_{m_{\text{T2}}^{100}\in[100,\infty)}$	0.12	16.8	$24.9^{+9.4}_{-7.0}$	0.5
$\text{SR}^{\text{0-jet}}_{m_{\text{T2}}^{100}\in[110,\infty)}$	0.09	12.2	$21.1^{+7.7}_{-6.3}$	0.5
$\text{SR}^{\text{0-jet}}_{m_{\text{T2}}^{100}\in[120,\infty)}$	0.07	9.5	$15.5^{+6.2}_{-4.4}$	0.5
$\text{SR}^{\text{0-jet}}_{m_{\text{T2}}^{100}\in[130,\infty)}$	0.10	13.9	$15.2^{+5.9}_{-3.8}$	0.5
$\text{SR}^{\text{0-jet}}_{m_{\text{T2}}^{100}\in[140,\infty)}$	0.06	8.0	$8.7^{+3.3}_{-2.4}$	0.5
$\text{SR}^{\text{1-jet}}_{m_{\text{T2}}^{100}\in[100,\infty)}$	0.24	33.9	$29.3^{+10.3}_{-7.7}$	0.29
$\text{SR}^{\text{1-jet}}_{m_{\text{T2}}^{100}\in[110,\infty)}$	0.10	14.0	$19.9^{+7.5}_{-5.9}$	0.5
$\text{SR}^{\text{1-jet}}_{m_{\text{T2}}^{100}\in[120,\infty)}$	0.06	8.9	$11.2^{+4.2}_{-2.7}$	0.5
$\text{SR}^{\text{1-jet}}_{m_{\text{T2}}^{100}\in[130,\infty)}$	0.03	4.0	$6.1^{+2.7}_{-1.7}$	0.5
$\text{SR}^{\text{1-jet}}_{m_{\text{T2}}^{100}\in[140,\infty)}$	0.02	2.9	$3.5^{+1.6}_{-0.6}$	0.5

Table 25: Left to right: 95% CL upper limits on the visible cross section ($\langle\epsilon\sigma\rangle^{95}_{\text{obs}}$) and on the number of signal events (S^{95}_{obs}). The third column (S^{95}_{exp}) shows the 95% CL upper limit on the number of signal events, given the expected number (and $\pm1\sigma$ excursions on the expectation) of background events. The last column indicates the discovery p-value ($p(s=0)$). The p-value is reported as 0.5 if the observed yield is smaller than the predicted.

7 Search for higgsinos at the HL-LHC

Naturalness arguments suggest that the absolute value of the Higgsino mass parameter $|\mu|$ should be near the electroweak scale $v \approx 246$ GeV. In these scenarios, the higgsino mass parameter is low compared to the bino and wino ones, i.e. $|\mu| \ll M_1, M_2$. After electroweak symmetry breaking, the four higgsino states give rise to two neutralinos $\tilde{\chi}_1^0, \tilde{\chi}_2^0$ and a chargino $\tilde{\chi}_1^\pm$. In models with $|\mu| \ll M_1, M_2$, the mass splitting between the $\tilde{\chi}_2^0$ and $\tilde{\chi}_1^0$ is about $m_Z^2/M_{1,2}$ [24]. Higgsino searches are particularly challenging due to the small cross sections and due to the low p_T of the particles arising from the $\tilde{\chi}_1^\pm$ and $\tilde{\chi}_2^0$ decays.

This chapter presents a study of the sensitivity of the HL-LHC to direct electroweakino pair production in models with small and intermediate mass splitting $\Delta m(\chi_2^0, \chi_1^0) = m(\chi_2^0) - m(\chi_1^0)$. The electroweakinos decay via off-shell W and Z bosons, $\tilde{\chi}_1^\pm \to W^* \tilde{\chi}_1^0$, $\tilde{\chi}_2^0 \to Z^* \tilde{\chi}_1^0$, resulting in a final state with two charged leptons and missing transverse momentum coming from the undetected χ_1^0. Due to the small mass splittings, a jet arising from initial-state radiation (ISR) is required, boosting the sparticle system and enhancing the p_T of the leptons and LSPs. In Figure 62 a diagram of one of the processes considered is shown. The analysis is performed simulating the High Luminosity LHC (HL-LHC) regime, where the center of mass energy will be increased to $\sqrt{s} = 14$ TeV, the average number of interactions per bunch crossing will reach $\langle\mu\rangle \sim 200$ and the data collected is expected to amount an integrated luminosity of $L \sim 3000$ fb^{-1}.

The results presented below were published and are also described in [147] and [148].

7.1 Sample generation and detector response

Monte Carlo (MC) simulated event samples are used to predict the background from SM processes and to model the Supersymmetry signal.

For the production of $t\bar{t}$ Powheg-Box v2 generator interfaced to Pythia 8 parton shower model is used. Events containing W or Z bosons with associated jets (W+jets and Z/γ^*+jets) are produced using the Sherpa v2.2.1 generator with the

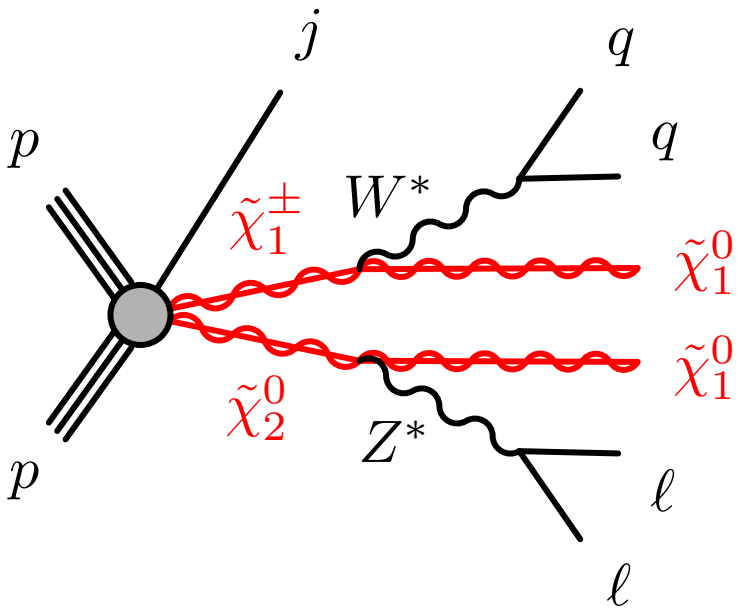

Figure 62: Diagram for chargino-neutralino production in an association with an ISR jet.

NNPDF30NNLO PDF set. Diboson processes (WW, WZ, ZZ) are simulated using the Sherpa v2.2.2 generator.

The signal samples are generated with MadGraph and the parton shower is made with Pythia 8. The following processes are generated: $pp \to \chi_1^{\pm}\chi_2^0, pp \to \chi_2^0\chi_1^0, pp \to \chi_1^{\pm}\chi_1^{\pm}$. MadSpin is used for the χ_2^0 and $\chi_1^{\pm}$ decay the to ℓ ($\ell = \mu, \tau$). The $\tilde{\chi}_1^0$ and $\tilde{\chi}_2^0$ masses are varied, while the $\tilde{\chi}_1^{\pm}$ masses are set to $m(\tilde{\chi}_1^{\pm}) = \frac{1}{2}[m(\tilde{\chi}_1^0) + m(\tilde{\chi}_2^0)]$ and pure higgsino states are assumed for the production cross sections.

The detector response is modelled with parameterised response functions based on studies performed with Geant 4 [49] simulations of the ATLAS upgraded detector in high luminosity conditions [149].

7.2 Particle reconstruction

The reconstruction of physics objects is performed at truth-level with parameterised detector functions [149].

The search targets final states with low p_{T} muons, down to $p_{\mathrm{T}} > 3$ GeV in the pseudorapidity range $|\eta| < 2.5$. Muons originating from pile-up interactions or from heavy flavour hadron decays, referred to as fake or non-prompt muons, are rejected

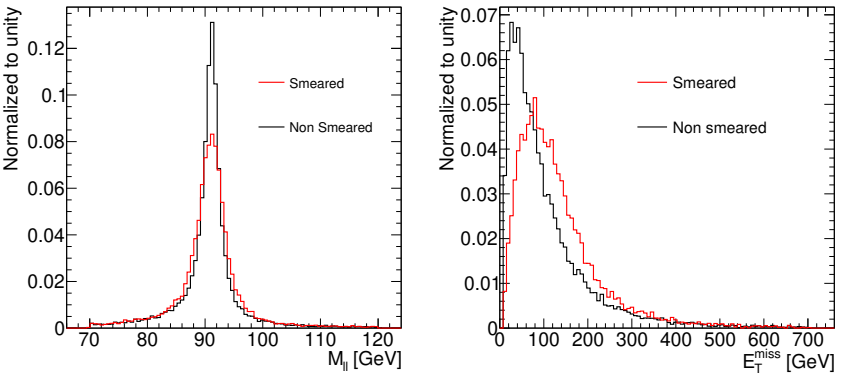

Figure 63: Left: $m_{\ell\ell}$ distribution for a $Z \to \mu\mu$ sample (left) and E_T^{miss} distribution for a $Z \to \tau\tau$ sample (right) without any smearing (black) and considering detector smearing (red). Distributions are normalized to unity.

applying an isolation to the muon candidates. Jets are reconstructed using the anti-k_t algorithm with a radius parameter of 0.4. Jets within $|\eta| < 2.8$ are considered and the jet energy is smeared according to a Gaussian. Jets originating from b-quark hadronization (b-jets) are tagged using a parameterisation model of the MV2c10 b-tagging algorithm [150]. In simulated $t\bar{t}$ events, the chosen working point identifies b-jets with an efficiency of 70%.

The magnitude of the missing transverse momentum (E_T^{miss}) is computed as the vector sum of the true momenta (at the particle level) of neutral weakly-interacting particles (neutrinos and neutralinos). It is then smeared according to a Gaussian, to simulate the detector response, with a function parameterised as a function of the average number of interactions per bunch crossing μ and the scalar sum of energy in the calorimeter $\sum E_{\text{T}}$.

In order to resolve particle overlaps (overlap removal) we employ the following scheme: candidate jets are required to be separated from candidate electrons by $\Delta R(e, \text{jet}) > 0.2$; if a jet and electron are within 0.2, then the jet is removed and the electron is kept; after this step, leptons (both e and μ) are removed if they are within $\Delta R < 0.4$ of a remaining jet.

In order to show how the detector smearing affects the kinematic distributions, in Figure 63 the detector smeared and non-smeared E_T^{miss} and $m_{\ell\ell}$ distributions for $Z \to \mu\mu, \tau\tau$ samples are depicted. As the figure shows, the E_T^{miss} distribution is shifted to higher values and the Z mass peak widens detector resolution effects are taken into account.

7.3 Event Selection

In this analysis, only events with two opposite-sign muons are used in the final selection, since the muon fake rate is not expected to grow as much as for electrons with the increased pile-up. The event selection follows an ISR-like topology, requiring a high p_{T} jet to recoil against the sparticle system. Therefore, the p_{T} of leading jet is required to be above 100 GeV and the azimuthal separation between the leading jet and the $\mathbf{E}_T^{\mathrm{miss}}$ has to be $\Delta\phi(\mathrm{jet}_1, E_T^{\mathrm{miss}}) > 2.0$. In order to isolate the signal processes from the SM background processes, further kinematic variables are employed:

- n_μ. Total number of muons in the event.
- n_{jets}. Total number of jets in the event
- $n_{\text{b-jets}}$. The total number of b-jets with $p_T > 30$ GeV.
- E_T^{miss}. The missing transverse momentum. Events with $E_T^{\mathrm{miss}} > 500$ GeV are selected in order to ensure that events can be triggered.
- $m_{\ell\ell}$. The invariant mass of the dilepton system. In higgsino events where both leptons originate from the Z^* decay, $m_{\ell\ell}$ is kinematically bounded by the value of mass splitting Δm. This feature will be exploited by dividing the SR in several $m_{\ell\ell}$ bins.
- $\Delta R(\ell, \ell)$. Angular separation between the two charged muons of the event. Small mass splittings end up in small angular separation of the leptons coming from the Z^* decay.
- $m_{\tau\tau}$. Invariant mass of two tau leptons, calculated as described in [151]. This variable approximates the mass of the leptonically decaying τ leptons when they are sufficiently boosted so that their decay products are parallel. The formal definition is $m_{\tau\tau}^2 = 2p_1^\ell p_2^\ell(1+\xi_1)(1+\xi_2)$. Where $p_{1,2}^\ell$ are the leptons four momenta, and $\xi_{1,2}$ are calculated by solving $\mathbf{E}_T^{\mathrm{miss}} = \xi_1 p_T^{\ell_1} + \xi_2 p_T^{\ell_2}$. The signed square root of $m_{\tau\tau}^2$ is then taken to calculate $m_{\tau\tau}$, i.e., $m_{\tau\tau} = \mathrm{sign}(m_{\tau\tau}^2)\sqrt{|m_{\tau\tau}^2|}$. The variable allows for negative values when $\mathbf{E}_T^{\mathrm{miss}}$ points to the opposite hemisphere of a leptons' p_{T} and $E_T^{\mathrm{miss}} > p_T^\ell$. This variable develops a peak for the $Z(\to \tau\tau)$ process.
- $E_T^{\mathrm{miss}}/H_{\mathrm{T}}^{\mathrm{lep}}$. Ratio of the E_T^{miss} to the scalar sum of the p_{T} of the two leptons. Background processes like $t\bar{t}$ and VV tend to have harder leptons, decreasing the

Table 26: Summary of the SR selection requirements.

Variable	SR Selection ($m_{\ell\ell} < 20\,\text{GeV}$)	SR Selection ($m_{\ell\ell} > 20\,\text{GeV}$)
n_μ	$= 2$	$= 2$
$p_{\text{T}}(\mu_{1,2})$ [GeV]	> 3	> 8
n_{jets}	≥ 1	≥ 1
$n_{\text{b-jets}}$	$= 0$	$= 0$
E_T^{miss} [GeV]	> 500	> 500
$\Delta R(\ell, \ell)$	< 2	< 2
$m_{\ell\ell}$ [GeV]	$[1, 20]$ excluding $[3.0, 3.2]$	$[20, 50]$
$p_{\text{T}}(\text{jet}_1)$ [GeV]	> 100	> 100
$\Delta\phi(j_1, E_T^{\text{miss}})$	> 2	> 2
$\min(\Delta\phi(j, E_T^{\text{miss}}))$	> 0.4	> 0.4
$m_{\tau\tau}$ [GeV]	< 0 or > 160	< 0 or > 160
$E_T^{\text{miss}}/H_{\text{T}}^{\text{lep}}$	$> \max(5, 15 - 2m_{\ell\ell})$	$> \max(10, 15 - 2m_{\ell\ell})$

value of $E_T^{\text{miss}}/H_{\text{T}}^{\text{lep}}$. In signal events, the E_T^{miss} is generated due p_{T} balancing against the ISR jet, while little contribution comes from the leptons, thus decreasing the $E_T^{\text{miss}}/H_{\text{T}}^{\text{lep}}$ value.

- $\min(\Delta\phi(j, E_T^{\text{miss}}))$. Missing transverse momentum originating from jet mismeasurements tend to be aligned with a specific jet axis.

The final Signal Region (SR) selections are summarised in Table 26. In Figure 64 the kinematic distributions of different variables used in the analysis are presented, where the full SR selection is applied except the variable shown itself. In order to benefit from the shapes of the $m_{\ell\ell}$ distributions from the signal, the SR is split into six different non-overlapping SRs, with $m_{\ell\ell} = [1, 3]$, $[3.2, 5]$, $[5, 10]$, $[10, 20]$, $[20, 30]$ and $[30, 50]$ GeV.

The leading irreducible backgrounds in the SR are $t\bar{t}$, single-top Wt, VV + jets ($V = Z, W$), and $Z/\gamma^*(\to \tau\tau)$ + jets. The dominant source of irreducible background arises from processes where one or more leptons are fake or non-prompt, such as in W+jets production. These arise mainly due to jets misidentified as leptons or semileptonic decays of heavy-flavor hadrons.

The $t\bar{t}$ and W+jets backgrounds in the SR are estimated by fitting the shape of the E_T^{miss} distribution to an exponential, in order to avoid statistical fluctuations at high E_T^{miss}. The fit is performed applying the full SR selection except the E_T^{miss} cut itself.

	SR					
$m_{\ell\ell}$ bin [GeV]	$[1,3]$	$[3.2,5]$	$[5,10]$	$[10,20]$	$[20,30]$	$[30,50]$
Total SM	2.5 ± 0.4	16.0 ± 2.5	62.4 ± 4.9	142.9 ± 10.7	102.6 ± 14.9	164 ± 20.2
$t\bar{t}$ events	1.7 ± 0.4	1.2 ± 0.2	7.5 ± 1.0	29.2 ± 4.2	21.8 ± 5.4	53.9 ± 9.2
VV events	0.05 ± 0.01	0.8 ± 0.2	15.4 ± 2.1	40.5 ± 5.9	50.2 ± 12.3	104.8 ± 18.0
W+jets events	0.08 ± 0.02	0.9 ± 0.2	8.9 ± 1.2	25.7 ± 3.7	4.7 ± 1.2	3.5 ± 0.6
Z+jets events	0.7 ± 0.2	13.1 ± 2.5	30.6 ± 4.2	47.4 ± 6.9	25.9 ± 6.4	1.8 ± 0.3

Table 27: Event yields in the SR with an integrated luminosity of $3000\,\text{fb}^{-1}$ at $\sqrt{s} = 14\,\text{TeV}$. The errors shown include statistical and systematic uncertainties.

This procedure is done in each $m_{\ell\ell}$ bin considered in the SR. The predicted values from the fit were found to be consistent with the values obtained directly from the MC simulation. For the rest of the backgrounds, the yields were taken directly from MC.

7.4 Results and Interpretation

The HistFitter framework [143], which utilises a profile-likelihood-ratio test statistic [144], is used to compute expected exclusion limits with the CL_s prescription [145]. The systematic uncertainties considered include a 30% uncertainty on the background modelling and an additional 20% systematic uncertainty correlated across bins. The theory uncertainty on the signal modelling is taken to be 15%.

The background yields for each $m_{\ell\ell}$ bin are presented in Table 27. At low $m_{\ell\ell}$, the main contribution is due to $t\bar{t}$ events. At intermediate $m_{\ell\ell}$ values, the $Z(\rightarrow \tau\tau)$+jets process dominates. Finally, as higher $m_{\ell\ell}$ values are approached, the diboson process becomes dominant. The $t\bar{t}$ and diboson yields include the component from misidentified leptons. For the lowest $m_{\ell\ell}$ bin the component of $t\bar{t}$ from misidentified leptons is 40%, while it is 15% in the highest $m_{\ell\ell}$ bin.

In Figure 65 the 95% CL expected exclusion limits in the $\text{m}(\tilde{\chi}_2^0)$, $\Delta m(\tilde{\chi}_2^0, \tilde{\chi}_1^0)$ mass plane are shown. With a luminosity of 3000 fb^{-1}, $\tilde{\chi}_2^0$ masses up to ~ 350 GeV and mass splittings down to about 2 GeV could be reached. The blue curve represents the 5σ discovery potential of the search. To compute the discovery potential, a single-bin discovery test is performed by integrating over all the $m_{\ell\ell}$ bins considered. Finally, Figure 66 presents the 95% expected exclusion limits in the $\tilde{\chi}_1^\pm, \Delta m(\tilde{\chi}_1^\pm, \tilde{\chi}_1^0)$ mass plane, for both the disappearing track and dilepton searches. When the chargino-

neutralino mass splitting is of the order of tens to hundreds of MeV, the charginos can be long-lived, leaving a disappearing track in the inner detector. The plot shows very good complementarity among searches in targeting these very interesting and motivated compressed scenarios.

Although the HL-LHC will have access to the very compressed region, more advanced techniques could help to further improve the results. For instance, by including the dielectron channel in the final state, or by being able to lower the p_{T} thresholds of the leptons below 3 GeV, the sensitivity could be enhanced. In addition, multivariate analysis techniques could also help in discriminating the signal over background.

Furthermore, if by the end of the HL-LHC this search finds no supersymmetric particles, there will be strong implications. For instance, it is exactly the low mass splitting region probed by this analysis where Supersymmetry is less fine-tuned and supported by string theory landscape expectations [152, 29].

Looking forward into the future, a possible upgrade of the LHC is the High-Energy LHC (HE-LHC) [153], where the center of mass energy would be increased to 27 TeV. However, since higgsinos have electroweak couplings, their cross section will not increase significantly, therefore this collider would specially benefit searches for squarks and gluinos. For this reason, electron-positron colliders could be a good way of exploring further the electroweak sector of Supersymmetry[1]. Interesting proposals include the ILC [154] and CLIC [155]. Higgsino searches prospects have been studied for the ILC [156], where the masses of the neutralinos could be measured[2] at the percent level for mass splittings of few GeV. Since the higgsino mass is comparable to the SUSY μ parameter, this parameter can also be extracted. Furthermore, the gaugino masses M_1 and M_2 depend on the mass splittings, thus allowing their determination.

Finally, for the possible 100 TeV upgrade of the LHC (FCC), studies show that for mass splittings of 20 GeV, the LSP mass can be constrained up to 1 TeV for a bino-higgsino mixtured state [157, 158]. This number matches the expectations for a pure higgsino dark matter candidate, which is expected to be ~ 1 TeV in order to account for the measured dark matter relic density.

[1] It is required that the e^+e^- collider satisfies $\sqrt{s} > 2m_{\tilde{\chi}_2^0, \tilde{\chi}_1^\pm}$.

[2] Due to the clean environment in e^+e^- colliders, the mass and energy distributions of the dilepton system can be precisely measured and can be used to extract the mass values of the neutralinos.

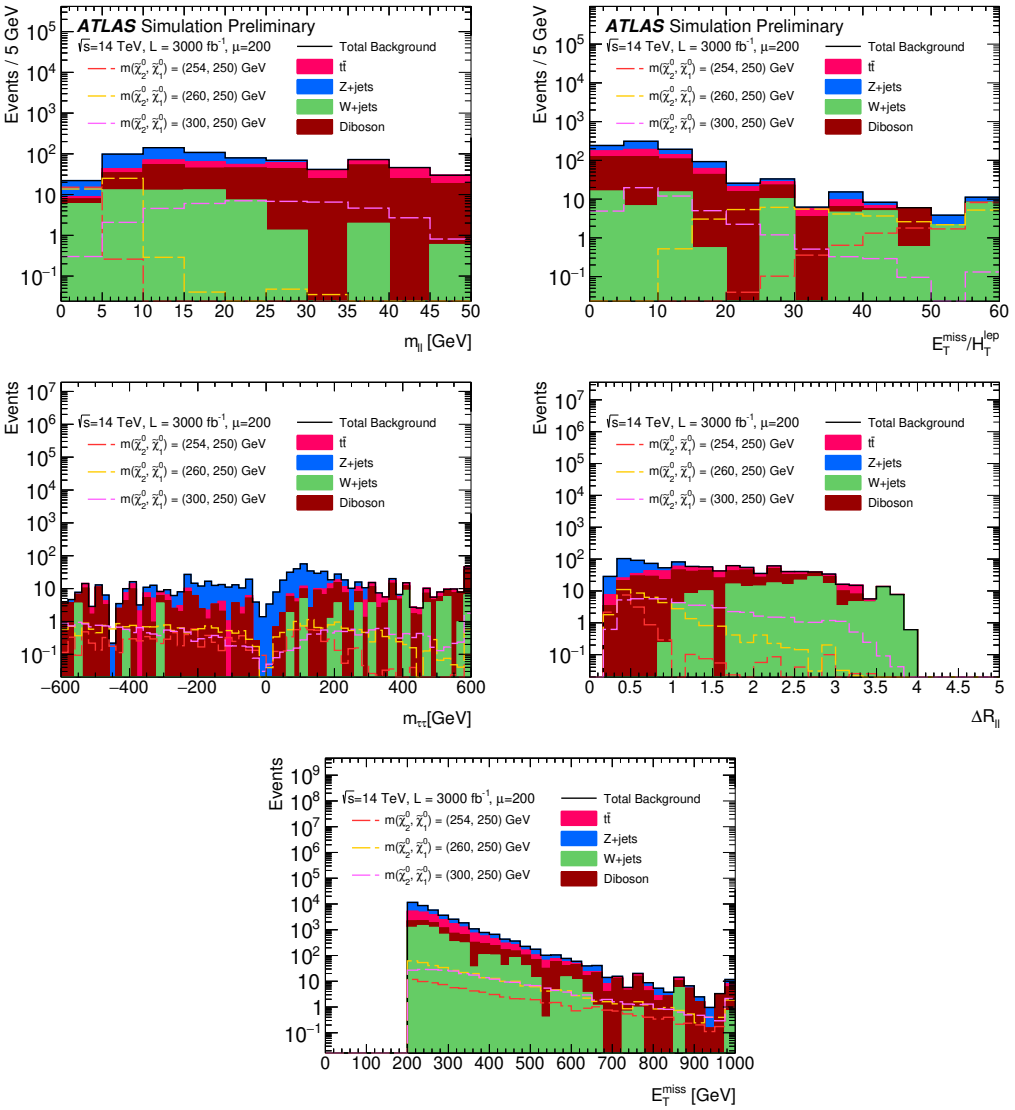

Figure 64: Background distributions of $m_{\ell\ell}$ (top left), $E_T^{\text{miss}}/H_{\text{T}}^{\text{lep}}$ (top right), $m_{\tau\tau}$ (middle left), $\Delta R(\ell,\ell)$ (midddle right) and E_T^{miss} (bottom) used for the SR optimisation. The variables are presented with the full SR selections implemented aside from the selection on the variable shown. Three signal models with $m(\chi_1^0) = 250$ GeV and different mass splittings ($\Delta m(\tilde{\chi}_2^0, \tilde{\chi}_1^0) = 4$, 10, and 50 GeV) are overlaid. The $m_{\ell\ell}$ and $E_T^{\text{miss}}/H_{\text{T}}^{\text{lep}}$ figures are taken from from [147].

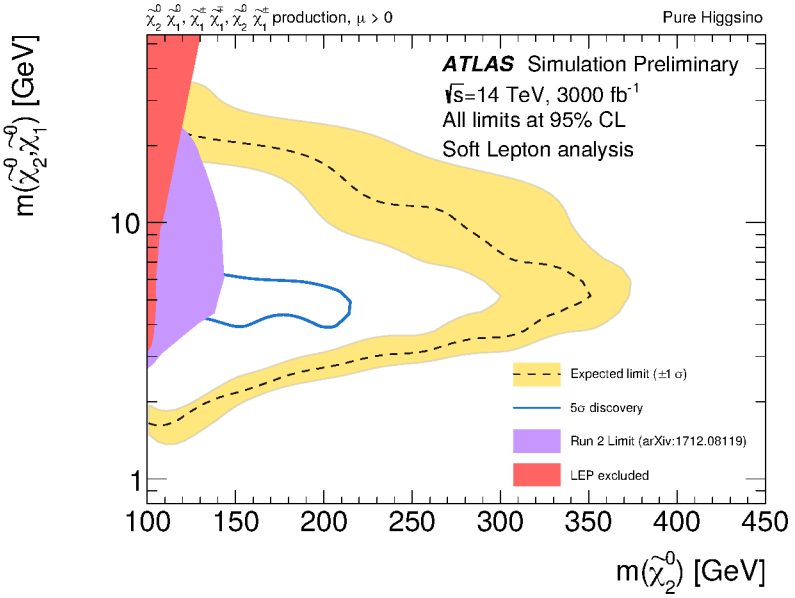

Figure 65: Expected exclusion limit (dashed line) in the $\Delta m(\tilde{\chi}_2^0, \tilde{\chi}_1^0)$-$m(\tilde{\chi}_2^0)$ mass plane, at 95% CL with 3000 fb^{-1}of 14 TeV proton-proton collision data in the context of a pure Higgsino LSP with $\pm 1\sigma$ (yellow band) from the associated systematic uncertainties. The blue curve presents the 5σ discovery potential of the search. The purple contour is the observed exclusion limit from the Run 2 analysis [151], corresponding to a luminosity of 36.1fb^{-1}. The figure also presents the limits on chargino production from LEP [23]. The relationship between the masses of the chargino and the two lightest neutralinos in this scenario is $m(\tilde{\chi}_1^\pm) = \frac{1}{2}(m(\tilde{\chi}_1^0) + m(\tilde{\chi}_2^0))$. Figure from [147].

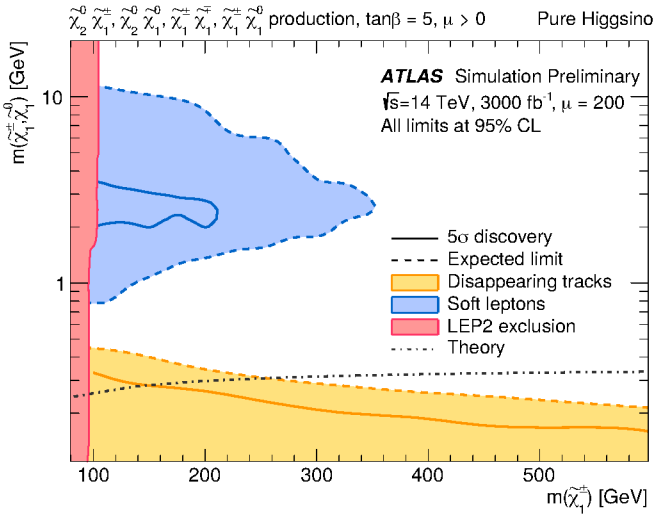

Figure 66: Expected exclusion at the 95% CL from the disappearing track and dilepton searches in the $\Delta m(\tilde{\chi}_1^\pm, \tilde{\chi}_1^0)$, $m(\tilde{\chi}_1^\pm)$ mass plane. The blue curve presents the exclusion limits from the dilepton search. The yellow contour presents the exclusion limit from the disappearing track search. The figure also presents the limits on chargino production from LEP [23]. The relationship between the masses of the chargino and the two lightest neutralinos in this scenario is $m(\tilde{\chi}_1^\pm) = \frac{1}{2}(m(\tilde{\chi}_1^0) + m(\tilde{\chi}_2^0))$. The theory curve is a prediction from a pure higgsino scenario taken from [159]. Figure from [147].

8 Conclusions

This thesis has presented the work performed between 2018 and 2021 related to a search for the superpartners of the Standard Model leptons, High-Luminosity LHC prospects on the search for higgsinos, a novel technique developed to estimate the Standard Model ZZ diboson process and the ongoing upgrade of the ATLAS Inner Tracker.

As searching for Beyond the Standard Model particles is one of the priorities of the LHC programme, the thesis focused on different aspects of Beyond the Standard Model searches: background estimation, ATLAS Run-2 data exploration and future prospects. In Chapter 5, I described a data-driven background estimation technique that I developed in order to estimate the ZZ background using $Z\gamma$ events from data. After a detailed description of all the sources of uncertainty, I showed that a combined theoretical uncertainty of about 4% can be obtained. This result encourages present ongoing searches to employ this method to try and reduce associated systematic uncertainties in the modelling of the ZZ process. Furthermore, this background estimation technique will also serve future LHC analyses or even future colliders, benefiting from the increased amount of collected data and thus reducing the statistical uncertainty on the $Z\gamma$ sample.
I also reported on a search for sleptons using the full available Run-2 ATLAS dataset, corresponding to 139 fb^{-1} at $\sqrt{s} = 13$ TeV. The phase-space targeted in this analysis is very challenging and of great physics interest. First, it is exactly in this region that the discovery of sleptons could explain the longstanding muon $g-2$ discrepancy, while also helping to justify the observed dark matter relic abundance via slepton-neutralino coannihilations. It is also challenging, since the detectable final-state particles are usually soft and dedicated searches are required to target these topologies. I demonstrated that it is possible to gain sensitivity in this region with the current ATLAS dataset. In the absence of new physics, the analysis sets world-leading constraints on the masses of the sleptons, in regions where LEP experiments still had the best sensitivity. Although this analysis excludes part of the preferred phase space to explain the measured the muon $g-2$, the increased amount of data collected

during Run 3 and future LHC upgrades will be crucial in order to continue exploring this region. Furthermore, due to the recent confirmation of the BNL muon $g-2$ measurement by the Fermilab Muon $g-2$ Experiment, the search for smuons will acquire special importance in the upcoming years.

Projecting Supersymmetry searches forward in time, I presented the sensitivity reach of a possible future search for higgsinos in scenarios with very compressed mass spectra in the HL-LHC phase. This region is also of great interest since compressed higgsinos are needed to avoid SUSY fine-tuning problems, while providing a dark matter candidate that satisfies the relic density constraints imposed by astrophysical observations. I showed that sensitivity to mass splittings of about 2 GeV can be reached in the High-Luminosity LHC phase, and most importantly, I demonstrated that SUSY discovery is also possible during this phase. On a pessimistic note, if no hints of SUSY are found by the end of the HL-LHC phase, it would imply that either some nice features of Supersymmetry, e.g. the explanation of dark matter, may have to be dropped from our initial assumptions, or that the Supersymmetric model under study (the MSSM) is too simplistic and a more complicated SUSY model is realised in nature. In addition, this result has not only strong implications for the HL-LHC era, but also serves as a very useful input for the future, as the results from the HL-LHC phase will provide decisive input to determining the nature of future colliders.

Finally, as an experimental activity in the context of the upgrade of the ATLAS Inner Detector, I designed a cooling box with the aim of emulating the temperature conditions of the HL-LHC. I showed that, although the conditions for sensor testing were not the most optimal, the modules were able to reach temperatures of about -15°C. This opens the possibility to reach even lower temperatures by having, among other things, better thermal insulation or using cold nitrogen instead of dry air to avoid condensation.

Appendix A

Dynamic cone isolation

It was already noted in Ref. [102] that requiring an isolation on the photon can alter the higher order corrections for the $Z\gamma$ process. Since the ZZ does not require isolation, at high p_T^V both processes can receive significantly different QCD corrections. A supplementary isolation definition was proposed to account for this difference. The idea is to define the new isolation cone in such a way that both processes receive the same higher order corrections at high p_T^V. To this end, a dynamic cone radius is defined

$$R_{dyn}(p_{\mathrm{T}}^{\gamma}, \epsilon_{\gamma}) = \frac{M_Z}{p_{\mathrm{T}}^{\gamma}\sqrt{\epsilon_{\gamma}}}, \tag{112}$$

chosen so that the invariant mass of a collinear photon-jet pair ($R_{\gamma j} \ll 1$) is $M_{\gamma j}^2 \simeq M_Z^2$, whenever $\Delta R(\gamma, j) = R_{dyn}$ and $p_{\mathrm{T}}^{j} = \epsilon_{\gamma} p_{\mathrm{T}}^{\gamma}$. In this way using the smooth cone with the dynamic radius ($R_0 \to R_{dyn}$), the $Z\gamma$ process tries to mimic the role of the Z boson mass in the ZZ process. One has to be aware that R_{dyn} can become infinitely large at low p_{T}^{γ}, therefore a minimum radius R_{min} has to be applied, from which the dynamic cone starts applying. Here we choose $R_{min} = 1$, and the other two parameters are chosen as in the smooth cone in Chapter 5, $\varepsilon_{dyn} = 0.075$, $n_{dyn} = 1$. This means that the cone starts becoming dynamic only above $M_Z/\sqrt{\epsilon} \sim 330$ GeV. Below this value, the dynamic isolation behaves effectively like the smooth cone isolation but with $R_0 = 1$. Therefore, in general, the dynamic cone will be more restrictive than the smooth cone, thus decreasing the cross section. This can be observed in Figure 67, where the LO, NLO and NNLO cross sections are shown for both isolation prescriptions.

The NLO, qqNNLO, NNLO and nNNLO K-factors are shown in Figure 68, where the $Z\gamma$ cross section has been calculated with both smooth and dynamic cone isolation defined in Equation 112. Starting with the NLO case, we find that, especially at low p_T^V, the disagreement between the ZZ and $Z\gamma$ (smooth) K-factors is about 20%. However, there is a clear trend towards high p_T^V, where the difference becomes smaller. On the other hand, when using the dynamic cone, the difference stays below 3% across the whole p_T^V range. At qqNNLO, we see again that the dynamic cone

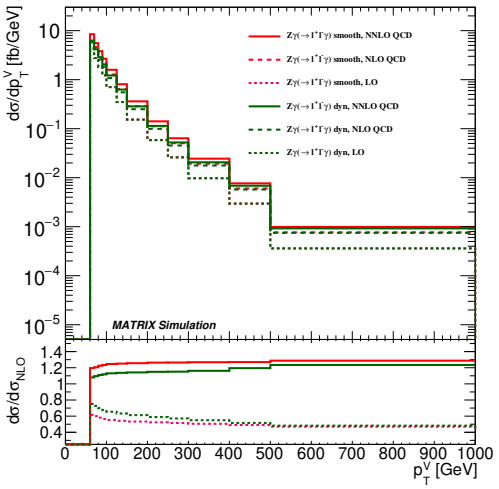

Figure 67: p_T^V distributions for $Z\gamma$ production at LO (dotted), NLO (dashed) and NNLO (solid) using smooth cone isolation (red) and dynamic cone isolation (green). The bottom frame shows the ratio of the LO and NNLO calculations to the NLO prediction.

keeps the difference between ZZ and $Z\gamma$ K-factors below 3%. Once the gluon-gluon contribution (NNLO) is included, the difference increases at low p_T^V, but again it gets reduced above $p_T^V \sim 330$ GeV. Finally, at nNNLO the difference becomes greater at low p_T^V, of about 10%, and below 5% at high p_T^V.

It was decided not to include the dynamic cone in the study in Chapter 5 since at nNNLO it does not significantly reduce the QCD uncertainty compared to the smooth cone. If a dynamic cone was used instead, one should also consider taking as an additional uncertainty the difference between the dynamic cone and smooth cone K-factors, since the smooth cone prescription is known to be closer to the experimental one.

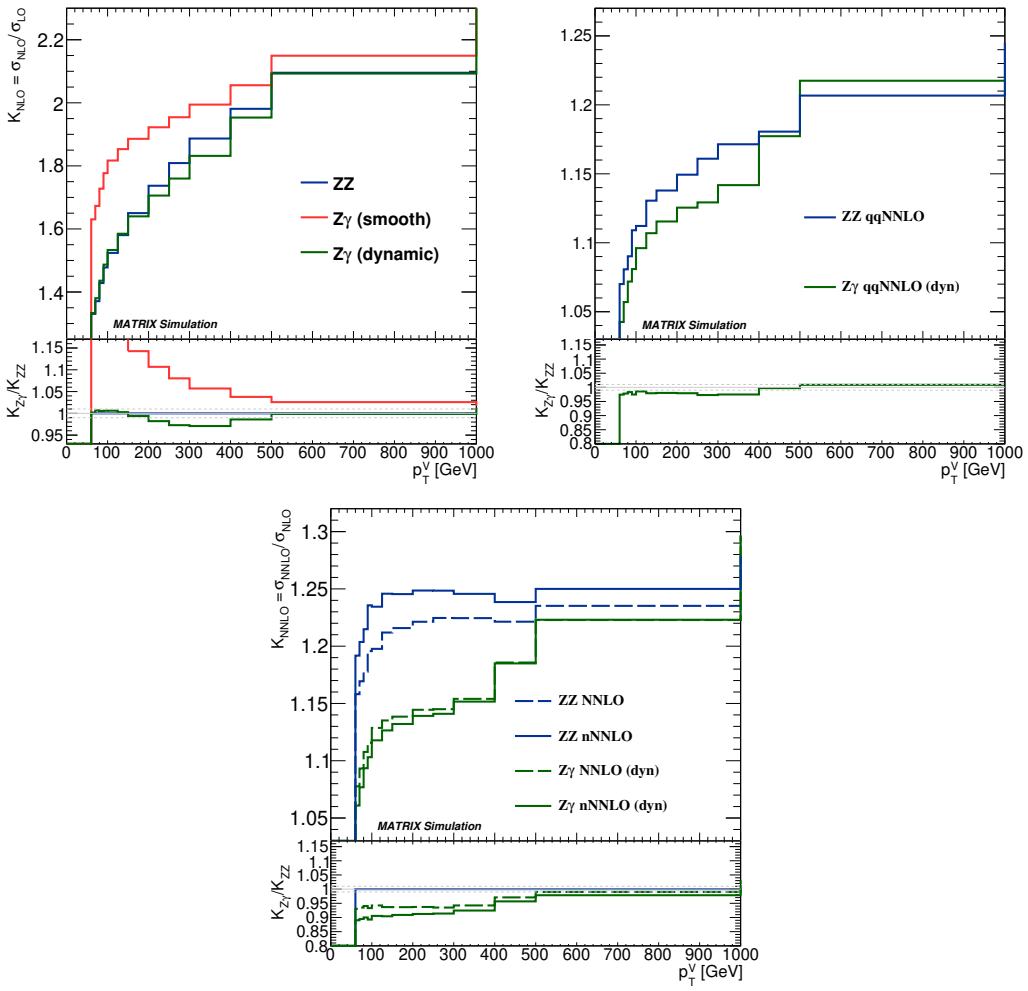

Figure 68: K-factors calculated at NLO (a), NNLO without including the gluon-induced processes (qqNNLO) (b) and NNLO and (n)NNLO (c) in QCD for the ZZ (blue) and $Z\gamma$ processes with smooth cone isolation (red) and with dynamic cone isolation (green) applied. The bottom panels show the ratio between the $Z\gamma$ and ZZ K-factors.

Appendix B

Limitations of sleptons analysis

One of the main reasons the last ATLAS analysis in [117] loses sensitivity for mass splittings approximately below the W boson mass is because of the strong m_{T2} and E_T^{miss} cuts applied, corresponding to > 100 and > 110, respectively. This can be observed in Figure 69, where normalised distributions for both variables are shown. Signal samples with $\Delta m(\tilde{\ell}, \tilde{\chi}_1^0) > m_W$ have long tails in both distributions, whereas the bulk of the $\Delta m = 50$ GeV sample resides below the above mentioned cuts. The analysis described in Chapter 6 tries to recover sensitivity in these more compressed scenarios, by relaxing these selections.

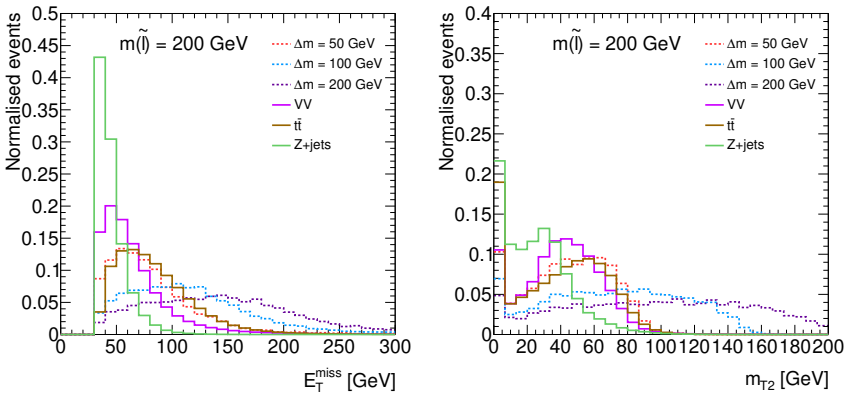

Figure 69: E_T^{miss} (left) and m_{T2} (right) normalised distributions for three representative backgrounds: VV (purple), $t\bar{t}$ (brown) and $Z+\mathrm{jets}$ (green) and three benchmark slepton signal samples (dashed) with $m(\tilde{\ell}) = 200$ GeV and different mass splittings $\Delta m = 50$ (red), 100 (blue), 200 GeV (purple).

Appendix C

Slepton analysis - m_{T2} variable and choice of m_{χ}

In this chapter it is described how the m_{χ} value was chosen in the calculation of $m_{T2}^{m_{\chi}}$. First, since the endpoint of the $m_{T2}^{m_{\chi}}$ variable depends on the mass splitting between the slepton and the lightest neutralino, we show in Figure 70 the endpoint for three different choices of $m_{\chi} = 0, 100, 200$ GeV. It is observed that, given a slepton mass, the $m_{T2}^{m_{\chi}}$ endpoint increases when the mass splitting increases. And for a given mass splitting, the $m_{T2}^{m_{\chi}}$ endpoint changes only by a few GeV across the slepton masses range. We also see that, for higher m_{χ} choices, the endpoints tend to shift to lower $m_{T2}^{m_{\chi}}$ values.

Now, to really see which choice of m_{χ} gives us the best sensitivity, Figure 71 depicts the significance values for various slepton samples and different m_{χ} choices. Since the main background is estimated from the DF channel in the SR, the statistical uncertainty of these events are used to calculate the significance. The significance is calculated per bin and then added in quadrature, emulating a multi-bin fit. We see that m_{T2}^{0}, m_{T2}^{100} and m_{T2}^{200} give similar performance. Since there is no significant difference between the three choices, $m_{\chi} = 100$ GeV is chosen as the nominal value for the analysis in Chapter 6.

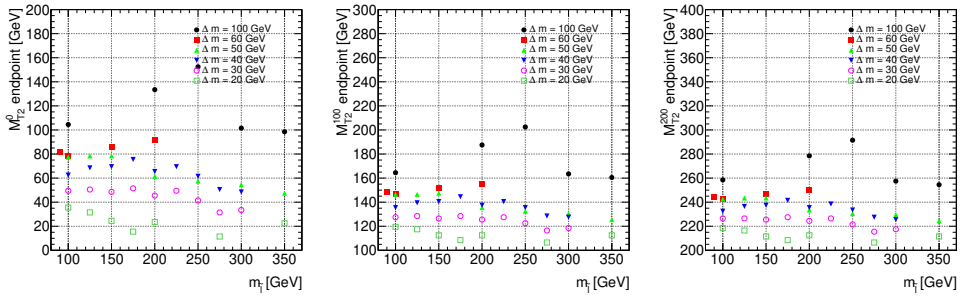

Figure 70: $m_{T2}^{m_{\chi}}$ endpoint for different mass splittings using different choices of the trial mass $m_{\chi} = 0, 100, 200$ GeV, as a function of $m_{\tilde{\ell}}$.

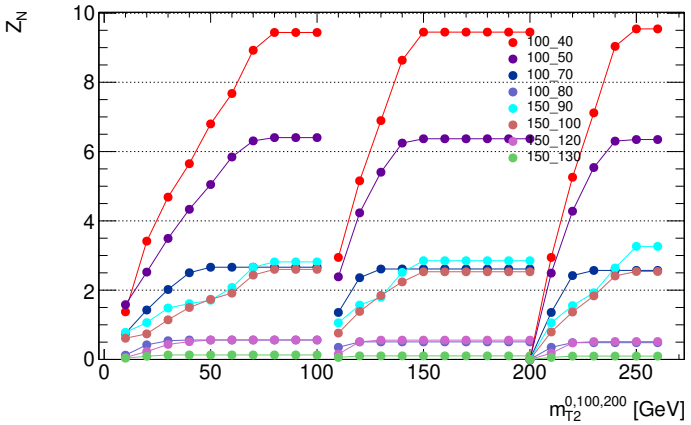

Figure 71: Significance value Z_N as a function of $m_{T2}^{m_\chi}$ for different slepton and LSP masses. The first number corresponds to the slepton mass and the second corresponds to the neutralino mass. The $m_{T2}^{m_\chi}$ cut is performed per bin and the significance values are then added in quadrature. The disitrbutions start at $0, 100, 200$ GeV for m_{T2}^0, m_{T2}^{100} and m_{T2}^{200}, respectively.

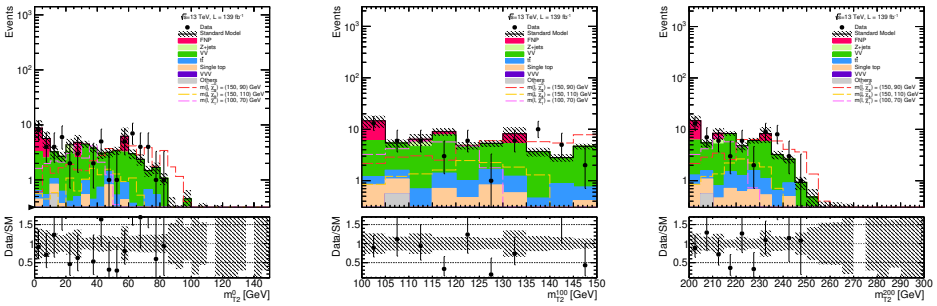

Figure 72: m_{T2}^0 (left), m_{T2}^{100} (middle) and m_{T2}^{200} (right) distributions in the 0-jet SR.

Appendix D

Selection optimisation slepton search

To further motivate the selections performed during the optimisation, Figure 73 shows normalised (to unity) distributions of the variables we cut on in the analysis.
Moreover, as explained in Chapter 6, the SRs have a strong cut in $p_T^{\ell_1}$ ($p_T^{\ell_1} > 140$ GeV), being a consequence of the E_T^{miss}significance cut applied. To illustrate this, Figure 74 depicts the correlation between E_T^{miss}significance and the transverse momenta of the leptons, shown for two signal models with $\Delta m = 30$ GeV and all the backgrounds. We can observe that applying a strong cut on E_T^{miss}significance pushes $p_T^{\ell_1}$ to high values, while low values $p_T^{\ell_2}$ are still realised for the signal models.
To try to exploit this correlation, we also explored the possibility of having a 2-dimensional cut in the E_T^{miss}significance$-p_T^{\ell_1}$ plane. To this end, we designed a linear cut of the form $p_T^{\ell_1} > m \cdot E_T^{\text{miss}}\text{significance} + n$, where m represents the slope and n the constant term. The result of the scan is shown in Figure 75, where the cut that gives the best significance corresponds to $m = -100$ GeV and $n = 950$ GeV. This cut is then applied and the sensitivity in the whole $m_{\tilde{\ell}} - m_{\tilde{\chi}_1^0}$ plane is reevaluated. This is shown if Figure 76. No significant improvement was obtained so the one dimensional cut on $p_T^{\ell_1}$ and E_T^{miss}significance was kept.
It was also explored whether lowering the E_T^{miss}significance and $p_T^{\ell_1}$ cuts depending on the m_{T2}^{100} range under study could improve the sensitivity. To this end, different E_T^{miss}significance and $p_T^{\ell_1}$ cuts where chosen for a benchmark m_{T2}^{100} cut of 130, obtaining the best result with the nominal cuts. This is shown in Figure 77.

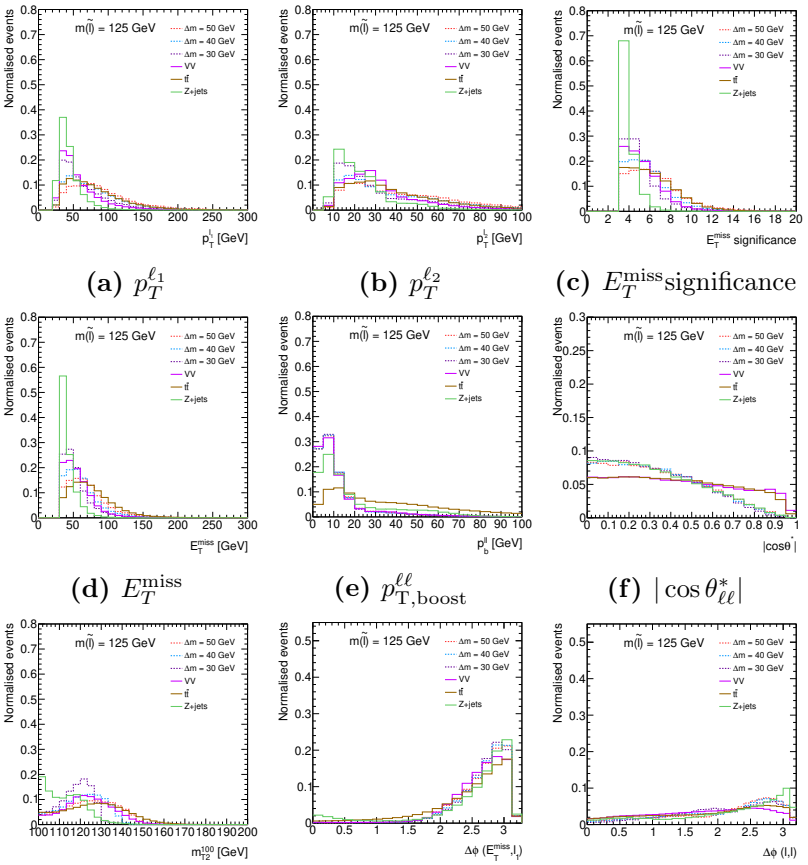

(a) $p_T^{\ell_1}$ **(b)** $p_T^{\ell_2}$ **(c)** E_T^{miss}significance

(d) E_T^{miss} **(e)** $p_{\text{T,boost}}^{\ell\ell}$ **(f)** $|\cos\theta^*_{\ell\ell}|$

(g) m_{T2}^{100} **(h)** $\Delta\phi_{E_T^{\text{miss}},\ell_1}$ **(i)** $\Delta\phi_{\ell,\ell}$

Figure 73: Normalised distributions for $Z+$jets (green), VV (purple) and $t\bar{t}$ (brown) and signal benchmarks $m\left(\tilde{\ell},\tilde{\chi}_1^0\right) = (125,75)$, $(125,95)$, $(125,105)$ GeV at preselection level.

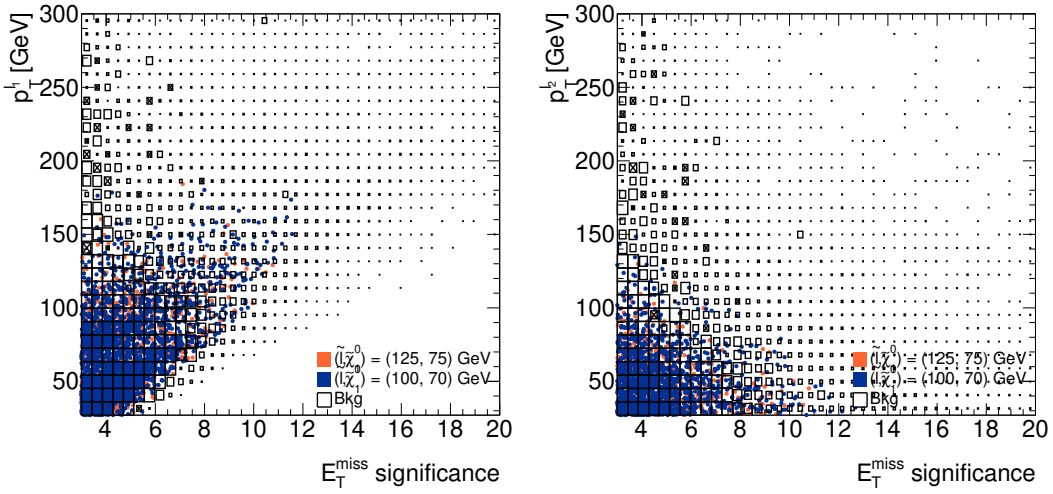

Figure 74: 2D plot showing the correlation between E_T^{miss}significance and $p_T^{\ell_1}$ (left), $p_T^{\ell_2}$ (right). The dotted points represent two different signal models : $m\left(\tilde{\ell}, \tilde{\chi}_1^0\right) = (150, 100)$ GeV (orange) and $m\left(\tilde{\ell}, \tilde{\chi}_1^0\right) = (200, 1)$ GeV (blue). The black boxes represent the SM background.

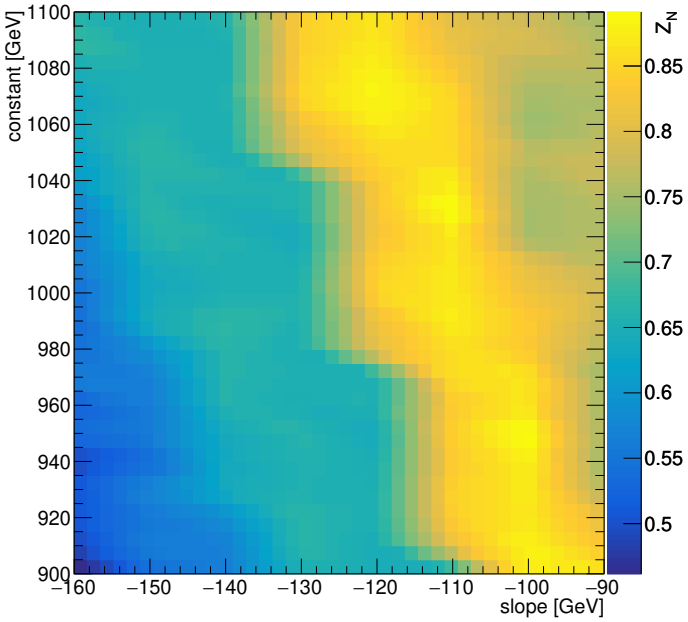

Figure 75: Result of scanning in the slope m and constant n plane. The z-axis represents the significance.

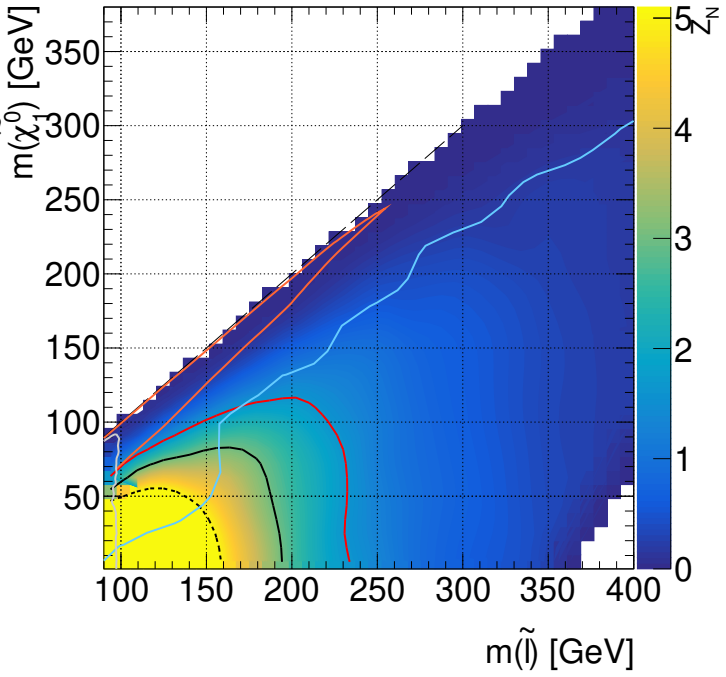

Figure 76: Significance values in the neutralino-slepton mass plane after applying 2D cut described in the text.

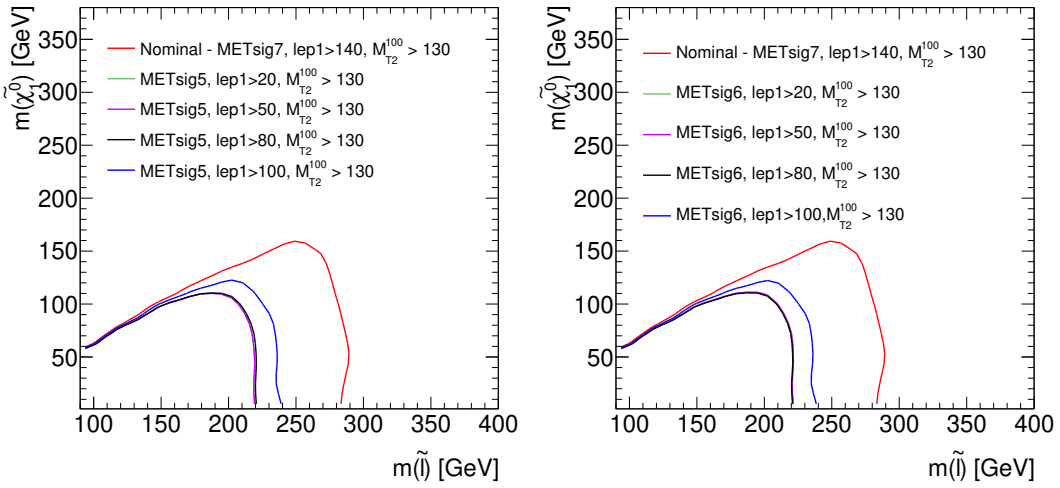

Figure 77: Expected exclusion contour for different $p_T^{\ell_1}$ and E_T^{miss}significance cut choices for $m_{\text{T2}}^{100} > 130$ GeV.

Appendix E

Transfer factor method

The transfer factor method consists in calculating the ratio between SF and DF events $R_{SF/DF}$ in a suitably defined control region, and then applying it to the DF events in the SR. The predicted SF events in the SR can be then obtained as

$$\begin{aligned} N_{ee}^{expected} &= R_e \times N_{DF} \\ N_{\mu\mu}^{expected} &= R_\mu \times N_{DF} \\ N_{SF}^{expected} &= R_{SF/DF} \times N_{DF} = (R_e + R_\mu) \times N_{DF}, \end{aligned} \tag{113}$$

where R_e (R_μ) is the ratio between the dielectron (dimuon) events and the DF events, i.e. $R_e = N_{ee}/N_{DF}$ ($R_\mu = N_{\mu\mu}/N_{DF}$). All the identification, reconstruction and trigger efficiencies are embedded in these transfer factors. The selection criteria of the control region ($\mathrm{CR}^{\mathrm{SF/DF}}$) defined to compute the transfer factors are summarised in Table 28, where it can be observed that the orthogonality with the SR is realized by inverting the cuts on $\cos\theta^*_{\ell\ell}$. The main requirements of this region are: to be

Variable	$\mathrm{CR}^{\mathrm{SF/DF}}$-0jet	$\mathrm{CR}^{\mathrm{SF/DF}}$-1jet
n_{jet-20}	$= 0$	$= 1$
$b_{bjet-20}$	$= 0$	0
$N_{\text{OS leptons}}$	$= 2$	$= 2$
$p_T^{\ell_1}$	> 140 GeV	> 100 GeV
$p_T^{\ell_2}$	> 20 GeV	> 50 GeV
E_T^{miss}significance	> 7	> 7
$p_{\text{T,boost}}^{\ell\ell}$	> 7	–
$\lvert\cos\theta^*_{\ell\ell}\rvert$	> 0.5	> 0.5

Table 28: Selection criteria in $\mathrm{CR}^{\mathrm{SF/DF}}$ defined to estimate the transfer factors R_e and R_μ .

orthogonal to the SRs and to have a similar $N_{SF/DF}$ ratio to that in the SR. The N_{SF}/N_{DF} comparison is shown in Table 29. We see that the transfer factors in

	MC	data
N_{SF}^{CR}/N_{DF}^{CR}(0-jet)	0.979 ± 0.031	0.97 ± 0.10
N_{SF}^{SR}/N_{DF}^{SR}(0-jet)	0.91 ± 0.08	–
N_{SF}^{CR}/N_{DF}^{CR}(1-jet)	0.938 ± 0.022	1.050 ± 0.077
N_{SF}^{SR}/N_{DF}^{SR}(1-jet)	0.978 ± 0.061	–

Table 29: Ratio between SF and DF events in CR^{eff} and in the SR for the 0-jet and 1-jet channels for data and MC.

$CR^{SF/DF}$ and the SR agree within statistical uncertainties. The obtained transfer factors R_e and R_μ computed in $CR^{SF/DF}$ are reported in Table 30 for MC and data. It can be observed that $R_{\mu,e}$ agree within statistical uncertainties in data and MC, except for R_e (1-jet), where an upward fluctuation for data is found. Different variables used in the analysis have been checked to see whether R_e and R_μ have any dependency. No such dependency was found.

Finally, the expected flavour symmetric background yields in the SR for the two methods are reported in Table 31. It can be observed that both methods lead to total yields which agree within 10%, which is the systematic uncertainty we apply to the FS estimate.

	MC	data
R_μ (0-jet)	0.47 ± 0.02	0.43 ± 0.05
R_e (0-jet)	0.51 ± 0.02	0.52 ± 0.08
R_μ (1-jet)	0.46 ± 0.03	0.45 ± 0.04
R_e (1-jet)	0.49 ± 0.01	0.59 ± 0.05

Table 30: Transfer factors R_e and R_μ for MC and data in $CR^{SF/DF}$.The reported uncertainties are only statistical.

Method	ee Events	$\mu\mu$ Events	Total
Eff. correction factors (0-j)	37.3 ± 4.5	32.9 ± 3.9	70.2 ± 8.3
Transfer Factor (0-j)	36.9 ± 7.1	30.5 ± 5.1	67.45 ± 12.3
Eff. correction factors (1-j)	41.0 ± 4.7	35.8 ± 4.1	76.8 ± 8.7
Transfer Factor (1-j)	46.02 ± 6.5	35.1 ± 5.1	81.9 ± 11.6

Table 31: Expected flavour symmetric background yields in the SR estimated using the data DF events in the SR, as obtained with two different methods: the κ and α efficiency correction factors and the transfer factors R_μ and R_e. Fakes are not being subtracted from the DF sample. Only statistical uncertainties are shown.

Appendix F

Derivation of the efficiency correction formula

Assuming that the number of a flavour-symmetric events in the ee and $\mu\mu$ channels will be twice the ones in the $e\mu$ channel (flavour universality), the number of ee,$\mu\mu$ and $e\mu$ events in a given region are, respectively,

$$\begin{aligned} N_{ee} =& N\varepsilon_e^{reco}\varepsilon_e^{reco}\varepsilon_{ee}^{trig}, \\ N_{\mu\mu} =& N\varepsilon_\mu^{reco}\varepsilon_\mu^{reco}\varepsilon_{\mu\mu}^{trig}, \\ N_{e\mu} =& 2N\varepsilon_e^{reco}\varepsilon_\mu^{reco}\varepsilon_{e\mu}^{trig}, \end{aligned} \tag{114}$$

where ε^{reco} and ε^{trig} correspond to the reconstruction and trigger efficiencies in a given channel ($ee, \mu\mu, e\mu$). To account for the differences in electron and muon efficiencies we introduce a new quantity, κ, defined as

$$\kappa = \sqrt{\frac{N_{\mu\mu}}{N_{ee}}} = \frac{\varepsilon_\mu^{reco}}{\varepsilon_e^{reco}}\sqrt{\frac{\varepsilon_{\mu\mu}^{trig}}{\varepsilon_{ee}^{trig}}}. \tag{115}$$

Now Equation 114 reads

$$\begin{aligned} N_{\mu\mu} &= \frac{1}{2}N_{e\mu}\kappa\alpha, \\ N_{ee} &= \frac{1}{2}N_{e\mu}\frac{1}{\kappa}\alpha, \end{aligned} \tag{116}$$

where we have defined $\alpha = \frac{\sqrt{\varepsilon_{ee}^{trig}\varepsilon_{\mu\mu}^{trig}}}{\varepsilon_{e\mu}^{trig}}$.

Appendix G

Data and Monte Carlo distributions

G.1 Data-MC CR$^{\text{eff}}$

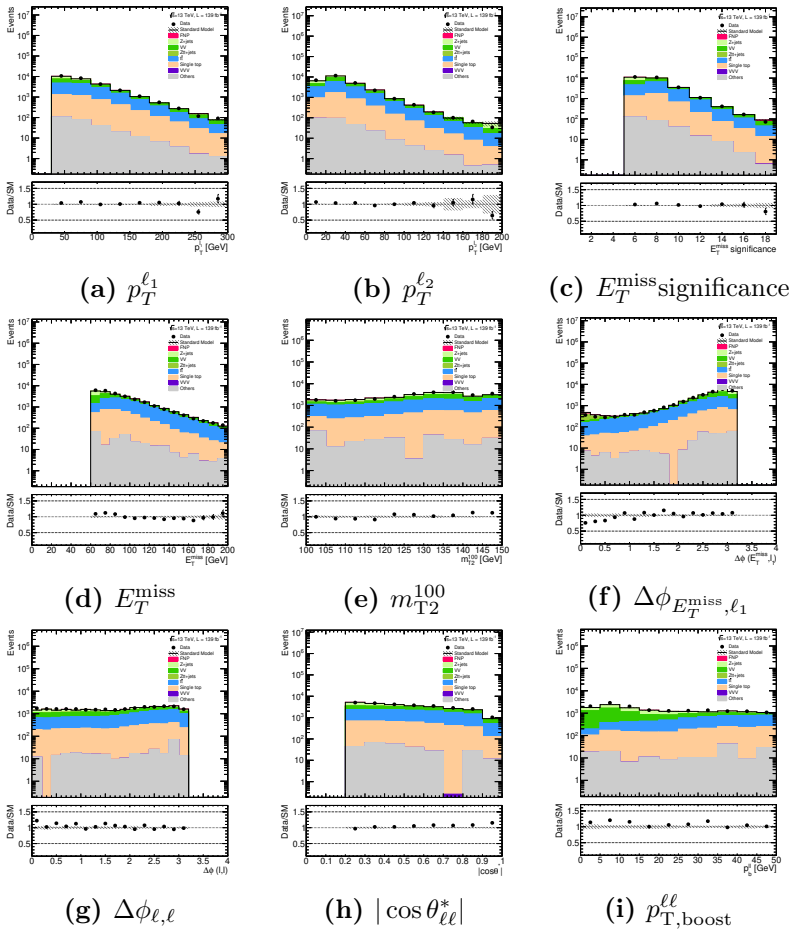

(a) $p_T^{\ell_1}$ (b) $p_T^{\ell_2}$ (c) E_T^{miss}significance

(d) E_T^{miss} (e) m_{T2}^{100} (f) $\Delta\phi_{E_T^{\text{miss}},\ell_1}$

(g) $\Delta\phi_{\ell,\ell}$ (h) $|\cos\theta^*_{\ell\ell}|$ (i) $p^{\ell\ell}_{\text{T,boost}}$

Figure 78: Data and MC distributions of the relevant variables in this analysis, for the ee channel and after the CR$^{\text{eff}}$ cuts in Table 17 are applied. The uncertainties shown are statistical only.

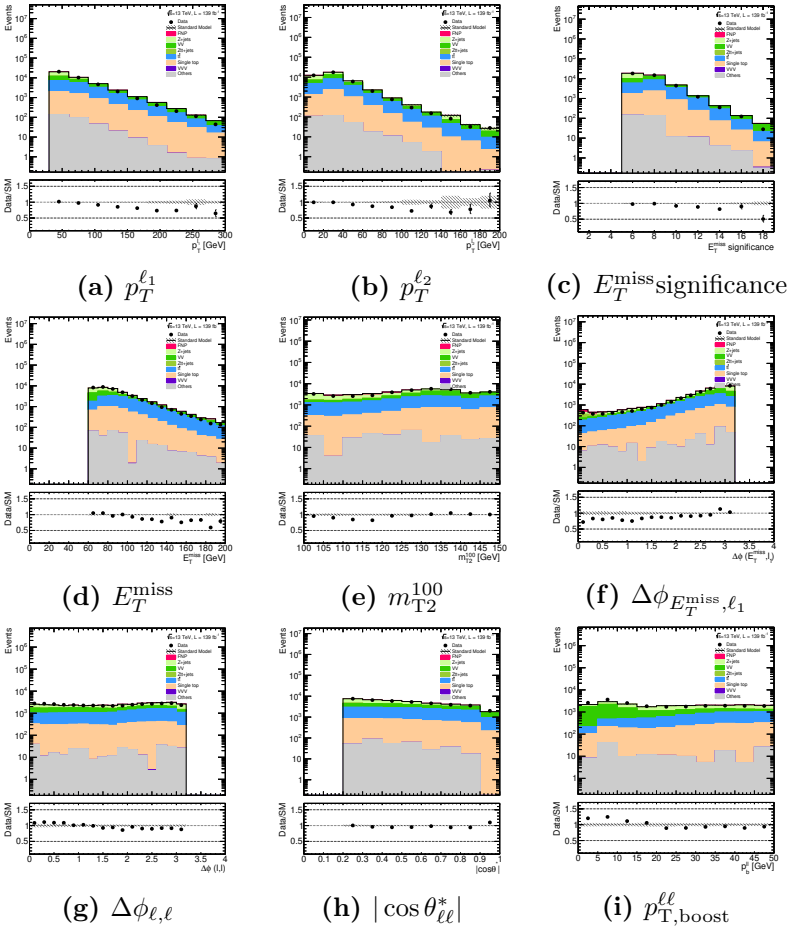

(a) $p_T^{\ell_1}$ (b) $p_T^{\ell_2}$ (c) E_T^{miss}significance

(d) E_T^{miss} (e) m_{T2}^{100} (f) $\Delta\phi_{E_T^{\text{miss}},\ell_1}$

(g) $\Delta\phi_{\ell,\ell}$ (h) $|\cos\theta^*_{\ell\ell}|$ (i) $p_{\text{T,boost}}^{\ell\ell}$

Figure 79: Data and MC distributions of the relevant variables in this analysis, for the $\mu\mu$ channel and after the CR^{eff} cuts in Table 17 are applied. The uncertainties shown are statistical only.

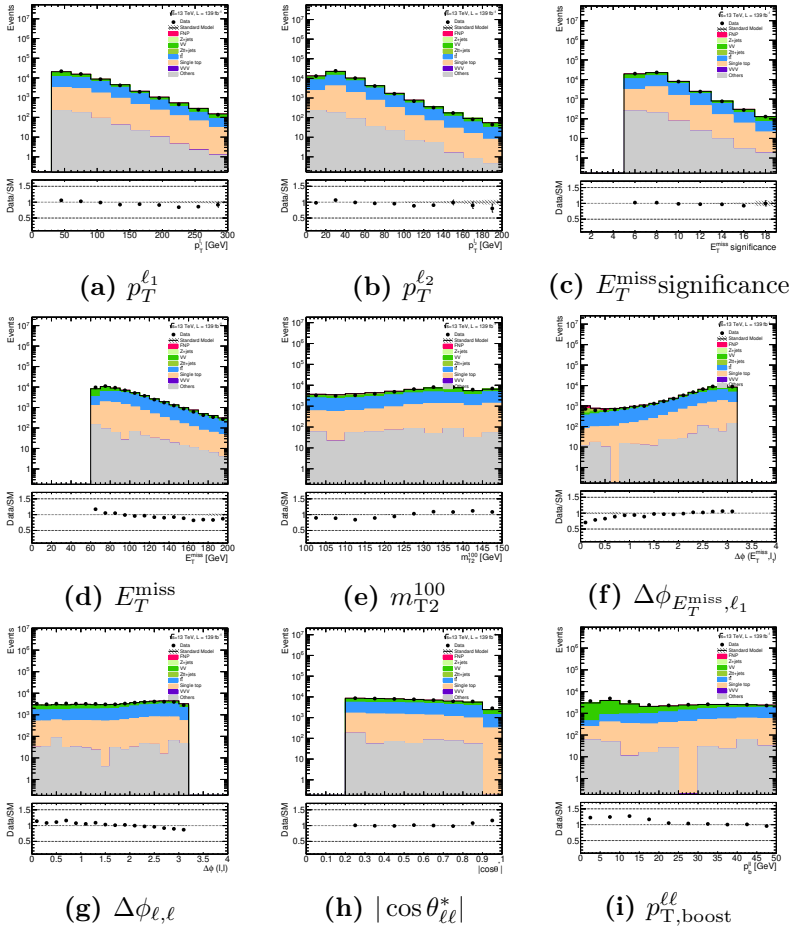

(a) $p_T^{\ell_1}$ (b) $p_T^{\ell_2}$ (c) E_T^{miss}significance

(d) E_T^{miss} (e) m_{T2}^{100} (f) $\Delta\phi_{E_T^{\text{miss}},\ell_1}$

(g) $\Delta\phi_{\ell,\ell}$ (h) $|\cos\theta^*_{\ell\ell}|$ (i) $p_{\text{T,boost}}^{\ell\ell}$

Figure 80: Data and MC distributions of the relevant variables in this analysis, for the DF channel and after the CR^{eff} cuts in Table 17 are applied. The uncertainties shown are statistical only.

G.2 Data-MC SRDF

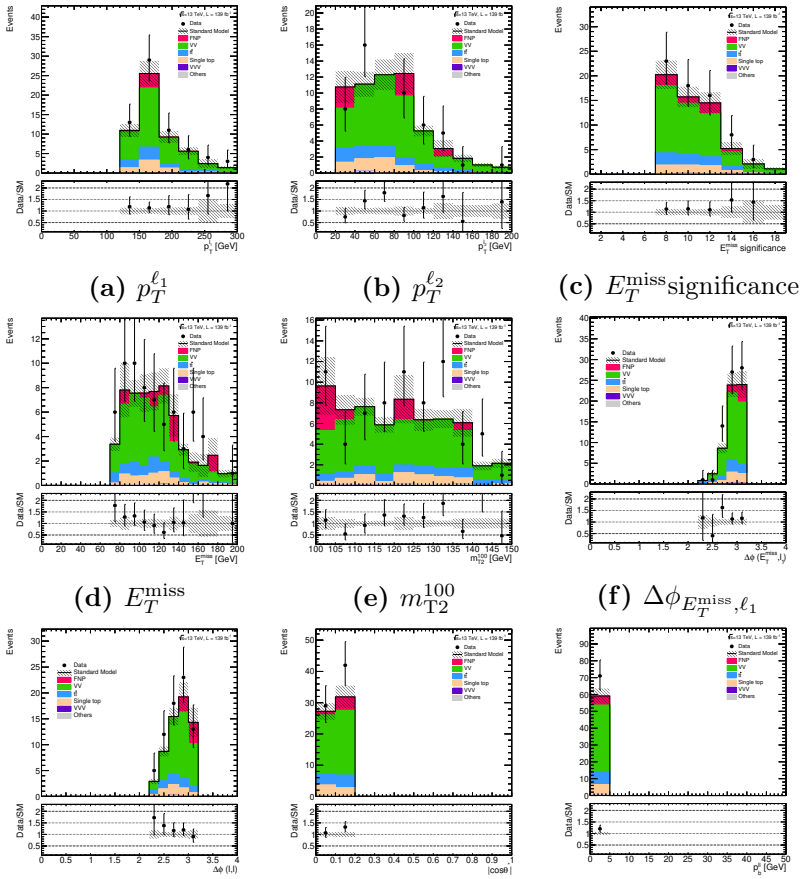

(a) $p_T^{\ell_1}$ **(b)** $p_T^{\ell_2}$ **(c)** E_T^{miss}significance

(d) E_T^{miss} **(e)** m_{T2}^{100} **(f)** $\Delta\phi_{E_T^{\text{miss}},\ell_1}$

(g) $\Delta\phi_{\ell,\ell}$ **(h)** $|\cos\theta^*_{\ell\ell}|$ **(i)** $p_{\text{T,boost}}^{\ell\ell}$

Figure 81: Data and MC distributions of the relevant variables in this analysis, for the DF channel in SR-0jet. This data is used in the final estimate of the flavour symmetric background. Only statistical uncertainties are shown.

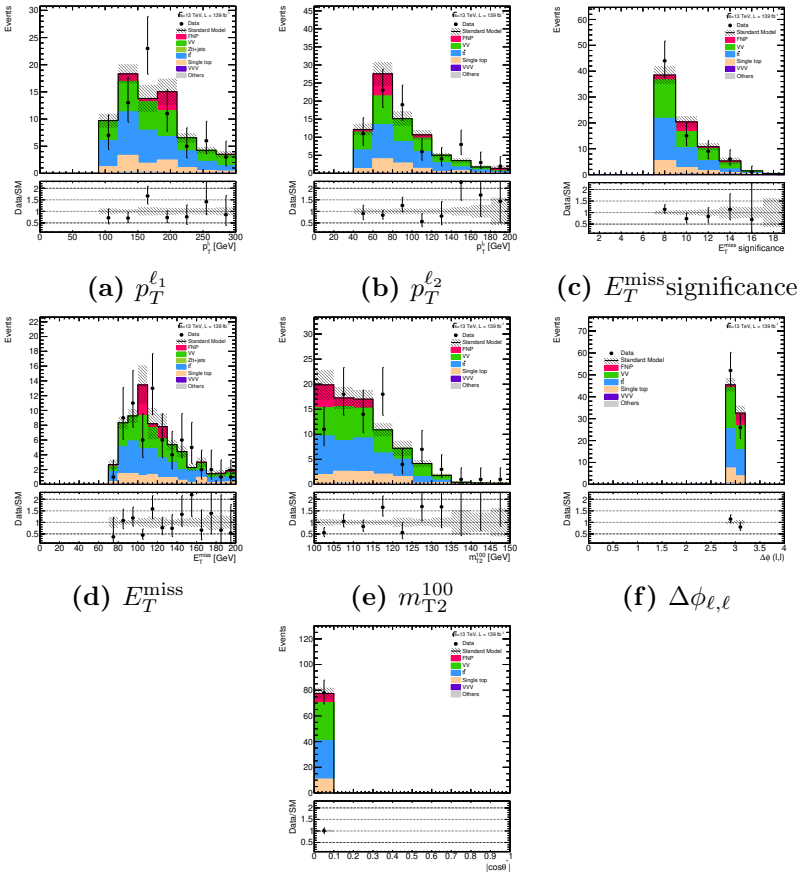

(a) $p_T^{\ell_1}$ **(b)** $p_T^{\ell_2}$ **(c)** E_T^{miss}significance

(d) E_T^{miss} **(e)** m_{T2}^{100} **(f)** $\Delta\phi_{\ell,\ell}$

(g) $|\cos\theta^*_{\ell\ell}|$

Figure 82: Data and MC distributions of the relevant variables in this analysis, for the DF channel in SR-1jet. This data is used in the final estimate of the flavour symmetric background. Only statistical uncertainties are shown.

G.3 Data-MC SR - MC cross check

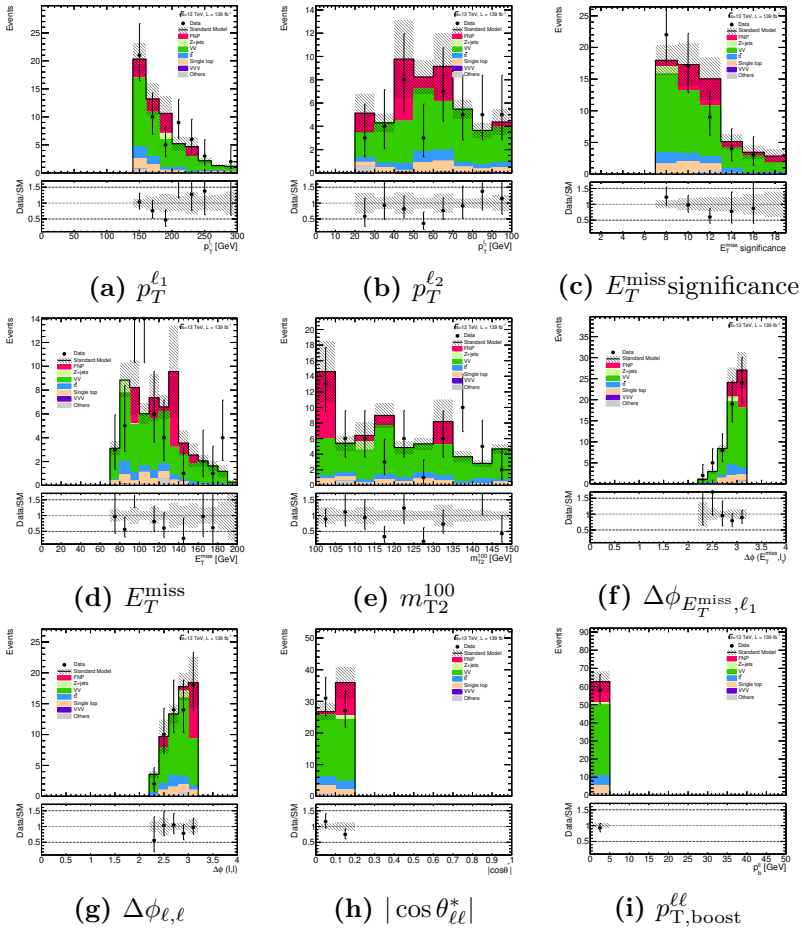

(a) $p_T^{\ell_1}$ (b) $p_T^{\ell_2}$ (c) E_T^{miss}significance

(d) E_T^{miss} (e) m_{T2}^{100} (f) $\Delta\phi_{E_T^{\text{miss}},\ell_1}$

(g) $\Delta\phi_{\ell,\ell}$ (h) $|\cos\theta^*_{\ell\ell}|$ (i) $p_{\text{T,boost}}^{\ell\ell}$

Figure 83: Data and MC distributions of the relevant variables in this analysis in SR-0jet. This corresponds to a cross-check of the modelling using pure MC instead of the data-driven flavour symmetric estimate. Only statistical uncertainties are shown.

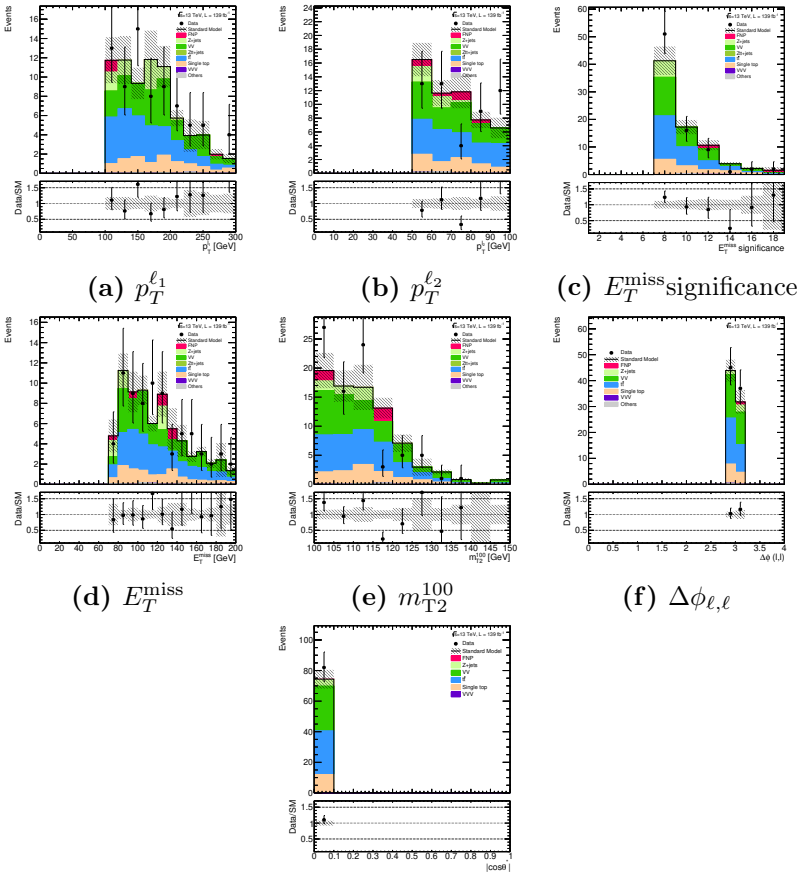

(a) $p_T^{\ell_1}$ **(b)** $p_T^{\ell_2}$ **(c)** E_T^{miss}significance

(d) E_T^{miss} **(e)** m_{T2}^{100} **(f)** $\Delta\phi_{\ell,\ell}$

(g) $|\cos\theta^*_{\ell\ell}|$

Figure 84: Data and MC distributions of the relevant variables in this analysis in SR-1jet. This corresponds to a cross-check of the modelling using pure MC instead of the data-driven flavour symmetric estimate. Only statistical uncertainties are shown.

Appendix H

Flavour symmetric background in $\mathrm{CR}^{\mathrm{eff}}$

In this chapter I show the data-MC agreement in $\mathrm{CR}^{\mathrm{eff}}$, which corresponds to the region where the efficiency correction factor κ is calculated in Chapter 6. Some important kinematic distributions are shown in Figure 85. In this figure, the "Flavour symmetric" background contribution (light blue) is estimated with the data-driven efficiency correction method described in Section 6.5. In both channels (ee and $\mu\mu$) the agreement looks healthy in all the kinematic variables used in the analysis. The dielectron channel is described better by the data, but potential mismodelling in $\mathrm{CR}^{\mathrm{eff}}$ could also be due to other backgrounds like Z+jets, due to its large contribution in this region. In fact, the dimuon trend is also observed when using MC (see Appendix G.1).

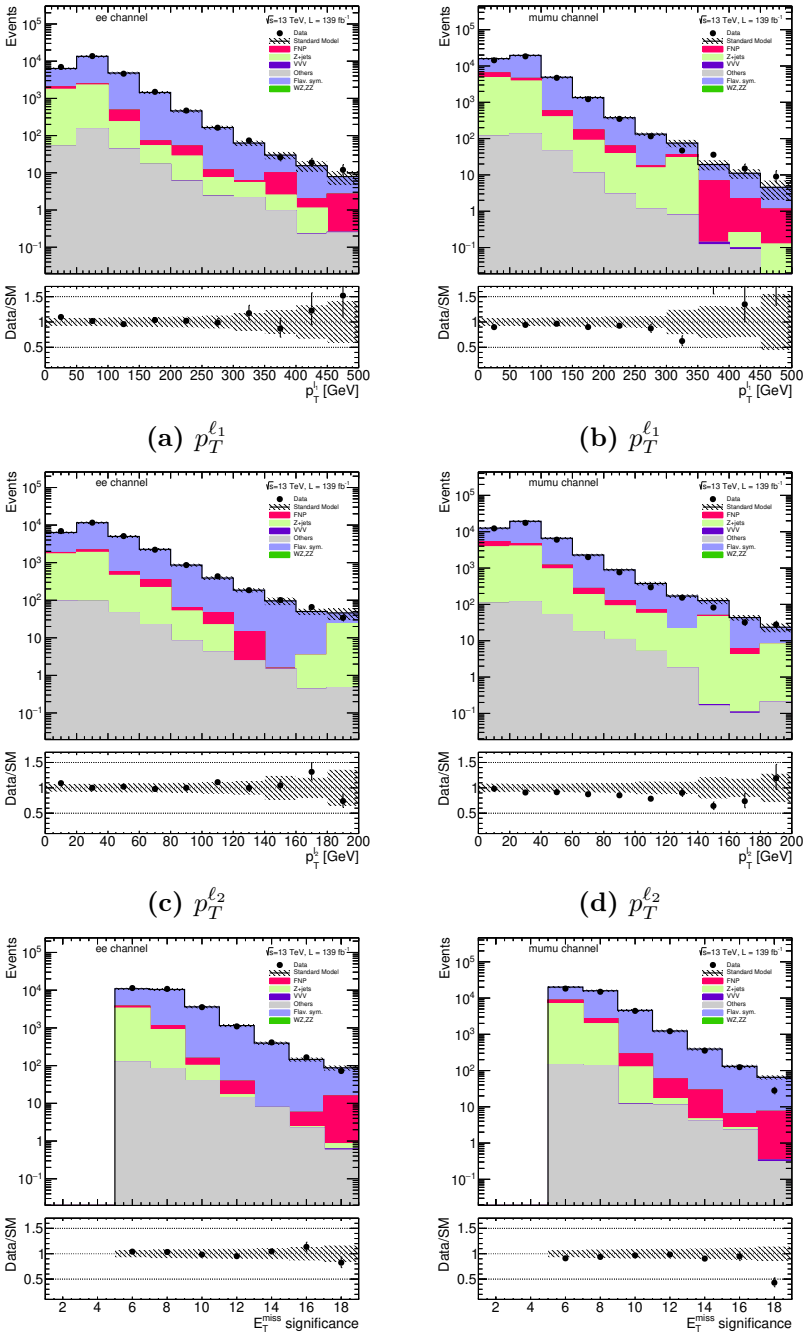

(a) $p_T^{\ell_1}$ **(b)** $p_T^{\ell_1}$

(c) $p_T^{\ell_2}$ **(d)** $p_T^{\ell_2}$

(e) E_T^{miss}significance **(f)** E_T^{miss}significance

Figure 85: Data and MC comparison in CR^{eff}. The "Flavour symmetric" background contribution (light blue) is estimated with the data-driven efficiency correction method described in Section 6.5. Statistical and systematic uncertainties are included for the Flavour symmetric background, whereas only statistical uncertainty is included for the minor backgrounds.

Appendix I

Additional tables

This chapter shows additional information on the specific SM background yields in the different regions used in the slepton search in Chapter 6.

- VR-0jet per m_{T2}^{100} bin in Table 32.
- VR-1jet per m_{T2}^{100} bin in Table 33.
- SR-0jet per m_{T2}^{100} bin in Table 34.
- SR-1jet per m_{T2}^{100} bin in Table 35.

VR-0jet - $m_{\mathrm{T2}}^{100} \in$	$[100-105]$	$[105-110]$	$[110-115]$	$[115-120]$	$[120-125]$	$[125-130]$	$[130-140]$	$[140-\infty)$
Observed events	42	17	16	17	17	26	27	19
MC exp. SM events	21.66 ± 10.51	13.55 ± 5.67	23.56 ± 6.41	18.23 ± 5.69	25.52 ± 6.09	20.86 ± 6.68	42.20 ± 9.64	19.86 ± 5.81
MC exp. other events	–	$0.00^{+0.01}_{-0.00}$	0.06 ± 0.02	0.00 ± 0.00	0.05 ± 0.03	0.00 ± 0.00	0.05 ± 0.05	0.00 ± 0.00
MC exp. VVV events	$0.01^{+0.01}_{-0.01}$	0.00 ± 0.00	0.01 ± 0.01	0.00 ± 0.00	$0.01^{+0.01}_{-0.01}$	0.01 ± 0.01	0.01 ± 0.00	0.01 ± 0.00
MC exp. ZZ events	0.00 ± 0.00	0.45 ± 0.18	1.68 ± 0.43	0.00 ± 0.00	0.00 ± 0.00	0.00 ± 0.00	1.32 ± 0.24	0.61 ± 0.15
MC exp. Zjets events	0.00 ± 0.00	0.00 ± 0.00	0.00 ± 0.00	0.00 ± 0.00	0.00 ± 0.00	$1.08^{+3.32}_{-1.08}$	$3.76^{+4.28}_{-3.76}$	$1.50^{+2.28}_{-1.50}$
MC exp. flavSym events	16.43 ± 8.19	13.10 ± 5.49	17.33 ± 4.87	18.18 ± 5.67	25.46 ± 6.08	19.77 ± 5.54	37.06 ± 7.81	17.74 ± 4.86
MC exp. FNP events	5.23 ± 3.32	0.00 ± 0.00	4.48 ± 1.50	$0.05^{+0.06}_{-0.05}$	0.00 ± 0.00	0.00 ± 0.00	0.00 ± 0.00	0.00 ± 0.00

Table 32: Expected and observed yields in the VR-0jet. The uncertainties on the SM background combine systematic and statistical uncertainties.

VR-1jet - $m_{T2}^{100} \in$	$[100-105]$	$[105-110]$	$[110-115]$	$[115-120]$	$[120-125]$	$[125-130]$	$[130-140]$	$[140-\infty)$
Observed events	115	111	115	80	55	15	14	5
MC exp. SM events	141.84 ± 31.74	92.24 ± 21.55	107.75 ± 24.54	68.20 ± 13.11	47.79 ± 10.12	22.01 ± 7.46	10.88 ± 5.26	$3.40^{+3.57}_{-3.40}$
MC exp. other events	1.03 ± 0.36	1.95 ± 0.37	0.97 ± 0.26	1.84 ± 1.25	0.46 ± 0.36	0.18 ± 0.12	$0.03^{+0.09}_{-0.03}$	$0.10^{+0.10}_{-0.10}$
MC exp. VVV events	0.02 ± 0.01	0.02 ± 0.00	0.01 ± 0.00	0.01 ± 0.00	0.01 ± 0.00	0.00 ± 0.00		-0.00 ± 0.00
MC exp. ZZ events	0.00 ± 0.00	0.00 ± 0.00	1.97 ± 0.31	0.00 ± 0.00	0.00 ± 0.00	0.00 ± 0.00	1.39 ± 0.43	0.00 ± 0.00
MC exp. Zjets events	19.98 ± 6.73	0.00 ± 0.00	15.33 ± 14.49	$1.20^{+3.07}_{-1.20}$	0.00 ± 0.00	1.15 ± 0.38	$0.09^{+3.88}_{-0.09}$	0.00 ± 0.00
flavSym events	109.85 ± 23.80	80.96 ± 19.21	78.86 ± 15.74	59.24 ± 11.16	42.26 ± 8.56	18.47 ± 5.43	9.36 ± 3.03	$3.30^{+3.48}_{-3.30}$
MC exp. FNP events	$10.95^{+12.35}_{-10.95}$	9.32 ± 6.16	10.61 ± 4.10	5.91 ± 2.00	5.06 ± 3.83	$2.22^{+4.01}_{-2.22}$	0.00 ± 0.00	0.00 ± 0.00

Table 33: Expected and observed yields in the VR-1jet. The uncertainties on the SM background combine systematic and statistical uncertainties.

$m_{T2}^{100} \in$	$[100, 105]$	$[105, 110]$	$[110, 115]$	$[115, 120]$	$[120, 125]$	$[125, 130]$	$[130, 140]$	$[140, \infty)$
Observed events	13	6	6	3	6	1	16	7
MC exp. SM events	15.90 ± 6.25	3.00 ± 3.00	9.47 ± 4.91	11.53 ± 4.92	8.90 ± 4.47	7.87 ± 4.11	18.15 ± 6.05	9.34 ± 4.38
MC exp. other events	$0.03^{+0.08}_{-0.03}$	0.00 ± 0.00	$0.03^{+0.03}_{-0.03}$	0.00 ± 0.00	0.00 ± 0.00	$0.01^{+0.05}_{-0.01}$	$0.05^{+0.06}_{-0.05}$	0.00 ± 0.00
MC exp. VVV events	0.01 ± 0.00	0.00 ± 0.00	–	0.00 ± 0.00	$0.00^{+0.07}_{-0.00}$	$0.00^{+0.02}_{-0.00}$	0.00 ± 0.00	0.00 ± 0.00
MC exp. ZZ events	0.64 ± 0.37	$0.01^{+0.38}_{-0.01}$	$0.01^{+0.01}_{-0.01}$	1.59 ± 1.47	$0.01^{+0.34}_{-0.01}$	$0.01^{+0.06}_{-0.01}$	$0.01^{+0.01}_{-0.01}$	2.98 ± 2.27
MC exp. Zjets events	$0.01^{+0.03}_{-0.01}$	$0.01^{+0.38}_{-0.01}$	$1.10^{+2.15}_{-1.10}$	$0.01^{+0.03}_{-0.01}$	$0.01^{+0.35}_{-0.01}$	$0.07^{+0.38}_{-0.07}$	$0.03^{+0.16}_{-0.03}$	$0.01^{+0.03}_{-0.01}$
flavSym events	6.58 ± 3.58	2.97 ± 2.77	7.54 ± 3.99	8.62 ± 4.18	8.87 ± 4.33	7.77 ± 4.07	15.96 ± 5.35	6.35 ± 3.74
MC exp. FNP events	8.63 ± 4.84	$0.01^{+0.38}_{-0.01}$	$0.78^{+1.08}_{-0.78}$	1.30 ± 1.21	$0.01^{+0.34}_{-0.01}$	$0.01^{+0.06}_{-0.01}$	$2.10^{+2.73}_{-2.10}$	0.01 ± 0.01

Table 34: Event yields in the 0-jet SR in each m_{T2}^{100} bin. The uncertainty includes both statistical and systematic contributions.

$m_{T2}^{100} \in$	$[100, 105]$	$[105, 110]$	$[110, 115]$	$[115, 120]$	$[120, 125]$	$[125, 130]$	$[130, 140]$	$[140, \infty$
Observed events	27	16	24	3	5	5	2	0
MC exp. SM events	11.70 ± 6.09	16.64 ± 5.66	14.35 ± 6.48	20.34 ± 5.88	5.58 ± 4.08	6.91 ± 3.89	4.62 ± 3.32	$2.40^{+2.49}_{-2.40}$
MC exp. other events	0.00 ± 0.00	$0.02^{+0.05}_{-0.02}$	$0.14^{+0.21}_{-0.14}$	0.23 ± 0.21	$0.01^{+0.02}_{-0.01}$	$0.03^{+0.54}_{-0.03}$	$0.05^{+0.06}_{-0.05}$	0.00 ± 0.00
MC exp. VVV events	0.01 ± 0.01	$0.00^{+0.01}_{-0.00}$	–	$0.01^{+0.01}_{-0.01}$	–	0.00 ± 0.00	–	0.00 ± 0.00
MC exp. ZZ events	2.02 ± 1.23	$0.05^{+0.12}_{-0.05}$	$0.01^{+0.01}_{-0.01}$	0.01 ± 0.01	$0.98^{+1.15}_{-0.98}$	$0.01^{+0.18}_{-0.01}$	$0.24^{+0.30}_{-0.24}$	$0.22^{+0.25}_{-0.22}$
MC exp. Zjets events	$1.65^{+2.40}_{-1.65}$	$0.53^{+1.44}_{-0.53}$	$2.28^{+4.34}_{-2.28}$	$0.01^{+0.46}_{-0.01}$	$0.18^{+0.22}_{-0.18}$	$0.01^{+0.18}_{-0.01}$	$0.09^{+0.51}_{-0.09}$	$0.02^{+0.32}_{-0.02}$
flavSym events	6.20 ± 4.71	16.04 ± 5.42	11.90 ± 4.64	17.78 ± 5.51	4.40 ± 3.84	6.85 ± 3.74	4.23 ± 3.25	$2.15^{+2.45}_{-2.15}$
MC exp. FNP events	1.81 ± 1.13	$0.01^{+0.03}_{-0.01}$	$0.01^{+0.02}_{-0.01}$	2.31 ± 1.83	$0.01^{+0.01}_{-0.01}$	$0.01^{+0.18}_{-0.01}$	$0.01^{+0.01}_{-0.01}$	$0.01^{+0.01}_{-0.01}$

Table 35: Event yields in the 1-jet SR in each m_{T2}^{100} bin. The uncertainty includes both statistical and systematic contributions.

Appendix J

Upper limits

Hypothesis tests

For a given observed data, it is crucial to be able to discriminate between two or more hypotheses, e.g., if the events contain only background or they contain background plus new physics signal. Suppose that two hypotheses are present, the *null hypothesis* H_0 and the *alternative hypothesis* H_1, and that the observed data consists of the measurement of a number of n variables $\mathbf{x} = (x_1, ..., x_n)$ randomly distributed according to some probability density function. A measurement on how compatible the observed data is with H_0 (or H_1) is given by the test statistic t, which is the value of a function of the measured sample $\mathbf{x}$, $t = t(\mathbf{x})$. If the number of observed events is adopted as test statistic, it is referred to as an event counting experiment.
A likelihood function is built for a set of observations $(\mathbf{x_1}, ..., \mathbf{x_N})$, with a set of (nuisance) parameters θ,

$$\mathcal{L}(\mathbf{x_1}, ..., \mathbf{x_N}; \theta) = Poiss \prod_{i=1}^{N} f(\mathbf{x}_i; \theta) = \frac{e^{-\nu(\theta)} \nu(\theta)^N}{N!} \prod_{i=1}^{N} f(\mathbf{x}_i; \theta), \tag{117}$$

where the $Poiss$ corresponds to a Poissonian factor corresponding to the probability of observing N events, being ν the expected number of events, and f are the probability density functions (PDFs). It is then desired to discriminate between the background-only hypothesis H_0 ($\nu = b$) and the signal (s) + background (b) hypothesis H_1 ($\nu = \mu s + b$), where the signal is scaled by μ, called *signal strength* (a value of $\mu = 0$ corresponds to a pure background distribution). The ratio of the likelihood function[1] evaluated under the hypotheses H_1 ($\mathcal{L}_{s+b}$) and H_0 ($\mathcal{L}_b$)

$$\lambda(\mu) = \frac{\mathcal{L}_{s+b}(\mathbf{x}; \mu, \theta)}{\mathcal{L}_b(\mathbf{x}; \theta)}, \tag{118}$$

[1] Different definitions of the likelihood ratio can be used for hypothesis testing, see [144].

defines the test statistic $t_\mu = -2\ln\lambda(\mu)$, which can be used as a measurement of the discrepancy between the data and a given hypothesis. With a single parameter of interest μ, if t_μ is plotted as a function of μ, the presence of a minimum at $\mu = \hat{\mu}$ could indicate the existence of a signal with signal strength $\hat{\mu}$.

The p-value

In order to claim a discovery given an observed data, it is required to determine whether the data sample is sufficiently inconsistent with the hypothesis that only background is present. In an event counting experiment, the probability p of counting a number of events greater or equal to the observed one in the case that the background-only hypothesis is true, is called p-value[2]. From the definition of p-value, the measurement of the inconsistency of the observed data with the background-only hypothesis is given by the *significance* (Z). The translation from p-value to significance is given by

$$p = \int_Z^\infty \frac{1}{\sqrt{2\pi}} e^{-x^2/2} dx = \frac{1}{2}\left[1 - \mathrm{erf}\left(\frac{Z}{\sqrt{2}}\right)\right]. \tag{119}$$

In particle physics, it is usually referred to as *observation* of the signal under investigation if the significance is at least 3σ ($Z = 3$). A discovery of the signal is claimed when the significance reaches 5σ ($Z = 5$). In order to exclude a signal hypothesis, a p-value below 0.05 is required (i.e., 95% confidence level), which corresponds to $Z = 1.64$.

The CL_s method

In the absence of any significant event excess in the observed data, upper limits and/or exclusion limits can be set on any signal model. To do so, two p-values are defined

$$\begin{aligned} \mathrm{CL}_{s+b}(\theta) &\equiv P_{s+b}(\lambda(\theta) \leq \tilde{\lambda}|\mu), \\ \mathrm{CL}_b(\theta) &\equiv P_b(\lambda(\theta) \leq \tilde{\lambda}|\mu = 0), \end{aligned} \tag{120}$$

which correspond to the signal+background and background-only hypothesis, respectively, for an observed $\lambda = \tilde{\lambda}$. From these p-values, the CL_s method [145] is defined as

$$\mathrm{CL}_s(\theta) = \frac{\mathrm{CL}_{s+b}(\theta)}{\mathrm{CL}_b(\theta)}. \tag{121}$$

[2]The largest p-value corresponds to the scenario that is more compatible with data.

The 95% confidence level (CL) limit on the signal strength μ is found by adjusting μ until $\mathrm{CL}_s(\mu) = 0.05$. The procedure can be repeated for different signal parameter assumptions (e.g. varying the mass of the signal) and a given model is excluded at 95% CL for a particular mass if $\mu(95\%\ \mathrm{CL}) < 1$. Usually, due to their complexity, CL_{s+b} and CL_b, are not obtained analytically and are determined numerically using randomly generated pseudo-experiments (toy Monte Carlo). The values of CL_{s+b} and CL_b are the fraction of generated pseudo-experiments with $\lambda(\theta) \leq \tilde{\lambda}$, assuming the presence of signal+background and background only, respectively. Since large amounts of pseudo-experiments can be computationally expensive, for large statistics asymptotic formulae are used as an approximation [144]. An example of test statistic distributions using toy Monte Carlo is illustrated in Figure 86.

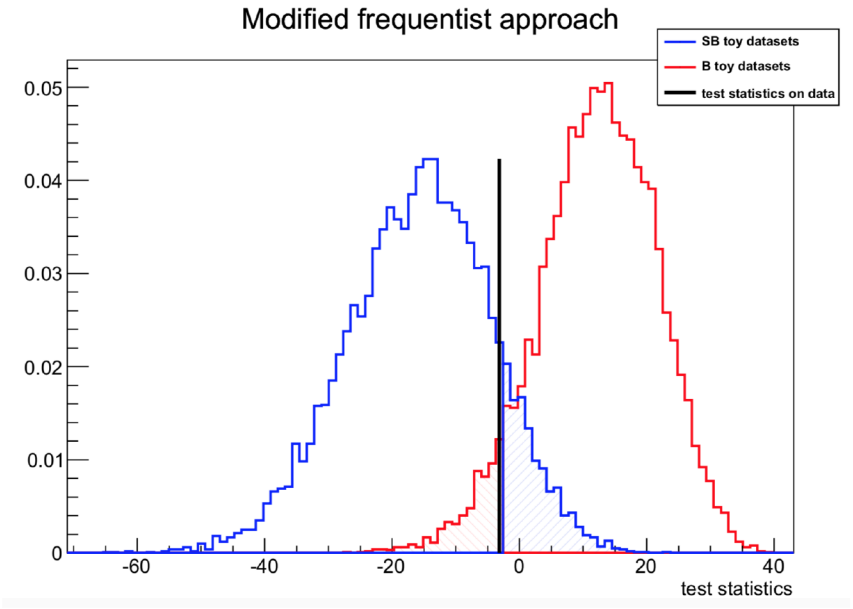

Figure 86: Example distribution of the test statistic $t_\mu = -2\ln\lambda$ for the background-only hypothesis (red) and signal+background hypothesis (blue). The black line corresponds to the test statistic measured in data. The hatched areas correspond to $1-\mathrm{CL}_b$ (red) and CL_{s+b} (blue). Figure taken from [160, 161].

List of Figures

List of Tables

Bibliography

[1] Cush, Public domain, via Wikimedia Commons, "See wikipedia, standard model," 2004. [Online; accessed 11-March-2021, 20:50 GMT].

[2] ATLAS Collaboration, "Observation of a new particle in the search for the Standard Model Higgs boson with the ATLAS detector at the LHC," *Phys. Lett. B*, vol. 716, pp. 1–29, 2012.

[3] CMS Collaboration, "Observation of a New Boson at a Mass of 125 GeV with the CMS Experiment at the LHC," *Phys. Lett. B*, vol. 716, pp. 30–61, 2012.

[4] S. Weinberg, "A model of leptons," *Phys. Rev. Lett.*, vol. 19, pp. 1264–1266, Nov 1967.

[5] A. Salam, "Weak and Electromagnetic Interactions," *Conf. Proc. C*, vol. 680519, pp. 367–377, 1968.

[6] S. Glashow, "Partial Symmetries of Weak Interactions," *Nucl. Phys.*, vol. 22, pp. 579–588, 1961.

[7] G. 't Hooft and M. Veltman, "Regularization and renormalization of gauge fields," *Nuclear Physics B*, vol. 44, no. 1, pp. 189 – 213, 1972.

[8] F. Englert and R. Brout, "Broken symmetry and the mass of gauge vector mesons," *Phys. Rev. Lett.*, vol. 13, pp. 321–323, Aug 1964.

[9] G. S. Guralnik, C. R. Hagen, and T. W. B. Kibble, "Global conservation laws and massless particles," *Phys. Rev. Lett.*, vol. 13, pp. 585–587, Nov 1964.

[10] P. W. Higgs, "Spontaneous symmetry breakdown without massless bosons," *Phys. Rev.*, vol. 145, pp. 1156–1163, May 1966.

[11] H. Fritzsch and M. Gell-Mann, "Current algebra: Quarks and what else?," *eConf*, vol. C720906V2, pp. 135–165, 1972.

[12] D. J. Gross and F. Wilczek, "Ultraviolet behavior of non-abelian gauge theories," *Phys. Rev. Lett.*, vol. 30, pp. 1343–1346, Jun 1973.

[13] S. Weinberg, "Non-abelian gauge theories of the strong interactions," *Phys. Rev. Lett.*, vol. 31, pp. 494–497, Aug 1973.

[14] T. Aoyama *et al.*, "The anomalous magnetic moment of the muon in the Standard Model," 6 2020.

[15] M. Abdughani, K.-I. Hikasa, L. Wu, J. M. Yang, and J. Zhao, "Testing electroweak SUSY for muon $g-2$ and dark matter at the LHC and beyond," *JHEP*, vol. 11, p. 095, 2019.

[16] M. Endo, K. Hamaguchi, S. Iwamoto, and T. Kitahara, "Muon $g-2$ vs LHC Run 2 in supersymmetric models," *JHEP*, vol. 04, p. 165, 2020.

[17] L. J. Hall and M. B. Wise, "Flavor changing higgs boson couplings," *Nuclear Physics B*, vol. 187, no. 3, pp. 397 – 408, 1981.

[18] S. L. Glashow and S. Weinberg, "Natural Conservation Laws for Neutral Currents," *Phys. Rev. D*, vol. 15, p. 1958, 1977.

[19] P. Ade *et al.*, "Planck 2015 results. XIII. Cosmological parameters," *Astron. Astrophys.*, vol. 594, p. A13, 2016.

[20] E. Komatsu, K. M. Smith, J. Dunkley, C. L. Bennett, B. Gold, G. Hinshaw, N. Jarosik, D. Larson, M. R. Nolta, L. Page, and et al., "Seven-year wilkinson microwave anisotropy probe (wmap) observations: Cosmological interpretation," *The Astrophysical Journal Supplement Series*, vol. 192, p. 18, Jan 2011.

[21] N. Arkani-Hamed, A. Delgado, and G. Giudice, "The Well-tempered neutralino," *Nucl. Phys. B*, vol. 741, pp. 108–130, 2006.

[22] K. Kowalska and E. M. Sessolo, "The discreet charm of higgsino dark matter - a pocket review," *Adv. High Energy Phys.*, vol. 2018, p. 6828560, 2018.

[23] ALEPH, DELPHI, L3, OPAL Experiments, "Combined LEP Chargino Results, up to 208 GeV for low DM," Tech. Rep. LEPSUSYWG/02-04.1, CERN, Geneva, Sep 2002.

[24] D. Barducci, A. Belyaev, A. K. M. Bharucha, W. Porod, and V. Sanz, "Uncovering Natural Supersymmetry via the interplay between the LHC and Direct Dark Matter Detection," *JHEP*, vol. 07, p. 066, 2015.

[25] M. Cirelli, N. Fornengo, and A. Strumia, "Minimal dark matter," *Nucl. Phys. B*, vol. 753, pp. 178–194, 2006.

[26] M. Beneke, R. Szafron, and K. Urban, "Sommerfeld-corrected relic abundance of wino dark matter with NLO electroweak potentials," 9 2020.

[27] M. Dine, W. Fischler, and M. Srednicki, "A simple solution to the strong cp problem with a harmless axion," *Physics Letters B*, vol. 104, no. 3, pp. 199 – 202, 1981.

[28] R. Peccei, "The Strong CP problem and axions," *Lect. Notes Phys.*, vol. 741, pp. 3–17, 2008.

[29] H. Baer, V. Barger, S. Salam, D. Sengupta, and K. Sinha, "Midi-review: Status of weak scale supersymmetry after LHC Run 2 and ton-scale noble liquid WIMP searches," 2 2020.

[30] P. A. M. Dirac and R. H. Fowler, "The quantum theory of the electron," *Proceedings of the Royal Society of London. Series A, Containing Papers of a Mathematical and Physical Character*, vol. 117, no. 778, pp. 610–624, 1928.

[31] P. A. M. Dirac and R. H. Fowler, "The quantum theory of the electron. part ii," *Proceedings of the Royal Society of London. Series A, Containing Papers of a Mathematical and Physical Character*, vol. 118, no. 779, pp. 351–361, 1928.

[32] J. Schwinger, "On quantum-electrodynamics and the magnetic moment of the electron," *Phys. Rev.*, vol. 73, pp. 416–417, Feb 1948.

[33] G. Bennett *et al.*, "Final Report of the Muon E821 Anomalous Magnetic Moment Measurement at BNL," *Phys. Rev. D*, vol. 73, p. 072003, 2006.

[34] B. Abi *et al.*, "Measurement of the Positive Muon Anomalous Magnetic Moment to 0.46 ppm," *Phys. Rev. Lett.*, vol. 126, p. 2021, 4 2021.

[35] T. Moroi, "The Muon anomalous magnetic dipole moment in the minimal supersymmetric standard model," *Phys. Rev. D*, vol. 53, pp. 6565–6575, 1996. [Erratum: Phys.Rev.D 56, 4424 (1997)].

[36] H. Fargnoli, C. Gnendiger, S. Paßehr, D. Stöckinger, and H. Stöckinger-Kim, "Two-loop corrections to the muon magnetic moment from fermion/sfermion loops in the MSSM: detailed results," *JHEP*, vol. 02, p. 070, 2014.

[37] G.-C. Cho, K. Hagiwara, Y. Matsumoto, and D. Nomura, "The MSSM confronts the precision electroweak data and the muon g-2," *JHEP*, vol. 11, p. 068, 2011.

[38] M. Bach, J.-h. Park, D. Stöckinger, and H. Stöckinger-Kim, "Large muon $(g-2)$ with TeV-scale SUSY masses for $\tan\beta \to \infty$," *JHEP*, vol. 10, p. 026, 2015.

[39] M. Endo, K. Hamaguchi, S. Iwamoto, and T. Kitahara, "Supersymmetric Interpretation of the Muon $g-2$ Anomaly," 4 2021.

[40] E. Bagnaschi *et al.*, "Likelihood Analysis of the pMSSM11 in Light of LHC 13-TeV Data," *Eur. Phys. J. C*, vol. 78, no. 3, p. 256, 2018.

[41] J. M. Butterworth, G. Dissertori, and G. P. Salam, "Hard Processes in Proton-Proton Collisions at the Large Hadron Collider," *Ann. Rev. Nucl. Part. Sci.*, vol. 62, pp. 387–405, 2012.

[42] R. D. Ball *et al.*, "Parton distributions for the LHC Run II," *JHEP*, vol. 04, p. 040, 2015.

[43] B. Andersson, G. Gustafson, G. Ingelman, and T. Sjöstrand, "Parton fragmentation and string dynamics," *Physics Reports*, vol. 97, no. 2, pp. 31 – 145, 1983.

[44] T. Sjöstrand, "The PYTHIA Event Generator: Past, Present and Future," *Comput. Phys. Commun.*, vol. 246, p. 106910, 2020.

[45] J.-C. Winter, F. Krauss, and G. Soff, "A Modified cluster hadronization model," *Eur. Phys. J. C*, vol. 36, pp. 381–395, 2004.

[46] M. Schonherr and F. Krauss, "Soft Photon Radiation in Particle Decays in SHERPA," *JHEP*, vol. 12, p. 018, 2008.

[47] K. Hamilton and P. Richardson, "Simulation of QED radiation in particle decays using the YFS formalism," *JHEP*, vol. 07, p. 010, 2006.

[48] T. Sjostrand, S. Mrenna, and P. Z. Skands, "A Brief Introduction to PYTHIA 8.1," *Comput. Phys. Commun.*, vol. 178, pp. 852–867, 2008.

[49] S. Agostinelli *et al.*, "GEANT4–a simulation toolkit," *Nucl. Instrum. Meth. A*, vol. 506, pp. 250–303, 2003.

[50] ATLAS Collaboration, "The ATLAS Simulation Infrastructure," *Eur. Phys. J. C*, vol. 70, pp. 823–874, 2010.

[51] S. P. Martin, "A Supersymmetry primer," *Adv. Ser. Direct. High Energy Phys.*, vol. 21, pp. 1–153, 2010.

[52] LHC SUSY Cross Section Working Group, "Cross-section plots." `https://twiki.cern.ch/twiki/bin/view/LHCPhysics/SUSYCrossSections`, April 2020.

[53] J. Alwall, P. Schuster, and N. Toro, "Simplified Models for a First Characterization of New Physics at the LHC," *Phys. Rev. D*, vol. 79, p. 075020, 2009.

[54] E. Mobs, "The CERN accelerator complex - 2019. Complexe des accélérateurs du CERN - 2019," Jul 2019. General Photo.

[55] ATLAS Experiment, "Multiple Year Collision Plots." `https://twiki.cern.ch/twiki/bin/view/AtlasPublic/LuminosityPublicResultsRun2`.

[56] ATLAS Collaboration, "Luminosity determination in pp collisions at $\sqrt{s} = 8$ TeV using the ATLAS detector at the LHC," *Eur. Phys. J. C*, vol. 76, no. 12, p. 653, 2016.

[57] G. Antchev *et al.*, "First measurement of elastic, inelastic and total cross-section at $\sqrt{s} = 13$ TeV by TOTEM and overview of cross-section data at LHC energies," *Eur. Phys. J. C*, vol. 79, no. 2, p. 103, 2019.

[58] ATLAS Collaboration, "The ATLAS Experiment at the CERN Large Hadron Collider," *JINST*, vol. 3, p. S08003, 2008.

[59] McFayden, Josh, "The LHC and ATLAS Detector."

[60] ATLAS Experiment, "Keeping the ATLAS Inner Detector in perfect alignment." https://atlas.cern/updates/experiment-briefing/inner-detector-alignment.

[61] ATLAS Collaboration, "Expected Tracking Performance of the ATLAS Inner Tracker at the HL-LHC," Tech. Rep. ATL-PHYS-PUB-2019-014, CERN, Geneva, Mar 2019.

[62] A. Rosenfeld and J. L. Pfaltz, "Sequential operations in digital picture processing.," *J. ACM*, vol. 13, no. 4, pp. 471–494, 1966.

[63] R. Frühwirth, "Application of kalman filtering to track and vertex fitting," *Nuclear Instruments and Methods in Physics Research Section A: Accelerators, Spectrometers, Detectors and Associated Equipment*, vol. 262, no. 2, pp. 444 – 450, 1987.

[64] S. Marzani, G. Soyez, and M. Spannowsky, *Looking inside jets: an introduction to jet substructure and boosted-object phenomenology*, vol. 958. Springer, 2019.

[65] ATLAS Collaboration, "Electron reconstruction and identification in the ATLAS experiment using the 2015 and 2016 LHC proton-proton collision data at $\sqrt{s}$ = 13 TeV," *Eur. Phys. J. C*, vol. 79, no. 8, p. 639, 2019.

[66] ATLAS Collaboration, "Muon reconstruction performance of the ATLAS detector in proton–proton collision data at $\sqrt{s}$ =13 TeV," *Eur. Phys. J. C*, vol. 76, no. 5, p. 292, 2016.

[67] M. Cacciari, G. P. Salam, and G. Soyez, "The anti-k_t jet clustering algorithm," *JHEP*, vol. 04, p. 063, 2008.

[68] ATLAS Collaboration, "Jet reconstruction and performance using particle flow with the ATLAS Detector," *Eur. Phys. J. C*, vol. 77, no. 7, p. 466, 2017.

[69] ATLAS Collaboration, "Jet energy scale measurements and their systematic uncertainties in proton-proton collisions at $\sqrt{s}$ = 13 TeV with the ATLAS detector," *Phys. Rev. D*, vol. 96, no. 7, p. 072002, 2017.

[70] ATLAS Collaboration, "Optimisation and performance studies of the ATLAS b-tagging algorithms for the 2017-18 LHC run," Tech. Rep. ATL-PHYS-PUB-2017-013, CERN, Geneva, Jul 2017.

[71] ATLAS Collaboration, "ATLAS b-jet identification performance and efficiency measurement with $t\bar{t}$ events in pp collisions at $\sqrt{s}$ = 13 TeV," *Eur. Phys. J. C*, vol. 79, no. 11, p. 970, 2019.

[72] ATLAS Collaboration, "Tagging and suppression of pileup jets with the ATLAS detector," Tech. Rep. ATLAS-CONF-2014-018, CERN, Geneva, May 2014.

[73] ATLAS Collaboration, "Pile-up subtraction and suppression for jets in ATLAS," Tech. Rep. ATLAS-CONF-2013-083, CERN, Geneva, Aug 2013.

[74] ATLAS Collaboration, "Object-based missing transverse momentum significance in the ATLAS detector," Tech. Rep. ATLAS-CONF-2018-038, CERN, Geneva, Jul 2018.

[75] C. Anastasiou, C. Duhr, F. Dulat, F. Herzog, and B. Mistlberger, "Higgs Boson Gluon-Fusion Production in QCD at Three Loops," *Phys. Rev. Lett.*, vol. 114, p. 212001, 2015.

[76] ATLAS Collaboration, "Search for chargino-neutralino production using recursive jigsaw reconstruction in final states with two or three charged leptons in proton-proton collisions at $\sqrt{s} = 13$ TeV with the ATLAS detector," *Phys. Rev.*, vol. D98, no. 9, p. 092012, 2018.

[77] ATLAS Collaboration, "Search for new phenomena using the invariant mass distribution of same-flavour opposite-sign dilepton pairs in events with missing transverse momentum in $\sqrt{s} = 13$ TeV pp collisions with the ATLAS detector," *Eur. Phys. J.*, vol. C78, no. 8, p. 625, 2018.

[78] ATLAS Collaboration, "Search for heavy ZZ resonances in the $\ell^+\ell^-\ell^+\ell^-$ and $\ell^+\ell^-\nu\bar{\nu}$ final states using proton–proton collisions at $\sqrt{s} = 13$ TeV with the ATLAS detector," *Eur. Phys. J. C*, vol. 78, no. 4, p. 293, 2018.

[79] CMS Collaboration, "Search for a new scalar resonance decaying to a pair of Z bosons in proton-proton collisions at $\sqrt{s} = 13$ TeV," *JHEP*, vol. 06, p. 127, 2018. [Erratum: JHEP 03, 128 (2019)].

[80] ATLAS Collaboration, "Search for an invisibly decaying Higgs boson or dark matter candidates produced in association with a Z boson in pp collisions at $\sqrt{s} = 13$ TeV with the ATLAS detector," *Phys. Lett.*, vol. B776, pp. 318–337, 2018.

[81] CMS Collaboration, "Searches for invisible decays of the Higgs boson in pp collisions at $\sqrt{s} = 7$, 8, and 13 TeV," *JHEP*, vol. 02, p. 135, 2017.

[82] CMS Collaboration, "Search for new phenomena in final states with two opposite-charge, same-flavor leptons, jets, and missing transverse momentum in pp collisions at $\sqrt{s} = 13$ TeV," *JHEP*, vol. 03, p. 076, 2018.

[83] J. Ohnemus and J. F. Owens, "Order-α_s calculation of hadronic zz production," *Phys. Rev. D*, vol. 43, pp. 3626–3639, Jun 1991.

[84] B. Mele, P. Nason, and G. Ridolfi, "Qcd radiative corrections to z boson pair production in hadronic collisions," *Nuclear Physics B*, vol. 357, no. 2, pp. 409 – 438, 1991.

[85] J. Ohnemus, "Order-α_s calculations of hadronic $W^{\pm}\gamma$ and $z\gamma$ production," *Phys. Rev. D*, vol. 47, pp. 940–955, Feb 1993.

[86] U. Baur, T. Han, and J. Ohnemus, "Qcd corrections and anomalous couplings in $z\gamma$ production at hadron colliders," *Phys. Rev. D*, vol. 57, pp. 2823–2836, Mar 1998.

[87] F. Cascioli, T. Gehrmann, M. Grazzini, S. Kallweit, P. Maierhöfer, A. von Manteuffel, S. Pozzorini, D. Rathlev, L. Tancredi, and E. Weihs, "ZZ production at hadron colliders in NNLO QCD," *Phys. Lett.*, vol. B735, pp. 311–313, 2014.

[88] M. Grazzini, S. Kallweit, and D. Rathlev, "$W\gamma$ and $Z\gamma$ production at the LHC in NNLO QCD," *JHEP*, vol. 07, p. 085, 2015.

[89] M. Grazzini, S. Kallweit, M. Wiesemann, and J. Y. Yook, "ZZ production at the LHC: NLO QCD corrections to the loop-induced gluon fusion channel," 2018.

[90] W. Hollik and C. Meier, "Electroweak corrections to gamma Z production at hadron colliders," *Phys. Lett.*, vol. B590, pp. 69–75, 2004.

[91] E. Accomando, A. Denner, and C. Meier, "Electroweak corrections to $W\gamma$ and $Z\gamma$ production at the LHC," *Eur. Phys. J.*, vol. C47, pp. 125–146, 2006.

[92] A. Denner, S. Dittmaier, M. Hecht, and C. Pasold, "NLO QCD and electroweak corrections to $Z + \gamma$ production with leptonic Z-boson decays," *JHEP*, vol. 02, p. 057, 2016.

[93] S. Kallweit, J. M. Lindert, S. Pozzorini, and M. Schönherr, "NLO QCD+EW predictions for $2\ell 2\nu$ diboson signatures at the LHC," *JHEP*, vol. 11, p. 120, 2017.

[94] A. Bierweiler, T. Kasprzik, and J. H. Kühn, "Vector-boson pair production at the LHC to $\mathcal{O}(\alpha^3)$ accuracy," *JHEP*, vol. 12, p. 071, 2013.

[95] J. Baglio, L. D. Ninh, and M. M. Weber, "Massive gauge boson pair production at the LHC: a next-to-leading order story," *Phys. Rev.*, vol. D88, p. 113005, 2013. [Erratum: Phys. Rev.D94,no.9,099902(2016)].

[96] M. Schönherr, "An automated subtraction of NLO EW infrared divergences," *Eur. Phys. J. C*, vol. 78, no. 2, p. 119, 2018.

[97] M. Grazzini, S. Kallweit, J. M. Lindert, S. Pozzorini, and M. Wiesemann, "NNLO QCD + NLO EW with Matrix+OpenLoops: precise predictions for vector-boson pair production," *JHEP*, vol. 02, p. 087, 2020.

[98] F. Buccioni, J.-N. Lang, J. M. Lindert, P. Maierhöfer, S. Pozzorini, H. Zhang, and M. F. Zoller, "OpenLoops 2," *Eur. Phys. J. C*, vol. 79, no. 10, p. 866, 2019.

[99] M. Grazzini, S. Kallweit, and M. Wiesemann, "Fully differential NNLO computations with MATRIX," *Eur. Phys. J.*, vol. C78, no. 7, p. 537, 2018.

[100] S. Dulat, T.-J. Hou, J. Gao, M. Guzzi, J. Huston, P. Nadolsky, J. Pumplin, C. Schmidt, D. Stump, and C. P. Yuan, "New parton distribution functions from a global analysis of quantum chromodynamics," *Phys. Rev.*, vol. D93, no. 3, p. 033006, 2016.

[101] S. Frixione, "Isolated photons in perturbative QCD," *Phys. Lett.*, vol. B429, pp. 369–374, 1998.

[102] J. M. Lindert *et al.*, "Precise predictions for $V+$ jets dark matter backgrounds," *Eur. Phys. J.*, vol. C77, no. 12, p. 829, 2017.

[103] M. Grazzini, S. Kallweit, and S. Devoto, "Private communication,"

[104] J. R. Andersen *et al.*, "Les Houches 2013: Physics at TeV Colliders: Standard Model Working Group Report," 2014.

[105] S. Catani, M. Fontannaz, J. P. Guillet, and E. Pilon, "Isolating Prompt Photons with Narrow Cones," *JHEP*, vol. 09, p. 007, 2013.

[106] J. M. Campbell, R. K. Ellis, and C. Williams, "Driving missing data at the LHC: NNLO predictions for the ratio of $\gamma + j$ and $Z + j$," *Phys. Rev.*, vol. D96, no. 1, p. 014037, 2017.

[107] Z. Bern, G. Diana, L. J. Dixon, F. Febres Cordero, S. Hoche, H. Ita, D. A. Kosower, D. Maitre, and K. J. Ozeren, "Driving Missing Data at Next-to-Leading Order," *Phys. Rev.*, vol. D84, p. 114002, 2011.

[108] J. M. Campbell, T. Neumann, and C. Williams, "$Z\gamma$ Production at NNLO Including Anomalous Couplings," *JHEP*, vol. 11, p. 150, 2017.

[109] J. M. Campbell, R. K. Ellis, and C. Williams, "Vector boson pair production at the LHC," *JHEP*, vol. 07, p. 018, 2011.

[110] L. Cieri, "Diphoton isolation studies," *Nucl. Part. Phys. Proc.*, vol. 273-275, pp. 2033–2039, 2016.

[111] S. Catani, L. Cieri, D. de Florian, G. Ferrera, and M. Grazzini, "Diphoton production at the LHC: a QCD study up to NNLO," *JHEP*, vol. 04, p. 142, 2018.

[112] L. Bourhis, M. Fontannaz, and J. P. Guillet, "Quarks and gluon fragmentation functions into photons," *Eur. Phys. J.*, vol. C2, pp. 529–537, 1998.

[113] A. Gehrmann-De Ridder and E. W. N. Glover, "Final state photon production at LEP," *Eur. Phys. J.*, vol. C7, pp. 29–48, 1999.

[114] A. Gehrmann-De Ridder, T. Gehrmann, and E. Poulsen, "Measuring the Photon Fragmentation Function at HERA," *Eur. Phys. J.*, vol. C47, pp. 395–411, 2006.

[115] J. Butterworth *et al.*, "PDF4LHC recommendations for LHC Run II," *J. Phys.*, vol. G43, p. 023001, 2016.

[116] B. Fuks, M. Klasen, D. R. Lamprea, and M. Rothering, "Revisiting slepton pair production at the Large Hadron Collider," *JHEP*, vol. 01, p. 168, 2014.

[117] ATLAS Collaboration, "Search for electroweak production of charginos and sleptons decaying into final states with two leptons and missing transverse momentum in $\sqrt{s} = 13$ TeV pp collisions using the ATLAS detector," *Eur. Phys. J. C*, vol. 80, no. 2, p. 123, 2020.

[118] ATLAS Collaboration, "Search for direct production of charginos, neutralinos and sleptons in final states with two leptons and missing transverse momentum in pp collisions at $\sqrt{s} = 8$ TeV with the ATLAS detector," *JHEP*, vol. 05, p. 071, 2014.

[119] A. M. Sirunyan *et al.*, "Search for supersymmetric partners of electrons and muons in proton-proton collisions at $\sqrt{s} = 13$ TeV," *Phys. Lett. B*, vol. 790, pp. 140–166, 2019.

[120] ATLAS Collaboration, "Performance of electron and photon triggers in ATLAS during LHC Run 2," *Eur. Phys. J. C*, vol. 80, no. 1, p. 47, 2020.

[121] ATLAS Collaboration, "Performance of the ATLAS muon triggers in Run 2," *JINST*, vol. 15, no. 09, p. P09015, 2020.

[122] P. Nason, "A new method for combining NLO QCD with shower Monte Carlo algorithms," *JHEP*, vol. 11, p. 040, 2004.

[123] S. Frixione, P. Nason, and C. Oleari, "Matching NLO QCD computations with Parton Shower simulations: the POWHEG method," *JHEP*, vol. 11, p. 070, 2007.

[124] S. Alioli, P. Nason, C. Oleari, and E. Re, "A general framework for implementing NLO calculations in shower Monte Carlo programs: the POWHEG BOX," *JHEP*, vol. 06, p. 043, 2010.

[125] ATLAS Collaboration, "Studies on top-quark Monte Carlo modelling for Top2016." ATL-PHYS-PUB-2016-020, 2016.

[126] T. Sjöstrand, S. Ask, J. R. Christiansen, R. Corke, N. Desai, P. Ilten, S. Mrenna, S. Prestel, C. O. Rasmussen, and P. Z. Skands, "An Introduction to PYTHIA 8.2," *Comput. Phys. Commun.*, vol. 191, p. 159, 2015.

[127] ATLAS Collaboration, "ATLAS Pythia 8 tunes to 7 TeV data." ATL-PHYS-PUB-2014-021, 2014.

[128] R. D. Ball *et al.*, "Parton distributions with LHC data," *Nucl. Phys. B*, vol. 867, p. 244, 2013.

[129] D. J. Lange, "The EvtGen particle decay simulation package," *Nucl. Instrum. Meth. A*, vol. 462, p. 152, 2001.

[130] S. Frixione, E. Laenen, P. Motylinski, B. R. Webber, and C. D. White, "Single-top hadroproduction in association with a W boson," *JHEP*, vol. 07, p. 029, 2008.

[131] J. Alwall *et al.*, "The automated computation of tree-level and next-to-leading order differential cross sections, and their matching to parton shower simulations," *JHEP*, vol. 07, p. 079, 2014.

[132] E. Bothmann *et al.*, "Event Generation with Sherpa 2.2," *SciPost Phys.*, vol. 7, p. 034, 2019.

[133] ATLAS Collaboration, "Searches for electroweak production of supersymmetric particles with compressed mass spectra in $\sqrt{s} = 13$ TeV pp collisions with the ATLAS detector," *Phys. Rev. D*, vol. 101, no. 5, p. 052005, 2020.

[134] "Formulae for Estimating Significance," Tech. Rep. ATL-PHYS-PUB-2020-025, CERN, Geneva, Sep 2020.

[135] A. Barr, "Measuring slepton spin at the LHC," *JHEP*, vol. 02, p. 042, 2006.

[136] C. G. Lester and D. J. Summers, "Measuring masses of semi-invisibly decaying particles pair produced at hadron colliders," *Phys. Lett. B*, vol. 463, pp. 99–103, 1999.

[137] A. Barr, C. G. Lester, and P. Stephens, "A variable for measuring masses at hadron colliders when missing energy is expected; m_{T2}: the truth behind the glamour," *J. Phys. G*, vol. 29, pp. 2343–2363, 2003.

[138] ALEPH, DELPHI, L3, OPAL Experiments, "Combined LEP Chargino Results, up to 208 GeV for low DM." `http://lepsusy.web.cern.ch/lepsusy/www/sleptons_summer04/slep_final.html`, Sep 2002.

[139] ATLAS Collaboration, "Measurement of the top quark-pair production cross section with ATLAS in pp collisions at $\sqrt{s} = 7$ TeV," *Eur. Phys. J. C*, vol. 71, p. 1577, 2011.

[140] ATLAS Collaboration, "Jet Calibration and Systematic Uncertainties for Jets Reconstructed in the ATLAS Detector at $\sqrt{s} = 13$ TeV," Tech. Rep. ATL-PHYS-PUB-2015-015, CERN, Geneva, Jul 2015.

[141] ATLAS Collaboration, "Electron and photon performance measurements with the ATLAS detector using the 2015–2017 LHC proton-proton collision data," *JINST*, vol. 14, no. 12, p. P12006, 2019.

[142] ATLAS Collaboration, "$E_{\mathrm{T}}^{\mathrm{miss}}$ performance in the ATLAS detector using 2015-2016 LHC p-p collisions," Tech. Rep. ATLAS-CONF-2018-023, CERN, Geneva, Jun 2018.

[143] M. Baak, G. J. Besjes, D. Côte, A. Koutsman, J. Lorenz, and D. Short, "HistFitter software framework for statistical data analysis," *Eur. Phys. J. C*, vol. 75, p. 153, 2015.

[144] G. Cowan, K. Cranmer, E. Gross, and O. Vitells, "Asymptotic formulae for likelihood-based tests of new physics," *Eur. Phys. J. C*, vol. 71, p. 1554, 2011. [Erratum: Eur. Phys. J. C **73** (2013) 2501].

[145] A. L. Read, "Presentation of search results: the cl_s technique," *Journal of Physics G: Nuclear and Particle Physics*, vol. 28, p. 2693, 2002.

[146] A. Aboubrahim, M. Klasen, and P. Nath, "What Fermilab $(g-2)_\mu$ experiment tells us about discovering SUSY at HL-LHC and HE-LHC," 4 2021.

[147] "ATLAS sensitivity to winos and higgsinos with a highly compressed mass spectrum at the HL-LHC," Tech. Rep. ATL-PHYS-PUB-2018-031, CERN, Geneva, Nov 2018.

[148] X. Cid Vidal *et al.*, *Report from Working Group 3: Beyond the Standard Model physics at the HL-LHC and HE-LHC*, vol. 7, pp. 585–865. 12 2019.

[149] ATLAS Collaboration, "Expected performance of the ATLAS detector at the High-Luminosity LHC," *ATL-PHYS-PUB-2019-005*, 2019.

[150] ATLAS Collaboration, "Technical Design Report for the ATLAS Inner Tracker Pixel Detector," *CERN-LHCC-2017-021*, 9 2017.

[151] ATLAS Collaboration, "Search for electroweak production of supersymmetric states in scenarios with compressed mass spectra at $\sqrt{s} = 13$ TeV with the ATLAS detector," *Phys. Rev. D*, vol. 97, no. 5, p. 052010, 2018.

[152] H. Baer, V. Barger, S. Salam, H. Serce, and K. Sinha, "LHC SUSY and WIMP dark matter searches confront the string theory landscape," *JHEP*, vol. 04, p. 043, 2019.

[153] A. Abada *et al.*, "HE-LHC: The High-Energy Large Hadron Collider: Future Circular Collider Conceptual Design Report Volume 4," *Eur. Phys. J. ST*, vol. 228, no. 5, pp. 1109–1382, 2019.

[154] P. Bambade *et al.*, "The International Linear Collider: A Global Project," 3 2019.

[155] "The Compact Linear Collider (CLIC) - Project Implementation Plan," vol. 4/2018, 12 2018.

[156] H. Baer, M. Berggren, K. Fujii, J. List, S.-L. Lehtinen, T. Tanabe, and J. Yan, "ILC as a natural SUSY discovery machine and precision microscope: From light Higgsinos to tests of unification," *Phys. Rev. D*, vol. 101, no. 9, p. 095026, 2020.

[157] N. Arkani-Hamed, T. Han, M. Mangano, and L.-T. Wang, "Physics opportunities of a 100 TeV proton–proton collider," *Phys. Rept.*, vol. 652, pp. 1–49, 2016.

[158] J. Bramante, P. J. Fox, A. Martin, B. Ostdiek, T. Plehn, T. Schell, and M. Takeuchi, "Relic Neutralino Surface at a 100 TeV Collider," *Phys. Rev. D*, vol. 91, p. 054015, 2015.

[159] S. D. Thomas and J. D. Wells, "Phenomenology of Massive Vectorlike Doublet Leptons," *Phys. Rev. Lett.*, vol. 81, pp. 34–37, 1998.

[160] L. Lista, "Setting limits and application to Higgs boson search," *EPJ Web of Conferences*, vol. 55, p. 03003, 2013.

[161] L. Lista, *Statistical Methods for Data Analysis in Particle Physics*, vol. 941. Springer, 2017.